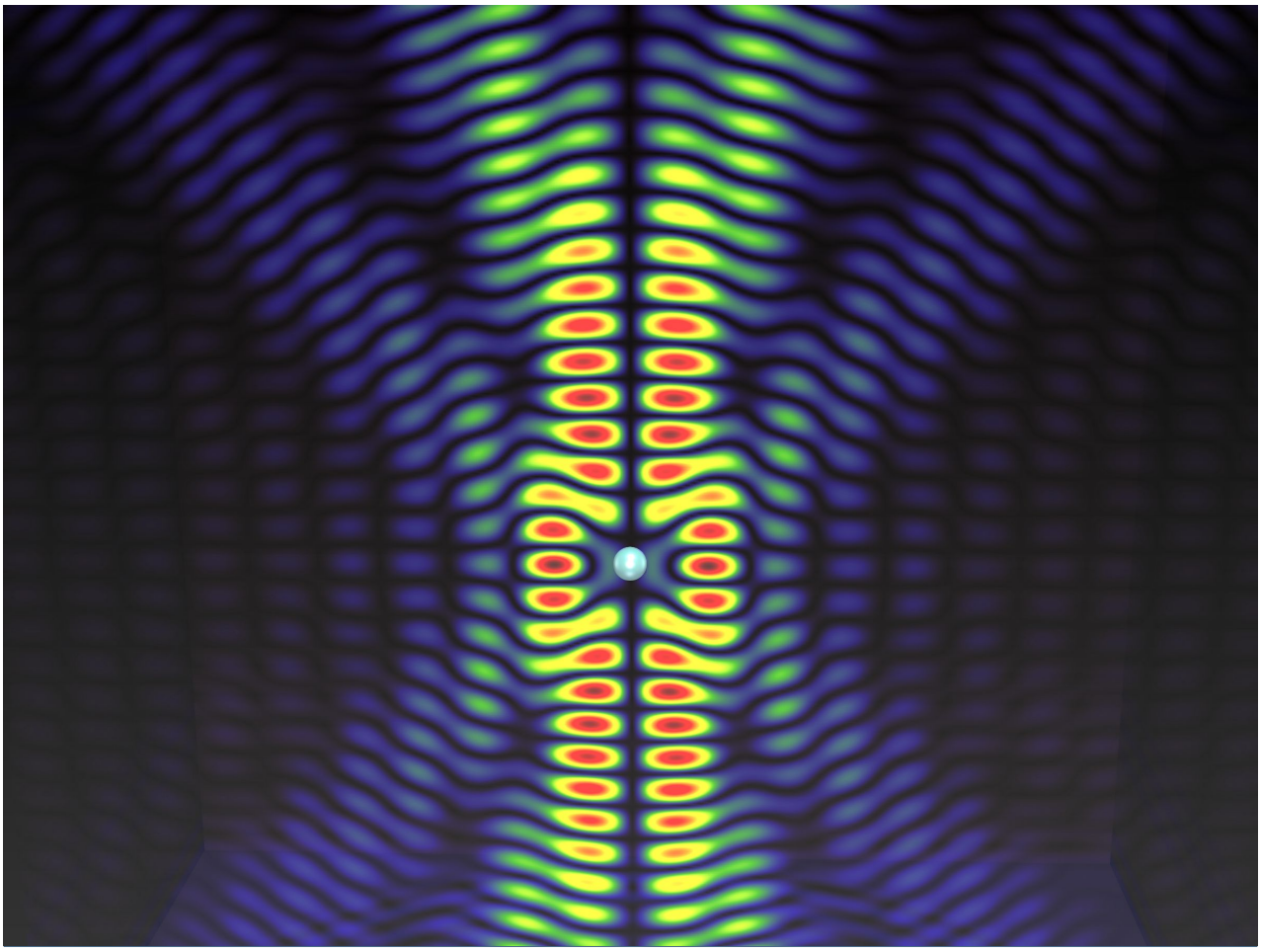
BEILSTEIN JOURNAL OF NANOTECHNOLOGY

Light–Matter interactions on the nanoscale

Edited by Chennupati Jagadish and Mohsen Rahmani



Generated on 12 November 2026, 11:32

Imprint

Beilstein Journal of Nanotechnology
www.bjnano.org
ISSN 2190-4286
Email: journals-support@beilstein-institut.de

The *Beilstein Journal of Nanotechnology* is published by the Beilstein-Institut zur Förderung der Chemischen Wissenschaften.

Beilstein-Institut zur Förderung der Chemischen Wissenschaften
Trakehner Straße 7–9
60487 Frankfurt am Main
Germany
www.beilstein-institut.de

The copyright to this document as a whole, which is published in the *Beilstein Journal of Nanotechnology*, is held by the Beilstein-Institut zur Förderung der Chemischen Wissenschaften. The copyright to the individual articles in this document is held by the respective authors, subject to a Creative Commons Attribution license.

The cover image by Andrey Miroshnichenko is licensed under CC-BY 4.0.

BEILSTEIN JOURNAL OF NANOTECHNOLOGY

Light–Matter interactions on the nanoscale

Mohsen Rahmani* and Chennupati Jagadish*

Editorial

Open Access

Address:
Research School of Physics and Engineering, The Australian National University, Canberra, ACT 2601, Australia

Email:
Mohsen Rahmani* - Mohsen.Rahmani@anu.edu.au;
Chennupati Jagadish* - Chennupati.Jagadish@anu.edu.au

* Corresponding author

Keywords:
light-matter interactions; nano-optics; nanophotonics; plasmonics

Beilstein J. Nanotechnol. **2018,** *9,* 2125–2127.
doi:10.3762/bjnano.9.201

Received: 07 July 2018
Accepted: 19 July 2018
Published: 10 August 2018

This article is part of the Thematic Series "Light–Matter interactions on the nanoscale".

Editor-in-Chief: T. Schimmel

© 2018 Rahmani and Jagadish; licensee Beilstein-Institut.
License and terms: see end of document.

At the beginning of the 20th century, researchers began harnessing the capabilities of electricity and magnetism. Today we are standing in a similar position as we contemplate the emergence of light–matter interactions at the nanoscale and how it will continue its exponential growth over the coming years. This research field, also called nanophotonics or nano-optics, is a subject of rapidly increasing scientific importance: controlling light–matter interactions beyond the diffraction limit. In contrast to optics, which is the concept of light rays, including absorption, transmission and reflection, photonics is the concept of light science, including emission, detection, amplification and control of light. Photonics offers a wide range of applications in different areas ranging from sensing and imaging, to solar cells and optical communication [1]. It is no surprise that many consider photonics to be the technology revolution of the 21st century.

Laser processing of thin-film multilayer structures has been one of the initial research directions in photonics [2]. This technique has been employed for many applications, including but not limited to the fabrication of polycrystalline silicon (poly-Si) thin-film transistors or MEMS/NEMS devices, as well as biomedical engineering [3,4]. Subsequently, with advances in photolithography, the microscale structure of materials began to attract much research interest due to their unique capability to interact with an applied electromagnetic wave in the radio frequency and terahertz regions [5]. This part of the spectrum has unique properties, such as being non-ionizing and subject to considerably less Rayleigh scattering [6]. In the last decade, by exploiting the rapid progress in computational and characterisation techniques, together with advances in techniques for the fabrication nanostructures, researchers performed detailed studies on the light–matter interaction in the visible and near-infrared region for nanostructures with dimensions on the order of (or even smaller than) the wavelength [7].

Metallic nanoparticles have been most heavily studied particles to bridge the gap between conventional optics and highly integrated nanophotonic components via stimulating the oscillation of free electrons on the surface, so-called surface plasmons [8]. Stimulated by the flourishing field of plasmonics, many novel effects have been suggested and even demonstrated, including super-scattering, clocking, control of the scattering direction, artificial antiferromagnetism, etc. [9]. Meanwhile, inverse plasmonics, that is, apertures in metallic films, has also been the subject of ongoing research [10]. Although many plasmonic ap-

plications have faced fundamental limitations (due to the ohmic losses in metals), the knowledge is still valuable for developing new strategies for light–matter interactions on the nanoscale.

High refractive index dielectric [11] and semiconductor [12] nanostructures have been recently exploited as an alternative to plasmonics [13]. Dielectrics and semiconductors benefit from negligible resistive losses. This advantage allows excitation at large light intensities for significant concentration of light at the nanoscale, which is not limited to interfaces. Such nanostructures have multipolar characteristics of both electric and magnetic resonant modes that could aid in the engineering of light behaviour at the nanoscale. Among various applications of dielectric nanostructures, metasurfaces, composed of a single or a few stacked layers of subwavelength nanostructures/particles, are growing in popularity [14]. This is because metasurfaces can offer a diverse range of applications, including sensing and optical tuning, dispersion engineering and polarization manipulation [14].

Recently, it has been demonstrated that light–matter interactions at the nanoscale can even be induced via sub-nanometer materials [15,16], for example, graphene [17]. The interaction of graphene with electromagnetic radiation is fascinating due to the two-dimensional confinement of electrons and the exceptional band structure of graphene. Graphene has a simple band structure with zero band gap, but its optical response is nontrivial. Subsequently, other two-dimensional (2D) materials, such as transition-metal dichalcogenides (TMDCs) or hexagonal boron nitride (hBN) [10] have also emerged as interesting platforms for nanophotonics. TMDCs, with their intrinsically broken inversion symmetry in crystal structure, have shown many advanced optical properties with potential applications such as in valleytronics. On the other hand, hBN has promising hyperbolic properties as well as the ability to host a range of single photon emitters (SPEs) for quantum photonic applications.

In summary, the field of photonics is ever growing and the life of people will be greatly influenced by the developments in this area. This Thematic Series can guide readers in understanding the physics of light matter–interaction with various kinds of nanostructures, including metallic (plasmonic), dielectric and semiconductor, 2D, as well as hybrid nanostructures [18]. Meanwhile, readers can become more familiar with the cutting edge advances in this respect.

Mohsen Rahmani and Chennupati Jagadish

Canberra, July 2018

ORCID® iDs

Mohsen Rahmani - https://orcid.org/0000-0001-9268-4793
Chennupati Jagadish - https://orcid.org/0000-0003-1528-9479

References

1. Mokkapati, S.; Jagadish, C. *Mater. Today* **2009,** *12,* 22–32. doi:10.1016/S1369-7021(09)70110-5
2. Tóth, Z.; Szörényi, T. *Appl. Phys. A: Solids Surf.* **1991,** *52,* 273–279. doi:10.1007/BF00324591
3. Kim, J.; Na, S. *Opt. Laser Technol.* **2007,** *39,* 1443–1448. doi:10.1016/j.optlastec.2006.10.001
4. Naghshine, B. B.; Kiani, A. *Beilstein J. Nanotechnol.* **2017,** *8,* 1749–1759. doi:10.3762/bjnano.8.176
5. Zaichun, C.; Rahmani, M.; Yandong, G.; Chong, C. T.; Minghui, H. *Adv. Mater.* **2012,** *24,* OP143–OP147. doi:10.1002/adma.201104575
6. Parkinson, P.; Lloyd-Hughes, J.; Gao, Q.; Tan, H. H.; Jagadish, C.; Johnston, M. B.; Herz, L. M. *Nano Lett.* **2007,** *7,* 2162–2165. doi:10.1021/nl071162x
7. Chen, L.; Zhou, Y.; Wu, M.; Hong, M. *Opto–Electron. Adv.* **2018,** *1,* 170001. doi:10.29026/oea.2018.170001
8. Gennaro, S. D.; Rahmani, M.; Giannini, V.; Aouani, H.; Sidiropoulos, T. P. H.; Navarro-Cía, M.; Maier, S. A.; Oulton, R. F. *Nano Lett.* **2016,** *16,* 5278–5285. doi:10.1021/acs.nanolett.6b02485
9. Giannini, V.; Fernández-Domínguez, A. I.; Heck, S. C.; Maier, S. A. *Chem. Rev.* **2011,** *111,* 3888–3912. doi:10.1021/cr1002672
10. Kim, S.; Toth, M.; Aharonovich, I. *Beilstein J. Nanotechnol.* **2018,** *9,* 102–108. doi:10.3762/bjnano.9.12
11. Lamprianidis, A. G.; Miroshnichenko, A. E. *Beilstein J. Nanotechnol.* **2018,** *9,* 1478–1490. doi:10.3762/bjnano.9.139
12. Jagadish, C.; Pearton, C. J. *Zinc oxide bulk, thin films and nanostructures: processing, properties, and applications;* Elsevier, 2011.
13. Kuznetsov, A. I.; Miroshnichenko, A. E.; Fu, Y. H.; Zhang, J.; Luk'yanchuk, B. *Sci. Rep.* **2012,** *2,* 492. doi:10.1038/srep00492
14. Rahmani, M.; Xu, L.; Miroshnichenko, A. E.; Komar, A.; Camacho-Morales, R.; Chen, H.; Zárate, Y.; Kruk, S.; Zhang, G.; Neshev, D. N.; Kivshar, Y. S. *Adv. Funct. Mater.* **2017,** *27,* 1700580. doi:10.1002/adfm.201700580
15. Chen, H.; Liu, M.; Xu, L.; Neshev, D. N. *Beilstein J. Nanotechnol.* **2018,** *9,* 780–788. doi:10.3762/bjnano.9.71
16. Wang, S.; Ouyang, X.; Feng, Z.; Cao, Y.; Gu, M.; Li, X. *Opto–Electron. Adv.* **2018,** *1,* 170002. doi:10.29026/oea.2018.170002
17. Glukhova, O. E.; Shmygin, D. S. *Beilstein J. Nanotechnol.* **2018,** *9,* 1254–1262. doi:10.3762/bjnano.9.117
18. Ward, J.; Kamali, K. Z.; Xu, L.; Zhang, G.; Miroshnichenko, A. E.; Rahmani, M. *Beilstein J. Nanotechnol.* **2018,** *9,* 460–467. doi:10.3762/bjnano.9.44

License and Terms

This is an Open Access article under the terms of the Creative Commons Attribution License (http://creativecommons.org/licenses/by/4.0). Please note that the reuse, redistribution and reproduction in particular requires that the authors and source are credited.

The license is subject to the *Beilstein Journal of Nanotechnology* terms and conditions: (https://www.beilstein-journals.org/bjnano)

The definitive version of this article is the electronic one which can be found at: doi:10.3762/bjnano.9.201

BEILSTEIN JOURNAL OF NANOTECHNOLOGY

Laser processing of thin-film multilayer structures: comparison between a 3D thermal model and experimental results

Babak B. Naghshine[1] and Amirkianoosh Kiani[*1,2]

Full Research Paper

Open Access

Address:
[1]Silicon Hall: Laser Micro/Nano Fabrication Facility, Department of Mechanical Engineering, University of New Brunswick, NB, Canada and [2]Department of Automotive, Mechanical and Manufacturing Engineering, University of Ontario Institute of Technology (UOIT), ON, Canada

Email:
Amirkianoosh Kiani[*] - amirkianoosh.kiani@uoit.ca

* Corresponding author

Keywords:
3D transient modelling; heat transfer; laser materials processing; nanosecond pulses; silicon; thin-film

Beilstein J. Nanotechnol. **2017,** *8,* 1749–1759.
doi:10.3762/bjnano.8.176

Received: 05 June 2017
Accepted: 09 August 2017
Published: 24 August 2017

This article is part of the Thematic Series "Light–Matter interactions on the nanoscale".

Guest Editor: M. Rahmani

© 2017 Naghshine and Kiani; licensee Beilstein-Institut.
License and terms: see end of document.

Abstract

In this research, a numerical model is introduced for simulation of laser processing of thin film multilayer structures, to predict the temperature and ablated area for a set of laser parameters including average power and repetition rate. Different thin-films on Si substrate were processed by nanosecond Nd:YAG laser pulses and the experimental and numerical results were compared to each other. The results show that applying a thin film on the surface can completely change the temperature field and vary the shape of the heat affected zone. The findings of this paper can have many potential applications including patterning the cell growth for biomedical applications and controlling the grain size in fabrication of polycrystalline silicon (poly-Si) thin-film transistors (TFTs).

Introduction

Laser processing of thin-film multilayer structures has been studied since the early 1990s [1]. However, the field has been largely neglected by researchers and there have been very few studies in this area [2-4]. On the other hand, it has many interesting applications that can introduce new possibilities to the art of laser processing. One of the most interesting applications is the fabrication of polycrystalline silicon (poly-Si) thin-film transistors (TFTs). In this method, a thin film of amorphous silicon (a-Si) is deposited on a glass substrate, where it is processed by a UV laser beam. Since a-Si has a very high absorption at UV spectrum, it can be recrystallized into poly-Si by the laser beam without causing any considerable temperature change in the substrate [5-7]. There are also various laser doping techniques such as spin coating the Si layer with a phosphorus- or boron-containing liquid before laser processing the surface for n- and p-type TFTs respectively [8]. Another important application is mask repairing for MEMS/NEMS device fabrication [4]. There are also many potential applications in biomedical engineering. It's been proven that laser processing a metallic surface can significantly improve the biocompatibility

in the ablated area and living cells can adhere better to the surface [9-13] whereas, the heat affected zone becomes less biocompatible and cells will avoid that area [14]. Therefore, the growing pattern of the cells can be controlled by laser processing of the surface which has many potential applications in biomedical engineering. As will be shown in this paper, the shape and size of these zones can be controlled by applying a thin-film layer on the surface. Altering the electrical properties of the surface for biosensor fabrication is one of the applications that has not been fully explored yet.

Modelling this process can be helpful in many ways. For instance, controlling the grain size of the resulting poly-Si layer is vital in the process of fabricating poly-Si TFTs [6,7]. This can be only obtained by controlling the temperature and cooling rate of the thin film during laser processing. As the process occurs over a very short time it's difficult to measure the temperature, and a proper thermal model can be the most useful tool for controlling the temperature. Another possible application is finding the best laser parameters and layer thickness for controlling the size of heat affected zone and ablated zone for patterning the cell, as mentioned in the previous paragraph.

Despite the necessity for thermal modelling of this process, there have been very few efforts in this area so far. In previous works, only simple one-dimensional models were used to calculate the temperature of different thin-film structures without considering the phase change [4,15].

There are many models for laser processing of bulk materials [16-21]. There are some analytical solutions to the one- or two-dimensional heat conduction equation to predict the temperature. An example can be found in the work of Hendow and Shakir, who solved the 2D equation to calculate the temperature field after irradiating the surface with two consecutive pulses [16]. Another example is the work of Chen et al. who solved the same equation for repetitive laser pulses [17]. There are also many numerical models that provide us with much more information about the process. Weidmann et al. carried out a numerical analysis by solving the 2D equation. They used Arhenius equation for estimation of the speed of ablation to predict the ablated area [18]. Sinha numerically solved the 2D heat equation assuming phase changes by changing the size of computational cells during ablation [19]. In some models plasma shielding was taken into account as an effective factor. An example can be seen in the work of Marla et al. who solved the 1D equation for temperature-dependent properties [20].

In this paper, a transient 3D model, which has been previously proven capable of precisely predicting the temperature and ablation zone for a bulk material [21], has been modified and used for a thin-film multilayer structure. In this model, the physical and thermal properties are assumed to be a function of temperature and space; plasma shielding and phase change are taken into account. The temperature field and ablated area will be for Si substrates that are coated with different thin-film layers at various laser parameters. Finally, a comparison will be made between the numerical and experimental results.

Results and Discussion

The samples were processed with different laser parameters (power and frequency) and the hole profiles were captured using the 3D optical profiler from at least ten different points for each sample.

Laser processing of Si substrate (bulk material)

The melting and boiling points of silicon are 1414 °C and 3538 °C respectively and the heats of fusion and vaporization are 1788 and 13637 kJ/kg [22]. After introducing all the physical properties and the plasma absorption of the silicon, the numerical analysis was carried out and calculated and measured profiles were compared to each other.

As can be seen in Table 1, the numerical and experimental results are in good agreement. The results for varying frequencies at 5 W are presented in Figure 1. The holes on the surface of the specimen that was processed at 75 kHz and 5 W were very shallow and it was difficult to capture a precise profile using the 3D optical profiler. This was mainly due to the noise captured by the equipment (there were some fluctuations around 0.2–0.3 μm on their surfaces). However, the 2D images of the sample's surface verify the formation of these shallow holes on the surface. This is in agreement with the calculated depth (0.4 μm).

Table 1: Measured and calculated data for the ablation cross-section for uncoated Si samples.

Power (W)	Frequency (kHz)	Averaged measured depth (μm)	Calculated depth (μm)	Accuracy (%)
5	25	1.6	1.8	87.5
5	50	1.4	1.5	92.9
5	75	–	0.4	–
10	50	2.2	2.1	95.6
15	50	1.9	1.9	100

Figure 2 shows the profiles for varying laser power at the repetition rate of 50 kHz. The hole profiles were successfully calculated and are in accordance with experimental results.

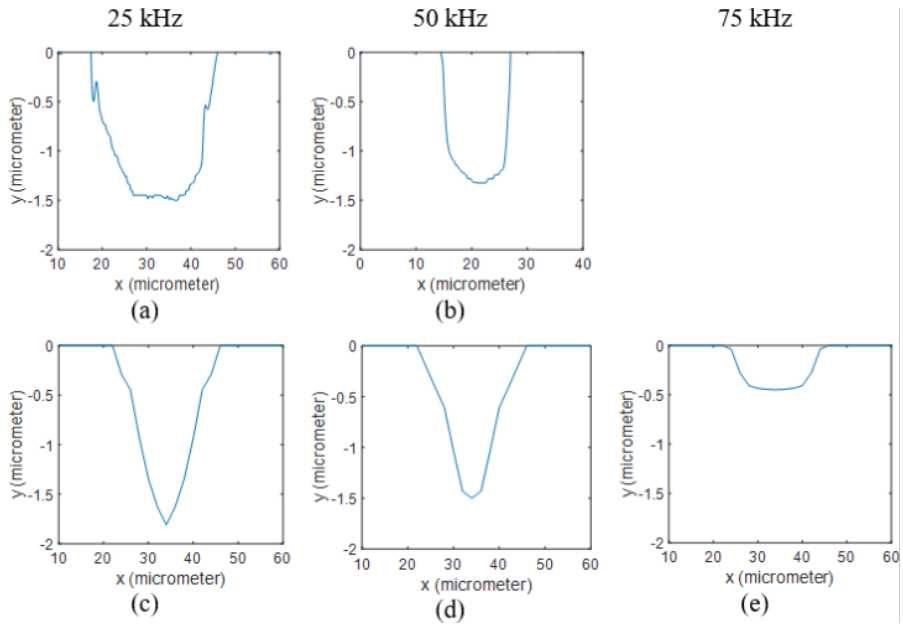


Figure 1: 2D profiles of uncoated Si samples processed at 5 W. Results obtained from measurements when using (a) 25 kHz and (b) 50 kHz are compared to the ones calculated through the numerical model at (c) 25 kHz, (d) 50 kHz and (e) 75 kHz.

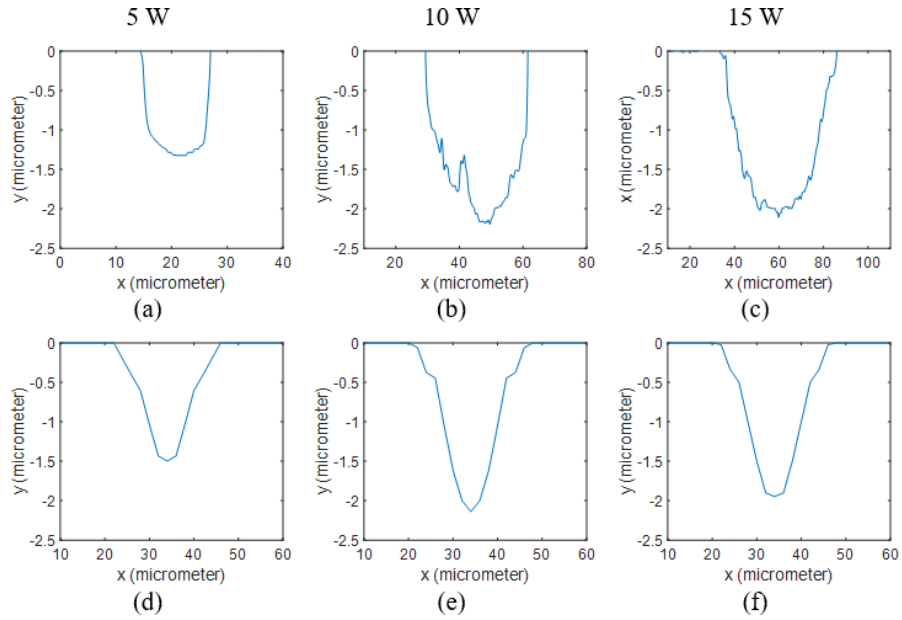


Figure 2: 2D profiles of uncoated Si samples processed at 50 kHz. Results obtained from measurements when using (a) 5 W, (b) 10 W and (c) 15 W are compared to the ones calculated through the numerical model at (d) 5 W, (e) 10 W and (f) 15 W.

The diameters of the holes at low frequencies and high powers are slightly larger in the experimental results. The laser-driven shock wave and the flow of the molten silicon, which were not considered in the model, can explain the smaller calculated hole diameter.

Figure 3 shows the temperature contour at the end of the pulse on the surface and cross-section of the silicon sheet for a repetition rate of 50 kHz and a power of 5 W. The melting point is highlighted and shows a molten zone formed around the ablated area. The pressure difference caused by the shock wave can

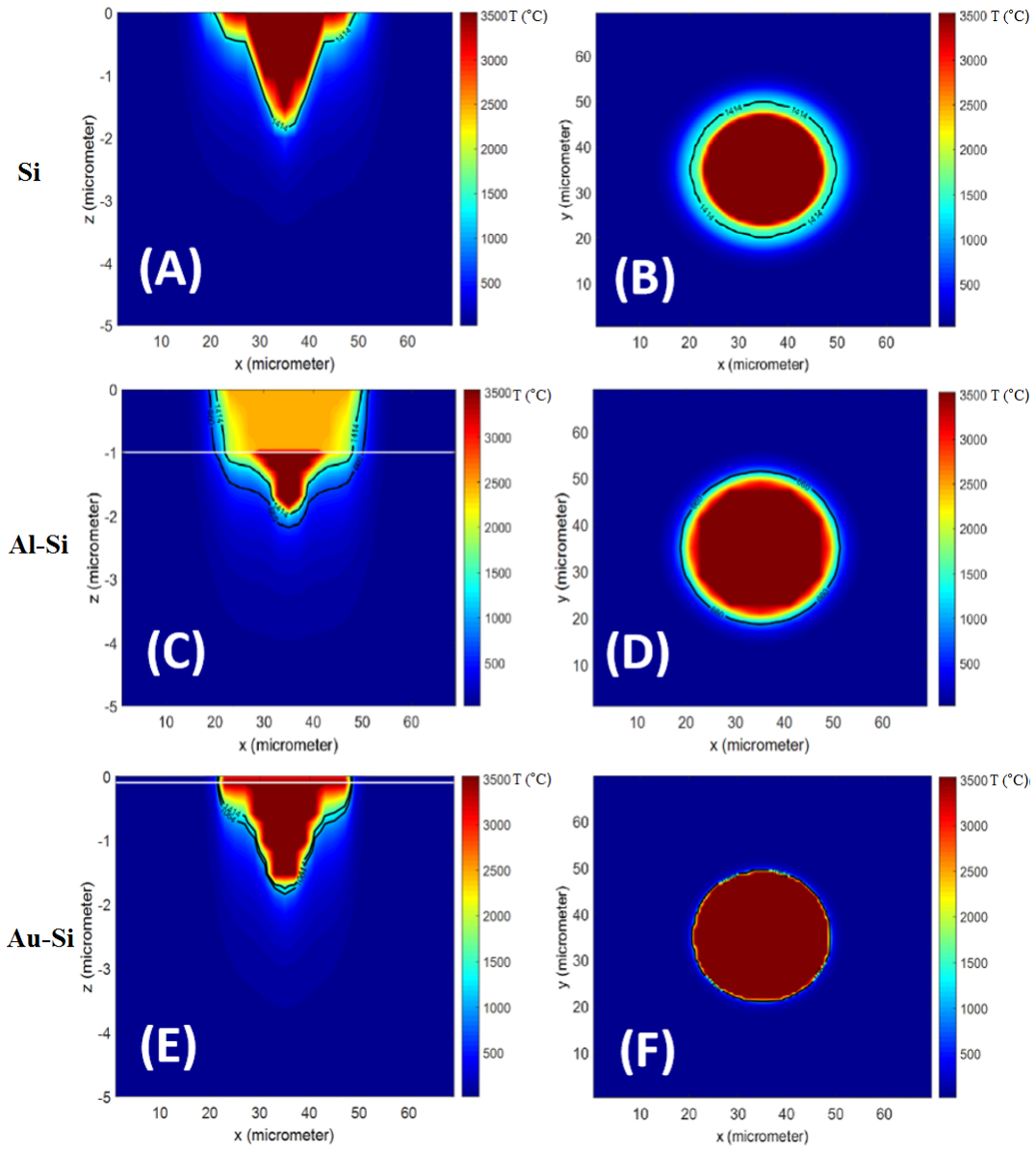


Figure 3: Temperature contours obtained from the numerical model at the end of the pulse at 50 kHz and 5 W for (a) cross-section of uncoated Si, (b) surface of uncoated Si, (c) cross-section of Al coated Si (d) surface of Al coated Si, (e) cross-section of Au coated Si, (f) surface of Au coated Si. The melting points of the materials are depicted by black lines and the interface between the layers is shown by white lines.

push away the molten material and make both molten and ablated zones slightly larger. At low frequencies and high powers, the peak power of the laser pulses would be larger, which results in a stronger shock wave. The fluid dynamics of the molten material is not in the scope of this paper and was not considered in the model.

Laser processing of Al-Si thin-film substrate

The melting and boiling points of aluminum are 660 °C and 2470 °C respectively and aluminum has a latent heat of fusion of 397 kJ/kg and a latent heat of vaporization of 10,800 kJ/kg [22]. The measured and calculated ablation depths are presented in Table 2. The surface profiles at different frequencies and 5 W are shown in Figure 4. By applying a thin aluminum film to the surface, the ablation depth was significantly increased at 75 kHz compared to bare silicon samples. This can be explained by the smaller latent heat of vaporization and lower boiling temperature of aluminum, which means more material can be ablated using the same amount of energy. This can be further verified by the deeper holes at 25 and 50 kHz. The other reason is the lower plasma absorption of aluminum compared to silicon based on the calculated plasma absorption functions. Since the

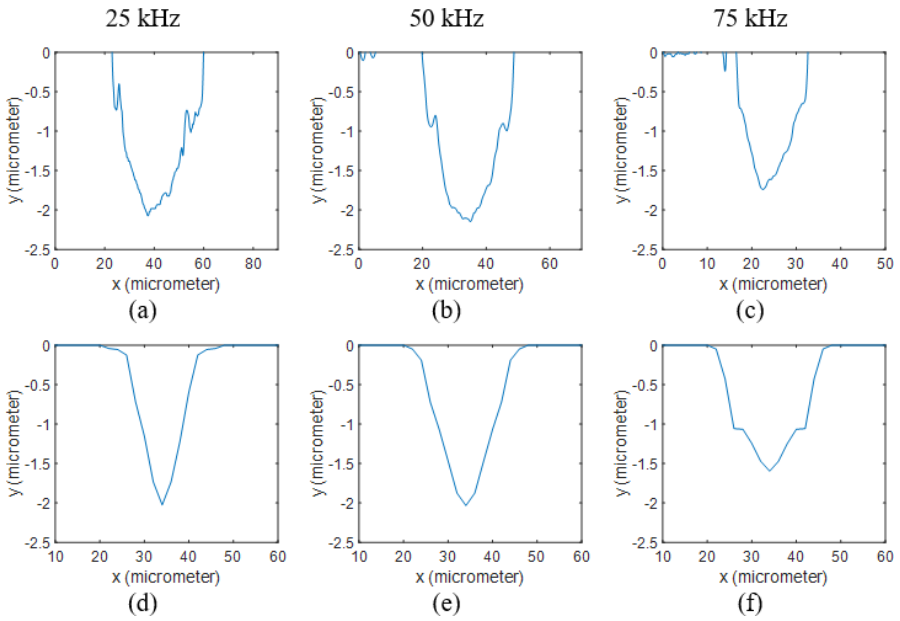


Figure 4: 2D profiles of Al coated Si samples processed at 5 W. Results obtained from measurements when using (a) 25 kHz, (b) 50 kHz and (c) 75 kHz are compared to the ones calculated through the numerical model at (d) 25 kHz, (e) 50 kHz and (f) 75 kHz.

Table 2: Measured and calculated data for the ablation cross-section for Al coated Si.

Power (W)	Frequency (kHz)	Averaged measured depth (µm)	Calculated depth (µm)	Accuracy (%)
5	25	2.1	2	95.2
5	50	2	2	100
5	75	1.5	1.6	93.3
10	50	2.4	2.5	95.8
15	50	3.7	4.1	89.2

single pulses are studied here, the processing time is extremely short and the material plume mainly contains the particles of the material of the thin film, which results in completely different plasma absorption functions for the three samples. Similar conclusions can be made from Figure 5 for various powers, and the holes are generally deeper in the aluminum coated samples. Furthermore, the predicted hole diameters are smaller than the actual values at low frequencies and high powers. This is because the stronger shock waves push the molten material away to the edges, which is not considered in the model.

At the interface of the two layers (1 µm away from the surface), the diameter of the hole can be seen suddenly decreasing in the silicon layer. This diameter change was apparent in the numerical results; however, it is not as obvious as in the experimental data. This can be explained by the results shown in Figure 3, which shows the maximum temperature at the end of the pulse on the surface and at the cross-section of the sample at 50 kHz and 5 W. In these contours, the melting points of aluminum and silicon are highlighted (660 and 1414 °C). It can be clearly seen that the molten zone in aluminum is slightly larger than silicon. Consequently, the molten aluminum is pushed away to the edges by the laser-driven shock wave. As mentioned in the previous section, the shock wave and fluid dynamics of the molten material are neglected in this model, which makes the predicted diameter reduction smaller compared to the actual profile at high pulse energies.

Laser processing of Au-Si thin-film structure

The variations of specific heat of gold with temperature are unknown. Consequently, c_p was kept constant at 129 J/kgK in the model. The melting point, boiling point, latent heat of fusion, and latent heat of vaporization are 1064 °C, 2970 °C, 64 kJ/kg and 1,736 kJ/kg respectively [22]. The calculated and measured hole profiles are shown in Figure 6 and Figure 7 and measured and calculated depths are shown in Table 3. It is evident that the holes became slightly deeper at high powers compared to bare silicon samples. This can be explained by the reasons stated in the previous section. Based on the calculated plasma absorption functions, the absorption is lower for gold-coated samples, and again, the shock wave pushed away the molten material (Figure 3), resulting in deeper and wider holes. However, the molten zone is very small for gold coated samples, which means the deeper holes created on the gold coated surface are mainly caused by the lower plasma absorption.

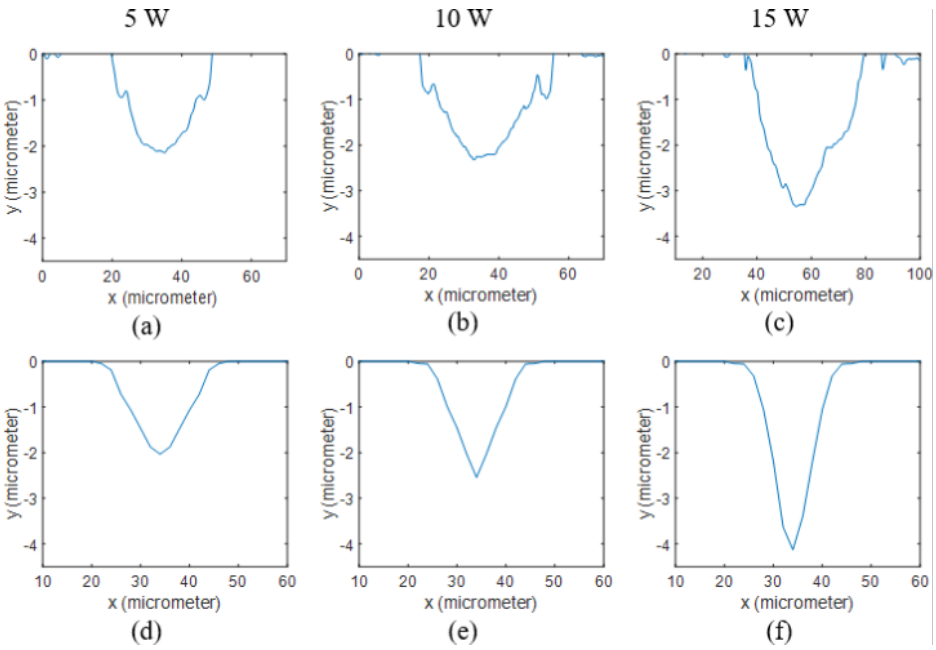


Figure 5: 2D profiles of Al coated Si samples processed at 50 kHz. Results obtained from measurements when using (a) 5 W, (b) 10 W and (c) 15 W are compared to the ones calculated through the numerical model at (d) 5 W, (e) 10 W and (f) 15 W.

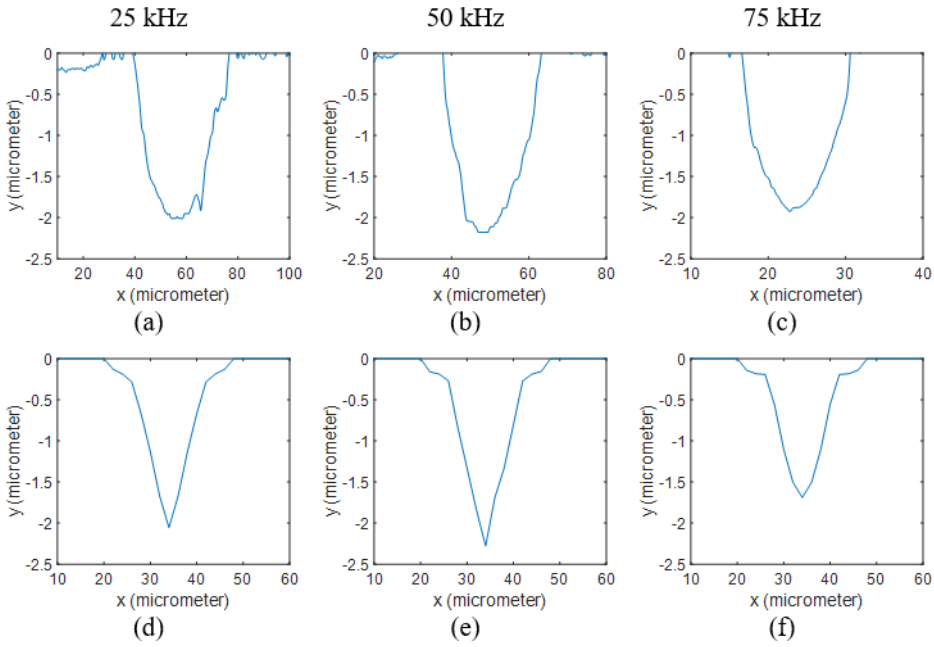


Figure 6: 2D profiles of Au coated Si samples processed at 5 W. Results obtained from measurements when using (a) 25 kHz, (b) 50 kHz and (c) 75 kHz are compared to the ones calculated through the numerical model at (d) 25 kHz, (e) 50 kHz and (f) 75 kHz.

The results presented in this paper can be manipulated for cell patterning applications. Figure 3 depicts that, the size and shape of the heat affected zone and ablated area can be significantly altered by applying a thin film on the surface. As mentioned earlier these are the areas that become less and more biocompatible respectively. As a result, controlling the size of these areas makes the concept of patterning the cell growth by laser processing even more attractive.

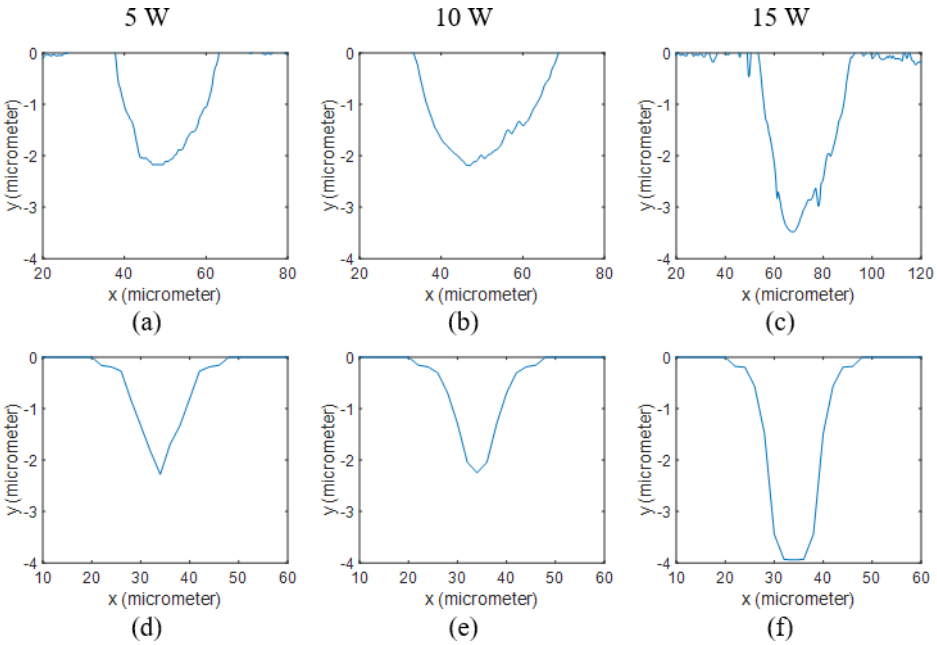


Figure 7: 2D profiles of Au coated Si samples processed at 50 kHz. Results obtained from measurements when using (a) 5 W, (b) 10 W and (c) 15 W are compared to the ones calculated through the numerical model at (d) 5 W, (e) 10 W and (f) 15 W.

Table 3: Measured and calculated data for the ablation cross-section for Au coated Si.

Power (W)	Frequency (kHz)	Averaged measured depth (μm)	Calculated depth (μm)	Accuracy (%)
5	25	2.1	2.1	100
5	50	2.2	2.3	95.5
5	75	1.8	1.7	94.4
10	50	2.1	2.2	95.2
15	50	3.6	3.9	91.7

Conclusion

The model introduced in this paper is able to precisely predict the ablation depth and temperature field of the thin-film coated samples processed by a single nanosecond pulse. Silicon substrates coated with gold and aluminium thin films and pure silicon sheets were treated by single nanosecond laser pulses and experimental and numerical results were compared. This model can be extremely helpful in the fabrication of poly-Si TFTs by predicting the temperature and cooling rate during the laser processing step for controlling the grain size. Moreover, it was proved that, by applying a thin film of different materials with different thicknesses on the surface the shape and size of the heat affected zone can be controlled. The model can be further modified in future studies for laser processing of thin film coated materials along a linear pattern by introducing the scanning speed and movement of the laser beam.

Experimental Setup

Materials

In this paper, three different samples (wafer by University Wafer, Inc.) were processed by the laser beam at different powers and repetition rates:

1. Single crystalline silicon wafer <100>
2. c-silicon wafer <100> coated by an aluminum layer with the thickness of 1 μm.
3. c-silicon wafer <100> coated by a very thin gold layer with a thickness around 100 nm.

The thin films were deposited on the surface of the samples using physical vapor deposition technique and the samples were purchased with thin-film coating and were directly used for laser processing.

Laser processing of thin-film structures

All the specimens were processed by an neodymium-doped yttrium aluminum garnet (Nd:YAG) nanosecond laser system (Bright Solutions SOL-20). Frequency and power can be directly controlled by changing the level of emission, whereas the pattern, line distance, and scanning speed are controlled using the EZCAD© software. The wavelength of the laser beam was 1064 nm and the pulse duration was extracted from performance curves provided by the manufacturer. An iris diaphragm reduced the diameter of the output beam from 9 mm to 8 mm. The beam then went to the galvo scanner (JD2204 by Sino-

Galvo), which has an input aperture of 10 mm and beam displacement of 13.4 mm. The scan lens of the galvo scanner focused the beam on the surface of the samples. The theoretical focused beam spot diameter was calculated to be around 20 µm and a Gaussian profile was assumed for the laser beam.

All the numerical analysis and experiments in this paper were carried out on single pulses. The laser pulses cannot be easily isolated due to limitations of the equipment. To isolate the single pulses, the scanning speed was set at its maximum value (around 1000 mm/s) and if the repetition rate was relatively low, the distance between the locations of two neighboring pulses on the surface would be long enough to remove the effect of the neighboring pulses. Therefore, a dotted pattern appears on the surface and each dot corresponds to a single pulse on the surface (Figure 8).

Three-dimensional (3D) optical profiler

A Zeta-20 Optical Profiler (Zeta Instruments) was used to obtain surface profiles of the samples for quantitative topography measurements. This optical profiler can capture 2D and 3D images of a surface, which allows us to see the profile of the holes generated by the laser beam on the surface of the samples.

Numerical model

Heat transfer model

Since nanosecond pulses (where the pulse duration is in the nanosecond range) are studied in this paper, the whole process is in the hot-ablation domain. Therefore, the process can be modelled using regular laws of heat transfer and thermodynamics. A 3D transient model that was previously proven to be accurate for laser processing of the bulk materials [21] was customized for a multilayer structure and used in this paper.

In this model, the 3D heat conduction equation (Equation 1) is solved for a cubic domain considering varying thermal properties that are a function of temperature. This domain is discretized into interactive cubic cells, which can become smaller or be taken out of the system during the ablation process.

$$\rho c_{\mathrm{p}} \frac{\partial T}{\partial t} = k\left(\frac{\partial^2 T}{\partial x^2} + \frac{\partial^2 T}{\partial y^2} + \frac{\partial^2 T}{\partial z^2}\right) + \frac{\partial k}{\partial x}\frac{\partial T}{\partial x} + \frac{\partial k}{\partial y}\frac{\partial T}{\partial y} + \frac{\partial k}{\partial z}\frac{\partial T}{\partial z}. \quad (1)$$

This equation was discretized and solved using the Douglas–Gunn method [23], where each time step is broken into three sub-steps, and at each sub-step, tridiagonal systems are solved implicitly in one of the spatial directions. By introducing δ^2 operator and κ for each spatial direction (Equation 5 and Equation 6), the difference equations for each sub-step can be written as follows (Equation 2 to Equation 4):

$$\begin{aligned} T_{ijk}^{n+1/3} - T_{ijk}^{n} = {} & \frac{\kappa_{ijk}^{x}\delta_x^2}{2}\left(T^{n+1/3} + T^{n}\right) + \kappa_{ijk}^{y}\delta_y^2 T^{n} + \kappa_{ijk}^{z}\delta_z^2 T^{n} \\ & + \frac{\kappa_{i+1jk}^{x} - \kappa_{i-1jk}^{x}}{8}\begin{pmatrix} T_{i+1jk}^{n+1/3} + T_{i+1jk}^{n} \\ -T_{i-1jk}^{n+1/3} - T_{i-1jk}^{n} \end{pmatrix} \\ & + \frac{\kappa_{ij+1k}^{y} - \kappa_{ij-1k}^{y}}{4}\left(T_{ij+1k}^{n} - T_{ij-1k}^{n}\right) \\ & + \frac{\kappa_{ijk+1}^{z} - \kappa_{ijk-1}^{z}}{4}\left(T_{ijk+1}^{n} - T_{ijk-1}^{n}\right). \end{aligned} \quad (2)$$

$$\begin{aligned} T_{ijk}^{n+2/3} - T_{ijk}^{n} = {} & \frac{\kappa_{ijk}^{x}\delta_x^2}{2}\left(T^{n+1/3} + T^{n}\right) + \frac{\kappa_{ijk}^{y}\delta_y^2}{2}\left(T^{n+2/3} + T^{n}\right) \\ & + \kappa_{ijk}^{z}\delta_z^2 T^{n} + \frac{\kappa_{i+1jk}^{x} - \kappa_{i-1jk}^{x}}{8}\begin{pmatrix} T_{i+1jk}^{n+1/3} + T_{i+1jk}^{n} \\ -T_{i-1jk}^{n+1/3} - T_{i-1jk}^{n} \end{pmatrix} \\ & + \frac{\kappa_{ij+1k}^{y} - \kappa_{ij-1k}^{y}}{8}\begin{pmatrix} T_{ij+1k}^{n+2/3} + T_{ij-1k}^{n} \\ -T_{ij-1k}^{n+2/3} - T_{ij-1k}^{n} \end{pmatrix} \\ & + \frac{\kappa_{ijk+1}^{z} - \kappa_{ijk-1}^{z}}{4}\left(T_{ijk+1}^{n} - T_{ijk-1}^{n}\right). \end{aligned} \quad (3)$$

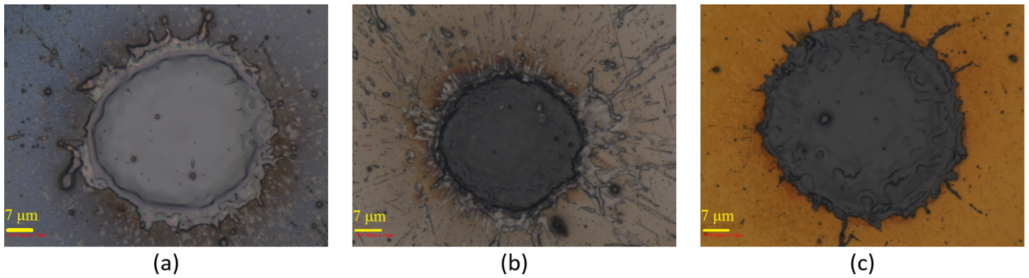


Figure 8: (a) Isolated pulse on the surface of silicon, (b) Isolated pulse on the surface of silicon coated by aluminum thin film, (c) Isolated pulse on the surface of silicon coated by gold thin film.

$$T_{ijk}^{n+1}-T_{ijk}^{n}=\frac{\kappa_{ijk}^{x}\delta_{x}^{2}}{2}\left(T^{n+1/3}+T^{n}\right)+\frac{\kappa_{ijk}^{y}\delta_{y}^{2}}{2}\left(T^{n+2/3}+T^{n}\right)+\frac{\kappa_{ijk}^{z}\delta_{z}^{2}}{2}\left(T^{n+1}+T^{n}\right)+\frac{\kappa_{i+1jk}^{x}-\kappa_{i-1jk}^{x}}{8}\begin{pmatrix}T_{i+1jk}^{n+1/3}+T_{i+1jk}^{n}\\-T_{i-1jk}^{n+1/3}-T_{i-1jk}^{n}\end{pmatrix}+\frac{\kappa_{ij+1k}^{y}-\kappa_{ij-1k}^{y}}{8}\begin{pmatrix}T_{ij+1k}^{n+2/3}+T_{ij+1k}^{n}\\-T_{ij-1k}^{n+2/3}-T_{ij-1k}^{n}\end{pmatrix}+\frac{\kappa_{ijk+1}^{z}-\kappa_{ijk-1}^{z}}{8}\left(T_{ijk+1}^{n+1}+T_{ijk+1}^{n}-T_{ijk-1}^{n+1}-T_{ijk-1}^{n}\right). \quad (4)$$

Where:

$$\delta_{x}^{2}T^{n}=T_{i+1jk}^{n}-2T_{ijk}^{n}+T_{i-1jk}^{n}, \quad (5)$$

$$\kappa_{ijk}^{x}=\frac{k_{ijk}^{n}\Delta t}{\rho c_{\mathrm{p}}\Delta x^{2}}. \quad (6)$$

Convection, radiation and laser irradiation are the boundary conditions at the surface. The laser beam has a Gaussian profile. On the back side, insulation boundary conditions are assumed. Convection and radiation are the boundary conditions of the other sides.

The flowchart of the computational code is shown in Figure 9. As can be seen, after calculating the temperature at the first two sub-steps, the temperature is calculated at the last sub-step. Whenever the calculated temperature passes the melting point or boiling point, the phase change algorithms are called and the last sub-step is repeated until convergence.

Phase change and ablation algorithms

Phase change and ablation algorithms were only applied in the last sub-step and at all the points where $T^{n+1/3}$ or $T^{n+2/3}$ were higher than the boiling point, they were reduced to the boiling temperature.

In the evaporation algorithm, the ablative energy (Equation 7) was calculated whenever the temperature of one or more cells was higher than the boiling temperature. In this equation, N is the number of cells with a temperature higher than boiling point.

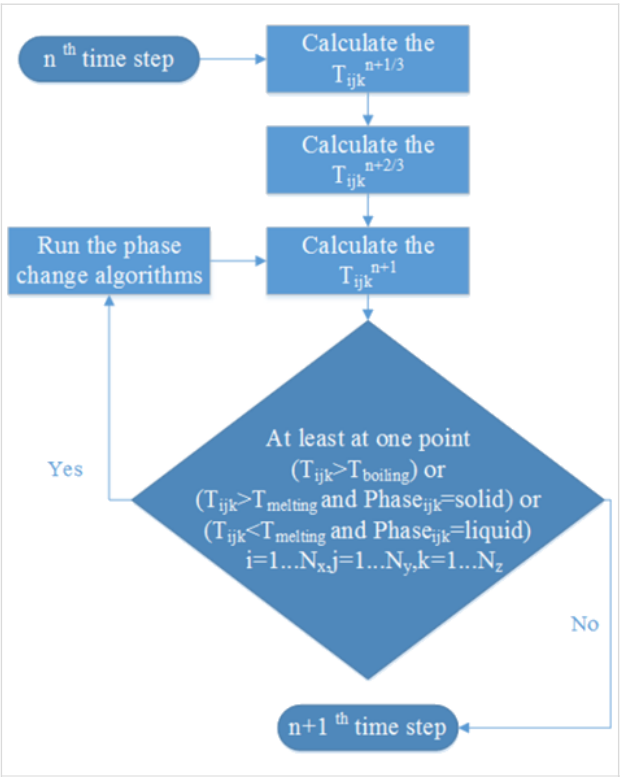


Figure 9: The computational flowchart at each time step.

$$\begin{aligned}Ablative\ energy&=\sum_{k=1}^{N}\rho\Delta x\Delta y\Delta z c_{\mathrm{p}}\left(T_{ijk}^{n+1}-T_{\mathrm{boiling}}\right)/\left(\Delta x\Delta y\Delta t\right)\\&=\sum_{k=1}^{N}\rho c_{\mathrm{p}}\Delta z\left(T_{ijk}^{n+1}-T_{\mathrm{boiling}}\right)/\Delta t\end{aligned} \quad (7)$$

If the ablative energy was enough to evaporate the top cell on the surface, then the cell was removed and its boundary conditions were transferred to the new top cell. Boundary conditions were updated for all the neighbouring cells and the laser energy was reduced by $\rho\Delta z L_{\mathrm{v}}/\Delta t$. Otherwise, if the energy was not enough, the cell became smaller (Δz was reduced by *Ablative energy* × $\Delta t/(\rho L_{\mathrm{v}})$) and the laser energy was decreased by the ablative energy. The last sub-step was repeated until convergence (*Ablative energy* = 0). Figure 10 shows the phase change flowchart for evaporation. Similar algorithms are considered for melting and solidification. As depicted in Figure 10, if the calculated temperature is above the boiling point, it will be determined if the whole cell should be removed or only its size must be reduced based on the described method. Then, the temperature is recalculated and this process is repeated until all the temperatures are below the boiling point.

Plasma shielding and power loss

A plasma absorption coefficient was introduced for the plasma shielding effect (Equation 8) [21].

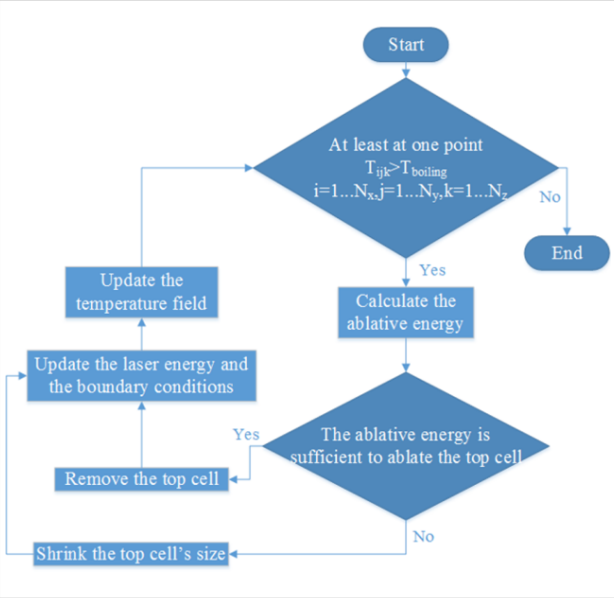


Figure 10: The flowchart of evaporation process.

$$\alpha_{\text{plasma}} = \alpha_{\max}\left(1-\exp\left(-c\psi\right)\right) \quad (8)$$

α_{max} is the maximum absorption that corresponds to the highest possible pulse power. ψ is non-dimensionalized pulse power, which is defined as the ratio of the pulse peak power to the highest possible peak power that can be generated by the laser beam. α_{max} and c are calculated from the experimental results.

Nomenclature

Table 4: Mathematical nomenclature.

ρ	density (kg/m^3)
c_p	specific heat (J/kgK)
T	temperature (K)
t	time (s)
k	thermal conductivity (W/mK)
h	convective heat transfer coefficient (W/m^{2}K)
σ	Stefan–Boltzmann constant (W/m^{2}K^4)
ε	emissivity
α	absorption
Δt	time step (s)
L_f	latent heat of fusion (J/kg)
L_v	latent heat of vaporization (J/kg)
Λ	optical thickness
α_{plasma}	plasma absorption
$h_{ablation}$	ablation depth (m)
E_a	energy absorbed by plasma (J)
α_{max}	maximum plasma absorption
ψ	non-dimensionalized pulse power

Acknowledgements

This research was funded by the National Sciences and Engineering Research Council (NSERC) Discovery Grant program, the New Brunswick Innovation Foundation (NBIF), and the McCain Foundation.

References

1. Tóth, Z.; Szörényi, T. *Appl. Phys. A: Solids Surf.* **1991,** *52,* 273–279. doi:10.1007/bf00324591
2. Yasumaru, N.; Miyazaki, K.; Kiuchi, J. *Appl. Phys. A: Mater. Sci. Process.* **2003,** *76,* 983–985. doi:10.1007/s00339-002-1979-2
3. Miyaji, G.; Miyazaki, K. *Opt. Express* **2008,** *16,* 16265–16271. doi:10.1364/oe.16.016265
4. Kim, J.; Na, S. *Opt. Laser Technol.* **2007,** *39,* 1443–1448. doi:10.1016/j.optlastec.2006.10.001
5. Jin, S.; Choe, Y.; Lee, S.; Kim, T.-W.; Mativenga, M.; Jang, J. *IEEE Electron Device Lett.* **2016,** *37,* 291–294. doi:10.1109/led.2016.2518705
6. Boyce, J. B.; Mei, P.; Fulks, R. T.; Ho, J. *Phys. Status Solidi A* **1998,** *166,* 729–741. doi:10.1002/(sici)1521-396x(199804)166:2<729::aid-pssa729>3.0.co;2-1
7. Kuriyama, H.; Kiyama, S.; Noguchi, S.; Kuwahara, T.; Ishida, S.; Nohda, T.; Sano, K.; Iwata, H.; Kawata, H.; Osumi, M.; Tsuda, S.; Nakano, S.; Kuwano, Y. *Jpn. J. Appl. Phys., Part 1* **1991,** *30,* 3700. doi:10.1143/jjap.30.3700
8. Ogane, A.; Hirata, K.; Horiuchi, K.; Nishihara, Y.; Takahashi, Y.; Kitiyanan, A.; Fuyuki, T. *Jpn. J. Appl. Phys.* **2009,** *48,* 071201. doi:10.1143/jjap.48.071201
9. Colpitts, C.; Ektesabi, A. M.; Wyatt, R. A.; Crawford, B. D.; Kiani, A. *J. Appl. Biomater. Funct. Mater.* **2017,** *15,* e84–e92. doi:10.5301/jabfm.5000327
10. Colpitts, C.; Kiani, A. *Nanomater. Nanotechnol.* **2016,** *6,* 8. doi:10.5772/62312
11. Radmanesh, M.; Ektesabi, A. M.; Wyatt, R. A.; Crawford, B. D.; Kiani, A. *Biointerphases* **2016,** *11,* 031009. doi:10.1116/1.4962066
12. Radmanesh, M.; Kiani, A. *J. Biomater. Nanobiotechnol.* **2015,** *6,* No. 57832. doi:10.4236/jbnb.2015.63017
13. Radmanesh, M.; Kiani, A. *J. Appl. Biomater. Funct. Mater.* **2016,** *14,* e70–e77. doi:10.5301/jabfm.5000258
14. Colpitts, C.; Ektesabi, A. M.; Wyatt, R. A.; Crawford, B. D.; Kiani, A. *J. Mech. Behav. Biomed. Mater.* **2017,** in press. doi:10.1016/j.jmbbm.2017.06.005
15. Bovatsek, J.; Tamhankar, A.; Patel, R. S.; Bulgakova, N. M.; Bonse, J. *Thin Solid Films* **2010,** *518,* 2897–2904. doi:10.1016/j.tsf.2009.10.135
16. Hendow, S. T.; Shakir, S. A. *Opt. Express* **2010,** *18,* 10188–10199. doi:10.1364/oe.18.010188
17. Chen, G.; Wang, Y.; Zhang, J.; Bi, J. *Int. J. Heat Mass Transfer* **2017,** *104,* 503–509. doi:10.1016/j.ijheatmasstransfer.2016.08.079
18. Weidmann, P.; Weber, U.; Schmauder, S.; Pedrini, G.; Osten, W. *Meccanica* **2016,** *51,* 279–289. doi:10.1007/s11012-015-0220-2
19. Sinha, S. *Ceram. Int.* **2015,** *41,* 6596–6603. doi:10.1016/j.ceramint.2015.01.106
20. Marla, D.; Bhandarkar, U. V.; Joshi, S. S. *Manuf. Lett.* **2014,** *2,* 13–16. doi:10.1016/j.mfglet.2013.12.001
21. Naghshine, B. B.; Kiani, A. *AIP Adv.* **2017,** *7,* 025007. doi:10.1063/1.4976725

22. Gale, W. F.; Totemeier, T. C. *Smithells metals reference book;* Butterworth-Heinemann: Burlington, MA, U.S.A., 2003.
23. Wang, T.-Y.; Chen, C. C. P. *IEEE Trans. VLSI Syst.* **2003,** *11,* 691–700. doi:10.1109/tvlsi.2003.812372

License and Terms

This is an Open Access article under the terms of the Creative Commons Attribution License (http://creativecommons.org/licenses/by/4.0), which permits unrestricted use, distribution, and reproduction in any medium, provided the original work is properly cited.

The license is subject to the *Beilstein Journal of Nanotechnology* terms and conditions: (http://www.beilstein-journals.org/bjnano)

The definitive version of this article is the electronic one which can be found at: doi:10.3762/bjnano.8.176

BEILSTEIN JOURNAL OF NANOTECHNOLOGY

Design of photonic microcavities in hexagonal boron nitride

Sejeong Kim*, Milos Toth and Igor Aharonovich

Letter

Open Access

Address:
School of Mathematical and Physical Sciences, University of Technology Sydney, Ultimo, NSW 2007, Australia

Email:
Sejeong Kim* - Sejeong.Kim-1@uts.edu.au

* Corresponding author

Keywords:
anisotropic optical materials; boron nitride; photonic crystals

Beilstein J. Nanotechnol. **2018,** *9,* 102–108.
doi:10.3762/bjnano.9.12

Received: 18 August 2017
Accepted: 12 December 2017
Published: 09 January 2018

This article is part of the Thematic Series "Light–Matter interactions on the nanoscale".

Guest Editor: M. Rahmani

© 2018 Kim et al.; licensee Beilstein-Institut.
License and terms: see end of document.

Abstract

We propose and design photonic crystal cavities (PCCs) in hexagonal boron nitride (hBN) for diverse photonic and quantum applications. Two dimensional (2D) hBN flakes contain quantum emitters which are ultra-bright and photostable at room temperature. To achieve optimal coupling of these emitters to optical resonators, fabrication of cavities from hBN is therefore required to maximize the overlap between cavity optical modes and the emitters. Here, we design 2D and 1D PCCs using anisotropic indices of hBN. The influence of underlying substrates and material absorption are investigated, and spontaneous emission rate enhancements are calculated. Our results are promising for future quantum photonic experiments with hBN.

Introduction

Hexagonal boron nitride (hBN) has recently emerged as an interesting platform for nanophotonics. This is mainly due to its promising hyperbolic properties [1,2] as well as the ability to host a range of single photon emitters (SPEs) that are of great interest for a myriad of nanophotonics and quantum photonic applications [3-10]. However, to further study light matter interactions based on the hBN SPEs, and to realize integrated nanophotonics systems, coupling of the emitters to optical cavities is essential [11-15].

Typically, SPEs can be coupled to optical cavities using two general approaches. The cavity is either made from the material that hosts the emitter (monolithic approach), or the emitter is coupled to a cavity made from a foreign material – also known as a hybrid approach [16]. The former process is preferred when attempting to maximize the field overlap between the emitters and the cavity modes, and is often employed when using materials that are amenable to scalable nanofabrication protocols, such as gallium arsenide or silicon [17,18], and more recently diamond and silicon carbide [19,20]. The hybrid approach is easier from the fabrication point of view but is inherently limited by the fact that the electric field maxima of optical modes are situated within the cavities, and optimal coupling therefore remains a challenge.

The optical properties of hBN make it an attractive candidate for a monolithic cavity system. In particular, hBN has a wide bandgap of ≈6 eV which makes it transparent in the visible spectral range that contains the zero phonon lines (ZPLs) of a range of ultra-bright emitters [21]. Furthermore, hBN has properties which are desirable for micro-resonators such as a high chemical stability and an excellent thermal conductivity [22,23].

In this work, we propose to use hBN for the fabrication of photonic crystal cavities (PCCs). We design two dimensional (2D) PCCs and show that they have high quality-factor (Q-factor) resonances in the visible spectral range, which overlap with the ZPLs of SPEs in hBN [24]. We further optimize the structures and model 1D nanobeam photonic crystals that exhibit a Q-factor in excess of ≈20,000. In the light of recent progress in direct-write etching of hBN [25], our results are promising for realization of high Q cavities and monolithic coupled systems made from this material.

Results and Discussion

We begin with a 2D photonic crystal that contains a line defect cavity. The L3 cavity has been widely investigated because it was the first to exceed an experimental Q-factor of 10,000 [26,27]. In this study, we used a commercial finite-difference time-domain (FDTD) software package (Lumerical Inc.). The 3D FDTD simulation domain for 2D (1D) photonic crystal was 7 μm × 7 μm × 1.2 μm (11 μm × 2 μm × 2 μm) which is discretised using uniform spatial and temporal grids of 15 nm and 0.03 fs. Birefringence of hBN is accounted for in our study by including both ordinary ($n_x = n_y = 1.72$) and extraordinary ($n = 1.84$) indices in the 3D FDTD method models. Figure 1a shows the shape and the size of typical hBN flakes prepared by scotch-tape exfoliation [9]. The lateral flake size varies from a few micrometers to few tens of micrometers while thickness varies from few tens of nanometers to a few micrometers, which is sufficient for the fabrication of practical photonic crystal cavities. The parameters used to define an L3 cavity are shown in Figure 1b. The cavity consists of a free-standing slab with a triangular photonic lattice with periodicity 'a'. The air hole radius in the mirror region and the radius of two side air holes are fixed at 0.33a and 0.22a, respectively. By tuning the periodicity 'a', one can tune the resonant wavelength whilst preserving the Q-factor. In this study, we used a = 270 nm and t = 280 nm to place the fundamental mode within the typical emission range of SPEs in hBN (550–700 nm). Two air holes at

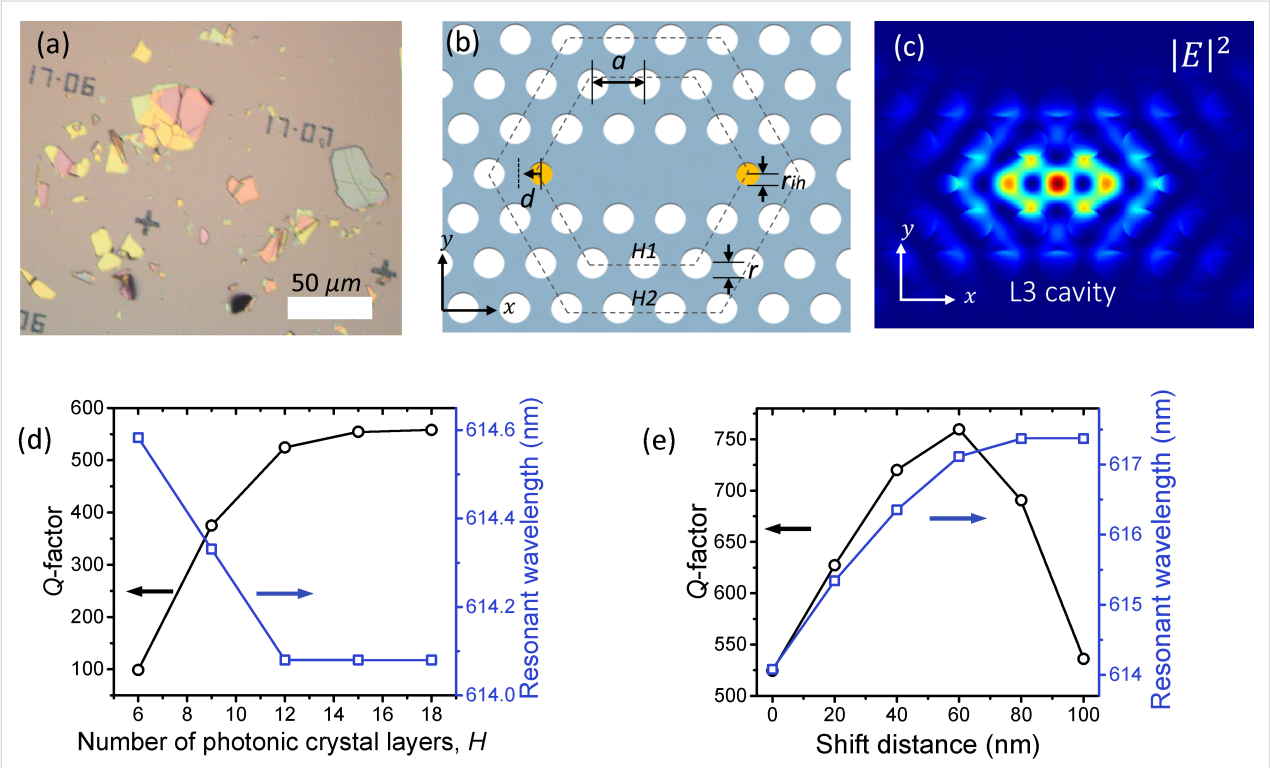


Figure 1: (a) Optical image of exfoliated hBN flakes. (b) Schematic of a 2D photonic crystal with an L3 cavity. The geometric parameters are the following: the period 'a', the radius of air holes 'r', the radius of two side air holes 'r_{in}', the shift distance of the side air holes 'd', the thickness of the hBN slab 't' and the number of photonic crystal layers 'H'. (c) Three-dimensional FDTD simulation of the electric field intensity profile of the fundamental mode of the L3 cavity. Q-factor and the resonant wavelength calculated as a function of (d) the number of photonic crystal layers 'H', and (e) the shift distance of the two side air holes 'd'.

the side of the cavity (yellow circles in Figure 1b) are decreased in size to reduce radiation losses [28]. For the purpose of design simplicity, we adopt tuning of the side air holes as the only means used to increase the *Q*-factor. Lastly, the number of photonic crystal layers comprising the cavity is denoted by '*H*' which act as a photonic mirror and the thickness of the hBN slab by '*t*'. The electric field intensity pattern of the L3 cavity calculated using 3D FDTD simulation is shown in Figure 1c. This is the lowest energy mode in the L3 cavity which is the most widely studied of high-*Q* 2D photonic cavities.

To optimize the design, we start by increasing the number of photonic crystal layers *H*, in order to increase the photonic mirror strength and to reduce the in-plane loss of the cavity. As shown in Figure 1d, the *Q*-factor of the mode starts to saturate at $H \approx 12$ because the *Q*-factor is limited not only by the in-plane component, but also by radiation loss. Considering both the *Q*-factor and scaling of the simulation time with domain size, we fixed *H* at 12 for subsequent modelling.

Radiation losses can be reduced by optimizing the side air hole positions, as is shown in Figure 1e, which reveals that the cavity *Q*-factor is greatest at a shift distance of 60 nm. Note that the mode resonance red shifts with increasing side hole separation due to an effective increase in cavity length.

Photonic crystal cavities with line defects can be described as Fabry–Pérot resonators [29]. Hence, the *Q*-factor can be enhanced by increasing the cavity length as for a Fabry–Pérot resonator [30], which can be tuned by varying number of missing air holes. Figure 2a shows the *Q*-factors of L3, L7, and L11 cavities with a slab thickness of 280 nm. The electric field intensity profiles of L7 and L11 are also shown in the figure (and that of the L3 cavity is shown in Figure 1c). The *Q*-factor of the fundamental mode increases with effective cavity length. For the L11 cavity, we additionally calculated the effect of the thickness of the 2D photonic crystal slab as is shown in Figure 2b. The simulated slab thickness is varied up to 300 nm since that is a realistic thickness of typical hBN flakes prepared

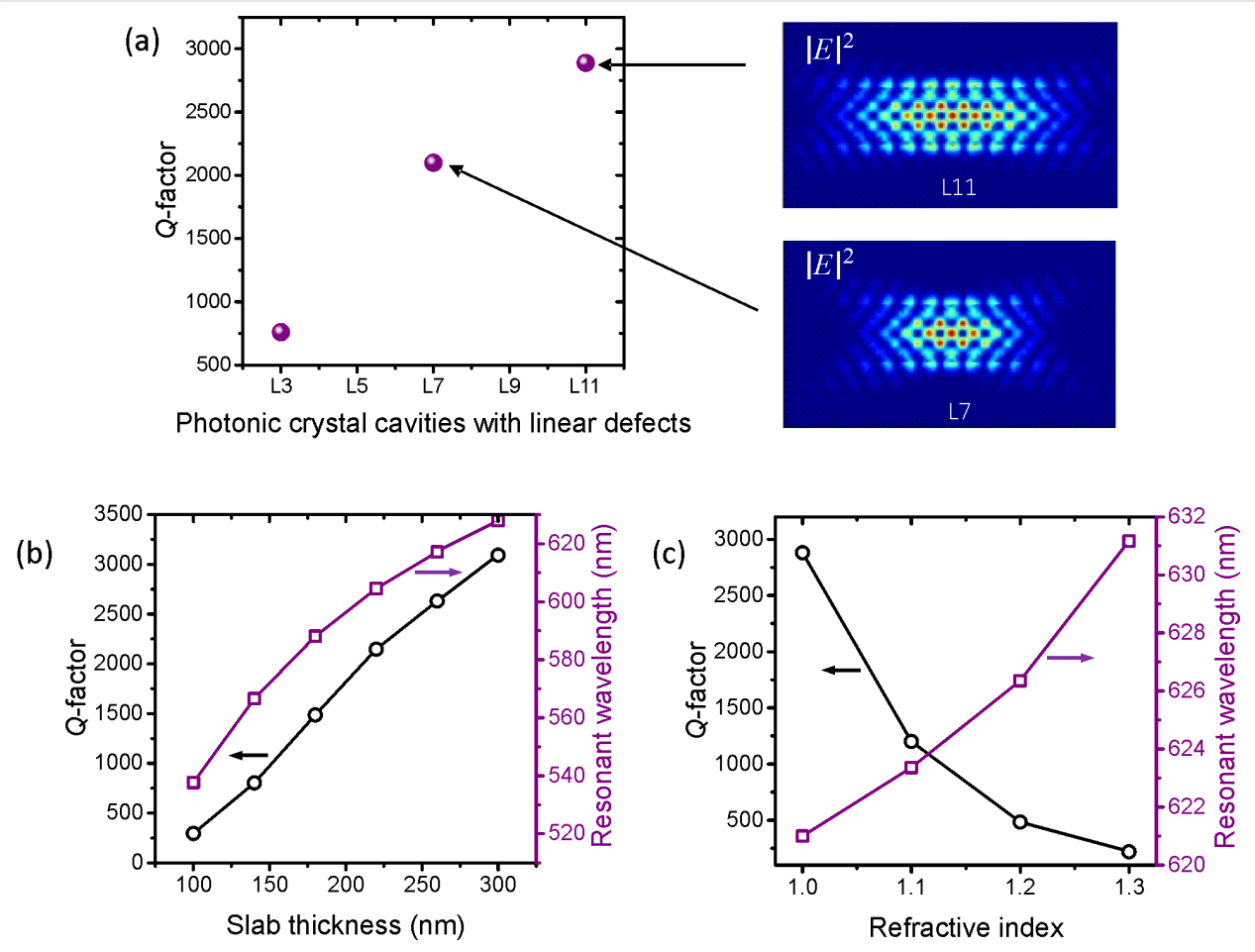


Figure 2: (a) Q-factors of various 2D photonic crystal cavities with an increasing number of linear defects, and the electric field intensity profiles of L7 and L11 cavities. Q-factor and resonant wavelength plotted as a function of (b) the slab thickness and (c) the refractive index of an underlying substrate.

by the scotch tape exfoliation method. Thicker slabs exhibit stronger light confinement, which results in higher *Q*-factors.

We also modelled the effect of the refractive index of an underlying substrate, as is shown in Figure 2c. Because the refractive index of hBN is relatively low compared to that of typical semiconductors, the increase in substrate index greatly degrades the *Q*-factor of the L11 cavity (and a similar effect is expected for the other cavities as well). This is, however, not a significant problem as the transfer of hBN flakes onto holey substrates is a straightforward process. Furthermore, use of aerogel material that is currently commercially available is another option to achieve low index substrates. We note that the overall *Q*-factor is lower than in typical semiconductor 2D photonic crystals due to the relatively low refractive index of hBN.

Next we investigate one dimensional nanobeam photonic crystal structures. 1D PCCs are advantageous in that they can easily have full photonic bandgap between the first and the second lowest photonic energy bands even when the effective index contrast is low [31]. The combination of a high *Q*-factor and a low refractive index enables a broad range of applications such as flexible photonic crystal devices and high figure of merit sensors [32]. Figure 3a shows the electric field intensity profile of the fundamental mode. The cavity is designed by modulating the periodicity whilst fixing the air hole radius [33]. The structure consists of a total of 31 air holes, 15 of which are modulated to create a cavity in the center, and the remaining 8 on each end act as photonic mirrors. In Figure 3b, we set the periodicity in the mirror region to 260 nm while the air hole radius and the nanobeam width are fixed at 70 nm and 300 nm, respectively. By increasing the thickness of the slab from 200 nm to 300 nm, the *Q*-factor increases, as is seen in Figure 3b, and *Q*-factors in excess of 20,000 can be realized. These values are achieved even without optimization of the remaining structural parameters, and are over an order of magnitude greater than the maximum *Q*-factor of a low-index 2D cavity. Next, we fix the thickness at 280 nm and tune the structural parameters to further increase the *Q*-factor of the mode. Figure 3c shows the *Q*-factor plotted as a function of the nanobeam width '*w*', showing that the *Q*-factor has a maximum at a width of 320 nm [34]. Introducing a substrate to the

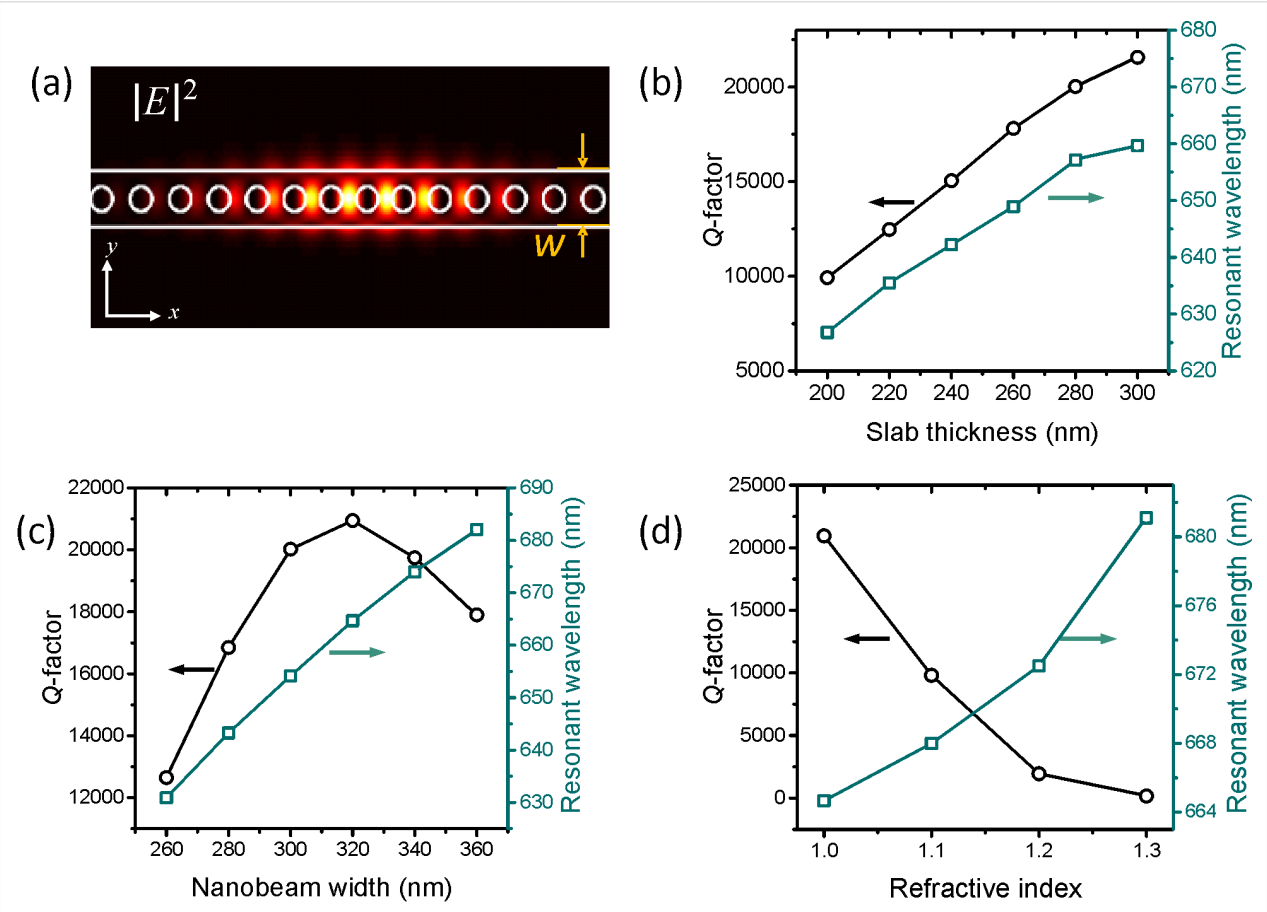


Figure 3: (a) Calculated electric field intensity distribution for a 1D photonic crystal cavity. 3D FDTD simulation of *Q*-factor versus (b) slab thickness, (c) nanobeam width '*w*', and (d) refractive index of the substrate, respectively.

nanobeam degrades the Q-factor as is shown in Figure 3d. A free-standing structure is preferred, as in the case of the 2D photonic crystals presented earlier.

We also consider the absorption losses in the cavity. Figure 4a shows the effect of the absorption by the cavity material. Many FDTD modelling studies of semiconductor photonic crystals include only the real part of the complex refractive index as a structural input which assumes that the material is transparent in the simulated wavelength regime. However, in the case of practical situations in which the cavity material exhibits finite absorption, the imaginary part should also be accounted for. The Q-factor of the fundamental mode in a free-standing nanobeam with a beam-width (w) of 320 nm and a slab thickness (t) of 280 nm is calculated as a function of the imaginary refractive index. An increase in imaginary refractive index (i.e., an increase in material absorption) causes the Q-factor to decrease significantly. Note that realistic Q-factor is determined by $1/Q=1/Q_{ideal} + 1/Q_{abs}$ (Q_{ideal}: Q-factor with lossless material, Q_{abs}: Q-factor with absorption losses) [35], which indicates the material loss restricts the maximum Q-factor that can obtained through experiment. Therefore, including imaginary refractive index for Q-factor calculation provides practical Q-factors.

Finally, we discuss the expected Purcell enhancement due to coupling of emitters to cavity modes. Figure 4b shows the spontaneous emission rate (γ_{sp}) of a quantum emitter in the nanobeam cavity relative to an emitter in free space (γ^0_{sp}). The Purcell enhancement ($\gamma_{sp}/\gamma^0_{sp}$) was found at any given spatial position by calculating the radiated power enhancement of the quantum emitter relative to that in free space. Because the fundamental mode of the nanobeam has a maximum in the high index region, the Q-factor is calculated across the dashed line (y-axis) shown in the inset (i.e., along the width of the 1D PCC). The dipole emitter in the simulation is y-polarized to match the polarization of the optical mode. The Purcell enhancement has a maximum in the center of the nanobeam where the electric field intensity is the greatest. The expected Purcell enhancement is greater than 100 over a range of more than 200 nm along the y-axis, as is seen in Figure 4b, which relaxes the experimental conditions to precisely position the SPE in the cavity. For a realistic case, with a SPE that exhibits a ZPL at 670 nm that is on resonance with the cavity mode, even moderate Q values of 20,000 (≈20 GHz linewidth), will yield a Purcell enhancement of ≈530. To realize the high Purcell enhancement experimentally, techniques for precise positioning of SPEs to the maximum intensity of the cavity mode are required. Two different approaches can suggest solutions to this problem. The first is to find pre-existing single emitters and post-fabricate optical cavities around them. The other approach is to deterministically create emitters in desired locations. Recent studies of hBN single emitters show promising results for both approaches [36,37].

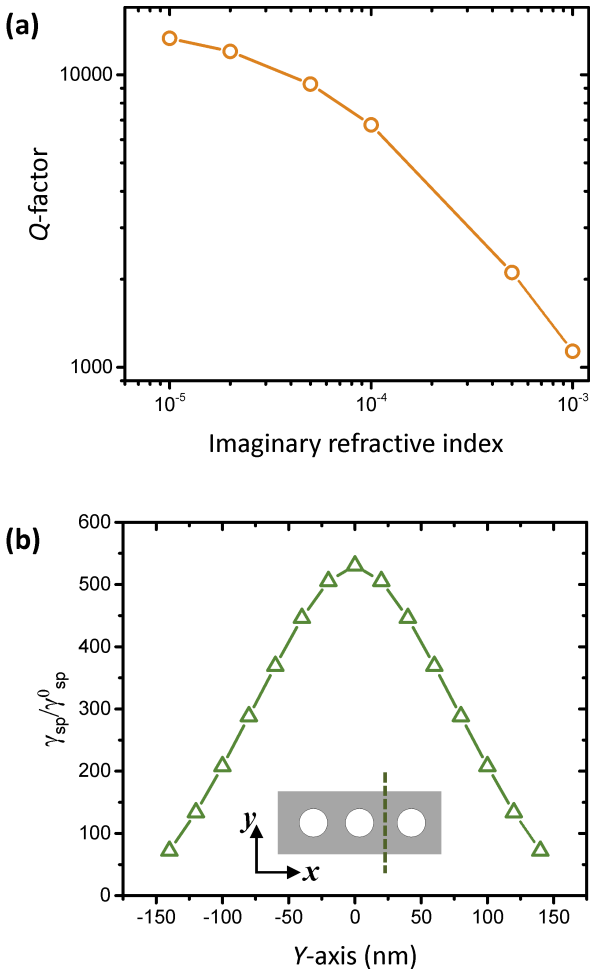


Figure 4: (a) Q-factor of the fundamental mode in a 1D photonic crystal cavity versus the imaginary refractive index coefficient of the material. (b) Spontaneous emission rate enhancement of a dipole emitter plotted as a function of distance across the 1D photonic crystal nanobeam cavity.

Conclusion

In summary, we described and optimized a number of 2D and 1D PCC designs in free-standing and supported hBN layers. Linear defect cavities were studied as representatives of 2D photonic crystals. Period modulation of a 1D nanobeam was used to achieve a theoretical Q-factor in excess of 20,000 simply by modulating the beam width of the structure. The effect of the imaginary refractive index on the Q-factor of a nanobeam was simulated, as was the Purcell factor, showing a strong interaction between a dipole emitter and the optical mode. The designs and analyses of the hBN photonic cavities presented in this work will pave a way to a broad range of ap-

plications enabled by integrated photonic circuits based on 2D materials.

Funding

Financial support from the Australian Research Council (DE130100592, DP140102721), the Asian Office of Aerospace Research and Development grant FA2386-17-1-4064 are gratefully acknowledged.

Acknowledgements

We thank Prof. Joshua D. Caldwell for useful discussions on hBN refractive index.

ORCID® iDs

Sejeong Kim - https://orcid.org/0000-0001-9836-3608

References

1. Caldwell, J. D.; Kretinin, A. V.; Chen, Y.; Giannini, V.; Fogler, M. M.; Francescato, Y.; Ellis, C. T.; Tischler, J. G.; Woods, C. R.; Giles, A. J.; Hong, M.; Watanabe, K.; Taniguchi, T.; Maier, S. A.; Novoselov, K. S. *Nat. Commun.* **2014,** *5,* No. 5221. doi:10.1038/ncomms6221
2. Dai, S.; Ma, Q.; Andersen, T.; Mcleod, A. S.; Fei, Z.; Liu, M. K.; Wagner, M.; Watanabe, K.; Taniguchi, T.; Thiemens, M.; Keilmann, F.; Jarillo-Herrero, P.; Fogler, M. M.; Basov, D. N. *Nat. Commun.* **2015,** *6,* No. 6963. doi:10.1038/ncomms7963
3. Bourrellier, R.; Meuret, S.; Tararan, A.; Stéphan, O.; Kociak, M.; Tizei, L. H.; Zobelli, A. *Nano Lett.* **2016,** *16,* 4317. doi:10.1021/acs.nanolett.6b01368
4. Chejanovsky, N.; Rezai, M.; Paolucci, F.; Kim, Y.; Rendler, T.; Rouabeh, W.; Fávaro de Oliveira, F.; Herlinger, P.; Denisenko, A.; Yang, S.; Gerhardt, I.; Finkler, A.; Smet, J. H.; Wrachtrup, J. *Nano Lett.* **2016,** *16,* 7037. doi:10.1021/acs.nanolett.6b03268
5. Feng, J.; Deschout, H.; Caneva, S.; Hofmann, S.; Lončarić, I.; Lazić, P.; Radenovic, A. *arXiv* **2017,** No. 1706.06313. https://arxiv.org/abs/1706.06313
6. Jungwirth, N. R.; Calderon, B.; Ji, Y.; Spencer, M. G.; Flatt, M. E.; Fuchs, G. D. *Nano Lett.* **2016,** *16,* 6052. doi:10.1021/acs.nanolett.6b01987
7. Kianinia, M.; Regan, B.; Tawfik, S. A.; Tran, T. T.; Ford, M. J.; Aharonovich, I.; Toth, M. *ACS Photonics* **2017,** *4,* 768. doi:10.1021/acsphotonics.7b00086
8. Martínez, L. J.; Pelini, T.; Waselowski, V.; Maze, J. R.; Gil, B.; Cassabois, G.; Jacques, V. *Phys. Rev. B: Condens. Matter Mater. Phys.* **2016,** *94,* 121405. doi:10.1103/PhysRevB.94.121405
9. Tran, T. T.; Bray, K.; Ford, M. J.; Toth, M.; Aharonovich, I. *Nat. Nanotechnol.* **2016,** *11,* 37. doi:10.1038/nnano.2015.242
10. Tran, T. T.; Wang, D.; Xu, Z.-Q.; Yang, A.; Toth, M.; Odom, T. W.; Aharonovich, I. *Nano Lett.* **2017,** *17,* 2634. doi:10.1021/acs.nanolett.7b00444
11. Englund, D.; Fushman, I.; Faraon, A.; Vučković, J. *Photonics Nanostruct. - Fundam. Appl.* **2009,** *7,* 56. doi:10.1016/j.photonics.2008.11.008
12. Faraon, A.; Santori, C.; Huang, Z.; Acosta, V. M.; Beausoleil, R. G. *Phys. Rev. Lett.* **2012,** *109,* 033604. doi:10.1103/PhysRevLett.109.033604
13. Kuhn, A.; Ljunggren, D. *Contemp. Phys.* **2010,** *51,* 289. doi:10.1080/00107511003602990
14. Müller, K.; Fischer, K. A.; Rundquist, A.; Dory, C.; Lagoudakis, K. G.; Sarmiento, T.; Kelaita, Y. A.; Borish, V.; Vučković, J. *Phys. Rev. X* **2015,** *5,* 031006. doi:10.1103/PhysRevX.5.031006
15. Sato, Y.; Tanaka, Y.; Upham, J.; Takahashi, Y.; Asano, T.; Noda, S. *Nat. Photonics* **2012,** *6,* 56. doi:10.1038/nphoton.2011.286
16. Benson, O. *Nature* **2011,** *480,* 193. doi:10.1038/nature10610
17. Harris, N. C.; Bunandar, D.; Pant, M.; Steinbrecher, G. R.; Mower, J.; Prabhu, M.; Baehr-Jones, T.; Hochberg, M.; Englund, D. *Nanophotonics* **2016,** *5,* 456. doi:10.1515/nanoph-2015-0146
18. Santori, C.; Fattal, D.; Vučković, J.; Solomon, G. S.; Yamamoto, Y. *Nature* **2002,** *419,* 594. doi:10.1038/nature01086
19. Bracher, D. O.; Zhang, X.; Hu, E. L. *Proc. Natl. Acad. Sci. U. S. A.* **2017,** *114,* 4060. doi:10.1073/pnas.1704219114
20. Faraon, A.; Barclay, P. E.; Santori, C.; Fu, K.-M. C.; Beausoleil, R. G. *Nat. Photonics* **2011,** *5,* 301. doi:10.1038/nphoton.2011.52
21. Cassabois, G.; Valvin, P.; Gil, B. *Nat. Photonics* **2016,** *10,* 262. doi:10.1038/nphoton.2015.277
22. Lin, Y.; Connell, J. W. *Nanoscale* **2012,** *4,* 6908. doi:10.1039/c2nr32201c
23. Liu, Z.; Gong, Y.; Zhou, W.; Ma, L.; Yu, J.; Idrobo, J. C.; Jung, J.; MacDonald, A. H.; Vajtai, R.; Lou, J.; Ajayan, P. M. *Nat. Commun.* **2013,** *4,* 2541. doi:10.1038/ncomms3541
24. Tran, T. T.; Elbadawi, C.; Totonjian, D.; Lobo, C. J.; Grosso, G.; Moon, H.; Englund, D. R.; Ford, M. J.; Aharonovich, I.; Toth, M. *ACS Nano* **2016,** *10,* 7331. doi:10.1021/acsnano.6b03602
25. Elbadawi, C.; Tran, T. T.; Kolibal, M.; Šikola, T.; Scott, J.; Cai, Q.; Li, L. H.; Taniguchi, T.; Watanabe, K.; Toth, M.; Aharonovich, I.; Lobo, C. *Nanoscale* **2016,** *8,* 16182. doi:10.1039/C6NR04959A
26. El Kurdi, M.; Checoury, X.; David, S.; Ngo, T.; Zerounian, N.; Boucaud, P.; Kermarrec, O.; Campidelli, Y.; Bensahel, D. *Opt. Express* **2008,** *16,* 8780. doi:10.1364/OE.16.008780
27. Schwagmann, A.; Kalliakos, S.; Ellis, D. J. P.; Farrer, I.; Griffiths, J. P.; Jones, G. A. C.; Ritchie, D. A.; Shields, A. J. *Opt. Express* **2012,** *20,* 28614. doi:10.1364/OE.20.028614
28. Akahane, Y.; Asano, T.; Song, B.-S.; Noda, S. *Nature* **2003,** *425,* 944. doi:10.1038/nature02063
29. Kim, S.-H.; Kim, G.-H.; Kim, S.-K.; Park, H.-G.; Lee, Y.-H.; Kim, S.-B. *J. Appl. Phys.* **2004,** *95,* 411. doi:10.1063/1.1633645
30. Hunger, D.; Steinmetz, T.; Colombe, Y.; Deutsch, C.; Hänsch, T. W.; Reichel, J. *New J. Phys.* **2010,** *12,* 065038. doi:10.1088/1367-2630/12/6/065038
31. Quan, Q.; Burgess, I. B.; Tang, S. K. Y.; Floyd, D. L.; Loncar, M. *Opt. Express* **2011,** *19,* 22191. doi:10.1364/OE.19.022191
32. Kim, S.; Kim, H.-M.; Lee, Y.-H. *Opt. Lett.* **2015,** *40,* 5351. doi:10.1364/OL.40.005351
33. Kim, S.; Ko, H.; Lee, C.; Kim, M.; Kim, K. S.; Lee, Y.-H.; Shin, K.; Cho, Y.-H. *Adv. Mater.* **2016,** *28,* 9765. doi:10.1002/adma.201603368
34. Kim, S.; Ahn, B.-H.; Kim, J.-Y.; Jeong, K.-Y.; Kim, K. S.; Lee, Y.-H. *Opt. Express* **2011,** *19,* 24055. doi:10.1364/OE.19.024055
35. Kreuzer, C.; Riedrich-Möller, J.; Neu, E.; Becher, C. *Opt. Express* **2008,** *16,* 1632. doi:10.1364/OE.16.001632
36. Kianinia, M.; Bradac, C.; Wang, F.; Sontheimer, B.; Tran, T. T.; Nguyen, M.; Kim, S.; Xu, Z.-Q.; Jin, D.; Schell, A. W.; Lobo, C. J.; Aharonovich, I.; Toth, M. *arXiv* **2017,** No. 1709.08683. https://arxiv.org/abs/1709.08683

37. Xu, Z.-Q.; Elbadawi, C.; Tran, T. T.; Kianinia, M.; Li, X.; Liu, D.; Hoffman, T. B.; Nguyen,, M.; Kim, S.; Edgar, J. H.; Wu, X.; Song, L.; Ali, S.; Ford, M. J.; Toth, M.; Aharonovich, I. *arXiv* **2017,** No. 1710.07010. https://arxiv.org/abs/1710.07010

License and Terms

This is an Open Access article under the terms of the Creative Commons Attribution License (http://creativecommons.org/licenses/by/4.0), which permits unrestricted use, distribution, and reproduction in any medium, provided the original work is properly cited.

The license is subject to the *Beilstein Journal of Nanotechnology* terms and conditions: (http://www.beilstein-journals.org/bjnano)

The definitive version of this article is the electronic one which can be found at: doi:10.3762/bjnano.9.12

BEILSTEIN JOURNAL OF NANOTECHNOLOGY

High-contrast and reversible scattering switching via hybrid metal-dielectric metasurfaces

Jonathan Ward[‡1], Khosro Zangeneh Kamali[‡1], Lei Xu[1], Guoquan Zhang[2], Andrey E. Miroshnichenko[1,3] and Mohsen Rahmani[*1]

Full Research Paper

Open Access

Address:
[1]Nonlinear Physics Centre, Australian National University, Canberra ACT 2601, Australia, [2]The MOE Key Laboratory of Weak Light Nonlinear Photonics, School of Physics and TEDA Applied Physics Institute, Nankai University, Tianjin 300457, China and [3]School of Engineering and Information Technology, University of New South Wales at the Australian Defence Force Academy, Canberra, ACT 2600, Australia

Email:
Mohsen Rahmani[*] - mohsen.rahmani@anu.edu.au

* Corresponding author ‡ Equal contributors

Keywords:
dielectrics; directionality; metasurfaces; Mie resonance; plasmonics; reversible tuning

Beilstein J. Nanotechnol. **2018,** *9,* 460–467.
doi:10.3762/bjnano.9.44

Received: 28 September 2017
Accepted: 11 January 2018
Published: 06 February 2018

This article is part of the Thematic Series "Light–Matter interactions on the nanoscale".

Associate Editor: A. J. Meixner

© 2018 Ward et al.; licensee Beilstein-Institut.
License and terms: see end of document.

Abstract

Novel types of optical hybrid metasurfaces consist of metallic and dielectric elements are designed and proposed for controlling the interference between magnetic and electric modes of the system, in a reversible manner. By employing the thermo-optical effect of silicon and gold nanoantennas we demonstrate an active control on the excitation and interference between electric and magnetic modes, and subsequently, the Kerker condition, as a directive radiation pattern with zero backscattering, via temperature control as a versatile tool. This control allows precise tuning optical properties of the system and stimulating switchable sharp spectral Fano-like resonance. Furthermore, it is shown that by adjusting the intermediate distance between metallic and dielectric elements, opposite scattering directionalities are achievable in an arbitrary wavelength. Interestingly, this effect is shown to have a direct influence on nonlinear properties, too, where 10-fold enhancement in the intensity of third harmonic light can be obtained for this system, via heating. This hybrid metasurface can find a wide range of applications in slow light, nonlinear optics and bio-chemical sensing.

Introduction

Metasurfaces are thin and flat surfaces that are created using subwavelength optical antennas with various optical properties patterned at interfaces [1,2], enabling control over the polarization, phase, amplitude, and dispersion of light. Metasurfaces are growing in popularity as their optical properties can be adapted to a diverse set of applications along the electromagnetic spectrum [3] including dispersion engineering [4], polarization manipulation [5,6], pulse shaping [7], sensing [8,9] and tuning

[10]. The first generation of metasurfaces mostly consisted of plasmonic nanostructures [11-13], which utilize the interaction between light and metallic nanoparticles to generate surface plasmon resonances, inducing a strong electromagnetic field on the metallic surface. They benefit from a large tunability and capability to significantly enhance the near-field intensity, and have remarkable advantages in controlling optical responses [14-18].

All-dielectric, high refractive index metasurfaces are the second generation of metasurfaces [19]. Besides their CMOS compatibility and low optical losses compared with plasmonic metasurfaces, all-dielectric metasurfaces offer ability to efficiently manipulate light at the nanoscale based on the simultaneous control of electric and magnetic Mie resonances [19]. Subsequently, the capability to control electric and magnetic resonances, offers a unique platform to engineer and tune the directionality of light emission [20,21]. Kerker et al. demonstrated that light scattering can be completely suppressed in certain directions from a subwavelength scatterer when the electric and magnetic responses are of the same order ($\varepsilon = \mu$) [22]. This causes destructive interference in the backward propagation direction and is known as the first Kerker condition. Within dielectric metasurfaces, it has been shown that an overlap of the electric and magnetic dipole resonances can generate a relatively broad spectral band Kerker condition [20,23,24].

In order to achieve high-performance compact optical devices with novel functionalities for applications in modern nanophotonics, tunability of metasurfaces is required, which has become a rapidly growing area of research. These tuning capabilities have been introduced via various techniques, such as phase-change media based antennas [25-27], the use of liquid crystals [28-30], doping [31,32], stretchable substrates [33,34], and electromechanical tuning of the resonator dimension [35], etc. Many of these techniques introduce permanent alterations to the system or the environment, which makes them irreversible, an undesirable characteristic. This allows for an active metasurface tuning mechanism that is reversible and reconfigurable.

Recently, a new technique for reversible tuning of metasurfaces has been proposed, which is based on the thermo-optical coefficient of materials [36,37]. This technique seems quite promising as it varies the temperature of the structure in an easy and reversible way. The large thermo-optical coefficient of dielectrics allows for active control of the devices optical properties by heating. This tunability can be done in a reversible and dynamic way using a parameter that is controlled externally. This tunable device then allows for flat optical components that are adjustable, like beam shapers and lenses [29]. Importantly, thermal tuning is only applicable to dielectric metasurfaces, as the low thermo-optical coefficient of most of noble metals, such as gold [38], makes plasmonic metasurfaces insensitive to variation in temperature.

Hybrid metal–dielectric nanostructures allow for combining the thermo-optical properties of both plasmonic and all-dielectric nanoantennas, simultaneously. Here, by taking advantage of different thermo-optical properties of metallic and dielectric metasurfaces, we propose a novel hybrid metasurface that provides a unique platform to tune the excitation of electric and magnetic modes and their interference in parallel. This leads to a unique capability to tune the Kerker condition in the near-IR, i.e., Kerker interference can be turned on and off in a completely reversible way. It is worth noting that this capability is not achievable with either dielectric or metallic metasurfaces alone, because electric resonance of metallic metasurfaces are essentially insensitive to heating, and magnetic and electric resonances of dielectric metasurface shift together during heating, with negligible change in the interference regime.

Results and Discussion

Our proposed technique to dynamically control the interference of the magnetic and electric resonances provides higher flexibility in tailoring the scattering of light in nanostructures. By employing an additional degree of freedom; coupling between plasmonic and dielectric resonances, we are able to engineer the excitation of the resonant responses over the whole system. Our well-designed hybrid metasurface (see Figure 1) can stimulate or avoid the Kerker condition, on demand. This unique capability can help to realize directional emission from metallic and dielectric nanoantennas. Our design consists of a periodic lattice of silicon cylinders with rectangular gold bars stacked above them, separated by a thin film of SiO_2. This metasurface is designed to stimulate a sharp interference between silicon and

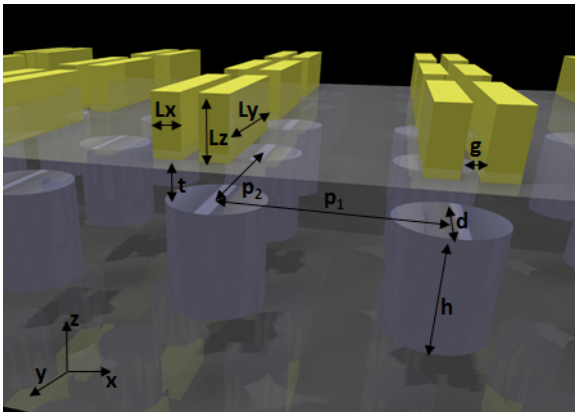


Figure 1: Diagram of the metasurface. The geometrical parameters are L_x = 100 nm, L_y = 600 nm, L_z = 200 nm, t = 200 nm, d = 400 nm, h = 400 nm, g = 60 nm, p_1 = 850 nm, p_2 = 850 nm.

gold lattice resonance around a wavelength of 1235 nm (see Figure 2a). It is an arbitrary wavelength, which can be chosen by a proper design. The reasoning for the NIR range is to avoid absorption in the silicon. The reason behind choosing gold nanobars, rather than simple gold discs, is the following: the system relies on the lattice separation of silicon discs, using gold discs provides limited options for designs as the only degrees of freedom are the diameter and height of the discs. However, employing bars can address this issue by providing one more degree of freedom using the height, width and length of the bars.

The thermal dependence of the energy gap with temperature for silicon can be described by the following relation [39]:

$$E_g(T) = E_g(0) - \frac{\alpha T^2}{T+\beta}, \quad (1)$$

where $E_g(0) = 1.1557$ eV is the energy gap at zero temperature, and $\alpha = 7.021 \times 10^{-4}$ eV/K and $\beta = 1108$ K are parameters fitted from experimental data in [39]. The relation between the variation of refractive index change and the temperature for silicon is given by Tripathy as [40]

$$n = n_0\left(1+\alpha e^{-\beta_2 E_g}\right), \quad (2)$$

where $n_0 = 1.73$, $\alpha = 1.9017$, and $\beta = 0.539$ $(\text{eV})^{-1}$. Figure 2a shows the corresponding thermal dependence of variation of the energy gap and refractive index with temperature in silicon, respectively, [37]. Subsequently, we employ the thermal dependence of silicon to further explore the thermal tunability of the designed hybrid metal–dielectric nanostructures.

Figure 2b demonstrates the transmission characteristics of each element in the hybrid metasurface, including silicon disk lattice,

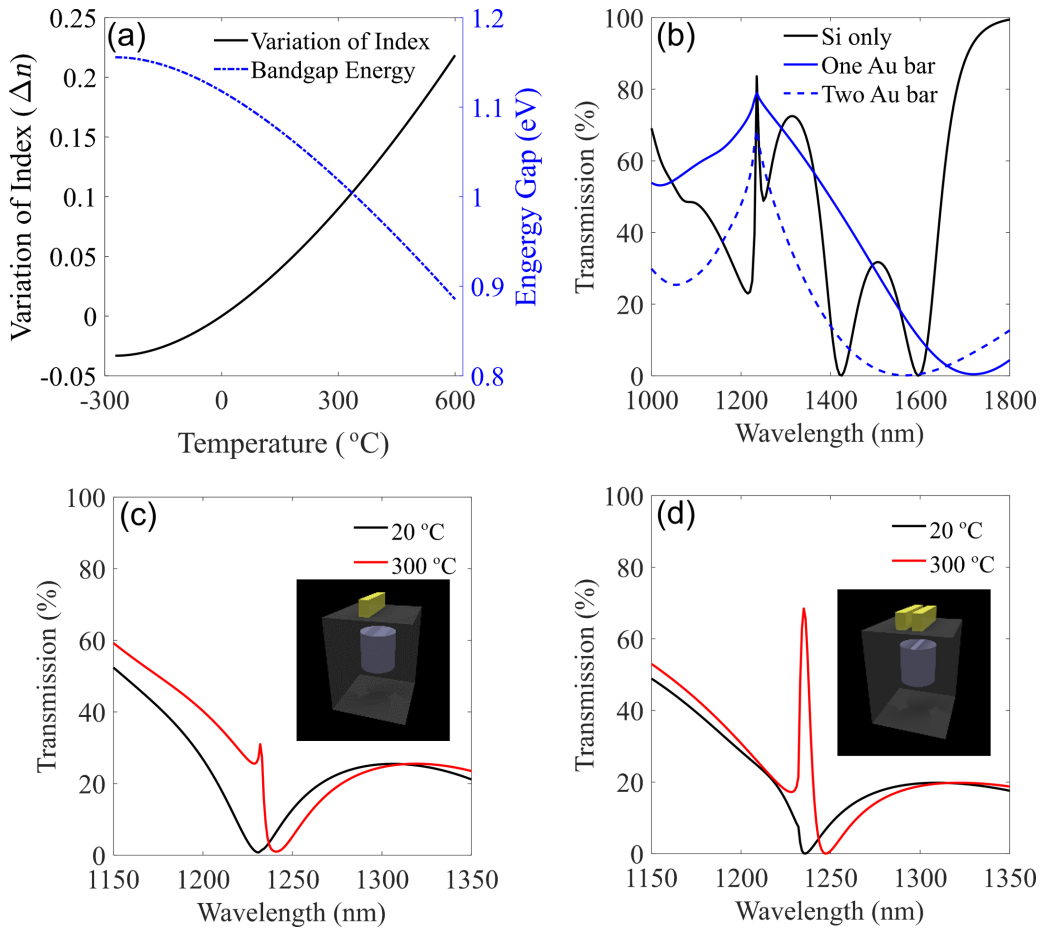


Figure 2: (a) Bandgap energy (blue curve) and variation of refractive index (dark curve) versus temperature change for bulk silicon [40]. (b) Transmission of silicon only (black), one gold bar (red), and two gold bars (blue) in the wavelength range 1000 to 1800 nm at room temperature. (c) The transmission of the silicon with one gold bar at room temperature (20 °C) and 300 °C, respectively. (d) The transmission of the silicon with two gold bars at room temperature (20 °C) and 300 °C, respectively.

one-gold-bar lattice, and two-gold-bar lattice, respectively. The polarization of the incident beam is along y direction (along the gold bar lengths). A grating resonance in the spectrum occurs around 1235 nm at the grating diffraction edge ($\lambda_0 = n \times D = 1.45 \times 850$ nm = 1232.5 nm) due to the constructive diffractive feedback among neighbouring antennas. Therefore, as can be seen, all these components, separately, exhibit a sharp resonance at the target wavelength.

Figure 2c and 2d show the transmission spectra of the hybrid metasurfaces with one gold bar and two gold bars, respectively. As it has been recently demonstrated, heating the system causes a variation in the refractive index of silicon nanostructures which further leads to a systematic shift in the resonances of the system [37]. However, in our design, due to the employment of the thermo-optical properties of both silicon and gold simultaneously, the hybrid metasurface shows a remarkable variation in optical scattering properties. Figure 2c shows a small Fano-like resonance which can be switched on and off near the wavelength 1235 nm, via heating. Interestingly, such effect can be enhanced significantly when adding a second gold bar on the top of each silicon element (see Figure 2d). As a result, around 70% tunability of transmission can be achieved in this wavelength via heating process.

In order to get a physical insight in this phenomenon, we have studied the mode decomposition of the hybrid system consisting of a pair of Au bars [41-43]. As can be seen in Figure 3a, before heating, in the wavelength range between 1150 and 1350 nm, the total scattering (Q) is determined mainly by the resonant excitations from magnetic dipole (MD) and magnetic quadrupole (MQ), and a small portion of excitation from electric quadrupole (EQ) and electric dipole (ED). These optically induced responses in the metasurface can be reflected from the transmission spectra shown in Figure 2c, where the transmission is suppressed in this range (black curve).

After heating, the scattering properties can be tuned drastically and a significant Fano-like resonance appears. The corresponding multipoles excitation after heating (at 300 °C) is shown in Figure 3b. As can be seen, rather than shifting the resonances in silicon metasurfaces as demonstrated recently [37], our hybrid design allows significant changes in the resonant excitation magnitude due to the variation of the magnetic–electric coupling during heating. All modes experience a drastic change around 1235 nm, where a clear interference between electric and magnetic modes (EQ, MQ, and ED, MD) takes place. Interestingly, after heating, around 1235 nm, EQ and MQ experience a comparable magnitude that enables Kerker scattering condition and suppress the backward scattering of light. This produces the Fano-like shape in the transmission spectrum (see Figure 2c,d).

By considering the response of a single unit cell, based on the excitation of the electric and magnetic multipole moments inside it, we further visualize the associated far field pattern

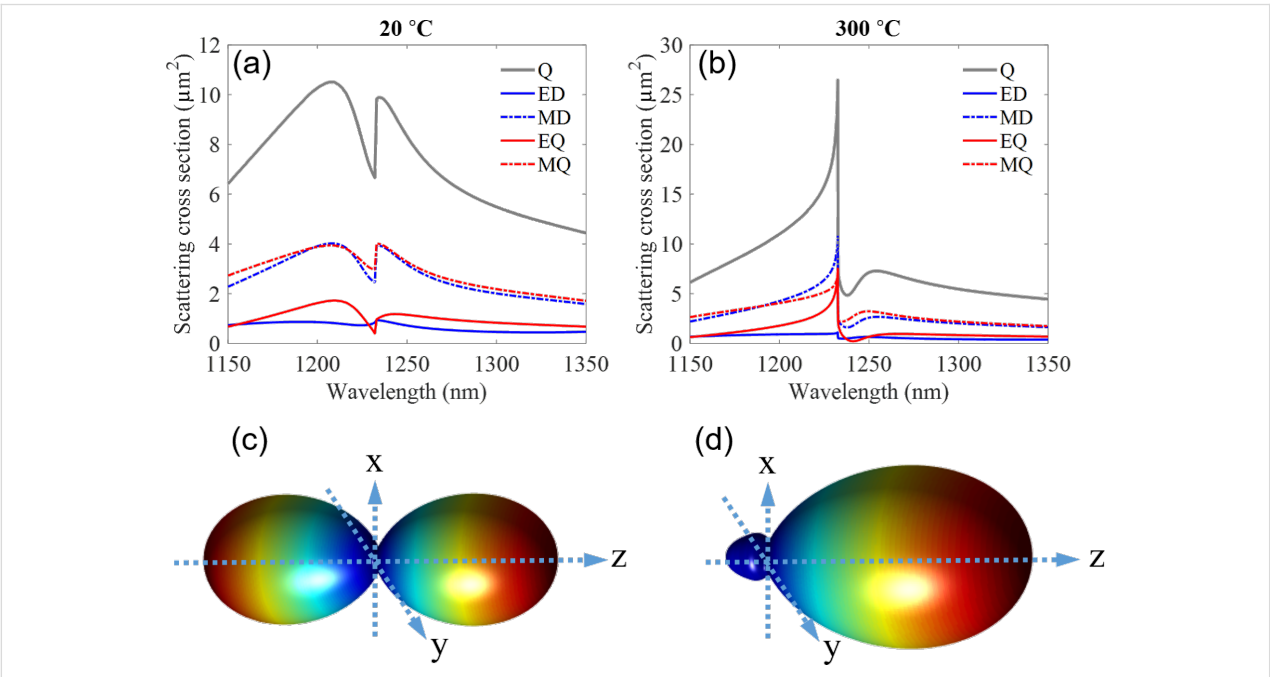


Figure 3: Scattering cross section (a) before and (b) after heating, including zoomed in on Kerker condition in the heated scattering cross section sample. Far-field radiation pattern (c) before and (d) after heating.

from such a single element. Taking the working wavelength being 1235 nm, as an example, Figure 3c and Figure 3d show the results before and after heating, respectively. Before heating, the forward and backward scattering are almost the same, which corresponds to a low transmission from the metasurface based on the scattering properties of resonant nanoparticles and metasurfaces [44,45]. However, after heating the sample to 300 °C, most of the scattered field is in the forward direction, and the backward scattering is suppressed. High scattering directionality is achieved based on the Kerker scattering condition. Similar to Huygens' metasurfaces [23], a high transmission can be observed in the spectra of the hybrid metasurface (see Figure 2c).

Interestingly, heating not only provides a reversible change in the optical properties, but also a dynamical one. Figure 4 shows the transmission spectrum during the heating process. As can be seen, there is a further redshift with increasing temperature, providing unique control on the light scattering from such hybrid metasurface. Take λ = 1235 nm as an example, Figure 4b shows the related transmission with increasing temperature during the heating process. In this case, the system exhibits zero transmission at room temperature, and after heating the sample to 300 °C, high transmission from the metasurface can be achieved. However, with further heating the sample to 600 °C, the transmission at such wavelength can be suppressed again through the same system.

Both plasmonic and dielectric modes exhibit intense near-field distributions [8,9,46]. It is well-known that the near-field associated with plasmonic and dielectric resonances of the individual particles extends some distance away from it [47,48]. These characteristics make the modes very sensitive to the environment [8,9,46]. Therefore, the interference between adjacent resonators within our hybrid system strongly depends on the environment near the nanostructures, such as the volume and refractive index. By employing this sensitivity, we further control the optical response of the metasurface by engineering the interactions between plasmonic and dielectric resonances through tuning the geometry of the intermediate SiO_2 layer. By altering the design slightly, one can make the metasurface behave differently in response to heat. Figure 5 shows the effect of the intermediate SiO_2 layer between silicon and gold structures. It demonstrates the importance of this layer in obtaining different and even reversible behaviour using the exact same silicon and gold nanostructures. Figure 5a demonstrate the case with t = 150 nm, where the heating from 20 °C to 600 °C causes only an enhanced transmission with a slight shift. However for the case of t = 250 nm (Figure 5b), such a heating gradient, can cause a clear fluctuation, where the system experiences an increase (solid red) and then a significant decrease (dashed red) at 1235 nm. Figure 5c illustrates an even larger disparity between the two elements where the minimum no longer exist and the resonance only grows when heated.

By utilizing such well-designed Fano-like resonance, further study was done on its effects on the nonlinear process, focusing on the third harmonic generation. Figure 6 shows the third harmonic conversion efficiency and the related electric near-field distributions in the silicon disk for a plane wave with

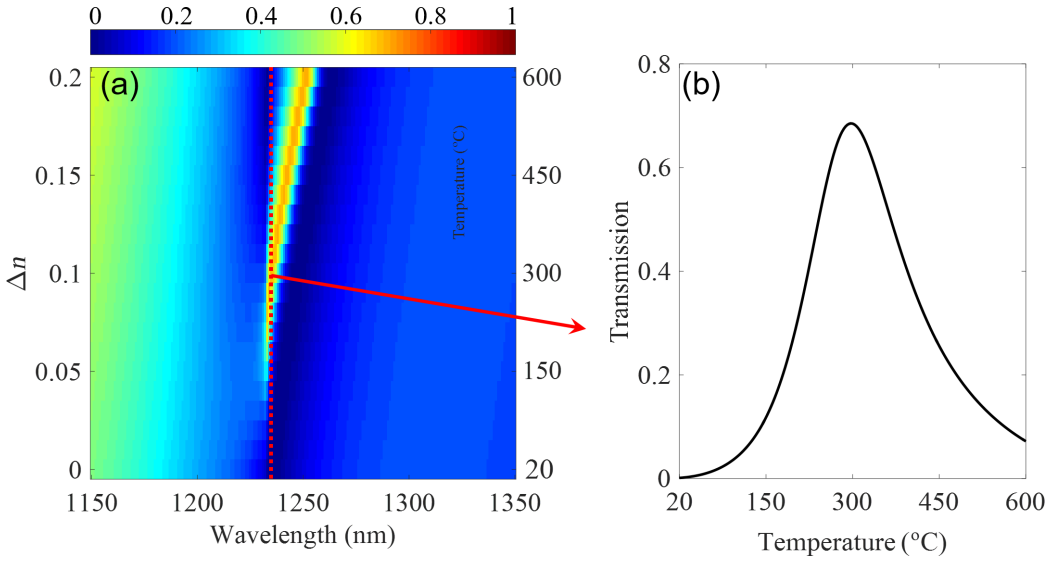


Figure 4: (a) The transmission spectrum during the heating process. (b) The transmission at 1235 nm during the heating process.

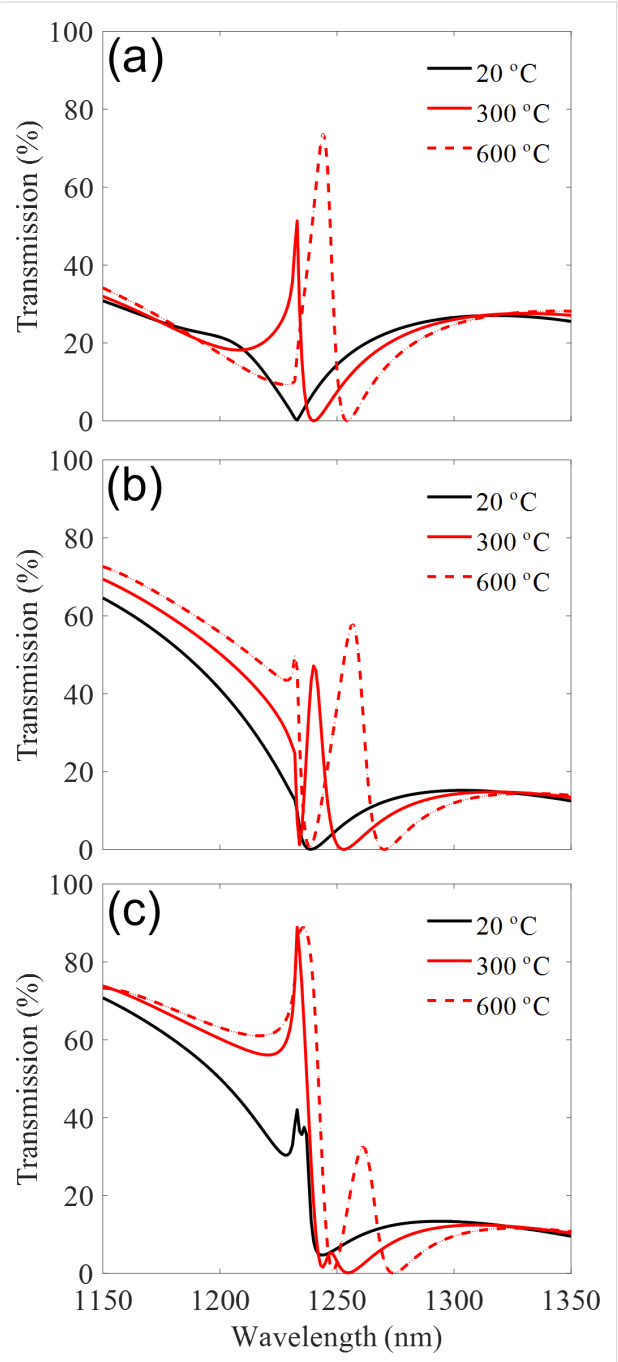


Figure 5: The transmission spectrum for three different SiO_2 thicknesses (a) t = 150 nm, (b) t = 250 nm and (c) t = 300 nm.

λ_{FW} = 1235 nm at I_0 = 1 GW/cm^2. As can be seen from Figure 6a, the efficiency of third harmonic generation can be enhanced by one order of magnitude due to the emergence of the Fano-like resonance during the heating process, from ≈10^{-6} to more than 4 × 10^{-5}. The calculated electric near-field distributions at the fundamental and harmonic wavelengths are depicted in Figure 6b and 6c for the sample at room temperature and Figure 6d and 6e after heating the sample to about 275 °C, respectively. With the emergence of the Fano-like resonance during the heating process, strong field localization and enhancement inside the silicon disk occurs as a result of the excitation and interferences between optically-induced electric and magnetic multipoles (see Figure 3a and 3b). The enhancement of the electric field further stimulates the nonlinear response, as can be clearly seen from the comparison between the electric near-field distributions at the harmonic wavelengths before and after heating the sample (Figure 6c and 6e). It is worth noting that while gold bars show a significant effect on the linear properties of the system after heating, the THG from gold bar is negligibly small compared to THG from silicon disk. It is because the light of the hybrid resonance is generally confined inside the silicon disk rather than the gold bars.

Conclusion

We have designed a hybrid metal–dielectric metasurface, composed of silicon disk and gold bar lattices, with a reversible switching capability of the Kerker scattering condition. The tunability is achieved by the active control on the excitation and interference between the electric and magnetic resonances through heating the metasurface. It is shown that the Kerker condition, based on high order multipoles (EQ and MQ), can be easily switched on and off by simply heating the system. Furthermore, through adjustment to the distance between the metallic and dielectric elements, scattering directionality can be switched at arbitrary wavelengths. We further investigated the THG process in such hybrid meta-dielectric metasurface, and have achieved multi-fold enhancement of THG based on the well-designed hybrid resonance during the heating process. Our hybrid metasurface provides much more flexibility for the control of light scattering, which serves as an important step towards tunable flat optics.

Methods

Here, we study the transmission properties of the nanostructures using rigorous coupled-wave analysis (RCWA) method [49,50] which has been widely used for modelling periodic optical structures due to its fast converging and accurate far-field calculations. We characterize the optical properties of the sample during the heating process based on the refractive index variations of the material at different temperatures, which has been measured experimentally [37].

The nonlinear process of our sample is emulated using the finite element method solver in COMSOL Multiphysics in the frequency domain. We assume an undepleted pump approximation and simulate the linear process firstly, and then obtain the nonlinear polarization inside the sample and employ it as a source for the electromagnetic simulation at the harmonic wavelength [43].

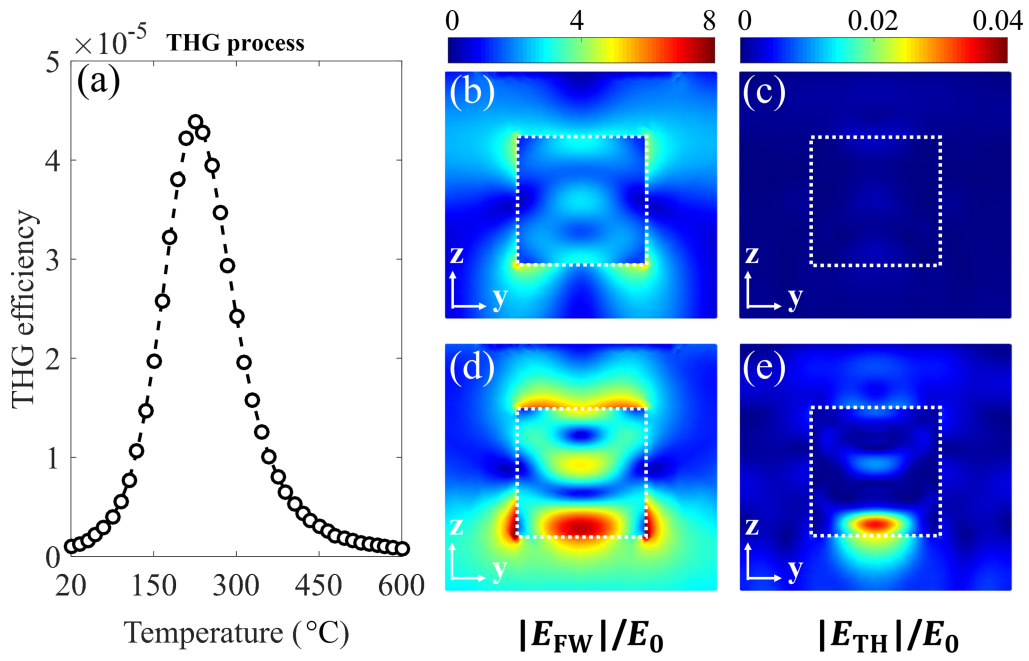


Figure 6: (a) Third harmonic generation efficiency (normalized by the incident pump for each unit cell) during the heating process pumped at the wavelength of 1235 nm. (b) and (c) show the electric near-field distributions at fundamental (left) and harmonic (right) wavelengths in the silicon disk at room temperature, respectively. (d) and (e) show the related calculations after heating the sample at 275 °C.

Acknowledgements

The authors acknowledge the funding support provided by the Australian Research Council (ARC). M.R. sincerely appreciates funding from ARC Discover Early Career Research Fellowship (DE170100250). L. X. is partially supported by the 111 project (Grant No. B07013). G. Z. acknowledges the financial support by NSFC (No. 11774182, No. 91750204).

ORCID® iDs

Khosro Zangeneh Kamali - https://orcid.org/0000-0002-3160-737X
Andrey E. Miroshnichenko - https://orcid.org/0000-0001-9607-6621

References

1. Yu, N.; Capasso, F. *Nat. Mater.* **2014,** *13,* 139–150. doi:10.1038/nmat3839
2. Zheludev, N. I.; Kivshar, Y. S. *Nat. Mater.* **2012,** *11,* 917–924. doi:10.1038/nmat3431
3. Mousavi, S. H.; Kholmanov, I.; Alici, K. B.; Purtseladze, D.; Arju, N.; Tatar, K.; Fozdar, D. Y.; Suk, J. W.; Hao, Y.; Khanikaev, A. B.; Ruoff, R. S.; Shvets, G. *Nano Lett.* **2013,** *13,* 1111–1117. doi:10.1021/nl304476b
4. Guo, Y.; Wang, Y.; Pu, M.; Zhao, Z.; Wu, X.; Ma, X.; Wang, C.; Yan, L.; Luo, X. *Sci. Rep.* **2015,** *5,* 8434. doi:10.1038/srep08434
5. Chen, X.; Huang, L.; Mühlenbernd, H.; Li, G.; Bai, B.; Tan, Q.; Jin, G.; Qiu, C.-W.; Zhang, S.; Zentgraf, T. *Nat. Commun.* **2012,** *3,* 1198. doi:10.1038/ncomms2207
6. Aieta, F.; Genevet, P.; Kats, M. A.; Yu, N.; Blanchard, R.; Gaburro, Z.; Capasso, F. *Nano Lett.* **2012,** *12,* 4932–4936. doi:10.1021/nl302516v
7. Walther, B.; Helgert, C.; Rockstuhl, C.; Setzpfandt, F.; Eilenberger, F.; Kley, E.-B.; Lederer, F.; Tünnermann, A.; Pertsch, T. *Adv. Mater.* **2012,** *24,* 6300–6304. doi:10.1002/adma.201202540
8. Bontempi, N.; Chong, K. E.; Orton, H. W.; Staude, I.; Choi, D.-Y.; Alessandri, I.; Kivshar, Y. S.; Neshev, D. N. *Nanoscale* **2017,** *9,* 4972–4980. doi:10.1039/C6NR07904K
9. Yavas, O.; Svedendahl, M.; Dobosz, P.; Sanz, V.; Quidant, R. *Nano Lett.* **2017,** *17,* 4421–4426. doi:10.1021/acs.nanolett.7b01518
10. Kildishev, A. V.; Boltasseva, A.; Shalaev, V. M. *Science* **2013,** *339,* 1232009. doi:10.1126/science.1232009
11. Meinzer, N.; Barnes, W. L.; Hooper, I. R. *Nat. Photonics* **2014,** *8,* 889–898. doi:10.1038/nphoton.2014.247
12. Geraci, G.; Hopkins, B.; Miroshnichenko, A. E.; Erkihun, B.; Neshev, D. N.; Kivshar, Y. S.; Maier, S. A.; Rahmani, M. *Nanoscale* **2016,** *8,* 6021–6027. doi:10.1039/C6NR00029K
13. Gennaro, S. D.; Rahmani, M.; Giannini, V.; Aouani, H.; Sidiropoulos, T. P. H.; Navarro-Cia, M.; Maier, S. A.; Oulton, R. F. *Nano Lett.* **2016,** *16,* 5278–5285. doi:10.1021/acs.nanolett.6b02485
14. Pors, A.; Nielsen, M. G.; Bozhevolnyi, S. I. *Optica* **2015,** *2,* 716–723. doi:10.1364/OPTICA.2.000716
15. Keren-Zur, S.; Avayu, O.; Michaeli, L.; Ellenbogen, T. *ACS Photonics* **2016,** *3,* 117–123. doi:10.1021/acsphotonics.5b00528
16. Wu, P. C.; Tsai, W.-Y.; Chen, W. T.; Huang, Y.-W.; Chen, T.-Y.; Chen, J.-W.; Liao, C. Y.; Chu, C. H.; Sun, G.; Tsai, D. P. *Nano Lett.* **2017,** *17,* 445–452. doi:10.1021/acs.nanolett.6b04446
17. Lee, J.; Tymchenko, M.; Argyropoulos, C.; Chen, P.-Y.; Lu, F.; Demmerle, F.; Boehm, G.; Amann, M.-C.; Alù, A.; Belkin, M. A. *Nature* **2014,** *511,* 65–69. doi:10.1038/nature13455
18. Almeida, E.; Shalem, G.; Prior, Y. *Nat. Commun.* **2016,** *7,* 10367. doi:10.1038/ncomms10367

19. Kuznetsov, A. I.; Miroshnichenko, A. E.; Brongersma, M. L.; Kivshar, Y. S.; Luk'yanchuk, B. *Science* **2016,** *354,* aag2472. doi:10.1126/science.aag2472
20. Liu, W.; Kivshar, Y. S. *Philos. Trans. R. Soc., A* **2017,** *375,* 20160317. doi:10.1098/rsta.2016.0317
21. Staude, I.; Miroshnichenko, A. E.; Decker, M.; Fofang, N. T.; Liu, S.; Gonzales, E.; Dominguez, J.; Luk, T. S.; Neshev, D. N.; Brener, I.; Kivshar, Y. *ACS Nano* **2013,** *7,* 7824–7832. doi:10.1021/nn402736f
22. Kerker, M.; Wang, D.-S.; Giles, C. L. *J. Opt. Soc. Am.* **1983,** *73,* 765–767. doi:10.1364/JOSA.73.000765
23. Decker, M.; Staude, I.; Falkner, M.; Dominguez, J.; Neshev, D. N.; Brener, I.; Pertsch, T.; Kivshar, Y. S. *Adv. Opt. Mater.* **2015,** *3,* 813–820. doi:10.1002/adom.201400584
24. Kruk, S.; Hopkins, B.; Kravchenko, I. I.; Miroshnichenko, A.; Neshev, D. N.; Kivshar, Y. S. *APL Photonics* **2016,** *1,* 030801. doi:10.1063/1.4949007
25. Michel, A.-K. U.; Chigrin, D. N.; Maß, T. W. W.; Schönauer, K.; Salinga, M.; Wuttig, M.; Taubner, T. *Nano Lett.* **2013,** *13,* 3470–3475. doi:10.1021/nl4006194
26. Wang, Q.; Rogers, E. T. F.; Gholipour, B.; Wang, C.-M.; Yuan, G.; Teng, J.; Zheludev, N. I. *Nat. Photonics* **2016,** *10,* 60–65. doi:10.1038/nphoton.2015.247
27. Li, P.; Yang, X.; Maß, T. W. W.; Hanss, J.; Lewin, M.; Michel, A.-K. U.; Wuttig, M.; Taubner, T. *Nat. Mater.* **2016,** *15,* 870–875. doi:10.1038/nmat4649
28. Minovich, A.; Farnell, J.; Neshev, D. N.; McKerracher, I.; Karouta, F.; Tian, J.; Powell, D. A.; Shadrivov, I. V.; Hoe Tan, H.; Jagadish, C.; Kivshar, Y. S. *Appl. Phys. Lett.* **2012,** *100,* 121113. doi:10.1063/1.3695165
29. Sautter, J.; Staude, I.; Decker, M.; Rusak, E.; Neshev, D. N.; Brener, I.; Kivshar, Y. S. *ACS Nano* **2015,** *9,* 4308–4315. doi:10.1021/acsnano.5b00723
30. Komar, A.; Fang, Z.; Bohn, J.; Sautter, J.; Decker, M.; Miroshnichenko, A.; Pertsch, T.; Brener, I.; Kivshar, Y. S.; Staude, I.; Neshev, D. N. *Appl. Phys. Lett.* **2017,** *110,* 071109. doi:10.1063/1.4976504
31. Jun, Y. C.; Brener, I. *J. Opt. (Bristol, U. K.)* **2012,** *14,* 114013. doi:10.1088/2040-8978/14/11/114013
32. Lewi, T.; Iyer, P. P.; Butakov, N. A.; Mikhailovsky, A. A.; Schuller, J. A. *Nano Lett.* **2015,** *15,* 8188–8193. doi:10.1021/acs.nanolett.5b03679
33. Kamali, S. M.; Arbabi, A.; Arbabi, E.; Horie, Y.; Faraon, A. *Nat. Commun.* **2016,** *7,* 11618. doi:10.1038/ncomms11618
34. Gutruf, P.; Zou, C.; Withayachumnankul, W.; Bhaskaran, M.; Sriram, S.; Fumeaux, C. *ACS Nano* **2016,** *10,* 133–141. doi:10.1021/acsnano.5b05954
35. Liu, A. Q.; Zhu, W. M.; Tsai, D. P.; Zheludev, N. I. *J. Opt. (Bristol, U. K.)* **2012,** *14,* 114009. doi:10.1088/2040-8978/14/11/114009
36. Lewi, T.; Evans, H. A.; Butakov, N. A.; Schuller, J. A. *Nano Lett.* **2017,** *17,* 3940–3945. doi:10.1021/acs.nanolett.7b01529
37. Rahmani, M.; Xu, L.; Miroshnichenko, A. E.; Komar, A.; Camacho-Morales, R.; Chen, H.; Zárate, Y.; Kruk, S.; Zhang, G.; Neshev, D. N.; Kivshar, Y. S. *Adv. Funct. Mater.* **2017,** *27,* 1700580. doi:10.1002/adfm.201700580
38. Palpant, B.; Rashidi-Huyeh, M.; Gallas, B.; Chenot, S.; Fisson, S. *Appl. Phys. Lett.* **2007,** *90,* 223105. doi:10.1063/1.2743936
39. Varshni, Y. P. *Physica (Amsterdam)* **1967,** *34,* 149–154. doi:10.1016/0031-8914(67)90062-6
40. Tripathy, S. K. *Opt. Mater.* **2015,** *46,* 240–246. doi:10.1016/j.optmat.2015.04.026
41. Bakker, R. M.; Permyakov, D.; Yu, Y. F.; Markovich, D.; Paniagua-Domínguez, R.; Gonzaga, L.; Samusev, A.; Kivshar, Y.; Luk'yanchuk, B.; Kuznetsov, A. I. *Nano Lett.* **2015,** *15,* 2137–2142. doi:10.1021/acs.nanolett.5b00128
42. Evlyukhin, A. B.; Fischer, T.; Reinhardt, C.; Chichkov, B. N. *Phys. Rev. B: Condens. Matter Mater. Phys.* **2016,** *94,* 205434. doi:10.1103/PhysRevB.94.205434
43. Wang, L.; Kruk, S.; Xu, L.; Rahmani, M.; Smirnova, D.; Solntsev, A.; Kravchenko, I.; Neshev, D.; Kivshar, Y. *Nanoscale* **2017,** *9,* 2201–2206. doi:10.1039/C6NR09702B
44. Bohren, C. F.; Huffman, D. R. *Absorption and Scattering of Light by Small Particles;* John Wiley & Sons: New York, 1983.
45. Chong, K. E.; Staude, I.; James, A.; Dominguez, J.; Liu, S.; Campione, S.; Subramania, G. S.; Luk, T. S.; Decker, M.; Neshev, D. N.; Brener, I.; Kivshar, Y. S. *Nano Lett.* **2015,** *15,* 5369–5374. doi:10.1021/acs.nanolett.5b01752
46. Yu, B.; Woo, J.; Kong, M.; O'Carroll, D. M. *Nanoscale* **2015,** *7,* 13196–13206. doi:10.1039/C5NR02217G
47. Rahmani, M.; Luk'yanchuk, B.; Hong, M. *Laser Photonics Rev.* **2013,** *7,* 329–349. doi:10.1002/lpor.201200021
48. Nielsen, M. P.; Lafone, L.; Rakovich, A.; Sidiropoulos, T. P. H.; Rahmani, M.; Maier, S. A.; Oulton, R. F. *Nano Lett.* **2016,** *16,* 1410–1414. doi:10.1021/acs.nanolett.5b04931
49. Hugonin, J. P.; Lalanne, P. *Reticolo software for grating analysis;* Institut d'Optique: Plaiseau, France, 2005.
50. Moharam, M. G.; Grann, E. B.; Pommet, D. A.; Gaylord, T. K. *J. Opt. Soc. Am. A* **1995,** *12,* 1068–1076. doi:10.1364/JOSAA.12.001068

License and Terms

This is an Open Access article under the terms of the Creative Commons Attribution License (http://creativecommons.org/licenses/by/4.0), which permits unrestricted use, distribution, and reproduction in any medium, provided the original work is properly cited.

The license is subject to the *Beilstein Journal of Nanotechnology* terms and conditions: (https://www.beilstein-journals.org/bjnano)

The definitive version of this article is the electronic one which can be found at: doi:10.3762/bjnano.9.44

BEILSTEIN JOURNAL OF NANOTECHNOLOGY

Valley-selective directional emission from a transition-metal dichalcogenide monolayer mediated by a plasmonic nanoantenna

Haitao Chen[1,2], Mingkai Liu[1], Lei Xu[1] and Dragomir N. Neshev[*1]

Full Research Paper

Open Access

Address:
[1]Nonlinear Physics Centre, Research School of Physics and Engineering, Australian National University, Canberra, ACT 2601, Australia and [2]College of Advanced Interdisciplinary Studies, National University of Defense Technology, Changsha 410073, China

Email:
Dragomir N. Neshev* - Dragomir.Neshev@anu.edu.au

* Corresponding author

Keywords:
2D materials, multipolar emission; nanoantenna; plasmonic; transition-metal dichalcogenides; valley polarization

Beilstein J. Nanotechnol. **2018,** *9,* 780–788.
doi:10.3762/bjnano.9.71

Received: 27 October 2017
Accepted: 26 January 2018
Published: 02 March 2018

This article is part of the Thematic Series "Light–Matter interactions on the nanoscale".

Guest Editor: M. Rahmani

© 2018 Chen et al.; licensee Beilstein-Institut.
License and terms: see end of document.

Abstract

Background: Two-dimensional (2D) transition-metal dichalcogenides (TMDCs) with intrinsically crystal inversion-symmetry breaking have shown many advanced optical properties. In particular, the valley polarization in 2D TMDCs that can be addressed optically has inspired new physical phenomena and great potential applications in valleytronics.

Results: Here, we propose a TMDC–nanoantenna system that could effectively enhance and direct emission from the two valleys in TMDCs into diametrically opposite directions. By mimicking the emission from each valley of the monolayer of WSe_2 as a chiral point-dipole emitter, we demonstrate numerically that the emission from different valleys is directed into opposite directions when coupling to a double-bar plasmonic nanoantenna. The directionality derives from the interference between the dipole and quadrupole modes excited in the two bars, respectively. Thus, we could tune the emission direction from the proposed TMDC–nanoantenna system by tuning the pumping without changing the antenna structure. Furthermore, we discuss the general principles and the opportunities to improve the average performance of the nanoantenna structure.

Conclusion: The scheme we propose here can potentially serve as an important component for valley-based applications, such as non-volatile information storage and processing.

Introduction

The inversion-symmetry breaking and quantum confinement in monolayer TMDCs offer unprecedented opportunities to explore valley-based physics and applications [1-3]. The valley pseudospin is associated with the degenerate energy extrema in momentum space [3]. In monolayer TMDCs that have a hexagonal lattice structure valleys of degenerate energy locate at the

corners of the hexagonal Brillouin zone: the K and K′ points [4,5]. In analogy to spintronics, the valley pseudospin could also be used as non-volatile information storage and processing, which is known as valleytronics [6-10]. In particular, monolayer TMDCs with direct bandgap at the K and K′ points [11] make it possible to control the valley degree freedom entirely optically. Optical pumping of excitons of a specific valley polarization has been demonstrated by polarization-resolved photoluminescence (PL) measurements [12-14], where the chirality of the PL emission is the same as the pumping light, since different valleys are addressed by the angular momentum of the excitation. Hence, one can switch the chirality of the PL emission from left to the right (and the other way around) by changing the polarization states of the pump beam. It can be envisioned that the dynamic excitation and control of carriers in different valleys is crucial for future valley-based information technologies and applications.

Inspired by such opportunities, a valley-based light emitting diode with controllable emission polarization [15], valley Hall effect [16], and valley-dependent photogalvanic effect have been explored. Excitonic valley coherence [17], valley- and spin-polarized Landau levels [18] and valley Zeeman effect [19-22] have also been studied in monolayer TMDCs. Different schemes to control the valley pseudospin in 2D TMDCs have been developed, including optical [23,24], magnetic [25,26] and electrical [17,27] control.

On the other hand, to facilitate device integration, it is preferable that light emission from 2D TMDCs can be controlled at the nanoscale. Recent advances in resonant metallic nanostructures, referred to as plasmonic nanoantenna, have shown great flexibility and capability for manipulation of the radiation of closely placed emitters [1,3,28]. Plasmonic nanoantenna could significantly modify the emission rate, the radiation pattern and the polarization of emission when their plasmonic modes are excited [29-31]. In particular, localized emitters could effectively excite the higher-order modes of the nanoantenna, which are usually only weakly coupled to free-space plane waves [32,33] but can dramatically modify the radiation of the emitters. Importantly, the near-field and far-field interference of the multiple plasmonic modes present in the nanoantenna offer an unprecedented capability to control all aspects of the emission of localized emitters [33-35]. While the radiation enhancement of emitters by multipolar antennas has been widely studied [33,36,37], the control of the directionality of emission is less explored. Although previous studies [38-42] have shown several designs for spin-dependent directional emission, these schemes are extremely sensitive to the position of the emitter to the nanoantenna, e.g., the directionality of emission would be reversed if the emitter is placed on the opposite side of the antenna. As such, the currently proposed schemes can not be employed to control the emission of delocalized chiral emitters, such as emission from exciton from the two valleys of a 2D TMDC material.

Here, we propose a plasmonic TMDC–nanoantenna system that can effectively route light emission from different valleys of TMDCs into opposite directions. Our nanoantenna can support electric dipole and electric quadrupole resonances, which can be excited, with engineered phases and amplitudes, by the chiral point-dipole emitters corresponding to each valley. Based on the phase-locked excitation and interferences of these resonances, we have shown that the scattering direction of the TMDC–nanoantenna system is valley-locked. Since the different valleys in TMDC can be addressed optically by circularly polarized optical pumping, we then can tune the emission direction of this coupled system by simply changing the circular polarization states of the pumping light. We believe that our scheme could provide useful insight for design of novel component such as couplers and routers in future valley-based information processing devices.

Results and Discussion

Concept

At resonances, the far-field radiation of the nanoantennna could be expanded into multipolar series. Equation 1 shows the first three terms, including the contribution of the electric dipole **p**, the electric quadrupole $\hat{Q}$ and the magnetic dipole **m** [43]:

$$\mathbf{E}(\mathbf{r}) = \frac{k_0^2 e^{ik_d r}}{4\pi\varepsilon_0 r}\left\{\left[\mathbf{n}\times\left(\mathbf{p}\times\mathbf{n}\right)\right] + \frac{ik_d}{6}\left[\mathbf{n}\times\left(\mathbf{n}\times\hat{Q}\mathbf{n}\right)\right] + \frac{1}{v_d}(\mathbf{m}\times\mathbf{n})\ldots\right\}, \quad (1)$$

where k_0 is the vacuum wavenumber and k_d is the wavenumber in the surrounding medium. v_d is the speed of light in the medium, **n** is the unit vector in the direction of emission, **r** is the coordinate vector, r = |**r**|.

From Equation 1, we can see that the far-field radiation is in-phase with the electric dipole moment, while there is a π/2 phase difference for the electric quadrupole. Thus, there is naturally a π/2 relative phase difference between the electric dipole and quadrupole contribution to the far-field emission, when their corresponding charges oscillate in phase. In this case, the parallel electric field components of electric dipole and electric quadrupole emission will interfere with each other depending on their relative phase and amplitude. When the amplitudes of the far-field components are comparable, the interference will be constructive in one direction and destructive in the other, for

π/2 or 3π/2 phase difference between the electric dipole and quadrupole. On the other hand, the far-field interference is prevented if the phase difference is 0 or π. Our design is based on this interference property, to tailor the emission directions from different valleys.

The basic idea of our concept for splitting the emission from the two valleys of the TMDCs via near-field coupling to a plasmonic nanoantenna is schematically shown in Figure 1a. When the coupled TMDC–nanoantenna system is excited by light of different circular polarizations, the emission from the two valleys (K and K′) will be emitted into opposite directions, as depicted by the two red arrows. The general concept of such valley splitting relies on the interference of multipolar modes excited in the nanoantenna, namely an electric dipole and an electric quadrupole, as shown in Figure 1b. When the parallel electric dipole and quadrupole are excited simultaneously with comparable amplitudes, the radiation direction will depend on the phase difference between the dipole and quadrupole, as discussed above. Thus, by changing the relative phase between the dipole and quadrupole from +π/2 to −π/2, we could effectively tune the radiation direction from one (solid arrow) to the other (dashed arrow).

Design and implementation

Since the emission from the TMDC monolayer solely comes from the in-plane exciton or trion charge carriers [44], the TMDC emitters could be practically modeled as chiral point-dipole emitters placed in the vicinity of the photonic structure [45]. To emulate such chiral emitters, corresponding to the two valleys in the TMDC monolayer, in our simulations we use two in-plane but orthogonal point dipoles that oscillate with π/2 phase difference (to emulate the rotation of the dipole). When a +π/2 or −π/2 phase difference is applied between these two emitters, we can emulate left or right chiral emitters [46] from carriers in the K and K′ valleys [47].

To achieve such a functionality, we need to construct an antenna that supports both an electric dipole and an electric quadrupole of the same strength and at the same operation wavelength. We hence start with a simple plasmonic nanoantenna consisting of two gold bars of different length. Different plasmonic modes could be excited in such a double-bar antenna when a localized emitter is placed in its proximity. The excitation of plasmonic modes depends on a couple of factors, including the antenna size, as well as the emitter position and orientation. By choosing proper size parameters, either the electric dipole mode or the "dark" quadrupole mode of the antenna can be excited predominantly by the point-dipole source. We choose a short bar with length L_p = 104 nm and width W_p = 25 nm, and a long bar with length L_q = 310 nm and width W_q = 70 nm. The height of the two bars is the same, 40 nm. A view of each bar of the antenna is shown in Figure 2a and Figure 2b, respectively. Two electric dipoles oriented along X (D_h) and Y (D_v) are placed 5 nm above the antenna in Z direction. The point-dipole emitters are 25 nm away from the bar antenna in Y direction. To mimic a practical experimental arrangement, the antenna is placed on top of a glass substrate. Electrical probes are located at the end of each gold bars to detect the electric phase and amplitude.

We start by studying the individual responses of each antenna bar, when excited by a local dipole emitter, orientated parallel or perpendicular to the bar. We perform numerical calculations using finite-integral frequency-domain simulations (CST Microwave Studio) with open boundary conditions. To avoid unphysical sharp edges, we model the gold bars having rounded corners with a radius of curvature of 5 nm. The permittivity of the gold in the visible and near-infrared spectral region is modeled based on experimental data from [48].

The intensity of the electric field along X direction (I) and phase information (φ) at the probe position when the structure is

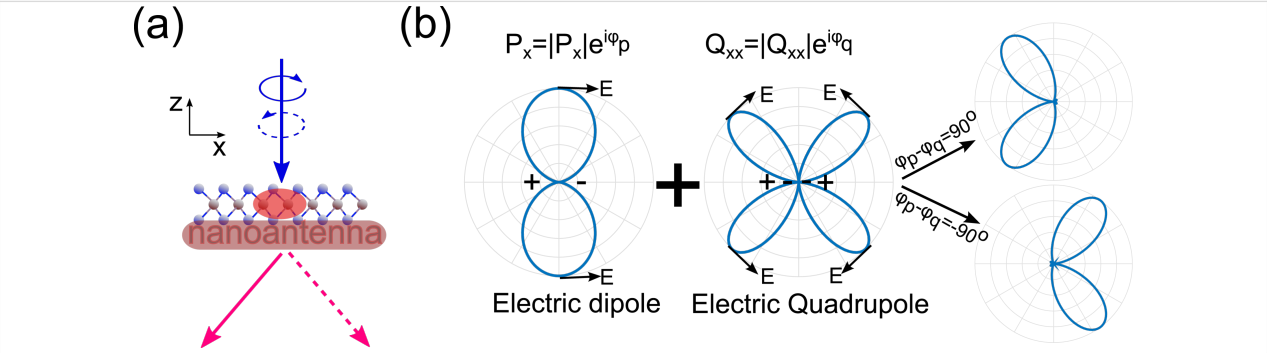


Figure 1: Design principles of the directional emission from the different TMDC valleys. (a) The proposed scheme to separate emission from different valleys through integrating with a properly designed nanoantenna. The directions of the emission from monolayer TMDCs depend on the polarization states of the excitation when different valleys are excited. (b) The working principle of the nanoantenna is based on the interference between the electric fields radiated from an electric dipole and an electric quadrupole; the direction of constructive interference depends on their relative phase.

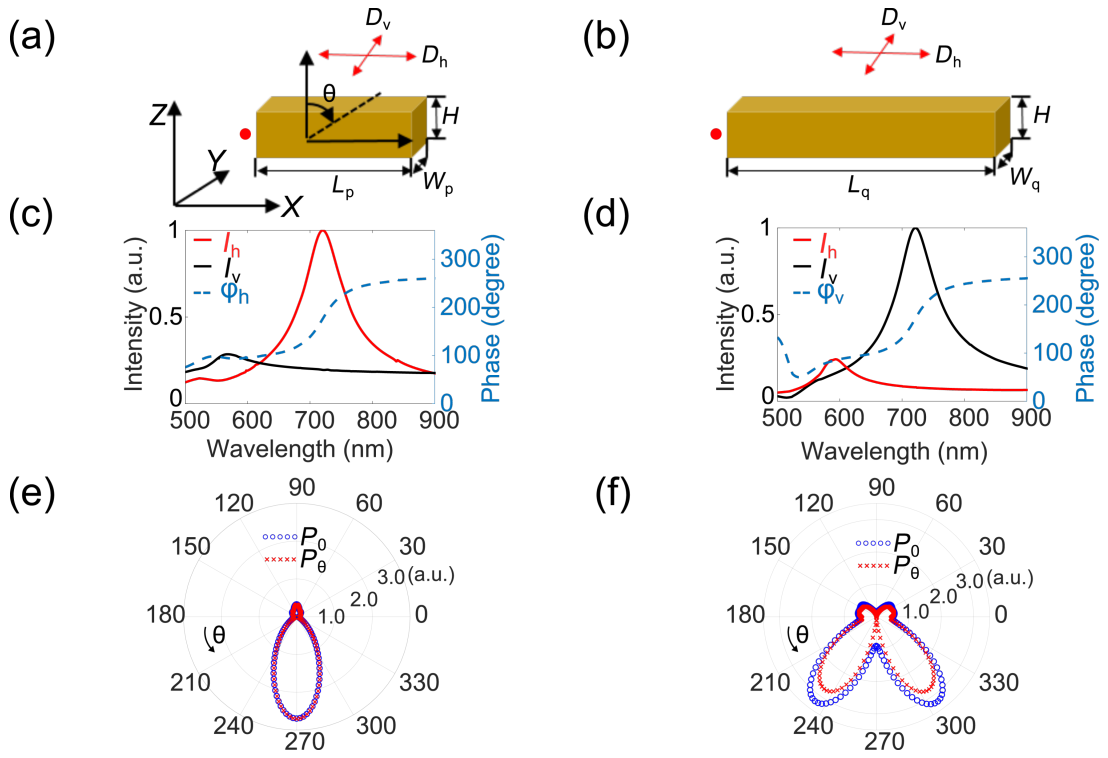


Figure 2: Characteristics of the bar antenna excited by an electric dipole emitter. (a, b) Schematic of the simulation setup for the short bar (a) and the long bar (b) antenna, respectively. The red arrows represent point-dipole emitters with *X* or *Y* orientations. The red spots represent electric probes. (c, d) The electric field intensity (*I*) and phase (φ) at the position of the probe when point-dipole emitters oriented along *X* and *Y* are used as an excitation source for the short and long bar, respectively. The subscript h and v represents the field induced by the point-dipole emitter along *X* and *Y* directions, respectively. We only show phase information for the short bar excited by a *X*-orientated emitter (φ_h) and the long bar excited by a *Y*-oriented emitter (φ_v). The field intensity is normalized to the larger one for emitters with different orientations. (e, f) Polar plot of the total (P_0) and azimuthal components (P_θ) of the far-field power distribution when the short bar is excited by a *X*-oriented dipole (e) and the long bar is excited by a *Y*-oriented dipole (f), respectively. The direction of θ is illustrated by arrows.

excited by local point-dipole emitters of different orientations, for short bar and long bar, are shown in Figure 2c and Figure 2d, respectively. For better comparison, we normalize the field intensity to the stronger one. As seen, for the short bar (Figure 2c), the field induced by the *X*-oriented point-dipole (I_h) dominates in the wavelength range of 700–750 nm. In contrast, the excited field from the *Y*-oriented point-dipole (I_v) dominates for the long bar in the same wavelength range (Figure 2d). Importantly, both of the electric field intensities show a resonant peak at the same wavelength of 715 nm.

The phase information detected by the probes corresponds to the phases of the oscillating charges, which defines the phases of the dipole and quadrupole moments. The phase information under the dominant excitation, labeled as φ_h and φ_v are shown in Figure 2c,d with dashed lines. We could observe that the two resonant modes are in phase. To further investigate the nature of the excited modes in each gold bar, we monitor the far-field radiation pattern of the *X*-oriented emitter coupled to the short bar and the *Y*-oriented emitter coupled to the long bar. The radiation patterns at the resonant wavelength are shown in Figure 2e and Figure 2f, respectively. Due to the existence of the high-index substrate, most of the emitted power goes into the lower half space. In the case of a *X*-oriented emitter and a short-bar antenna (Figure 2e), the radiation pattern shows a typical dipole-emission profile. In the case of a *Y*-oriented emitter and a long-bar antenna, the emission shows a typical quadrupole profile (Figure 2f). In the same polar plots, we show both the total radiated power (P_0 – blue circles) and the azimuthal power component (power contributed from azimuthal electric field, P_θ – red circles). As seen from Figure 2e and Figure 2f, in both cases the azimuthal component (P_θ) is the dominant polarization component, which is expected for both dipole and quadrupole radiation from bar antennas along the *X* direction. By examining the vectorial near-field profiles (shown in Figure S1, Supporting Information File 1), we further confirm that the electric dipole mode is excited dominantly by the *X*-oriented point-dipole, while the electric quadrupole mode in the long bar is excited by the *Y*-oriented point dipole. Thus, the far-field radiation of these dipole and quadrupole will have a phase difference of π/2. Note that we have fine-tuned the geometry of the antennas in order to have them resonate around 715 nm, which

matches the experimentally measured emission wavelength of monolayer WSe_2. The parameters of the two bars are also optimized such that the radiated electric far-fields have comparable intensities.

After investigating the response of the individual gold bars, we perform simulation for the combined antenna consisting of two closely spaced gold bars coupled to a chiral point-dipole emitter. A schematic of the antenna–emitter system is shown in Figure 3a. The gap between the two bars is set to 50 nm and the chiral emitter is located in the center of the gap. The chiral emitter is again modeled as two orthogonal electric dipoles with a relative phase of Δφ, where Δφ = ±90°, corresponding to right or left circularly polarized emission, respectively. The calculated radiation patterns of the total emission (side view) are shown in Figure 3b, for both Δφ = 90° and −90°. Due to the interference of the fields emitted from the electric dipole of the antenna and electric quadrupole contributions, the radiation from the chiral point-dipole is directed either to the left or to the right, depending on its chirality. In contrast, for the case without the nanoantenna, the radiation does not show preferred directionality (shown in Figure S2, Supporting Information File 1). Importantly, the directionality could be effectively switched by changing the sign of the phase difference (circular polarization state of the point dipole).

Figure 3c,d compares the polar plots of the total (P_0) and azimuthal power component (P_θ) distributions. It is clear that the azimuthal power component is the dominant contribution to the radiation. This confirms that the directional emission is indeed a result of the interference between the electric dipole mode from the short gold bar and the electric quadrupole mode from the long gold bar. To quantify the observed directionality, we define the front-to-back ratio (F/B) as ratio between the total power emitted in the forward half-space to the power emitted in the backward half-space. The F/B value is 4.7 dB for the total power, and 6.0 dB for the azimuthal power component, which could be distinguished by adding a polarizer in the detection arm of a possible experiment. The directionality for the total radiation is slightly weaker than for the azimuthal component because of contributions from higher order modes excited in the long bar. Since the valley polarization of the monolayer TMDCs (corresponding to the chirality of the point-dipole emitters) depends on the polarization states of the pumping laser, we could easily tune the emission directionality from our proposed TMDC nanoantenna system just by changing the pumping polarization from left to right circular states.

As an important step of our study, we evaluate the emission enhancements brought by the plasmonic nanoantenna. The radiation enhancement is defined as the total power radiated by the

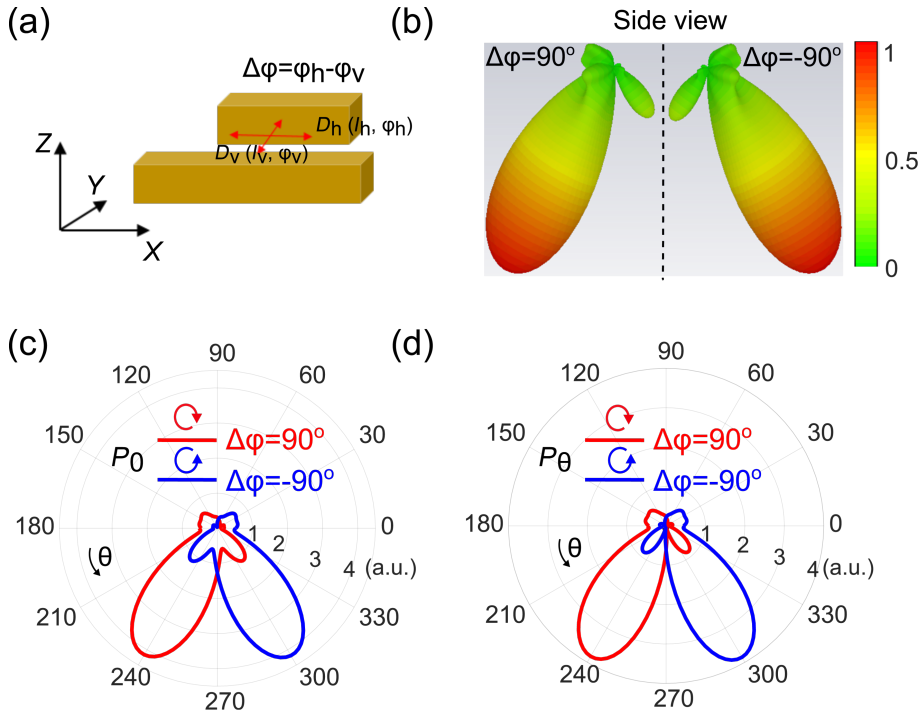


Figure 3: Radiation properties of a double-bar plasmonic antenna. (a) Schematic view of the double-bar antenna. Δφ represents the phase difference between the *X*- and *Y*-oriented point-dipole emitters. Δφ = ±90°is used to mimic right or left chiral emitters, respectively. (b) Side view of far-field pattern when Δφ = ±90°. (c, d) Polar plots of the total radiated power (P_0) and the azimuthal component (P_θ) in the far field, respectively. We show both cases of Δφ = ±90°.

two orthogonal dipole emitters (defining the chiral point dipole) coupled to the antenna, normalized to the case with no antenna. We find that the radiation is dramatically enhanced, up to 15 times at the resonant wavelength, when the chiral emitter is positioned in the center, between the two bars. In addition, we test the robustness of our design with respect to the emission wavelength. We find that the directionality is preserved in the spectral range from 680 nm to 750 nm. This broadband response makes our design suitable to control the emission from monolayer TMDCs, such as WSe_2 in its entire emission range. Thus, the simple nanoantenna we propose here could effectively enhance the emission intensity and simultaneously tune the valley-based emission directionality from the TMDCs.

As discussed, the modes excited in the plasmonic nanoantenna depend on the position of the emitter. In a monolayer TMDC, however, the emitters (e.g., excitons) can be distributed randomly and homogeneously over the entire monolayer. Hence, to evaluate the directionality of emission from the average distribution of emitters on top of the double-bar antenna, we perform calculations for different positions of the point-dipole emitters and average the radiation patterns taking into account the contribution from the multiple emitters. Two cases have been considered. Firstly, we investigate the average directionality when the emitters are positioned inside the gap between the two gold bars. We calculate the emission for three different positions inside the gap, as shown in Figure 4a and then add up the radiated powers. The polar plot of the total power and the azimuthal power components are shown in Figure 4b and Figure 4c, respectively. The plots show radiation patterns, which are similar to the radiation from the central dipole position (Figure 3c,d). However, the front-to-back ratio decreases a bit after the averaging. This is due to the fact that for the locations away from the center, the directionality is reduced as compared to the central position. Nevertheless, the average directionality still remain relatively high, namely F/B = 3.4 dB for the total power and 4.2 dB for the azimuthal power component.

After averaging over more positions outside the gaps (we take nine typical positions, as shown in Figure 4d), the directionality is reduced a little further. However, as shown in Figure 4e and Figure 4f, we still observe reasonably good directionality. Thus, we can conclude, that despite the different positions of the emitters (being on both sides of the antenna) the directionality of emission is generally preserved and it can be tuned by changing the chirality of the emitters (the relative phase shift between the *X*-oriented and *Y*-oriented point-dipole emitters). Therefore, the scheme we proposed here can be used effectively to direct emis-

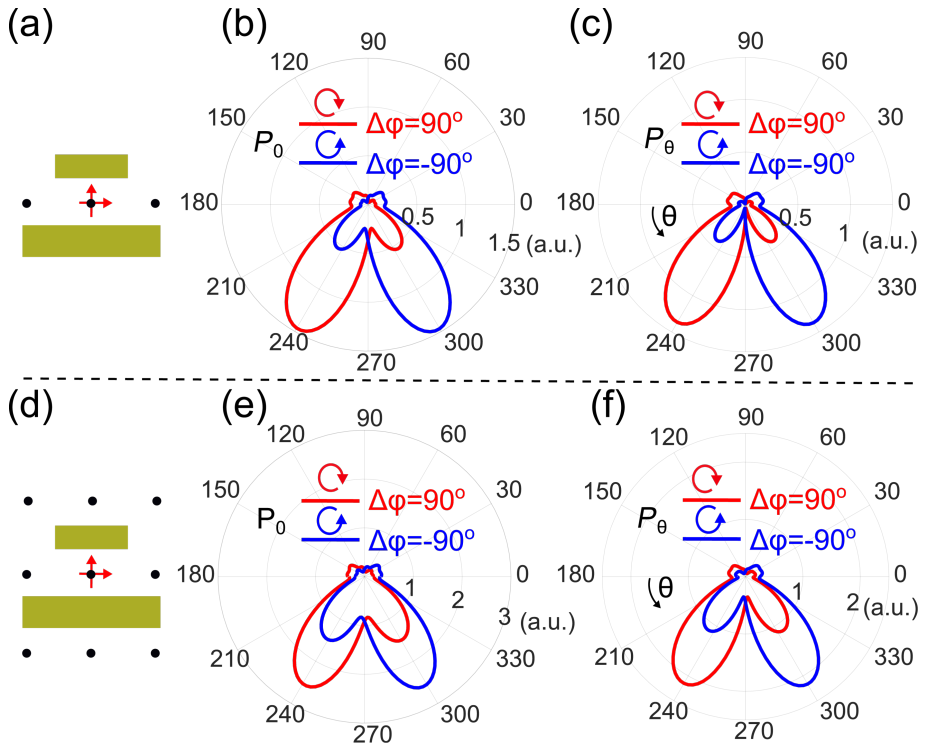


Figure 4: Emission pattern averaged over multiple emitters. (a) Schematic of the three emitter positions inside the gap between the two bars, used to evaluate the average effects. (b, c) Polar plot of the total (P_0) and azimuthal component (P_θ) of the far-field power distribution, after averaging over all three positions. (d) Schematic of the nine emitter positions used in simulations. (e, f) Polar plot of the total (P_0) and the azimuthal (P_θ) components of the far-field power distribution, after averaging over all the nine positions.

sion from different valleys in monolayer TMDCs (corresponding to different chiral emitters) into different directions.

We believe that with the development of material fabrication techniques, nanostructures of TMDCs [49-51] could also be readily fabricated, so one can control the position and size of the TMDCs nanosheets with respect to the antenna. Thus, a system consisting of a double-bar antenna and a TMDC nanosheet only inside the gap between the bars could in principle serve as efficient light source with tunable emission directions.

To further understand our system and seek for possible ways to improve the average directionality, we compare the total radiation power for the emitters at different positions, shown in Figure 4d. The chiral emitter placed at the central position, results in best directionality and emits two to five times stronger than the dipoles at other positions. The average directionality could be better if the central position had a much stronger emission power. Indeed, directional emission from local emitters enabled by plasmonic nanoantenna is highly sensitive to the position of the emitters [33,37]. The hotspots of the nanoantenna presented here might affect the observed directionality too, while the accurate effects rely on experimental studies. To improve the directionality, we do require antenna structures with very strong hot spots, such that the emission shows good directionality when the emitters are located at these spots. This might direct us to further improve our structures by introducing antenna shapes like bow-ties [52] or split-ring-resonators [37]. However, such structures have more geometric parameters and more higher-order modes when excited by point-dipole emitters, hence the process to optimize the geometry is difficult and time-consuming. Moreover, any complex plasmonic structures requires more demanding fabrication efforts in practice. In contrast, the proposed double-bar antenna has simple mode profiles, it is easy to optimize in size and the fabrication process is relatively straightforward.

Conclusion

In conclusion, we propose and numerically demonstrate a novel concept to control the emission intensity and direction from different valleys in monolayer TMDCs using multi-mode plasmonic nanoantennas. We design a nanoantenna based on two gold bars, of which the dipole and quadrupole modes can be excited dominantly at the same frequency. The interference between the dipole and quadrupole modes results in directional emission, where the directionality of emission depends on the phase difference between these two modes. By emulating emission from different valleys in TMDCs with chiral point-dipole emitters of opposite chirality, we have shown that a simple two-bar plasmonic nanoantenna represents a feasible platform to direct the emission (left circular or right circular) from distinct valleys into different directions. This is due to the coupling of the chiral emitters to the two dominant plasmonic modes in the double-bar nanoantenna. Directionality of up to 6 dB and a radiation power enhancement of up to 15 times could be achieved in this coupled system. Since the valleys in TMDCs can be addressed optically, we can change the emission direction of this TMDC–nanoantenna system by simply changing the circular polarization states of the pumping light. In addition, we discuss the reasons for the reduced directionality when averaging over different positions of the emitter and propose the possible ways to address this issue, either by structuring the TMDC materials or by designing new plasmonic nanoantennas. The scheme we propose here could be potentially useful in future valley-based devices, and could in general, be applicable for circular dichroism measurements of chiral molecules.

Supporting Information

Supporting Information File 1

Additional experimental data.
Supporting Information features vectorial near-field profiles for the dipole-nanoantenna system, and the radiation pattern of chiral emitters without nanoantenna.
[https://www.beilstein-journals.org/bjnano/content/supplementary/2190-4286-9-71-S1.pdf]

Acknowledgements

We acknowledge the financial support by the Australian Research Council through Discovery Projects. We thank Yuri Kivshar, Sergey Kruk and Carsten Rockstuhl for the useful discussions.

ORCID® iDs

Haitao Chen - https://orcid.org/0000-0002-0272-2264
Dragomir N. Neshev - https://orcid.org/0000-0002-4508-8646

References

1. Xia, F.; Wang, H.; Xiao, D.; Dubey, M.; Ramasubramaniam, A. *Nat. Photonics* **2014,** *8,* 899–907. doi:10.1038/nphoton.2014.271
2. Xu, X.; Yao, W.; Xiao, D.; Heinz, T. F. *Nat. Phys.* **2014,** *10,* 343–350. doi:10.1038/nphys2942
3. Mak, K. F.; Shan, J. *Nat. Photonics* **2016,** *10,* 216–226. doi:10.1038/nphoton.2015.282
4. Yao, W.; Xiao, D.; Niu, Q. *Phys. Rev. B* **2008,** *77,* 235406. doi:10.1103/PhysRevB.77.235406
5. Xiao, D.; Liu, G.-B.; Feng, W.; Xu, X.; Yao, W. *Phys. Rev. Lett.* **2012,** *108,* 196802. doi:10.1103/PhysRevLett.108.196802
6. Rycerz, A.; Tworzydło, J.; Beenakker, C. W. J. *Nat. Phys.* **2007,** *3,* 172–175. doi:10.1038/nphys547
7. Xiao, D.; Yao, W.; Niu, Q. *Phys. Rev. Lett.* **2007,** *99,* 236809. doi:10.1103/PhysRevLett.99.236809

8. Shkolnikov, Y. P.; De Poortere, E. P.; Tutuc, E.; Shayegan, M. *Phys. Rev. Lett.* **2002,** *89,* 226805. doi:10.1103/PhysRevLett.89.226805
9. Wolf, S. A.; Awschalom, D. D.; Buhrman, R. A.; Daughton, J. M.; von Molnár, S.; Roukes, M. L.; Chtchelkanova, A. Y.; Treger, D. M. *Science* **2001,** *294,* 1488–1495. doi:10.1126/science.1065389
10. Ohkawa, F. J.; Uemura, Y. *J. Phys. Soc. Jpn.* **1977,** *43,* 925–932. doi:10.1143/JPSJ.43.925
11. Mak, K. F.; Lee, C.; Hone, J.; Shan, J.; Heinz, T. F. *Phys. Rev. Lett.* **2010,** *105,* 136805. doi:10.1103/PhysRevLett.105.136805
12. Mak, K. F.; He, K.; Shan, J.; Heinz, T. F. *Nat. Nanotechnol.* **2012,** *7,* 494–498. doi:10.1038/nnano.2012.96
13. Zeng, H.; Dai, J.; Yao, W.; Xiao, D.; Cui, X. *Nat. Nanotechnol.* **2012,** *7,* 490–493. doi:10.1038/nnano.2012.95
14. Cao, T.; Wang, G.; Han, W.; Ye, H.; Zhu, C.; Shi, J.; Niu, Q.; Tan, P.; Wang, E.; Liu, B.; Feng, J. *Nat. Commun.* **2012,** *3,* 887. doi:10.1038/ncomms1882
15. Zhang, Y. J.; Oka, T.; Suzuki, R.; Ye, J. T.; Iwasa, Y. *Science* **2014,** *344,* 725–728. doi:10.1126/science.1251329
16. Mak, K. F.; McGill, K. L.; Park, J.; McEuen, P. L. *Science* **2014,** *344,* 1489–1492. doi:10.1126/science.1250140
17. Jones, A. M.; Yu, H.; Ghimire, N. J.; Wu, S.; Aivazian, G.; Ross, J. S.; Zhao, B.; Yan, J.; Mandrus, D. G.; Xiao, D.; Yao, W.; Xu, X. *Nat. Nanotechnol.* **2013,** *8,* 634–638. doi:10.1038/nnano.2013.151
18. Wang, Z.; Shan, J.; Mak, K. F. *Nat. Nanotechnol.* **2017,** *12,* 144–149. doi:10.1038/nnano.2016.213
19. Rostami, H.; Asgari, R. *Phys. Rev. B* **2015,** *91,* 075433. doi:10.1103/PhysRevB.91.075433
20. Srivastava, A.; Sidler, M.; Allain, A. V.; Lembke, D. S.; Kis, A.; Imamoğlu, A. *Nat. Phys.* **2015,** *11,* 141–147. doi:10.1038/nphys3203
21. Li, Y.; Ludwig, J.; Low, T.; Chernikov, A.; Cui, X.; Arefe, G.; Kim, Y. D.; van der Zande, A. M.; Rigosi, A.; Hill, H. M.; Kim, S. H.; Hone, J.; Li, Z.; Smirnov, D.; Heinz, T. F. *Phys. Rev. Lett.* **2014,** *113,* 266804. doi:10.1103/PhysRevLett.113.266804
22. Stier, A. V.; McCreary, K. M.; Jonker, B. T.; Kono, J.; Crooker, S. A. *Nat. Commun.* **2016,** *7,* 10643. doi:10.1038/ncomms10643
23. Ye, Z.; Sun, D.; Heinz, T. F. *Nat. Phys.* **2017,** *13,* 26–29. doi:10.1038/nphys3891
24. Hsu, W.-T.; Chen, Y.-L.; Chen, C.-H.; Liu, P.-S.; Hou, T.-H.; Li, L.-J.; Chang, W.-H. *Nat. Commun.* **2015,** *6,* 8963. doi:10.1038/ncomms9963
25. Aivazian, G.; Gong, Z.; Jones, A. M.; Chu, R.-L.; Yan, J.; Mandrus, D. G.; Zhang, C.; Cobden, D.; Yao, W.; Xu, X. *Nat. Phys.* **2015,** *11,* 148–152. doi:10.1038/nphys3201
26. Smoleński, T.; Goryca, M.; Koperski, M.; Faugeras, C.; Kazimierczuk, T.; Bogucki, A.; Nogajewski, K.; Kossacki, P.; Potemski, M. *Phys. Rev. X* **2016,** *6,* 021024. doi:10.1103/PhysRevX.6.021024
27. Wu, S.; Ross, J. S.; Liu, G.-B.; Aivazian, G.; Jones, A.; Fei, Z.; Zhu, W.; Xiao, D.; Yao, W.; Cobden, D.; Xu, X. *Nat. Phys.* **2013,** *9,* 149–153. doi:10.1038/nphys2524
28. Wang, Q. H.; Kalantar-Zadeh, K.; Kis, A.; Coleman, J. N.; Strano, M. S. *Nat. Nanotechnol.* **2012,** *7,* 699–712. doi:10.1038/nnano.2012.193
29. Kühn, S.; Håkanson, U.; Rogobete, L.; Sandoghdar, V. *Phys. Rev. Lett.* **2006,** *97,* 017402. doi:10.1103/PhysRevLett.97.017402
30. Anger, P.; Bharadwaj, P.; Novotny, L. *Phys. Rev. Lett.* **2006,** *96,* 113002. doi:10.1103/PhysRevLett.96.113002
31. Ringler, M.; Schwemer, A.; Wunderlich, M.; Nichtl, A.; Kürzinger, K.; Klar, T. A.; Feldmann, J. *Phys. Rev. Lett.* **2008,** *100,* 203002. doi:10.1103/PhysRevLett.100.203002
32. Liu, M.; Lee, T.-W.; Gray, S. K.; Guyot-Sionnest, P.; Pelton, M. *Phys. Rev. Lett.* **2009,** *102,* 107401. doi:10.1103/PhysRevLett.102.107401
33. Curto, A. G.; Taminiau, T. H.; Volpe, G.; Kreuzer, M. P.; Quidant, R.; Van Hulst, N. F. *Nat. Commun.* **2013,** *4,* 1750. doi:10.1038/ncomms2769
34. Rodriguez, S. R. K.; Bernal Arango, F.; Steinbusch, T. P.; Verschuuren, M. A.; Koenderink, A. F.; Gómez Rivas, J. *Phys. Rev. Lett.* **2014,** *113,* 247401. doi:10.1103/PhysRevLett.113.247401
35. Kruk, S. S.; Decker, M.; Staude, I.; Schlecht, S.; Greppmair, M.; Neshev, D. N.; Kivshar, Y. S. *ACS Photonics* **2014,** *1,* 1218–1223. doi:10.1021/ph500288u
36. Decker, M.; Staude, I.; Shishkin, I. I.; Samusev, K. B.; Parkinson, P.; Sreenivasan, V. K. A.; Minovich, A.; Miroshnichenko, A. E.; Zvyagin, A.; Jagadish, C.; Neshev, D. N.; Kivshar, Y. S. *Nat. Commun.* **2013,** *4,* 2949. doi:10.1038/ncomms3949
37. Hancu, I. M.; Curto, A. G.; Castro-López, M.; Kuttge, M.; van Hulst, N. F. *Nano Lett.* **2014,** *14,* 166–171. doi:10.1021/nl403681g
38. Rodríguez-Fortuño, F. J.; Marino, G.; Ginzburg, P.; O'Connor, D.; Martínez, A.; Wurtz, G. A.; Zayats, A. V. *Science* **2013,** *340,* 328–330. doi:10.1126/science.1233739
39. Mitsch, R.; Sayrin, C.; Albrecht, B.; Schneeweiss, P.; Rauschenbeutel, A. *Nat. Commun.* **2014,** *5,* 5713. doi:10.1038/ncomms6713
40. le Feber, B.; Rotenberg, N.; Kuipers, L. *Nat. Commun.* **2015,** *6,* 6695. doi:10.1038/ncomms7695
41. Bliokh, K. Y.; Smirnova, D.; Nori, F. *Science* **2015,** *348,* 1448–1451. doi:10.1126/science.aaa9519
42. Lodahl, P.; Mahmoodian, S.; Stobbe, S.; Rauschenbeutel, A.; Schneeweiss, P.; Volz, J.; Pichler, H.; Zoller, P. *Nature* **2017,** *541,* 473–480. doi:10.1038/nature21037
43. Evlyukhin, A. B.; Reinhardt, C.; Chichkov, B. N. *Phys. Rev. B* **2011,** *84,* 235429. doi:10.1103/PhysRevB.84.235429
44. Schuller, J. A.; Karaveli, S.; Schiros, T.; He, K.; Yang, S.; Kymissis, I.; Shan, J.; Zia, R. *Nat. Nanotechnol.* **2013,** *8,* 271–276. doi:10.1038/nnano.2013.20
45. Noori, Y. J.; Cao, Y.; Roberts, J.; Woodhead, C.; Bernardo-Gavito, R.; Tovee, P.; Young, R. J. *ACS Photonics* **2016,** *3,* 2515–2520. doi:10.1021/acsphotonics.6b00779
46. Jackson, J. D. *Classical Electrodynamics;* John Wiley & Sons Inc.: New York, NY, USA, 1998.
47. Abernethy, C. D.; Codd, G. M.; Spicer, M. D.; Taylor, M. K. *J. Am. Chem. Soc.* **2003,** *125,* 1128–1129. doi:10.1021/ja0276321
48. Johnson, P. B.; Christy, R. W. *Phys. Rev. B* **1972,** *6,* 4370. doi:10.1103/PhysRevB.6.4370
49. Coleman, J. N.; Lotya, M.; O'Neill, A.; Bergin, S. D.; King, P. J.; Khan, U.; Young, K.; Gaucher, A.; De, S.; Smith, R. J.; Shvets, I. V.; Arora, S. K.; Stanton, G.; Kim, H.-Y.; Lee, K.; Kim, G. T.; Duesberg, G. S.; Hallam, T.; Boland, J. J.; Wang, J. J.; Donegan, J. F.; Grunlan, J. C.; Moriarty, G.; Shmeliov, A.; Nicholls, R. J.; Perkins, J. M.; Grieveson, E. M.; Theuwissen, K.; McComb, D. W.; Nellist, P. D.; Nicolosi, V. *Science* **2011,** *331,* 568–571. doi:10.1126/science.1194975
50. Choi, J.; Chen, H.; Li, F.; Yang, L.; Kim, S. S.; Naik, R. R.; Ye, P. D.; Choi, J. H. *Small* **2015,** *11,* 5520–5527. doi:10.1002/smll.201501431
51. Cheng, F.; Xu, H.; Xu, W.; Zhou, P.; Martin, J.; Loh, K. P. *Nano Lett.* **2017,** *17,* 1116–1120. doi:10.1021/acs.nanolett.6b04715

52. Kinkhabwala, A.; Yu, Z.; Fan, S.; Avlasevich, Y.; Müllen, K.; Moerner, W. E. *Nat. Photonics* **2009,** *3,* 654–657. doi:10.1038/nphoton.2009.187

License and Terms

This is an Open Access article under the terms of the Creative Commons Attribution License (http://creativecommons.org/licenses/by/4.0), which permits unrestricted use, distribution, and reproduction in any medium, provided the original work is properly cited.

The license is subject to the *Beilstein Journal of Nanotechnology* terms and conditions: (https://www.beilstein-journals.org/bjnano)

The definitive version of this article is the electronic one which can be found at: doi:10.3762/bjnano.9.71

BEILSTEIN JOURNAL OF NANOTECHNOLOGY

Theoretical study of strain-dependent optical absorption in a doped self-assembled InAs/InGaAs/GaAs/AlGaAs quantum dot

Tarek A. Ameen[*,‡1], Hesameddin Ilatikhameneh[*,‡1], Archana Tankasala[1], Yuling Hsueh[1], James Charles[1], Jim Fonseca[1], Michael Povolotskyi[1], Jun Oh Kim[2], Sanjay Krishna[3], Monica S. Allen[4], Jeffery W. Allen[4], Rajib Rahman[1] and Gerhard Klimeck[1]

Full Research Paper

Open Access

Address:
[1]Network for Computational Nanotechnology, Department of Electrical and Computer Engineering, Purdue University, West Lafayette, IN 47907, USA, [2]Korean Research Institute of Standards and Sciences, Daejeon 34113, South Korea, [3]Department of Electrical and Computer Engineering, Ohio State University, Columbus, OH 43210, USA and [4]Air Force Research Laboratory, Munitions Directorate, Eglin AFB, FL 32542, USA.

Email:
Tarek A. Ameen[*] - tameen@purdue.edu;
Hesameddin Ilatikhameneh[*] - hilatikh@purdue.edu

* Corresponding author ‡ Equal contributors

Keywords:
anharmonic atomistic strain model; biaxial strain ratio; configuration interaction; optical absorption; quantum qot filling; self-assembled quantum dots; semi-empirical tight-binding; sp3d5s* with spin–orbit coupling (sp3d5s*_SO)

Beilstein J. Nanotechnol. **2018,** *9,* 1075–1084.
doi:10.3762/bjnano.9.99

Received: 02 November 2017
Accepted: 09 February 2018
Published: 04 April 2018

This article is part of the Thematic Series "Light–Matter interactions on the nanoscale".

Guest Editor: M. Rahmani

© 2018 Ameen et al.; licensee Beilstein-Institut.
License and terms: see end of document.

Abstract

A detailed theoretical study of the optical absorption in doped self-assembled quantum dots is presented. A rigorous atomistic strain model as well as a sophisticated 20-band tight-binding model are used to ensure accurate prediction of the single particle states in these devices. We also show that for doped quantum dots, many-particle configuration interaction is also critical to accurately capture the optical transitions of the system. The sophisticated models presented in this work reproduce the experimental results for both undoped and doped quantum dot systems. The effects of alloy mole fraction of the strain controlling layer and quantum dot dimensions are discussed. Increasing the mole fraction of the strain controlling layer leads to a lower energy gap and a larger absorption wavelength. Surprisingly, the absorption wavelength is highly sensitive to the changes in the diameter, but almost insensitive to the changes in dot height. This behavior is explained by a detailed sensitivity analysis of different factors affecting the optical transition energy.

Introduction

Self-assembled quantum dots are employed as light absorbers in many optoelectronic devices, such as quantum-dot infrared photodetectors (QDIPs) [1,2], and intermediate-band solar cells (IBSCs) [3,4]. The optical properties of quantum dots (QDs) can be tuned through shape, dimensions and composition of the dots making them attractive for optoelectronic applications. Moreover, their sensitivity to normally incident light make them advantageous over other nanostructures, such as quantum wells, that are insensitive to normally incident light [2].

The absorption coefficient α(λ) of quantum dots is an important parameter that needs to be precisely designed for the proper operation of these devices. An accurate model for the absorption coefficient α(λ) is therefore crucial in the design and prediction of the device behavior. Therefore, this study aims to fill the gaps in current absorption models, namely the atomistic strain and band structure calculations that are needed for accurate description of the bound states. Moreover, doped devices require evaluation of many-particle configuration interaction (CI) calculations for a proper treatment of the optical transitions. The effects of alloy mole fraction of the strain controlling layer and quantum dot dimensions are also discussed.

Self-assembled quantum dots have around 10% lattice strain [5]. Atomistic strain models like that of Keating [6], or anharmonic models [7] are typically used to determine the relaxed atom positions. The anharmonic strain model has additional strain parameters with anharmonic corrections added to the harmonic model, which improves its accuracy. Without anharmonic corrections, the harmonic potential underestimates the repulsion at smaller bond lengths and also fails to capture the weakening of atomic forces at large atomic separation [8].

The anharmonic strain parameters were originally optimized to obtain correct Grüneisen parameters for accurate phonon dispersion calculations [7]. However, we show that the original parameter set cannot reproduce the experimental optical absorption peaks in quantum dots [9]. Using these parameters to determine strain in quantum wells does not agree with the well-known analytical solution of strain in quantum wells. Optimizing the parameters to obtain correct biaxial strain ratios in quantum wells is shown here to improve the accuracy of quantum dot simulations as compared with experimental measurements. The Hamiltonian is constructed with semi-empirical tight-binding with 20-orbital sp3d5s* basis per atom, including spin–orbit interaction (sp3d5s*_SO) [10]. The absorption coefficient is calculated by employing Fermi's golden rule.

In the following sections the simulated system and the numerical tools employed in simulations are described, then the theoretical aspects of the problem and optimization of the strain model are discussed. Lastly, the results of the simulation are presented including a sensitivity analysis of the absorption to various quantum dot parameters.

Multi-Million-Atom Simulation

As shown in the Figure 1, the investigated QD system [11] has a dome-shaped InAs quantum dot with a base diameter of 20 nm and a height of 5 nm. The wetting layer is two monolayers. The measured system has been doped with sheet doping of two electrons per dot. The strain controlling layer is made of $In_{0.15}Ga_{0.85}As$ and is sandwiched between two layers of GaAs each with a thickness of 1 nm. Next, there are two layers of $Al_{0.22}Ga_{0.78}As$, each with a thickness of 2 nm. The rest of the structure is made of $Al_{0.07}Ga_{0.93}As$. The dimensions of the simulated QD systems are 60 nm × 60 nm × 60 nm. The strain simulation contains around ten million atoms and the atomistic grid is as shown in Figure 2.

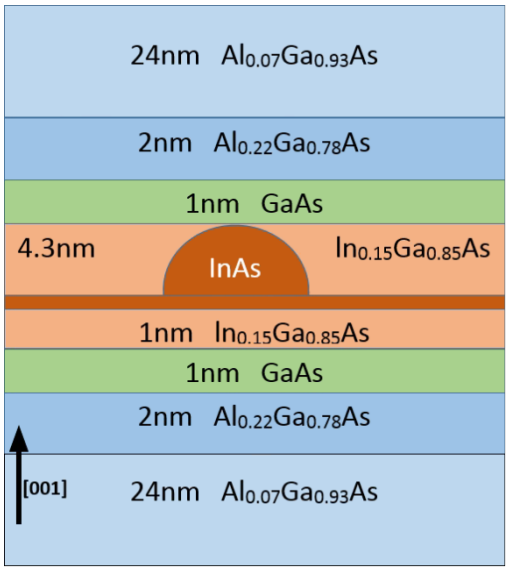


Figure 1: A schematic of the measured and simulated QD system. The dimensions of the simulated structure are 60 nm × 60 nm × 60 nm. The quantum dot is dome-shaped InAs with a base diameter of 20 nm and a height of 5 nm, with a wetting layer of two monolayers. The strain control layer of $In_{0.15}Ga_{0.85}As$ is sandwiched between two 1 nm layers of GaAs, and two 2 nm layers of $Al_{0.22}Ga_{0.78}As$. The rest of the structure is made of $Al_{0.07}Ga_{0.93}As$.

The band structure calculations do not need all of atoms to be included in the simulation, since bound states decay exponentially outside the quantum dot. The band structure calculations are performed using a 40 nm × 40 nm × 20 nm box surrounding the quantum dot. This box contains only 1.5 million atoms. Well-defined and well-calibrated tight-binding models are

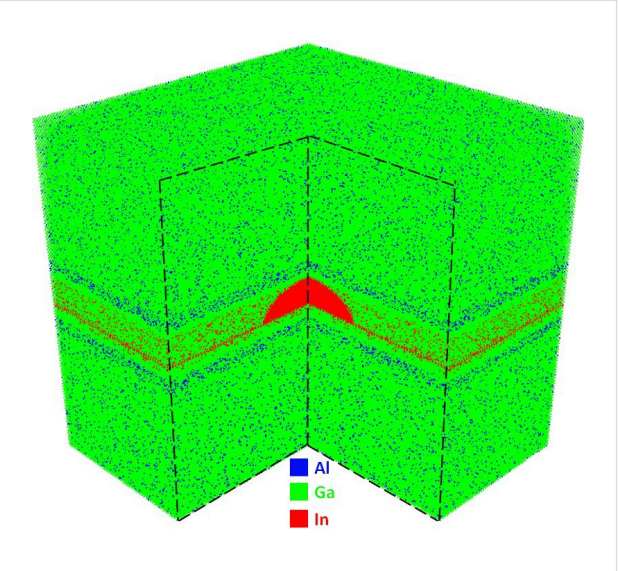


Figure 2: The atomistic grid of the simulated QD showing only cations (Al,Ga,In) to emphasize the randomness of the simulated alloys. The number of atoms used for the strain simulation is approximately 10 million atoms, while for band structure calculations only approximately 1.5 million atoms are used.

needed to enable such large-scale device simulations. Early works on tight-binding models started from analytical effective mass extractions from the usually only numerically defined model [12]. Later semi-automatic mapping methods using genetic algortithms were introduced [13] followed by DFT-based projection methods [14,15]. Each atom has 20 orbitals in the sp3d5s*_SO tight-binding basis. Strain and electronic structure simulations of such large systems are computationally demanding and require highly scalable computational codes. The code used for our simulations is the Nano Electronic MOdeling tool in version 5 ("NEMO5") [16-22].

Theoretical Model

Atomistic strain model

The Harmonic Keating strain model, introduced in [6], has the elastic energy given by

$$E = \frac{3}{8}\sum_{m,n}\left[\frac{\alpha_{mn}}{d_{mn}^2}\left(r_{mn}^2 - d_{mn}^2\right)^2 + \sum_{k>n}\frac{\beta_{mnk}}{d_{mn}d_{mk}}\left(r_{mn}\cdot r_{mk} - d_{mn}\cdot d_{mk}\right)\right], \quad (1)$$

where r_{mn} is the displacement vector from atom m to atom n for the strained crystal as shown in Figure 3, while d_{mn} is the same vector for the unstrained crystal. The coefficient α corresponds to the force constant of the bond length distortion, the bond-stretching coefficient. While β is the bond-bending coefficient that corresponds to the force constant of the bond angle (θ) distortion. The difference between the dot products reduces to the difference in cos(θ).

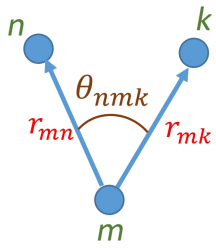


Figure 3: Bond lengths and bond angle for three neighboring atoms *m*, *n*, and *k*.

The summation includes nearest neighbors only and the total energy is minimized with respect to the individual atomic positions, thus relaxing the structure. The problem with the harmonic Keating potential given by Equation 1 is that it produces a symmetric energy profile around the equilibrium interatomic distance and angle. Thus, the Keating model fails to reproduce the weakening of the strain energy with increasing bond length and underestimates the repulsive forces at close atomic separations [7,8]. The anharmonic correction of the Keating model proposed by Lazarenkova et al. [7,8] solves this problem by modifying the two parameters α and β of the Keating model and making them functions of bond length r and bond angle θ as given by

$$\begin{aligned}\alpha_{mn} &= \alpha_{mn}^0\left(1 - A_{mn}\frac{r_{mn}^2 - d_{mn}^2}{d_{mn}^2}\right),\\ \beta_{mnk} &= \beta_{mnk}^0\left(1 - B_{mnk}\left(\cos\left(\theta_{mnk}\right) - \cos\left(\theta_{mnk}^0\right)\right)\right)\\ &\times\left(1 - C_{mnk}\frac{r_{mn}\cdot r_{mk} - d_{mn}\cdot d_{mk}}{d_{mn}\cdot d_{mk}}\right).\end{aligned} \quad (2)$$

A, B and C are anharmonic correction coefficients. A and C describe the dependence of bond-stretching coefficient α and bond-bending coefficient β on the bond length strain, while B describes the dependence of bond-bending coefficient (β) on angle deformation. The anharmonic model was developed to simulate phonon dispersion and transport and the anharmonic strain parameters were optimized to reproduce the Grüneisen parameters $\gamma_i = -(V/\omega_i)(\delta\omega_i/\delta V)$, which are a measure of the dependence of the phonon mode frequencies on strain. Simulating the strain in quantum dots with the original anharmonic strain parameters produces inaccurate results.

In addition, simulating strain in quantum wells with these parameters gives strain tensor components that do not match the

analytical solution of the strain in quantum wells as shown in Table 1. The parameters of the model have been tuned to reproduce the biaxial strain ratio σ of InAs in order to capture the strain distribution in quantum wells and quantum dots made from InAs. The biaxial strain ratio σ of InAs is 1.053 [23]. Only the parameter α^0 has been tuned to 19.35 Nm^{-1} while keeping the rest of the strain parameters as reported in [7]. Table 1 shows the atomistic strain calculated for InAs/GaAs quantum well, as shown in Figure 4, before and after tuning. The analytical expressions for the strain components in quantum wells are $\varepsilon_{\parallel} = (a_{GaAs} - a_{InAs})/a_{InAs}$ and $\varepsilon_{\perp} = -\sigma\varepsilon_{\parallel}$[24], where a is the lattice constant.

Table 1: Strain calculated for the InAs/GaAs quantum well. Tuning has improved the anharmonic strain results in the quantum well.

method	$\varepsilon_{\parallel}$	$\varepsilon_{\perp}$
analytical	−6.68%	7.04%
anharmonic before tuning	−6.68%	8.9%
anharmonic after tuning	−6.68%	7.04%

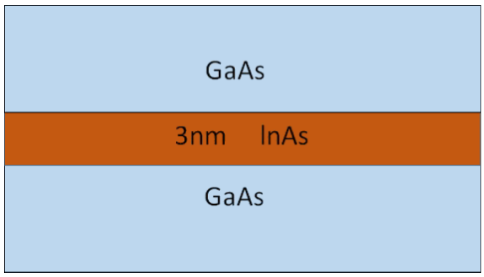


Figure 4: An InAs/GaAs quantum well of thickness 3 nm used for the optimization of the anharmonic strain model.

Electronic structure and absorption

The eigenstates of the system were calculated with a Hamiltonian constructed from semi-empirical tight-binding sp3d5s*_SO basis. The Slater–Koster tight-binding [25] parameters for InAs, GaAs and AlAs are taken from [26,27]. Boykin et al. show the effect of including strain on the tight-binding Hamiltonian [10]. These parameters are well established and previously verified with experimental measurements of quantum dots [28-31].

For the absorption coefficient α, Fermi's golden rule has been used to calculate the absorption coefficient [32,33],

$$\alpha(\omega) = \frac{2\pi\omega n_{\text{dots}}}{\acute{n}\varepsilon_0 c}\sum_{i,f}\left|\underline{d_{fi}}\cdot\underline{\hat{e}}\right|^2\delta\left(E_f - E_i - \hbar\omega\right)\left(F_i - F_f\right), \quad (3)$$

where n_{dots} is the number of quantum dots per unit volume, ω is the photon angular frequency, E_i and E_f are initial and final energies of the transition, F_i and F_f are occupation probability of the initial and final states, ń is the refractive index of the material, c is the speed of light in free space, ε_0 is the free space permittivity, $\underline{\hat{e}}$ is the polarization of the incident light, and $\underline{d_{fi}}$ is the first-order dipole moment that is given by $\underline{d_{fi}} = q\langle\psi_f\,|\,\underline{r}\,|\,\psi_i\rangle$, where q is the electron charge.

For transitions between bound states in valence and conduction bands, $F_i = 1$, while F_f depends on the energy level and doping. Normally, quantum dots are occupied by a number of electrons equal to the average number of dopants per dot [34]. This approach is reasonable for quantum dots that are far from heavily doped regions. However, it is not appropriate for quantum dots adjacent to heavily doped regions, such as contacts. In addition, to calculate optical transitions of doped quantum dots, the many-particle states of the quantum dot are evaluated using atomistic configuration interaction [35]. The method accurately captures the electron–electron interactions in electrons bound to dopant atoms in silicon. The single-particle states of the quantum dot are obtained from atomistic tight-binding calculations in NEMO5. These single-electron and hole states are used to construct many-particle Slater determinants, of all possible configurations. Using a full configuration interaction method [36], a many-particle Hamiltonian is constructed and diagonalized in the basis of Slater determinants to obtain the many-particle energies and wavefunctions.

Results and Discussion

Simulation versus experimental results

The model is validated with the measured absorption spectrum [11] of the QD system. Figure 5 shows the calculated and measured absorption spectrum of the device. The simulation result matches very well with the measured absorption and the error in estimating the energy of the absorption peak is less than 3%. This small error can be attributed to idealizing the quantum dot shape, ignoring the slight uncertainty in the material compositions and the variations in the quantum dot dimensions. The doping is 1.5 electrons per dot. The inclusion of many-particle configuration interaction (CI) in calculating the energy transitions significantly improves the agreement between simulations and experiment for the doped quantum dot system. The larger peak in the simulated absorption both with and without CI corresponds to quantum dots occupying one electron (1e) transitioning to an excited state of two electrons and one hole (2e1h), while the lower peak corresponds to the portion of quantum dots occupying two electrons (2e) transitioning to an excited state of three electrons and one hole (3e1h). Including the CI in the simulation results in a reduction in the absorption wavelength due to the repulsive nature of the interaction that in-

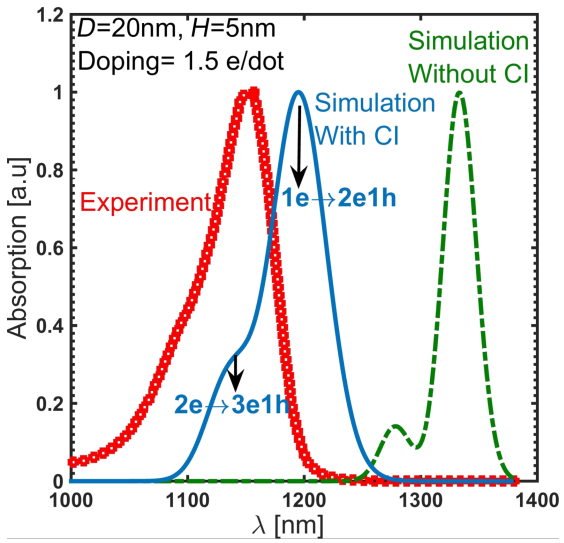


Figure 5: The simulated and the measured absorption spectrum of the QD system. The quantum dot is sample D from [11], which is a dome-shaped QD with a base diameter of 20 nm and height of 5 nm. The doping is 1–2 electrons per dot, which is assumed to be 1.5 here. The inclusion of many-particle configuration interaction (CI) to calculate the energy transitions significantly improves the agreement of the simulation and the experimental measurements. The higher peak corresponds to quantum dots occupying one electron (1e) transitioning to an excited state of two electrons and one hole (2e1h), while the lower peak corresponds to quantum dots occupying two electrons (2e) transitioning to an excited state of three electrons and one hole (3e1h). The error is less than 3% in calculating the absorption peak photon energy.

creases the transition energy. Additional comparisons with experimental measurements are provided in the discussion of the effect of alloy mole fraction on the strain-controlling layer.

Band structure and states

Figure 6 shows the wavefunction probability density of the first eight non-degenerate states of both electrons and holes. It is worth noting that the hole ground state has an s-orbital-like shape.

QDs have a complicated band profile since multiple effects such as geometric confinement, strain and alloy disorder, can cause major changes in the band edges of the bulk material. It is important to know where the wavefunctions of the electrons and holes are localized due to these disordered band edges, as the spatial overlap between the states determines the optical absorption spectrum. Hence, one can look at the conduction and valence band edges along arbitrary lines passing through the quantum dot. This can be done using deformation potential theory, which gives the shift of band edges due to small lattice deformations. The shift in the band edges due to lattice strain for zincblende materials is given by [37]:

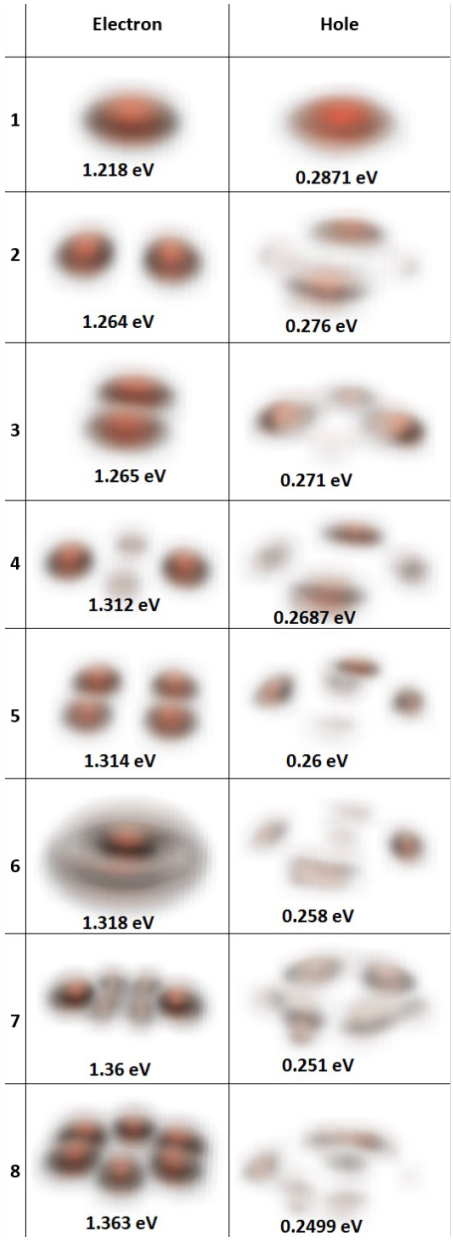


Figure 6: The magnitude square of the wave functions of the electron and hole states. Only the first eight electron and hole states are plotted.

$$\begin{aligned}\Delta E_{\mathrm{c}} &= a_{\mathrm{c}}\varepsilon_{\mathrm{H}},\\ \Delta E_{\mathrm{vHH}} &= a_{\mathrm{v}}\varepsilon_{\mathrm{H}} + \frac{b}{2}\varepsilon_{\mathrm{B}},\\ \Delta E_{\mathrm{vLH}} &= a_{\mathrm{v}}\varepsilon_{\mathrm{H}} - \frac{b}{2}\varepsilon_{\mathrm{B}},\end{aligned} \tag{4}$$

where ΔE_{c} is the shift in the conduction band edge, ΔE_{vHH} and ΔE_{vLH} are the shifts in the heavy and light hole band edges, respectively. a_{c}, a_{v}, and b are the deformation potential coeffi-

cients of the material. In these simulations, the parameters recommended for III–V materials by [38] are used. ε_H and ε_B are the hydrostatic and biaxial strain components, which are linear combinations of the atomistic strain components: $\varepsilon_H = \varepsilon_{xx} + \varepsilon_{yy} + \varepsilon_{zz}$ and $\varepsilon_B = \varepsilon_{xx} + \varepsilon_{yy} - 2\varepsilon_{zz}$ [37], where z is the growth direction. Figure 7 shows the band edges along two lines through the middle of the quantum dot along the [001] and [110] directions. The unstrained band edges show a significant effect of strain on the band edges.

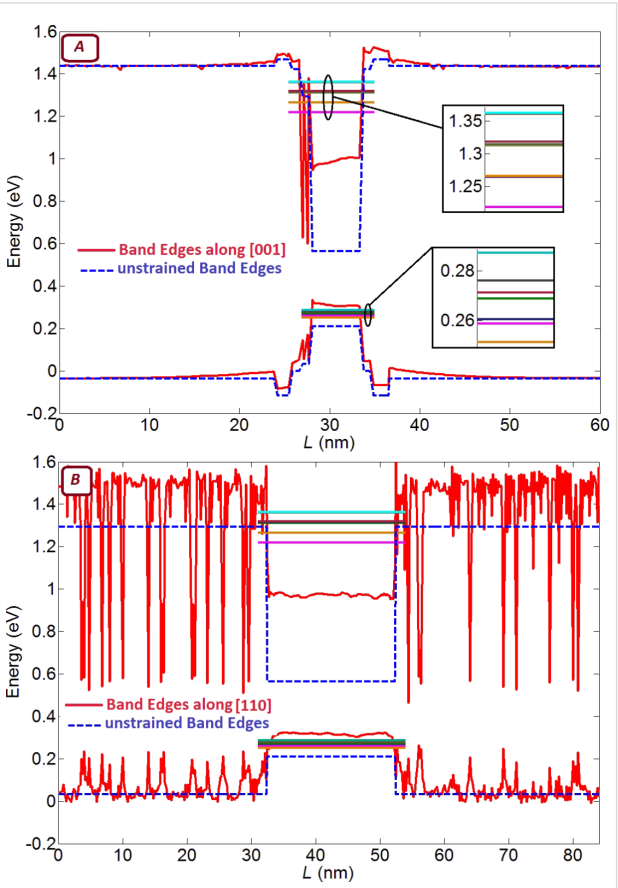


Figure 7: The conduction and valence band edges (solid lines) along a line through the middle of the quantum dot in the (A) [001] and (B) [110] directions. The dashed lines are the band edges of the unstrained bulk materials, drawn to show the significant effect of strain on deforming the band structure. The solid horizontal lines in the quantum dots are plotted at the energies corresponding to electron and hole confined states. The noisy red lines in (B) indicate the local band edges in the explicitly represented atomistic alloy. In an atomistic representation of an alloy one obtains an explicitly fluctuating band edge [26].

Effect of quantum dot dimensions

Figure 8 shows the effect of variations in quantum dot diameter and height on the in-plane polarized absorption spectrum. An increasing dot diameter results in a red-shift of the absorption peaks, while increasing the dot height does not have a significant effect on the absorption wavelength. In contrast to the simple particle-in-a-box problem, which predicts a stronger sensitivity to the smaller dimension (the height), our simulations show that absorption wavelength is much more sensitive to changing the dot diameter than to changing the height.

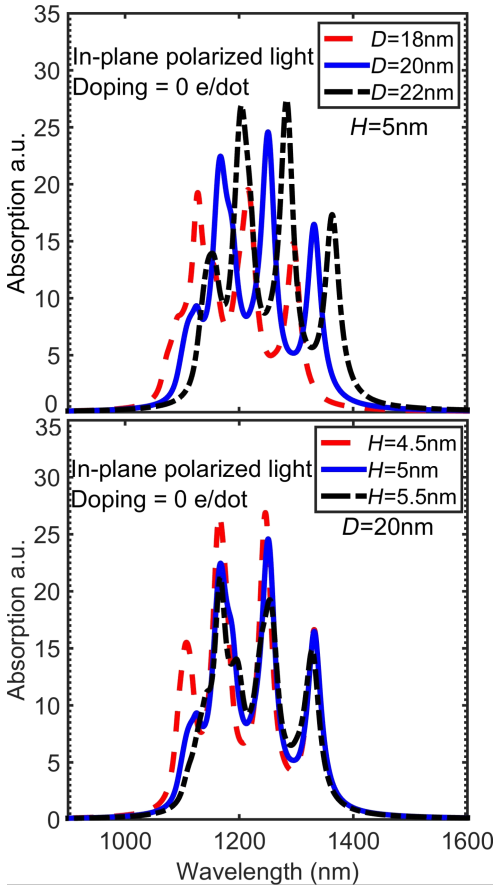


Figure 8: The in-plane polarized absorption spectrum calculated for (A) different diameters and (B) different heights of the quantum dot. Increasing the dot diameter results in a shift of the peaks towards longer wavelengths, while increasing the dot height does not have a significant effect on the wavelength.

The effects of changing dimensions on the energy transition ΔE between the hole and electron ground states can be understood with a simple analytical model. This transition has two contributions: strain and confinement. The strain shifts the band edges and affects the energy gap E_g, while the confinement increases the minimum allowed energy of electron E_{elec} and hole E_{hole} with respect to the band edges. Let $E_{box} = E_{elec} + E_{hole}$, then the transition energy E is

$$\Delta E = E_g + E_{box}. \quad (5)$$

Due to the sign of the deformation potential and strain, the valence band edge inside the quantum dot is of a heavy hole, from Equation 4

$$E_g = E_{g,bulk} + (a_c - a_v)\varepsilon_H - \frac{b}{2}\varepsilon_B. \quad (6)$$

Figure 9 shows the effect of changing diameter and height on the hydrostatic and biaxial strain. The magnitude of the biaxial strain increases with increasing diameter and decreases with increasing height, while the magnitude of the hydrostatic strain changes slightly in the direction opposite to the biaxial strain. Increasing the height is equivalent to the decreasing diameter in terms of changing the strain in the quantum dot since it depends almost entirely on the aspect ratio not on the individual dimensions [39]. Increasing the diameter reduces the energy gap, which further reduces the optical transition energy, while increasing the height increases the energy gap, which works against the reduction in confinement energy. In the case of varying height, this compensation results in almost the same optical transition energy. Although the variations in the hydrostatic strain are smaller than variations in the biaxial strain, as shown in Figure 9, the hydrostatic strain variations cannot be neglected. This is due to the stronger weight of deformation potential for hydrostatic strain. For example, $a_c - a_v$ = -6 eV is six times higher than $b/2 = -1$ eV for InAs. Also, changing one of the dimensions either increases or decreases the hydrostatic strain, and it has the opposite effect on biaxial strain (decreases or increases), but the hydrostatic and biaxial strain work together in the same direction on the energy gap since they have opposite signs in Equation 6.

To get an expression for E_{box}, the dome-shaped quantum dot is approximated to be a disc of cylinder radius R and height H. One can easily obtain E_{box} by solving an effective-mass Hamiltonian in the cylindrical coordinates,

$$E_{box} = \frac{\hbar^2}{2}\left(\frac{1}{m_e} + \frac{1}{m_h}\right)\left(\frac{\pi^2}{H^2} + \frac{X_{01}^2}{m_h}\right), \quad (7)$$

where m_e, m_h are the effective masses of electron and the heavy hole, and X_{01} = 2.405 is the Bessel function of the first kind with order zero. Note that effective masses for the electron and heavy hole under strain are different from that in the bulk, and the effective masses of InAs are $m_e = 0.1m_0$ and $m_h = 0.48m_0$ [26].

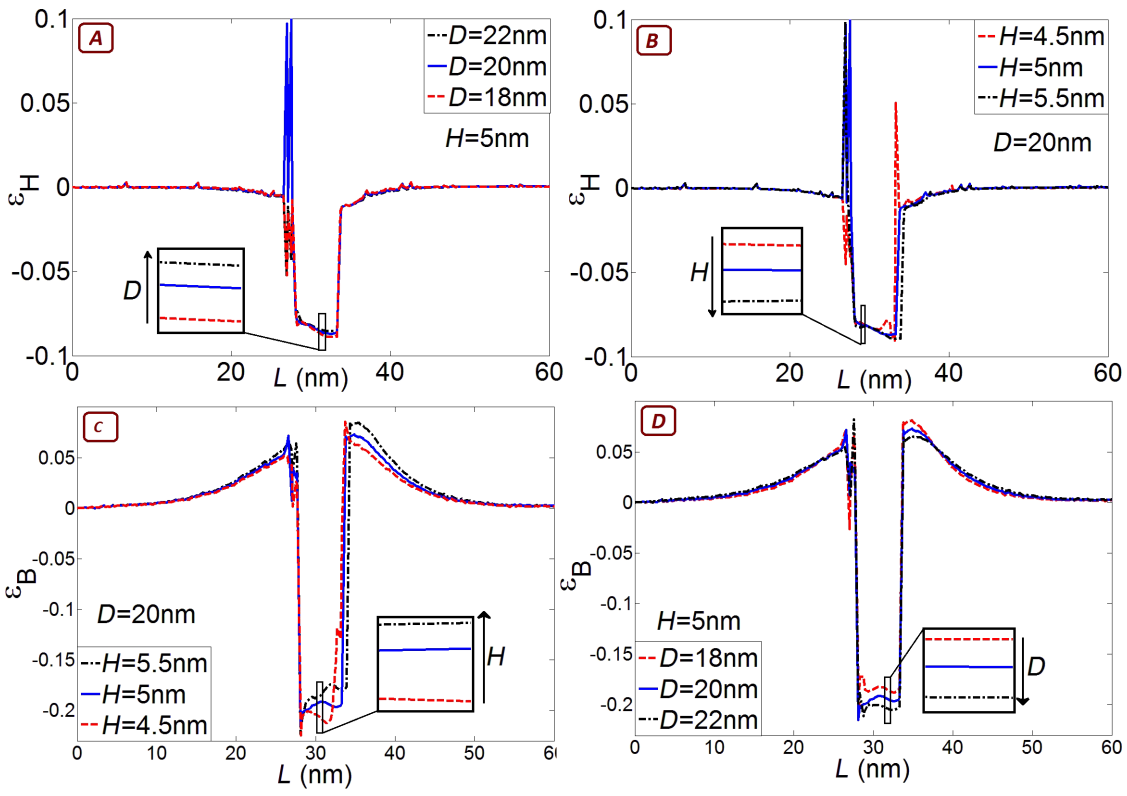


Figure 9: Hydrostatic ε_H and biaxial ε_B strain with different dimensions along a line through the middle of the quantum dot in the [001] direction. (A) ε_H as a function of different dot diameters; (B) ε_H as a function of different dot heights; (C) is ε_B as a function of different dot diameters; (D) ε_B as a function of different dot heights. The magnitude of the biaxial strain increases with increasing diameter and decreases with increasing height, while the hydrostatic strain evolves in the opposite direction.

For a quantum dot of $D = 20$ nm and $H = 5$ nm, the sensitivity of the confinement energy to the dot radius is

$$\frac{\delta E_{\text{box}}}{\delta R} = -\hbar^2 X_{01}^2 \left(\frac{1}{m_e} + \frac{1}{m_h}\right)\frac{1}{R^3} \approx -5\ \text{meV/nm},$$

and the sensitivity of the energy gap to the dot radius is

$$\frac{\delta E_g}{\delta R} = \left(a_c - a_v\right)\frac{\delta\varepsilon_H}{\delta R} - \frac{b}{2}\frac{\delta\varepsilon_B}{\delta R} \approx -17\ \text{meV/nm},$$

which give a total sensitivity of the optical transition $(\delta\Delta E)/\delta R \approx -22$ meV/nm.

Similarly for variations in height,

$$\frac{\delta E_{\text{box}}}{\delta H} = -\hbar^2 \pi^2 \left(\frac{1}{m_e} + \frac{1}{m_h}\right)\frac{1}{H^3} \approx -68\ \text{meV/nm},$$

$$\frac{\delta E_g}{\delta H} = \left(a_c - a_v\right)\frac{\delta\varepsilon_H}{\delta H} - \frac{b}{2}\frac{\delta\varepsilon_B}{\delta H} \approx 65\ \text{meV/nm},$$

which give $(\delta\Delta E)/\delta H \approx -3$ meV/nm. Increasing the dot radius causes both contributions to reduce the transition energy. Increasing the dot height causes both contributions to work against each other, which reduces the sensitivity of the transition energy to dot height.

Strain controlling layer

Changing the mole fraction of In in the InGaAs strain controlling layer (capping layer) is a convenient way to tune the absorption peak. The effect of mole fraction has been studied on a slightly different system, reported in [9], which helps us further validate the results of the simulations. The system reported in [9] is almost the same as in [11] except for two differences: (i) it is not doped and, (ii) it uses GaAs instead of AlGaAs. Figure 10 shows the experimental and simulation results of the optical transitions of the QD systems reported in [9]. Unlike the earlier discussed experiments, quantum dots in [9] are undoped and have been measured at various strain controlling layer compositions. The optimization of the anharmonic strain model greatly improves the simulation results. Increasing the mole fraction of In increases the transition wavelength. This is further explained by examining the effect of changing the mole fraction on hydrostatic and biaxial strain and the band edges. Figure 11 shows the hydrostatic and biaxial strain along a lines passing through the middle of the quantum dot in the [001] direction for different mole fractions of In. As shown in these figures, the hydrostatic and biaxial strain change with the In mole fraction in the same way they change with diameter. That is, increasing the In mole fraction results in an increase in the magnitude of the biaxial strain and a decrease in the magnitude of the hydrostatic strain. This leads to a lower energy gap and larger absorption wavelength, as shown in Figure 10.

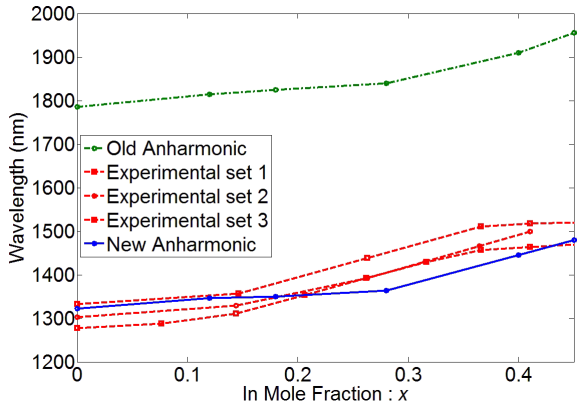


Figure 10: Experimental and simulation results of the optical transition of the QD system reported in [9]. Increasing the In mole fraction increases the transition wavelength. The optimization of the anharmonic strain model has greatly improved the simulation results.

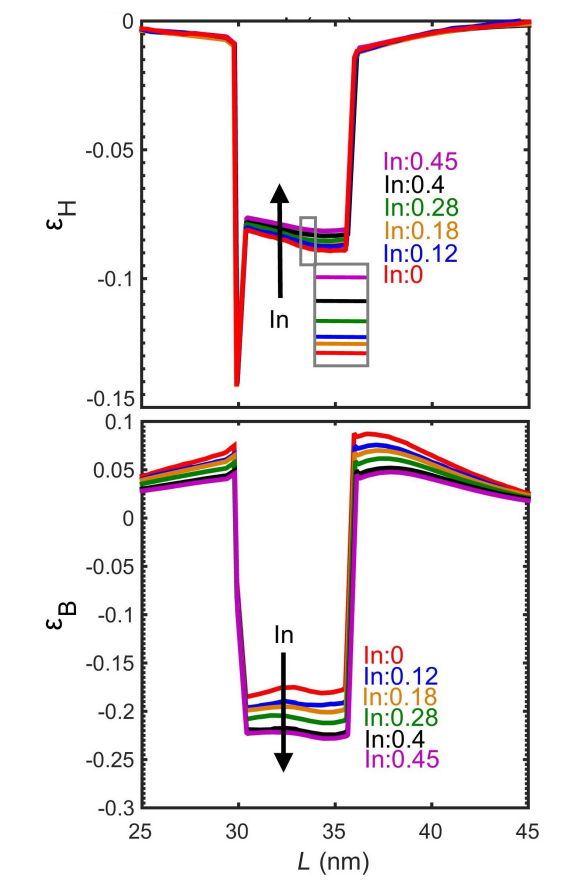


Figure 11: Hydrostatic and biaxial strain with different mole fractions of In along a line passing through the middle of the quantum dot in the [001] direction.

Conclusion

In this paper, a detailed theoretical study of the optical absorption and strain behavior in self-assembled quantum dots has been presented. Self-assembled quantum dots are highly strained heterostructures and a rigorous atomistic strain model is needed to accurately calculate the electronic states in the system. In addition, many-particle configuration interaction has been accounted for, to properly simulate doped quantum dots. The models accurately describe the complex coupled underlying physics. This improvement is shown by the closer agreement with experimental data. The simulations reproduce the experimental results with an error below 3%. The model was implemented in NEMO5 and used to simulate characteristics of an InAs/GaAs/AlAs quantum dot systems. Increasing the dot diameter results in a shift of the absorption peaks towards longer wavelengths, while increasing the dot height does not have a significant effect on wavelength. When the diameter is changed, the band gap and confinement energies work with each other, whereas when the height is changed, the band gap and confinement energies work against each other. Increasing the mole fraction if In in the strain controlling layer works in the same way as increasing the dot diameter and changes the strain leading to longer absorption wavelengths.

In conclusion, the method presented here provides a way to incorporate the inhomogeneous environment of QDs in simulations by taking into account device geometry and quantum confinement, alloy disorder, electrostatics, many-particle interactions, and spatially varying strain distribution. Such details are needed to interpret and guide experimental measurements and device design with quantitative accuracy.

Acknowledgements

The authors (MSA and JWA) are thankful for the funding support through AFOSR Lab Task 17RWCOR398 (PO: Dr. K. Caster). The use of nanoHUB.org computational resources operated by the Network for Computational Nanotechnology funded by the US National Science Foundation under grant EEC-1227110, EEC-0228390, EEC-0634750, OCI-0438246, and OCI-0721680 is gratefully acknowledged. This research was supported in part by computational resources provided by Information Technology at Purdue University. NEMO5 developments were critically supported by an NSF Peta-Apps award OCI-0749140 and by Intel Corp. Any opinions, findings, and conclusions or recommendations expressed in this material are those of the authors and do not necessarily reflect the views of the National Science Foundation. This research is part of the Blue Waters sustained-petascale computing project, which is supported by the National Science Foundation (award number ACI 1238993) and the state of Illinois. Blue Waters is a joint effort of the University of Illinois at Urbana-Champaign and its National Center for Supercomputing Applications. This work is also part of the Advanced Nanoelectronic Device Design with Atomistic Simulations PRAC allocation supported by the National Science Foundation (award number OCI-1640876). This work used the Extreme Science and Engineering Discovery Environment (XSEDE), which is supported by National Science Foundation grant number ACI-1548562.

ORCID® iDs

Tarek A. Ameen - https://orcid.org/0000-0003-1455-5579
Jim Fonseca - https://orcid.org/0000-0002-8886-7535
Gerhard Klimeck - https://orcid.org/0000-0001-7128-773X

References

1. Liu, H. C.; Gao, M.; McCaffrey, J.; Wasilewski, Z. R.; Fafard, S. *Appl. Phys. Lett.* **2001,** *78,* 79–81. doi:10.1063/1.1337649
2. Razeghi, M. *Technology of Quantum Devices;* Springer: Berlin, Germany, 2010.
3. López, A. B. C.; Vega, A. M.; López, A. L. *Next Generation of Photovoltaics;* Springer: Berlin, Germany, 2012.
4. Luque, A.; Martí, A.; Stanley, C. *Nat. Photonics* **2012,** *6,* 146–152. doi:10.1038/nphoton.2012.1
5. Pryor, C.; Kim, J.; Wang, L. W.; Williamson, A. J.; Zunger, A. *J. Appl. Phys.* **1998,** *83,* 2548–2554. doi:10.1063/1.366631
6. Keating, P. N. *Phys. Rev.* **1966,** *145,* 637. doi:10.1103/PhysRev.145.637
7. Lazarenkova, O. L.; von Allmen, P.; Oyafuso, F.; Lee, S.; Klimeck, G. *Superlattices Microstruct.* **2003,** *34,* 553–556. doi:10.1016/j.spmi.2004.03.057
8. Lazarenkova, O. L.; von Allmen, P.; Oyafuso, F.; Lee, S.; Klimeck, G. *Appl. Phys. Lett.* **2004,** *85,* 4193–4195. doi:10.1063/1.1814810
9. Tatebayashi, J.; Nishioka, M.; Arakawa, Y. *Appl. Phys. Lett.* **2001,** *78,* 3469–3471. doi:10.1063/1.1375842
10. Boykin, T. B.; Klimeck, G.; Bowen, R. C.; Oyafuso, F. *Phys. Rev. B* **2002,** *66,* 125207. doi:10.1103/PhysRevB.66.125207
11. Barve, A. V.; Sengupta, S.; Kim, J. O.; Montoya, J.; Klein, B.; Shirazi, M. A.; Zamiri, M.; Sharma, Y. D.; Adhikary, S.; Godoy, S. E.; Jang, W.-Y.; Fiorante, G. R. C.; Chakrabarti, S.; Krishna, S. *IEEE J. Quantum Electron.* **2012,** *48,* 1243–1251. doi:10.1109/JQE.2012.2208621
12. Boykin, T. B.; Klimeck, G.; Bowen, R. C.; Lake, R. *Phys. Rev. B* **1997,** *56,* 4102. doi:10.1103/PhysRevB.56.4102
13. Klimeck, G.; Bowen, R. C.; Boykin, T. B.; Salazar-Lazaro, C.; Cwik, T. A.; Stoica, A. *Superlattices Microstruct.* **2000,** *27,* 77–88. doi:10.1006/spmi.1999.0797
14. Tan, Y.; Povolotskyi, M.; Kubis, T.; He, Y.; Jiang, Z.; Klimeck, G.; Boykin, T. B. *J. Comput. Electron.* **2013,** *12,* 56–60. doi:10.1007/s10825-013-0436-0
15. Tan, Y.; Povolotskyi, M.; Kubis, T.; Boykin, T. B.; Klimeck, G. *Phys. Rev. B* **2016,** *94,* 045311. doi:10.1103/PhysRevB.94.045311
16. Towns, J.; Cockerill, T.; Dahan, M.; Foster, I.; Gaither, K.; Grimshaw, A.; Hazlewood, V.; Lathrop, S.; Lifka, D.; Peterson, G. D.; Roskies, R.; Wilkins-Diehr, N. *Comput. Sci. Eng.* **2014,** *16,* 62–74. doi:10.1109/MCSE.2014.80

17. Steiger, S.; Povolotskyi, M.; Park, H.-H.; Kubis, T.; Klimeck, G. *IEEE Trans. Nanotechnol.* **2011,** *10,* 1464–1474. doi:10.1109/TNANO.2011.2166164
18. Fonseca, J. E.; Kubis, T.; Povolotskyi, M.; Novakovic, B.; Ajoy, A.; Hegde, G.; Ilatikhameneh, H.; Jiang, Z.; Sengupta, P.; Tan, Y.; Klimeck, G. *J. Comput. Electron.* **2013,** *12,* 592–600. doi:10.1007/s10825-013-0509-0
19. Ameen, T. A.; Ilatikhameneh, H.; Huang, J. Z.; Povolotskyi, M.; Rahman, R.; Klimeck, G. *IEEE Trans. Electron Devices* **2017,** *64,* 2512–2518. doi:10.1109/TED.2017.2690626
20. Ilatikhameneh, H.; Salazar, R. B.; Klimeck, G.; Rahman, R.; Appenzeller, J. *IEEE Trans. Electron Devices* **2016,** *63,* 2871–2878. doi:10.1109/TED.2016.2565582
21. Ameen, T. A.; Ilatikhameneh, H.; Valencia, D.; Rahman, R.; Klimeck, G. Engineering the optical transitions of self-assembled quantum dots. In *2015 International Workshop on Computational Electronics (IWCE),* 2015; pp 1–4.
22. Ameen, T.; Ilatikhameneh, H.; Charles, J.; Hsueh, Y.; Chen, S.; Fonseca, J.; Povolotskyi, M.; Rahman, R.; Klimeck, G. Optimization of the anharmonic strain model to capture realistic strain distributions in quantum dots. In *2014 IEEE 14th International Conference on Nanotechnology (IEEE-NANO),* 2014; pp 921–924.
23. Hammerschmidt, T.; Kratzer, P.; Scheffler, M. *Phys. Rev. B* **2007,** *75,* 235328. doi:10.1103/PhysRevB.75.235328
24. Sun, Y.; Thompson, S. E.; Nishida, T. *Strain effect in semiconductors;* Springer: Berlin, Germany, 2010; Vol. 1.
25. Slater, J. C.; Koster, G. F. *Phys. Rev.* **1954,** *94,* 1498. doi:10.1103/PhysRev.94.1498
26. Klimeck, G.; Oyafuso, F.; Boykin, T. B.; Bowen, R. C.; von Allmen, P. *Comput. Model. Eng. Sci.* **2002,** *3,* 601–642. doi:10.3970/cmes.2002.003.601
27. Boykin, T. B.; Kharche, N.; Klimeck, G.; Korkusinski, M. *J. Phys.: Condens. Matter* **2007,** *19,* 036203. doi:10.1088/0953-8984/19/3/036203
28. Klimeck, G.; Ahmed, S. S.; Bae, H.; Kharche, N.; Clark, S.; Haley, B.; Lee, S.; Naumov, M.; Ryu, H.; Saied, F.; Prada, M.; Korkusinski, M.; Boykin, T. B. *IEEE Trans. Electron Devices* **2007,** *54,* 2079–2089. doi:10.1109/TED.2007.902879
29. Usman, M.; Heck, S.; Clarke, E.; Spencer, P.; Ryu, H.; Murray, R.; Klimeck, G. *J. Appl. Phys.* **2011,** *109,* 104510. doi:10.1063/1.3587167
30. Neupane, M. R.; Rahman, R.; Lake, R. K. *Phys. Chem. Chem. Phys.* **2015,** *17,* 2484–2493. doi:10.1039/C4CP03711A
31. Neupane, M. R.; Lake, R. K.; Rahman, R. *J. Appl. Phys.* **2011,** *110,* 074306. doi:10.1063/1.3642970
32. Ameen, T. A.; El-Batawy, Y. M.; Abouelsaood, A. A. *J. Appl. Phys.* **2013,** *113,* 083101. doi:10.1063/1.4793269
33. Ameen, T. A.; El-Batawy, Y. M. *J. Appl. Phys.* **2013,** *113,* 193102. doi:10.1063/1.4805061
34. Ameen, T. A.; El-Batawy, Y. M.; Abouelsaood, A. A. *J. Appl. Phys.* **2014,** *115,* 063703. doi:10.1063/1.4864762
35. Tankasala, A.; Salfi, J.; Bocquel, J.; Voisin, B.; Usman, M.; Klimeck, G.; Simmons, M. Y.; Hollenberg, L. C.; Rogge, S.; Rahman, R. *arXiv* **2017,** No. 1703.
36. Szabo, A.; Ostlund, N. S. *Modern quantum chemistry: Introduction to advanced electronic structure theory;* Dover Publications: Mineola, NY, U.S.A., 1996.
37. Bir, G. L.; Pikus, G. E.; Shelnitz, P.; Louvish, D. *Symmetry and strain-induced effects in semiconductors;* Wiley: New York, NY, U.S.A., 1974.
38. Vurgaftman, I.; Meyer, J. R.; Ram-Mohan, L. R. *J. Appl. Phys.* **2001,** *89,* 5815–5875. doi:10.1063/1.1368156
39. Ilatikhameneh, H.; Ameen, T. A.; Klimeck, G.; Rahman, R. *IEEE J. Quantum Electron.* **2016,** *52,* 7000308. doi:10.1109/JQE.2016.2573959

License and Terms

This is an Open Access article under the terms of the Creative Commons Attribution License (http://creativecommons.org/licenses/by/4.0), which permits unrestricted use, distribution, and reproduction in any medium, provided the original work is properly cited.

The license is subject to the *Beilstein Journal of Nanotechnology* terms and conditions: (https://www.beilstein-journals.org/bjnano)

The definitive version of this article is the electronic one which can be found at: doi:10.3762/bjnano.9.99

BEILSTEIN JOURNAL OF NANOTECHNOLOGY

The electrical conductivity of CNT/graphene composites: a new method for accelerating transmission function calculations

Olga E. Glukhova* and Dmitriy S. Shmygin

Full Research Paper

Open Access

Address:
Saratov State University, Saratov, Russian Federation

Email:
Olga E. Glukhova* - glukhovaoe@info.sgu.ru; Dmitriy S. Shmygin - shmygin.dmitriy@gmail.com

* Corresponding author

Keywords:
carbon composites; electronic properties; interpolation; quantum transport; transmission function

Beilstein J. Nanotechnol. **2018,** *9,* 1254–1262.
doi:10.3762/bjnano.9.117

Received: 01 November 2017
Accepted: 28 March 2018
Published: 20 April 2018

This article is part of the Thematic Series "Light–Matter interactions on the nanoscale".

Guest Editor: M. Rahmani

© 2018 Glukhova and Shmygin; licensee Beilstein-Institut.
License and terms: see end of document.

Abstract

We present a new universal method to accelerate calculations of transmission function and electrical conductance of 2D materials, the supercell of which may contain hundreds or thousands of atoms. The verification of the proposed method is carried out by exemplarily calculating the electrical characteristics of graphene and graphane films. For the first time, we calculated the transmission function and electrical conductance of pillared graphene, composite film of carbon nanotubes (CNTs)/graphene. The electrical conductance of different models of this material was calculated in two mutually perpendicular directions. Regularities in resistance values were found.

Introduction

The development of technologies for the synthesis of graphene nanomaterials has led to an expansion of the scope of their application. One of the graphene composites that have been actively studied in the last few years is pillared graphene [1]. It is a graphene layer, connected seamlessly by single-walled carbon nanotubes (SWCNTs). One of the advantages of this material is its high strength and resistance to mechanical stress [2-4]. In combination with high electrical capacity and efficient electronic transfer between graphene sheets, this nanomaterial has already been recognized as promising as an electrode for storage batteries and supercapacitors [5-7]. There remain many questions about the conductive properties of pillared graphene and their dependence on the length and diameter of the nanotubes. At the moment, there is no experimental data on the conductivity of pillared graphene, so the theoretical prediction of the transmission regularities in this material is relevant. However, the calculation of the electrical conductance of pillared graphene by quantum mechanical methods is difficult due to its

large supercell. These calculations require too much time, even when using modern computing tools.

The non-equilibrium Green function (NEGF) method with density functional tight-binding (DFTB) scheme or density functional theory (DFT) scheme is used to calculate the electrical conductance of molecular structures consisting of atoms of various elements with high accuracy [8]. Within the NEGF formalism, each system represents left and right electrodes and the molecules between them. The probability that an electron will transmit from the left to the right electrode is described by the transmission function $T(E)$. The dependence of the transmission function on the energy of the electron in the system is characteristic for each point of the reciprocal lattice. The final form of $T(E)$ depends on the number of k-points in the reciprocal lattice, because $T(E)$ average over these lattice points. Using the convergent transmission function it is possible to find the electrical conductance of the nanostructure. However, in order to obtain a converged form of the averaged transmission function, it may be necessary to calculate it in a set of points in the reciprocal lattice, which is unattainable for a large number of atoms in the considered system. In this connection, the development of methods for accelerating the calculation of the transmission function without a significant loss in the accuracy of calculations has particular relevance and significance for research of the electrical conductive properties of new composite materials. At present, such accelerating techniques are practically absent. We found only one work [9] in which the authors attempted to propose an algorithm that accelerates the calculations of the transmission function of large systems. However, the solution proposed in above mentioned paper did not significantly increase the computational speed, which is especially critical at considering new carbon composite materials such as pillared graphene and other varieties of graphene–nanotube structures. The purpose of this work is to propose an alternative approach to the calculation of transmission function and electrical conductance of composite nanomaterials, which allows us to investigate the electrophysical properties of atomic structures with hundreds and thousands of atoms in the supercell. The verification of the proposed approach is carried out by the example of calculations of the transmission function and electrical conductance of perspective 2D carbon materials, namely graphene, graphane and a graphene–carbon nanotube hybrid composite.

Computational Details

In order to calculate the electrical conductance we use the Green–Keldysh functions and the Landauer–Büttiker formalism [8]. The calculation of energy and band structure is carried out by the DFT method in the tight-binding approximation [10-12] within the Kvazar software package [13]; the parametrization pbc-0-3 was used [14-16]. The electrical conductance is described by the expression:

$$G = \frac{I}{V} = \frac{e^2}{h} \int_{-\infty}^{\infty} T(E) F_T(E-\mu) \mathrm{d}E, \quad (1)$$

where $T(E)$ is the transmission function characterizing the quantum mechanical transparency of the conducting channel as a function of the energy of the electron moving along it, μ is the Fermi energy of the electrode, e is the charge of the electron, and h is the Planck constant. The thermal broadening function $F_T(E)$ is calculated by the formula:

$$F_T(E) = \frac{1}{4k_\mathrm{B}T} \mathrm{sech}^2 \frac{E}{2k_\mathrm{B}T}, \quad (2)$$

where k_B is the Boltzmann constant, and T is the temperature. The transmission function is given by:

$$T(E) = \frac{1}{N} \sum_{k=1}^{N} \mathrm{Tr}\left[\Gamma_\mathrm{S}(E) G_\mathrm{C}^\mathrm{A}(E) \Gamma_\mathrm{D}(E) G_\mathrm{C}^\mathrm{R}(E)\right], \quad (3)$$

where $G_\mathrm{C}^\mathrm{A}(E)$ and $G_\mathrm{C}^\mathrm{R}(E)$ are, respectively, the advanced and retarded Green matrices (describing the contact with the electrodes), $\Gamma_\mathrm{S}(E)$ and $\Gamma_\mathrm{D}(E)$ are, respectively, the level broadening matrices for source and drain. The function $T(E)$ is found by summation over the entire Brillouin zone (BZ) and N is the number of points in the reciprocal space. The accuracy of calculating $T(E)$ is determined by the segmentation of the reciprocal space and the considered number of energies values. The calculation will be reliable when the function $T(E)$ does not change with decreasing pitch of the change in the wave number k. For example, for finitely segmented BZ with limits a and b, the function $T(E)$ converges to its true form for $N \geq 10^3$. For materials in which the cell contains of the order of several hundreds or thousands of atoms, the calculation of $T(E)$ at a single point (for a fixed k) takes a rather long time, thus making 10^3 calculations impossible. For example, for a 2D crystal cell with 472 atoms, the calculation of the transmission function averaged over 288 points of the reciprocal space takes almost four days for the parallel calculation in 24 processes (Intel® Xeon® CPU E5-2660 v2 with a frequency of 2.2 GHz). If the BZ is not a segment, but a 2D or 3D figure, the number N increases by orders of magnitude. In the next section, a method will be described to reduce the number of reciprocal space points and energy values for which a transmission function calculation is required, without substantially losing accuracy of the shape of $T(E)$.

Results and Discussion

Description and verification of the method for accelerating transmission-function calculations

Let us demonstrate the proposed method for calculating $T(E)$ for two different N by using the example of a graphene monolayer. Figure la shows the considered system, that is, the unit cell connected to the electrodes. Since we calculated the conductance of this material (graphene), the same cells act as electrodes. Electrodes are translated to infinity along the Y-direction, and they are semi-infinite along X. The central cell is also translated to infinity over Y. Thus, the wave number k_y varies within $(-\pi/a_y; \pi/a_y)$, where a_y is the unit cell size along the Y-direction (as shown in Figure 1a, the software VMD [17] was used for visualization). The calculated functions $T(E)$ from Equations 1–3 with different values of N are shown in Figure 1b. For a small step of the decomposition dk = 0.1 1/Å (N = 15), the function has a step-like form. When the step of the decomposition is reduced to dk = 0.0015 1/Å (N = 984), the curve takes the correct well-known form for a graphene monolayer. The transmission function is represented in conductance quanta e^2/h.

For each point of the reciprocal lattice, the calculated $T(E)$ function is additionally processed. The values of $T(E)$ near the transition area between the steps are refined to make them more abrupt. In many cases, this procedure allows us to eliminate the need for a more detailed decomposition of the energy interval. For this, within transmission-function calculations we used an interval-halving technique, which allows one to obtain a 16-times more accurate boundary value between the steps for four iterations. Each iteration reduces the difference between the energies E_1 and E_2 by a factor of two (E_1 is the last energy value for a certain k-point at which $T = T(E_1)$, E_2 is the first energy value for the same k-point at which $T = T(E_2)$ and $T(E_2) \neq T(E_1)$), since the value of the transmission function at the midpoint $E_3 = 0.5(E_1 + E_2)$, which is either $T(E_1)$ or $T(E_2)$, is determined. Then, the interval (E_1, E_3) is considered if $T(E_3) = T(E_2)$, or the interval (E_3, E_2) if $T(E_3) = T(E_1)$. Therefore, four similar iterations yield a 16-fold reduction of the energy difference between two adjacent steps of the transmission function.

To eliminate the step-like form of the averaged transmission function, we interpolate the function $T(E)$ between two neighbouring points of the reciprocal lattice. Figure 2a shows step plots of $T(E)$ for three different numbers k_y. In general, independently of k_y, interpolation for each point of the polygonal chain determines the nearest points with energy having the same value of the function $T(E)$ and belonging to the neighbouring polyline. The picture of the distribution of points in this case

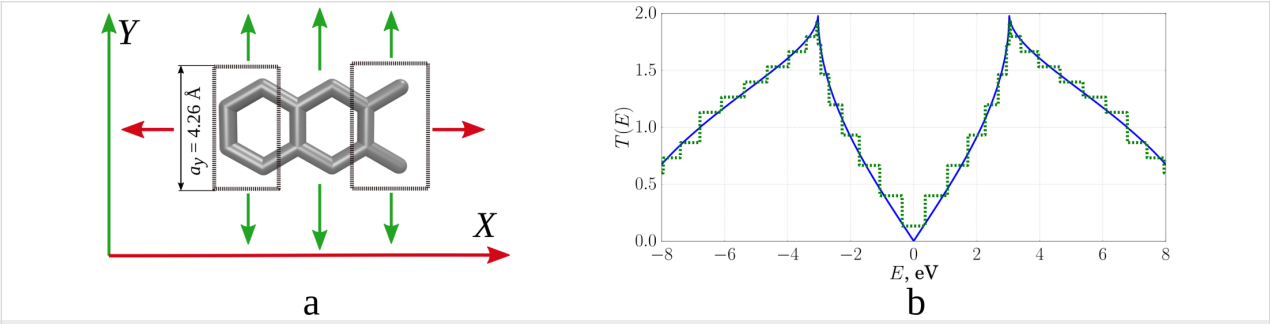


Figure 1: Graphene: a) unit cell with electrodes; b) transmission function (green: dk = 0.1 1/Å, blue: dk = 0.0015 1/Å).

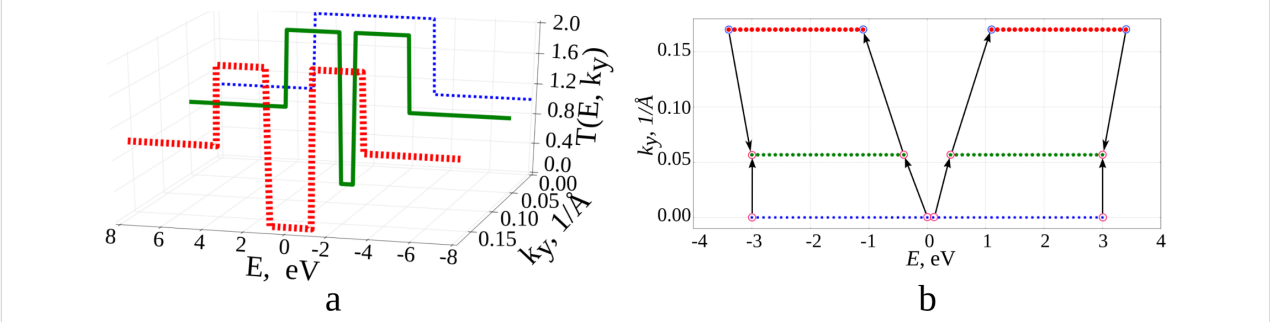


Figure 2: Transmission function: a) $T(E)$ for three different k_y; b) the distribution of points of the transmission function for different energies and quantities k_y for a fixed value of $T(E)$ = 2.

has the form shown in Figure 2b, when one value of $T(E) = 2$ is fixed. Thus, all the points of neighbouring polygonal lines having the same value of $T(E)$ are first found, and then the nearest ones are selected from the energy difference. If a polyline has two adjacent lines, then each point of this polyline can have no more than one near point on each of them. Similarly, in the case of a single neighbouring polyline, there will not be more than one near point for each point on the polygonal chain. If the difference in the values of the transmission function exceeds one, additional points are added. For example, if for some value of k_y the transmission function undergoes a jump on passing from a point with energy E_i to a point with energy E_{i+1}, with $T_{i+1} - T_i = 2$, then an additional point will be added to this polygonal chain. This point is characterized by an energy value of 0.5 ($E_{i+1} + E_i$) and the transmission function at this point is equal to T_i +1. This is necessary in order to find the nearest point with the value of the transmission function $T_i + 1$.

Next, the nearest points found are used to add additional points between them, lying on the segment connecting these points. All additional points have the same value of *T(E)* as the nearest points. The number of points added depends on the length of the segment connecting the nearest points on different polygonal chains. The longer the lengths of the segment, the more additional points are added. If an additional point has not been used to form the connecting segment, it is not used to construct an interpolating function. The starting points and the remaining added points are used to construct the interpolating function.

The interpolating two-dimensional function $T_1(E, ky)$ makes it possible to realize a detailed decomposition over k_y values, ensuring smoothing of the initial roughness. Figure 3a shows maps of the transmission function $T(E)$: Figure 3a, top – before the interpolation procedure (there are additional points obtained by interval-halving technique); Figure 3a, bottom – after applying the constructed interpolating function $T_1(E, ky)$. The step-like behaviour of the function $T(E)$ has disappeared everywhere, except for the region near the Fermi level (0.0 eV here). Indeed, there may exist "special regions" for which the original partitioning by k_y was too coarse. Special regions are determined by the researcher in the gradient of the image. Areas of smooth colour change indicate the lack of partitioning for this

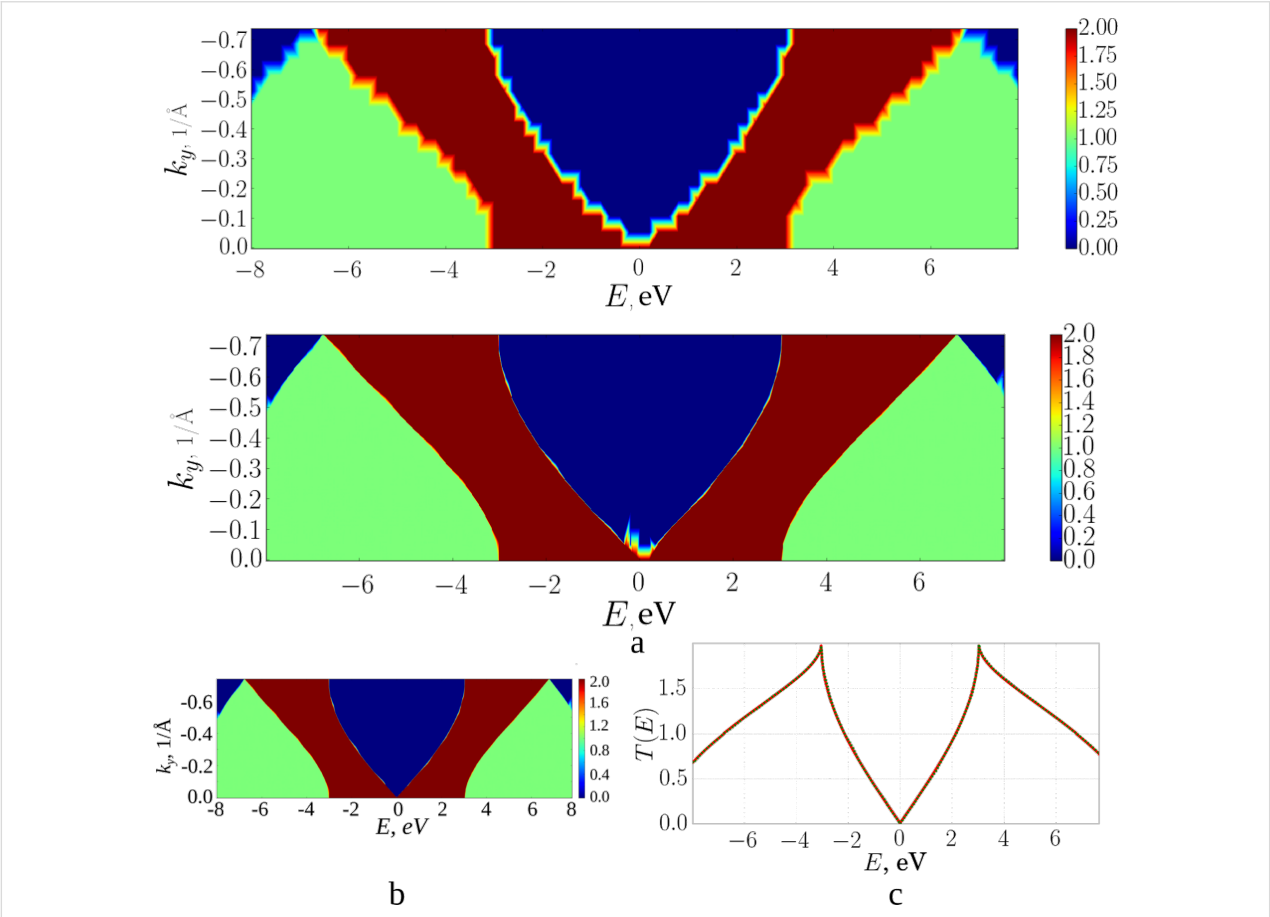


Figure 3: Graphene transmission function: a) a map of $T(E)$ for the initial partitioning over k_y (from above) and after applying the interpolating function $T_1(E, k_y)$; b) a map of $T(E)$ after applying the interpolating function $T_2(E, k_y)$; c) averaged $T(E)$ over all k_y (green: interpolated, red: converged).

area. Calculations with a more particular partition are additionally carried out for this area, but already in a narrow range of values: from 0 to 0.2 1/Å for k_y, and from −0.3 to 0.3 eV for E. The next step is the construction of a new interpolating function $T_2(E, ky)$. Figure 3b shows the map of the transmission function after applying $T_2(E, ky)$, Figure 3c show the function $T(E)$ averaged over all k_y. The solid curve shows the calculation with the distance between two neighbouring points in reciprocal lattice of 0.0015 1/Å, the dotted line shows the result of applying the developed method. The norm of the difference between the interpolated and the converged values is 0.68%. Time taken to obtain the average transmission function (with parallel calculation using eight processes on the Intel Xeon CPU E5-2690 v4 CPU with a frequency of 2.6 GHz) varies: 34 minutes, 2 seconds per accurate calculation and 2 minutes, 22 seconds to obtain the final values of the interpolated graph. Note that, in general, the time taken to add points depends on the amount of input data, and not on the number of atoms in the considered structure.

The proposed method for calculating the transmission function was also tested with the example of graphane. Figure 4 present the results of the study of a graphane fragment using the proposed method. The number of points for accurate calculation is 720, for the rough approximation it is 24. The calculation times for the transmission function (for parallel calculation using eight processes on the Intel Xeon E5-2690 v4 CPU with a frequency of 2.6 GHz) for accurate calculation and interpolation are 146 minutes, 29 seconds and 7 minutes, 21 seconds, respectively. The norm of the difference between the interpolated values and the ones obtained from the direct calculation is 1.79%.

The results of solving the test problems show that the transmission function calculations were accelerated by factor of 14.38 for graphene and of 19.92 for graphane by using the method developed here. Nevertheless, the speed of calculations is limited by the complexity of the dependence of the transmission function on energy and the considered point of the reciprocal lattice. The higher the rate of change in the transmission function, the more detailed calculations are needed.

The accuracy of the results of the transmission function calculations obtained using the proposed method depends on the size of the unit cell and the chosen reciprocal lattice vector k. The test problems solved for graphene and graphane show that the

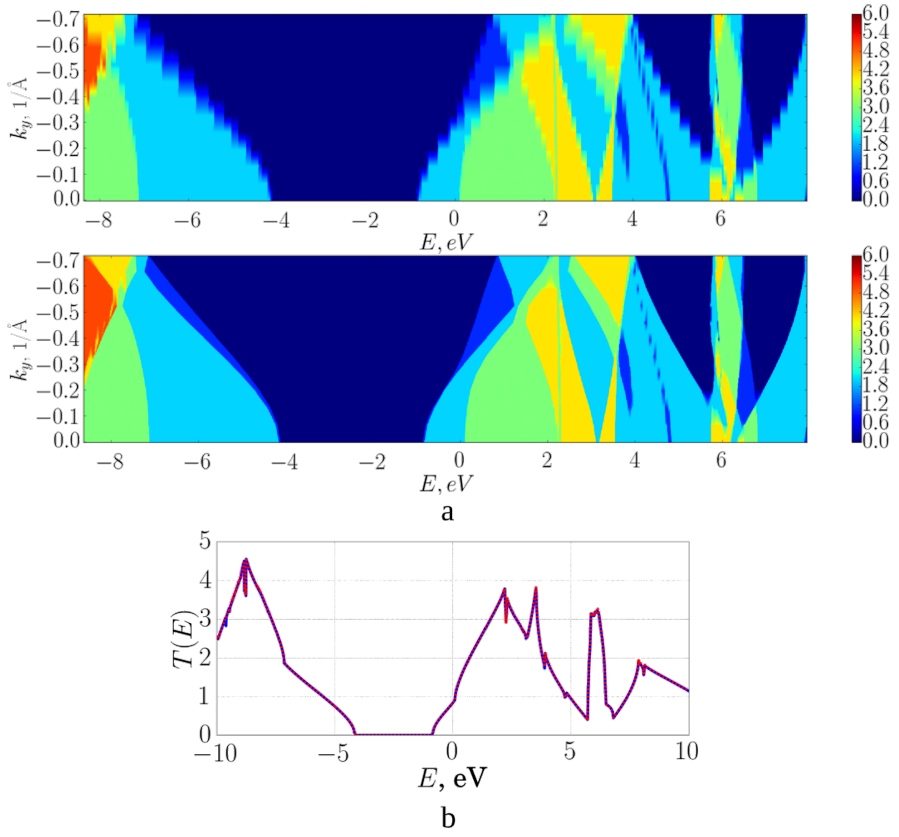


Figure 4: Graphane transmission function: a) a map of $T(E)$ for the initial partitioning over k_y (top) and (bottom) after applying the interpolating function $T(E, k_y)$; b) averaged $T(E)$ over all k_y (blue: interpolated, red: converged).

discrepancy between the values of the transmission function calculated without the developed method and with its application was about 1–2%.

Transmission function and conductance of 2D graphene/CNT composites

Using the developed method for calculating the transmission function we investigated the transmission functions and electrical conductance of 2D graphene/CNT composites. The investigated film was modelled by two layers of graphene connected by single-layer armchair tubes (9,9) with a diameter of 1.23 nm (tubes of diameter 1–1.5 nm are typical for such composite materials). The distance between the tubes was equal to 2.1 nm, the length of the tubes (i.e., the distance between the layers of graphene) ranged from 1.1 to 2.4 nm. The graphene sheet had a length of 2.45 nm along the *X*-axis and 2.13 nm along the *Y*-axis for each unit cell. Figure 5a shows the atomic structure of a pillared graphene film with an inter-tube distance of 2.1 nm. The tubes are connected seamlessly with graphene, i.e., the CNT smoothly passes into the graphene sheet, and the junction contains not only hexagons, but also defects in the form of pentagons, heptagons and octagons. In order to calculate the electrical conductance in the *X*- and *Y*-directions, as in the case of the graphene monolayer, a central supercell and supercell electrodes are separated (see Figure 5b). The conductance calculation scheme corresponds to the electronic transport along *X* (along the zigzag edge) in the left figure, and along *Y* (along the armchair edge) in the right figure. In this case the supercell consists of 580 atoms with a distance between the graphene layers of 2.4 nm. The conductance was calculated using the developed method because of the large number of atoms. The plots of the function $T(E)$ averaged over all k in the case of electron transport in the *X*-and *Y*-directions are shown in Figure 5c.

Similarly, the transmission functions $T(E)$ were calculated for all models of supercells of a composite on the basis of CNT

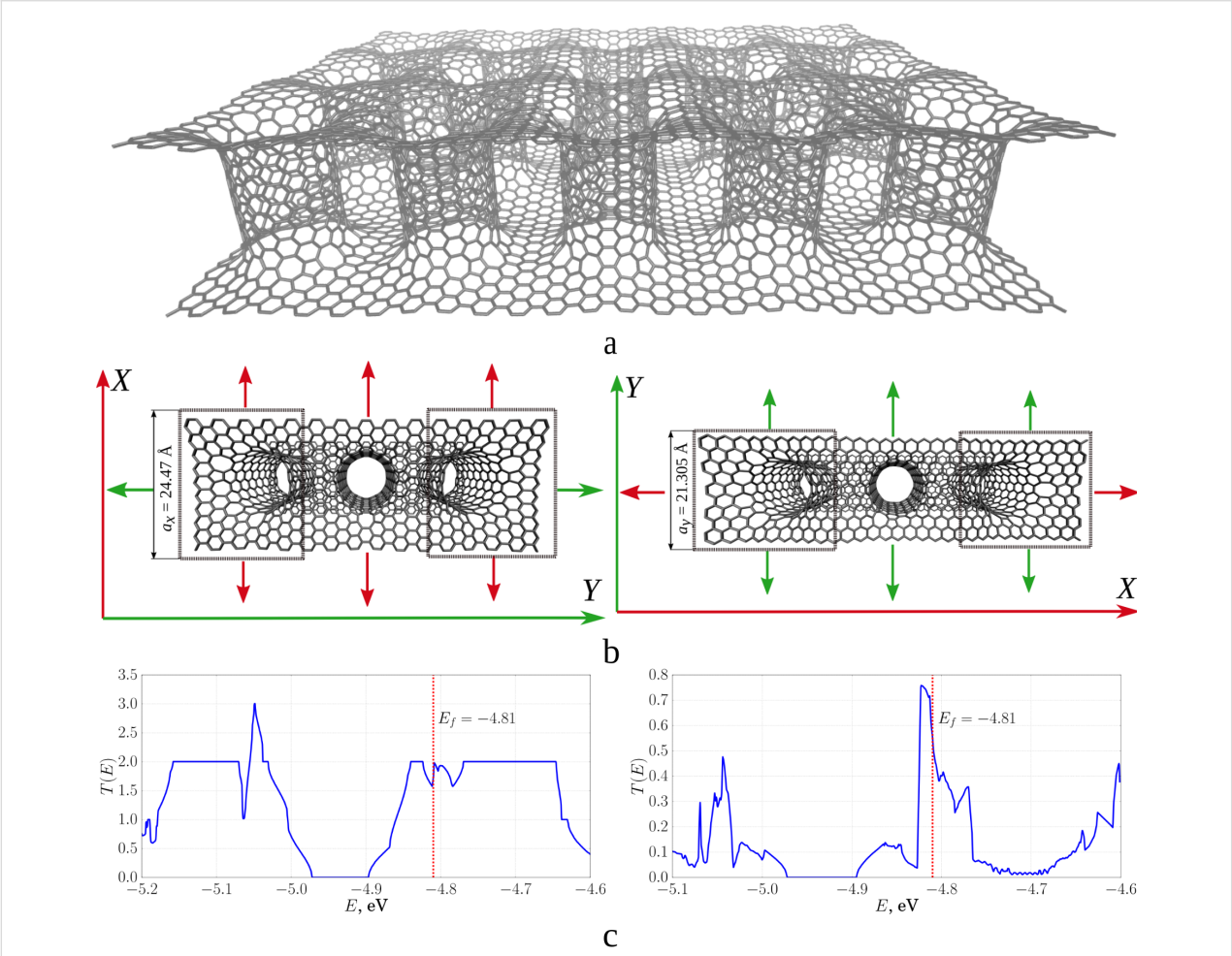


Figure 5: 2D composite of pillared graphene based on CNT (9,9) with a length of 2.4 nm: a) atomic structure; b) schematic representation of the cell of the composite and electrodes in the case of electron transport along *X* (left) and *Y* (right); c) transmission functions along the *X*- (left) and *Y*- (right) directions.

(9,9) at the same distance between tubes of 2.1 nm. The conductance and resistance of the pillared graphene film were calculated based on the calculated $T(E)$. Table 1 shows the corresponding data: tube length, number of atoms in the transmitted cell, calculated Fermi level, conductance and resistance. The Fermi level is in the interval (−4.88 eV; −4.73 eV), that is, it is shifted downward compared to ideal CNTs of the same diameter (−4.66 eV). Conductance and resistance behave non-monotonically. It can be said that the resistance oscillates around a value of 12 kΩ in the *Y*-direction for single-layer composites, and around a value of 90 kΩ in the *X*-direction only with larger amplitude.

Similar investigations were carried out for two-layer pillared graphene (Figure 6). The graphene sheet length was 4.8 nm along the *X*-axis and 4.12 nm along the *Y*-axis for each unit cell.

The resistance for two-layer composites averages 10.2 kΩ in the *Y*-direction and 29.32 kΩ in the *X*-direction. The difference between the resistance in the *X*- and Y-directions is significantly lower for two-layer composite in comparison with single-layer composite. The conductivity in the *Y*-direction has increased for all the considered situations (see Table 2), while the conductance value decreased in the *X*-direction for a composite with nanotube lengths of 1.1 and 1.84 nm.

A comparison of the plots of the transmission functions for single-layer and two-layer composite is shown in Figure 7.

Based on obtained results, we can conclude that for the single-layer pillared graphene film, the resistance in the direction of the *Y*-axis (zigzag edge of the graphene sheet) varies insignificantly and does not depend on the distance between the graphene layers. For a two-layer composite, the average resistance depends on the axis direction. This can be explained by the high electrical conductance of graphene nanostructures with a zigzag edge. The conductance of these ribbons does not depend on the width of the ribbon and weakly depends on its topology. In the direction of the *X*-axis (armchair edge of graphene sheet), the electrical conductance of single- and two-layer composites depends significantly on the topology of the film. The resistance changes drastically with the increase in the CNT length.

Conclusion

We created a new universal method for calculating the electron-transmission function and electrical conductance at quantum transport in composite nanomaterials. This method allows us to investigate the electrophysical properties of atomic structures, which contain hundreds and thousands of atoms in the transmitted supercell. By the example of monolayer graphene and graphane it was shown that the developed method significantly reduces the calculation time of the transmission function. The error of the calculation was equal to 0.68% and 1.79% for graphene and graphane, respectively. A number of competitive advantages of the proposed approach compared to other methods in the literature are: Our approach does not use the Dijkstra method used in [9]. There is no need to construct a distance matrix and to find the shortest path in the plot. Also, the program implementation of our approach is simpler. Besides, our approach ensures a higher acceleration rate in calculations of the transmission functions of polyatomic structures. In particular, by the example of the graphene fragment, it was shown that the calculation speed of transmission function using our approach is three times higher than the calculation speed in the method proposed in [9]. Also, we introduce an additional part in the runtime of calculations, not only at the post-processing stage. The limitations of our method are that a too coarse

Table 1: Data of investigated single-layer composite films and the results of modelling.

length of the tube, nm	number of atoms in the supercell of the composite	direction of translation	Fermi energy, eV	conductivity, μS	resistance, kΩ
0.60	400	*X*	−4.74	135.93	7.35
		Y		11.03	90.65
0.85	436	*X*	−4.88	32.48	30.79
		Y		8.32	120.12
1.10	472	*X*	−4.85	92.21	10.85
		Y		24.89	40.18
1.34	508	*X*	−4.73	142.96	6.99
		Y		10.41	96.05
1.59	544	*X*	−4.85	72.26	13.65
		Y		13.19	75.78
1.84	580	*X*	−4.81	122.08	8.19
		Y		19.8	50.5

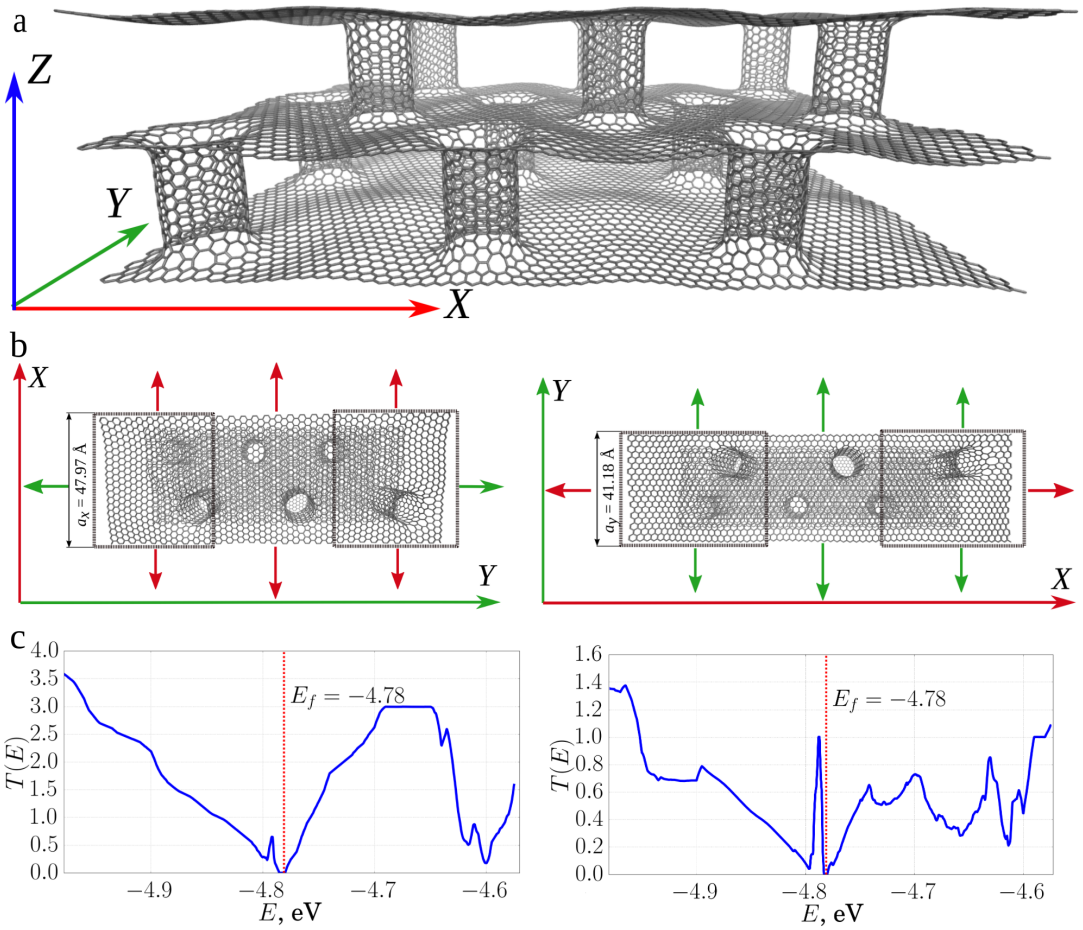


Figure 6: Two-layer 2D composite of pillared graphene based on CNT (9,9) with a length of 2.4 nm: a) atomic structure; b) schematic representation of the cell of the composite and electrodes in electronic transport along X (left) and along Y (right); c) transmission functions along the *X*- (left) and *Y*- (right) directions.

Table 2: Data of investigated two-layer composite films and the results of modeling.

length of the tube, nm	number of atoms in the supercell of the composite	direction of translation	Fermi energy, eV	conductance, μS	resistance, kΩ
0.60	2400	*X*	−4.712	141.26	7.08
		Y		41.66	24.00
1.10	2544	*X*	−4.798	84.82	11.79
		Y		30.30	33.00
1.84	2760	*X*	−4.781	86.06	11.62
		Y		32.31	30.95

k-point sampling or a too coarse energy sampling will lead unrealistic results, in spite of any post-processing scheme.

Using developed method we obtained new knowledge about the electrical conductive properties of a new composite material, namely pillared graphene. The calculated electrical conductance and resistance of the pillared graphene film showed that the current flow is more preferable along the zigzag edge of the graphene sheet both for single-layer and two-layer composites. The average resistance value in this direction was 12 kΩ for the single-layer composite. This value is close to the resistance value of an ideal nanotube. For the two-layer composite, the average resistance was 10.2–29.3 kΩ depending on the direction. This can be explained by the high electrical conductance of graphene nanostructures with a zigzag edge. The conductance of these ribbons does not depend on the width of the ribbon and

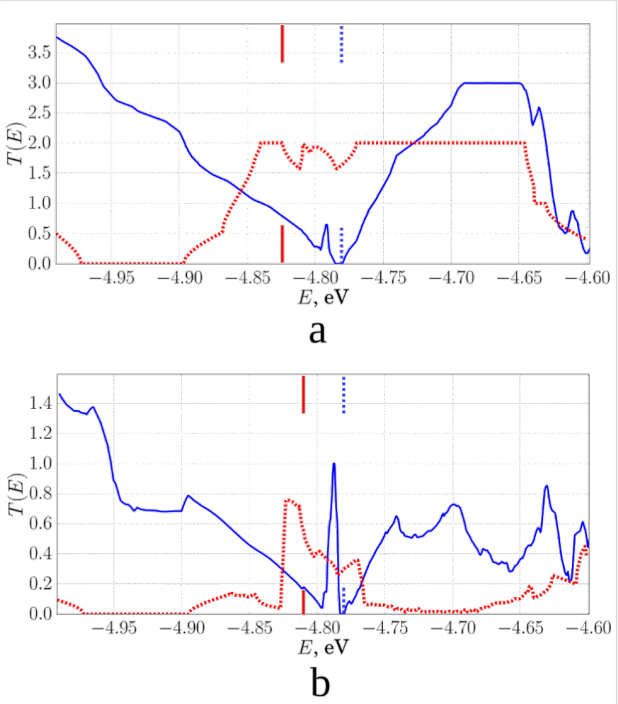


Figure 7: Plots of the transmission functions for two-layer (blue) and single-layer (red) composites (the tube length in the composite was equal to 1.84 nm): a) in the direction of the *X*-axis, along the zigzag edge; b) in the direction of the *Y*-axis, along the armchair edge. In addition, the values of the Fermi energy for composites are shown by short lines of the corresponding color.

weakly depends on its topology. In the direction of the armchair edge of the graphene sheet, the electrical conductance depends significantly on the topology of the film. The resistance changes drastically with the increase in CNT length. Using the analogy with graphene nanoribbons, it can be seen that the regularities in the electronic transport along the armchair edge are determined by the width of the ribbon and its morphology. In summary, we can conclude that the pillared graphene films with nanotubes having a diameter of 1.23 nm are characterized by a relatively high electrical conductivity. Due to high strength and conductivity, these films, provided a developed surface and pores for filling with the necessary connections, could be successfully applied in electronic devices and as electrodes of storage batteries.

Acknowledgements

The research described in this paper was supported by the grant of the Russian Science Foundation #15-29-01025 and by the Russian Presidential scholarship 2018-2020 #SP-892.2018.1.

ORCID® iDs

Olga E. Glukhova - https://orcid.org/0000-0002-5670-2058
Dmitriy S. Shmygin - https://orcid.org/0000-0002-7216-275X

References

1. Sasaki, R.; Shintani, K. *MRS Adv.* **2017,** *2,* 45–50. doi:10.1557/adv.2016.634
2. Wang, C.-H.; Fang, T.-H.; Sun, W.-L. *J. Phys. D: Appl. Phys.* **2014,** *47,* 405302. doi:10.1088/0022-3727/47/40/405302
3. Wang, Y.; Zhu, Y.; Wang, F.; Liu, X.; Wu, H. *Carbon* **2017,** *118,* 588–596. doi:10.1016/j.carbon.2017.03.092
4. Shahsavari, R.; Sakhavand, N. *Carbon* **2015,** *95,* 699–709. doi:10.1016/j.carbon.2015.08.106
5. Jiang, L.; Sheng, L.; Long, C.; Wei, T.; Fan, Z. *Adv. Energy Mater.* **2015,** *5,* 1500771. doi:10.1002/aenm.201500771
6. Lin, J.; Zhong, J.; Bao, D.; Reiber-Kyle, J.; Wang, W. *J. Nanosci. Nanotechnol.* **2012,** *12,* 1770–1775. doi:10.1166/jnn.2012.5198
7. Wang, Q.; Dong, Z.; Qu, L.; Yan, J.; Fan, Z. *Energy Storage Mater.* **2015,** *1,* 42–50. doi:10.1016/j.ensm.2015.09.001
8. Datta, S. *Quantum Transport: Atom to Transistor;* Cambridge University Press: New York, NY, U.S.A., 2005. doi:10.1017/CBO9781139164313
9. Falkenberg, J. T.; Brandbyge, M. *Beilstein J. Nanotechnol.* **2015,** *6,* 1603–1608. doi:10.3762/bjnano.6.164
10. Elstner, M.; Seifert, G. *Philos. Trans. R. Soc., A* **2014,** *372,* 20120483. doi:10.1098/rsta.2012.0483
11. Elstner, M.; Porezag, D.; Jungnickel, G.; Elsner, J.; Haugk, M.; Frauenheim, T.; Suhai, S.; Seifert, G. *Phys. Rev. B* **1998,** *58,* 7260–7268. doi:10.1103/PhysRevB.58.7260
12. Pecchia, A.; Penazzi, G.; Salvucci, L.; Di Carlo, A. *New J. Phys.* **2008,** *10,* 065022. doi:10.1088/1367-2630/10/6/065022
13. Open multiprocessor software package for molecular modelling "KVAZAR". http://nanokvazar.ru/ (accessed Oct 31, 2017).
14. Köhler, C.; Seifert, G.; Frauenheim, T. *Chem. Phys.* **2005,** *309,* 23–31. doi:10.1016/j.chemphys.2004.03.034
15. Aradi, B.; Hourahine, B.; Frauenheim, T. *J. Phys. Chem. A* **2007,** *111,* 5678–5684. doi:10.1021/jp070186p
16. Humphrey, W.; Dalke, A.; Schulten, K. *J. Mol. Graphics* **1996,** *14,* 33–38. doi:10.1016/0263-7855(96)00018-5
17. VMD - Visual Molecular Dynamics, molecular graphics software for MacOS X, Unix, and Windows. http://www.ks.uiuc.edu/Research/vmd/ (accessed Oct 31, 2017).

License and Terms

This is an Open Access article under the terms of the Creative Commons Attribution License (http://creativecommons.org/licenses/by/4.0), which permits unrestricted use, distribution, and reproduction in any medium, provided the original work is properly cited.

The license is subject to the *Beilstein Journal of Nanotechnology* terms and conditions: (https://www.beilstein-journals.org/bjnano)

The definitive version of this article is the electronic one which can be found at:
doi:10.3762/bjnano.9.117

BEILSTEIN JOURNAL OF NANOTECHNOLOGY

New 2D graphene hybrid composites as an effective base element of optical nanodevices

Olga E. Glukhova*[1], Igor S. Nefedov[2,3], Alexander S. Shalin[2] and Michael M. Slepchenkov[1]

Letter

Open Access

Address:
[1]Department of Physics, Saratov State University, Astrakhanskaya street 83, 410012 Saratov, Russia, [2]Laboratory Nanooptomechanics, ITMO University, St. Petersburg, 197101, Russia and [3]Aalto University, School of Electrical Engineering, P.O. Box 13000, 00076 Aalto, Finland

Email:
Olga E. Glukhova* - glukhovaoe@info.sgu.ru; Igor S. Nefedov - igor.nefedov@aalto.fi; Alexander S. Shalin - alexandesh@gmail.com; Michael M. Slepchenkov - slepchenkovm@mail.ru

* Corresponding author

Keywords:
absorption coefficient; 2D CNT–graphene hybrid nanocomposite; optical conductivity; optical nanodevices; topological models

Beilstein J. Nanotechnol. **2018,** *9,* 1321–1327.
doi:10.3762/bjnano.9.125

Received: 01 November 2017
Accepted: 29 March 2018
Published: 30 April 2018

This article is part of the Thematic Series "Light–Matter interactions on the nanoscale".

Guest Editor: M. Rahmani

© 2018 Glukhova et al.; licensee Beilstein-Institut.
License and terms: see end of document.

Abstract

For the first time, we estimated perspectives for using a new 2D carbon nanotube (CNT)–graphene hybrid nanocomposite as a base element of a new generation o optical nanodevices. The 2D CNT–graphene hybrid nanocomposite was modelled by two graphene monolayers between which single-walled CNTs with different diameters were regularly arranged at different distances from each other. Spectra of the real and imaginary parts of the diagonal elements of the surface conductivity tensor for four topological models of the hybrid nanocomposite have been obtained. The absorption coefficient for p-polarized and s-polarized radiation was calculated for different topological models of the hybrid nanocomposite. It was found that the characteristic peaks with high intensity appear in the UV region at wavelengths from 150 to 350 nm (related to graphene) and in the optical range from 380 to 740 nm irrespective of the diameter of the tubes and the distance between them. For waves corresponding to the most intense peaks, the absorption coefficient as a function of the angle of incidence was calculated. It was shown that the optical properties of the hybrid nanocomposite were approximately equal for both metallic and semiconductor nanotubes.

Findings

The applicability of graphene hybrid nanocomposites in the field of optical communications has been hinted to by the active research for the last six years, in which the unique properties of these hybrid nanocomposites as electro-optic materials for optical modulators of different types has been demonstrated [1-4]. One of the newest and hitherto only little investigated

modifications of graphene is a 2D-hybrid composite composed of graphene monolayers and CNTs covalently bonded to them [5-8]. The hybrid 2D film exhibits high performance as photosensitive element of photodetectors in the range of 100–700 nm. It was found that a single photon absorbed by the film induces electron transport of 10^5 electrons, and the response time amounts to ca. 100 microseconds [9]. It should be noted that modern synthesis technologies for such composites have allowed us to provide "cross-linking" between CNTs and graphene during synthesis without further scattering of charge carriers by defects [10,11].

The purpose of this work is the evaluation of perspectives for using the new 2D CNT–graphene hybrid nanocomposite as a base element of new optical nanodevices. Predictive in silico investigations were carried out using the popular and reliable quantum-mechanical SCC DFTB method [12,13]

The 2D CNT–graphene hybrid film was modelled by two graphene monolayers between which single-walled CNTs with different diameters were regularly arranged at different distances from each other. As was shown earlier [14], the composites with zigzag tubes (n, 0) (n = 10, 12, 14, 16, 18, 20) at a distance of 9–15 hexagons (with the step equal to unity) between them are thermodynamically stable. In this work, two composite models for the tubes (12,0) and (18,0) with metallic conductivity, and two models of semiconducting tubes (14,0) and (16,0) have been considered. These topological forms were previously discovered by experimental investigations [11]. The atomistic model of the composite unit cell was obtained by means of the original "method of magnifying glass" described in detail in [14] using the SCC DFTB method. Figure 1 shows a general view of the composite fragment with its unit cell. Blue balls mark atoms of CNT, black balls mark atoms of graphene.

Investigation of the interaction with the incident electromagnetic waves (EMW) in the optical, UV, and IR ranges was performed based on Maxwell's equations. Figure 2 shows one of the configurations for the wave vector of the incident wave with respect to the atomic cell of the hybrid nanocomposite. In this case a plane electromagnetic wave with the wave vector k falls on the composite, which lies in the XZ-plane. The angle θ is the angle of incidence, the vectors **E** and **H** correspond to the electric field strength and magnetic field strength, respectively. The host medium is vacuum. In this configuration the wave is p-polarized (or E-wave).

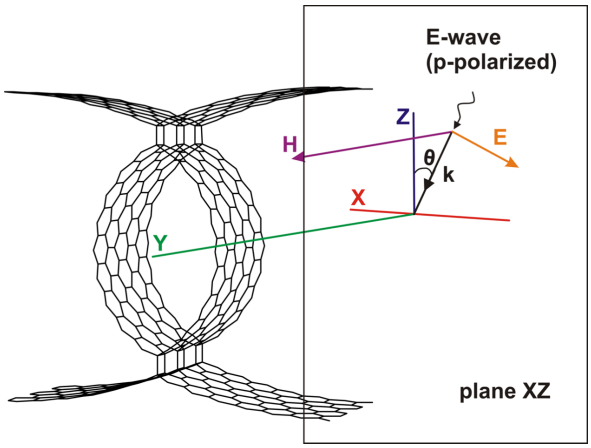


Figure 2: A fragment of the 2D CNT–graphene hybrid nanocomposite and configuration of an incident electromagnetic wave.

To determine the coefficient of reflection, transmission and absorption, Maxwell's equations for the electric and magnetic fields in a vacuum with the 2D CNT–graphene composite as an interface have been considered. Assuming a plane-wave solution, Maxwell's equations can be written in the form

$$\begin{aligned} \mathbf{k}\times\mathbf{E} &= \omega\mathbf{H}, \\ \mathbf{k}\times\mathbf{H} &= -\omega\mathbf{E}, \end{aligned} \tag{1}$$

where **E** and **H** are the electric and the magnetic field strength, respectively, **k** is the wave vector and ω is the frequency of the

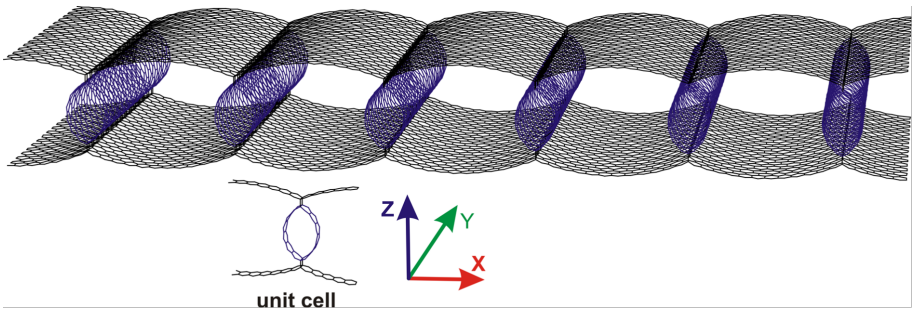


Figure 1: Topological model of 2D CNT-graphene hybrid nanocomposite.

incident electromagnetic radiation. The following boundary conditions were specified at the interface:

$$\begin{aligned}\mathbf{n}\times\left(\mathbf{E}_1-\mathbf{E}_2\right)=0,\\ \mathbf{n}\times\left(\mathbf{H}_1-\mathbf{H}_2\right)=\mathbf{j},\end{aligned} \tag{2}$$

where $\mathbf{j} = \sigma_{xx}E_x + \sigma_{yy}E_y$ is the surface current density in the hybrid nanocomposite, induced by the incident radiation, σ_{xx} and σ_{yy} are the components of the 2D surface conductivity tensor. The indices 1 and 2 refer to the fields in the half-spaces $z > 0$ and $z < 0$, respectively, $\mathbf{n}$ is a normal vector to the surface. In future, we intend to solve the boundary-value problem for the two separate cases of the polarization of the incident radiation, either parallel to the plane of the incident radiation (p-polarization) or normal (s-polarization). A well-known scheme for obtaining the relations between the amplitudes of the incident, refracted and reflected s- and p-polarized waves when passing through the interface based on Maxwell's equations was used [15]. Assuming a value of the amplitude of the electric field equal to 1, one can write for the case of a p-polarized wave:

$$\begin{aligned}E_1^x &= 1+R,\\ E_2^x &= T,\end{aligned} \tag{3}$$

where R and T are the reflection and the transmission coefficient, respectively. Due to continuity of the tangent components of the electric field at the composite surface one can write:

$$1+R=T. \tag{4}$$

For the tangent components of the magnetic field at the composite surface one can write:

$$\frac{1-R-T}{Z_0}=J_x=\sigma_{xx}(1+R), \tag{5}$$

where Z_0 is the characteristic impedance of free space and J_x is the x-component of the surface current density vector. The final expression obtained for the reflection and transmission coefficients, R and T, in the case of a p-polarized incident wave takes the following form:

$$\begin{aligned}R&=\frac{-\sigma_{xx}Z_0}{2+\sigma_{xx}Z_0},\\ T&=\frac{2}{2+\sigma_{xx}Z_0}\end{aligned} \tag{6}$$

and in the case of s-polarization

$$\begin{aligned}R&=\frac{-\sigma_{yy}Z_0}{2+\sigma_{yy}Z_0},\\ T&=\frac{2}{2+\sigma_{yy}Z_0}\end{aligned} \tag{7}$$

where Z_0 is defined for the p-polarized wave as $Z_0 = E_x/H_y = \eta\cdot\cos\theta$, and for the s-polarized wave as $Z_0 = -E_y/H_y = \eta/\cos\theta$, where θ is the angle of incidence $\eta = 120\pi\ \Omega$ is the input impedance of vacuum. Taking into account expressions for the reflection and transmission coefficients, is it possible to find the absorption coefficient by the following formula

$$A=1-|R|^2-T^2. \tag{8}$$

To calculate the elements of the complex optical conductivity tensor, the Kubo–Greenwood formula [16] that determines the conductivity as a function of photon energy Ω was used. It can be written as [17]:

$$\begin{aligned}\sigma_{\alpha\beta}(\Omega)=\frac{2e^2\hbar}{\mathrm{i}m_e^2S_{\mathrm{cell}}}\frac{1}{N_{\mathbf{k}}}\sum_{k\in\mathrm{BZ}}^{N_k}\sum_{m,n}\frac{\hat{P}_\alpha^{nm}(\mathbf{k})\cdot\hat{P}_\beta^{mn}(\mathbf{k})}{E_n(\mathbf{k})-E_m(\mathbf{k})+\Omega+\mathrm{i}\eta}\\ \times\frac{f_\beta\left[E_n(\mathbf{k})-\mu\right]-f_\beta\left[E_m(\mathbf{k})-\mu\right]}{E_n(\mathbf{k})-E_m(\mathbf{k})},\end{aligned} \tag{9}$$

where $f_\beta(x) = 1/\{1 + \exp[\beta(x - \mu)]\}$ is the Fermi–Dirac function of the chemical potential μ with the inverse of the thermal energy $\beta = 1/k_BT$; S_{cell} is the area of the supercell; $N_{\mathbf{k}}$ is the number of k-points needed to sample the Brillouin zone (BZ); $\hat{P}_\alpha^{nm}$ and $\hat{P}_\beta^{mn}$ are the matrix elements corresponding to the α- and β-components of the momentum operator vector; m_e and e are the free-electron mass and electron charge; $E_n(\mathbf{k})$ and $E_m(\mathbf{k})$ and are the sub-band energies of, respectively, valence band and conductivity band. The spin degeneracy is already taken into account in the above equations by the factor 2, η is a phenomenological parameter characterizing electron scattering processes.

To calculate the elements of the impulse matrix $\hat{P}_\alpha^{nm}(\mathbf{k})$, the known substitution $P(\mathbf{k})\rightarrow(m_e/h)\nabla_{\mathbf{k}}\hat{H}(\mathbf{k})$ was used, where $\hat{H}(\mathbf{k})$ is the Hamiltonian. The detailed description for the calculation of the matrix elements of the momentum operator is given in [18]. The Hamiltonian was constructed within the SCC DFTB2 method. Figure 3 and Figure 4 show the spectra of the real and imaginary parts of the diagonal elements of the surface conductivity tensor for four topological models of 2D

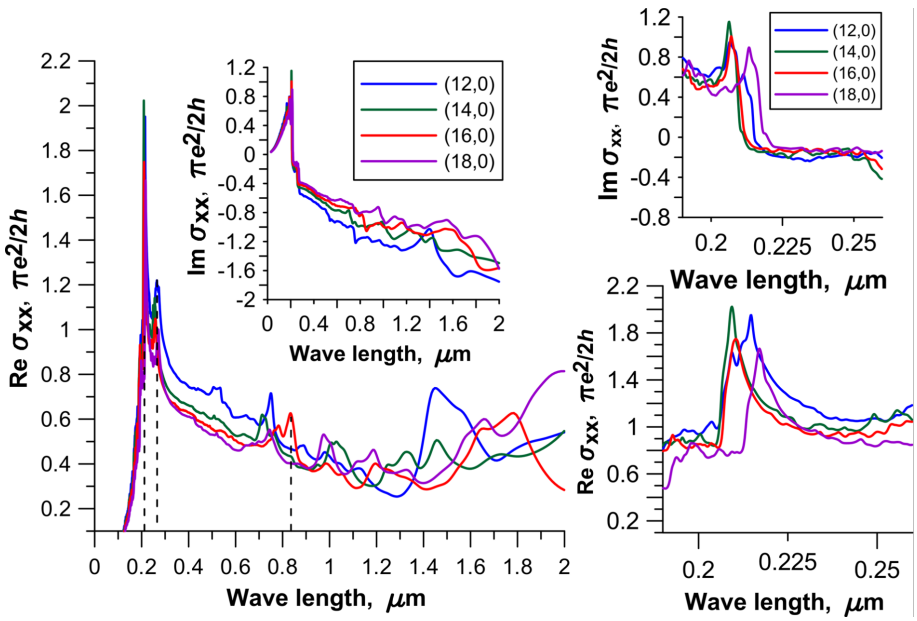


Figure 3: The optical conductivity of 2D CNT–graphene hybrid nanocomposites with an intertube distance of 13 hexagons in the direction perpendicular to the nanotube axis. The insets on the right side show the graphs of optical conductivity for the wavelength range of 190–260 nm.

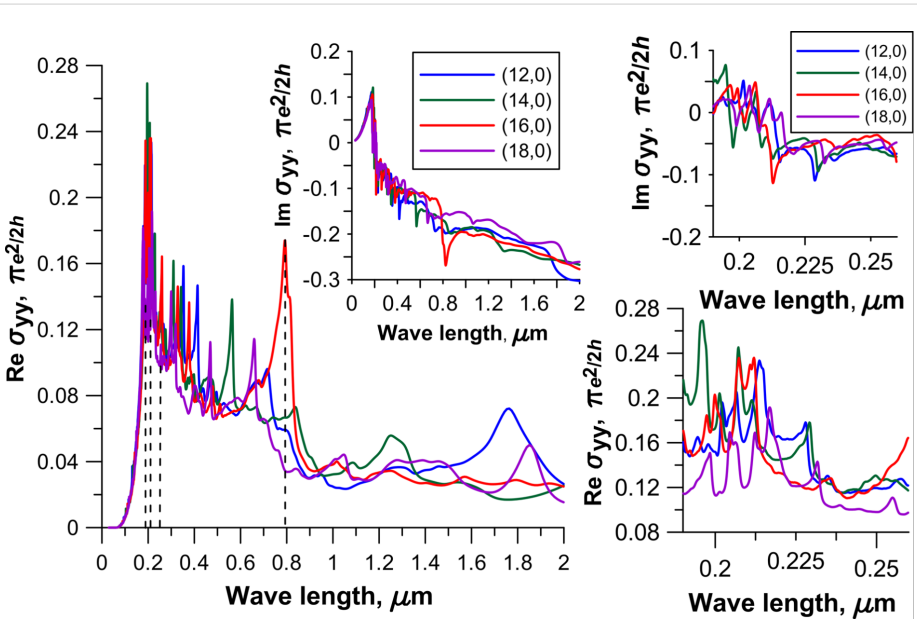


Figure 4: The optical conductivity of 2D CNT–graphene hybrid nanocomposites with an intertube distance of 13 hexagons along the nanotube axis. The insets on the right side show the graphs of optical conductivity for the wavelength range of 190–260 nm.

CNT–graphene hybrid nanocomposites with an intertube distance of 13 hexagons and four types of CNTs. An analysis of the spectrum profile for both tensor elements indicates the presence of prominent peaks in the wavelength range from 190 to 260 nm. The appearance of these peaks is due to the manifestation of pure graphene in the 2D CNT–graphene hybrid nanocomposite, so these peaks have a greater intensity for all the considered topological models hybrid nanocomposites. At the same time the spectrum profile of σ_{xx} is similar to the spectrum of graphene, while the spectrum of σ_{yy} has complex and multiple peaks. As previously shown [14], a complex profile of the conductivity spectrum along the nanotube axis is due to the influence of nanotubes. The appeared multiple peaks are characteristic for the conductivity spectrum of isolated individual

CNTs. It should also be noted that the intensity of the maximum peak, observed at a frequency of 6 eV (206.6 nm) for pure free graphene, is reduced with the appearance of graphene ripple during the formation of the hybrid nanocomposite. As a result, the intensity of the peaks of the CNT–graphene film is higher than that of pure graphene and individual nanotubes (for details see Figure 6 in [14]).

Special attention should be paid to the peak of great intensity observed in the wavelength range of 800–830 nm for models with tube (16,0) (Figure 4). One can expect unusual properties of the hybrid nanocomposite when interacting with an incident electromagnetic wave in this range, in particular for reflected and absorbed waves. For other intertube distances the spectra are similar with only minor changes.

The calculation results of the absorption of electromagnetic waves of the CNT–graphene hybrid nanocomposite are presented in Figure 5 and Figure 6. These figures show two cases of the polarization for different topological models of the hybrid nanocomposite. Figure 5 shows the profile of the absorption coefficient (A) for four types of the tubes with an intertube distance of 13 hexagons, and Figure 6 presents the models of CNT–graphene hybrid nanocomposites with tube (18,0) at four intertube distances: 9, 11, 13 and 15 hexagons.

The analysis of the diagrams in Figure 5 and Figure 6, and also analysis of the calculated data for other models of the composite indicate characteristic peaks with high intensity for all topological models of CNT–graphene hybrid nanocomposites in the UV region at wavelengths from 150 to 350 nm (due to the graphene) and in the optical range from 380 to 740 nm. Intense peaks are absent in the IR region. The presence of the peaks with high intensity is typical for graphene at wavelengths from 150 to 250 nm, so the presence of peaks in the UV region is inevitable in this range. However, the maximum absorption of graphene is less than that of the CNT–graphene hybrid nanocomposite by almost 100%, i.e., the composite is more promising for the use in optical nanodevices than pure graphene.

For wavelengths corresponding to the most intense peaks, a diagram of the dependence of absorption coefficient (Equation 8) on the angle of incidence was calculated for two cases: 1) the wave vector lies in the XZ-plane; 2) the wave vector lies in the YZ-plane. Figure 7 shows the change in the absorption coefficient for two types of polarized waves incident at different angles on the film of tubes (18,0) between the graphene sheets at a distance of 13 hexagons from each other. Diagrams for wavelengths of 250, 388, 454, 524 and 637 nm were calculated. These values were chosen in accordance with the calculated graphs, similar to Figure 5 and Figure 6. This choice was due to perspectives for using the investigated CNT–graphene hybrid nanocomposite film as a working part of optical antennas or polarizers. According to Figure 7 for all wavelengths the maximum absorption is observed for a p-wave at incidence angles of 85–87° for the irradiation in the YZ-plane, and at angles of 85–90° for the irradiation in the XZ-plane. The absorption reaches values of 45–50% at these angles of incidence. Thus, one can say that the optical properties of the composite do not explicitly depend on the type of the tubes.

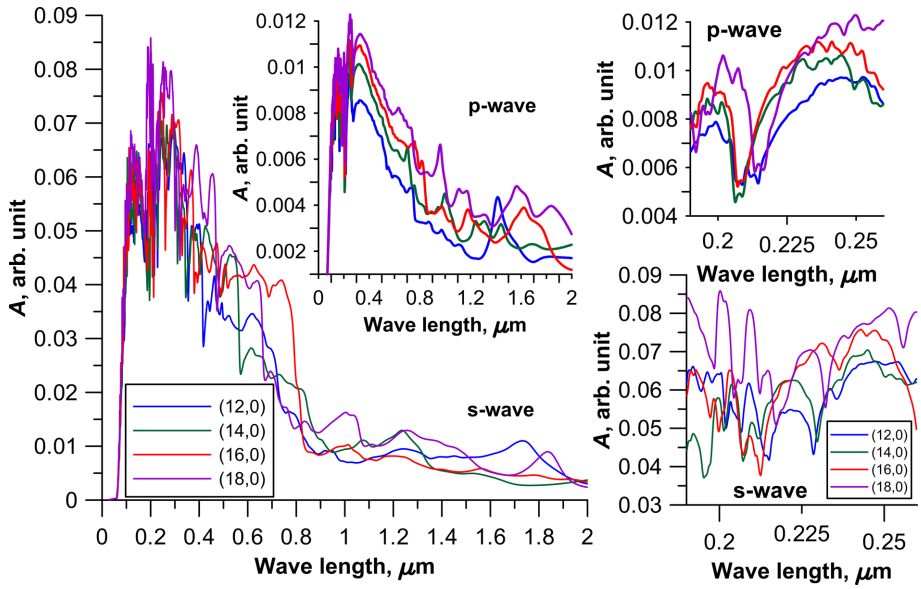


Figure 5: The absorption coefficient of 2D CNT–graphene hybrid nanocomposites with an intertube distance of 13 hexagons. The insets on the right side show the absorption coefficient for the wavelength range of 190–260 nm.

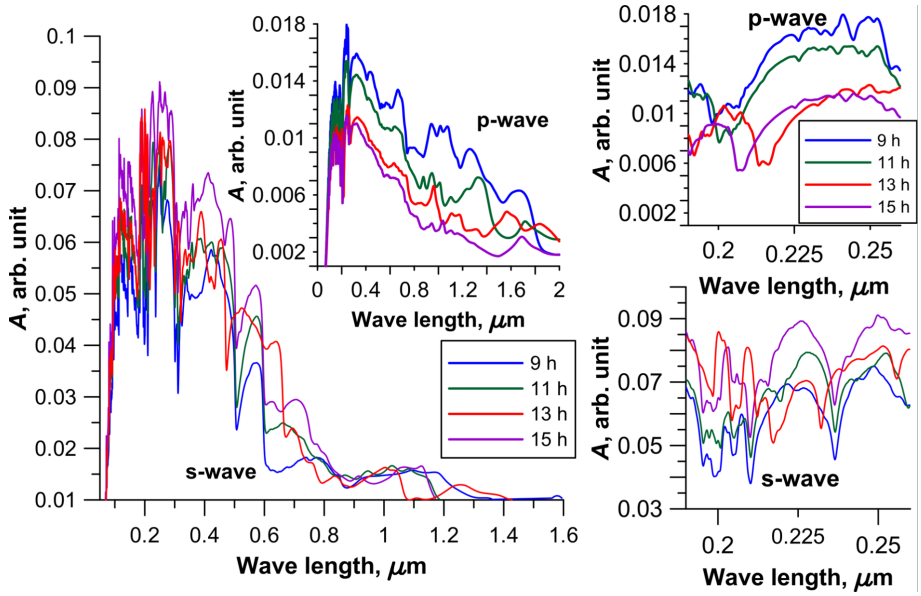


Figure 6: The absorption coefficient of 2D CNT-graphene hybrid nanocomposite with the same tube (18,0) and different intertube distances. The insets on the right side show the absorption coefficient for the wavelength range of 190–260 nm.

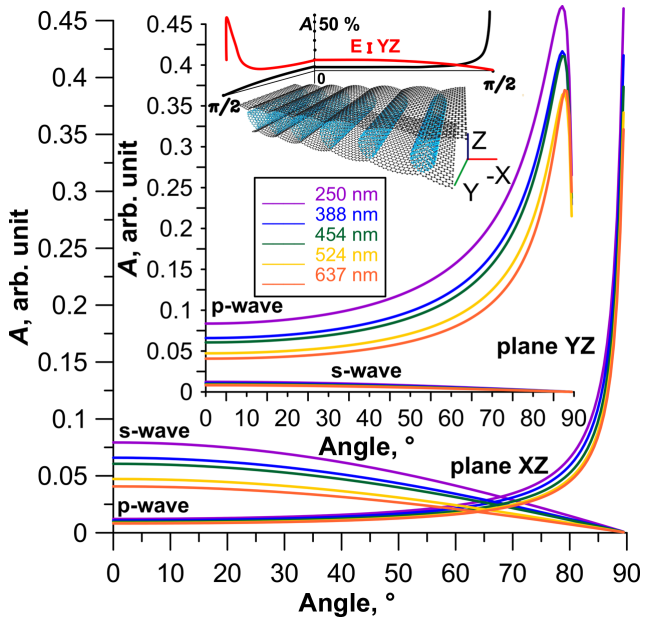


Figure 7: Absorption coefficient of a 2D CNT–graphene hybrid nanocomposite (tube (18,0), 13 hexagons intertube distance) as a function of the angle of incidence at different wavelengths.

In summary, it can be concluded that the new 2D CNT–graphene hybrid nanocomposite is very promising for optoelectronic devices. In particular, the established regularities of change in absorbance as a function of the angle of incidence of the electromagnetic wave allows us to suggest the possibility of using the CNT–graphene film as a polarizer for electro-optical and magneto-optical thin film modulators. The advantages of such polarizers are a wide spectral range and low loss.

Acknowledgements

The research described in this paper was supported by the grant of the Russian Science Foundation #15-07-06307 and Russian Presidential scholarship 2016-2018 # SP-3135.2016.1.

ORCID® iDs

Olga E. Glukhova - https://orcid.org/0000-0002-5670-2058
Igor S. Nefedov - https://orcid.org/0000-0001-9265-3786
Alexander S. Shalin - https://orcid.org/0000-0003-2220-5181

References

1. Mikhailov, S. A. *Phys. Rev. B* **2016,** *93,* 085403. doi:10.1103/PhysRevB.93.085403
2. Cheng, J. L.; Vermeulen, N.; Sipe, J. E. *New J. Phys.* **2014,** *16,* 053014. doi:10.1088/1367-2630/16/5/053014
3. Auditore, A.; De Angelis, C.; Locatelli, A.; Boscolo, S.; Midrio, M.; Romagnoli, M.; Capobianco, A.-D.; Nalesso, G. *Opt. Lett.* **2013,** *38,* 631–633. doi:10.1364/OL.38.000631
4. Hendry, E.; Hale, P. J.; Moger, J.; Savchenko, A. K.; Mikhailov, S. A. *Phys. Rev. Lett.* **2010,** *105,* 097401. doi:10.1103/PhysRevLett.105.097401
5. Maarouf, A. A.; Kasry, A.; Chandra, B.; Martyna, G. J. *Carbon* **2016,** *102,* 74–80. doi:10.1016/j.carbon.2016.02.024
6. Gorkina, A. L.; Tsapenko, A. P.; Gilshteyn, E. P.; Koltsova, T. S.; Larionova, T. V.; Talyzin, A.; Anisimov, A. S.; Anoshkin, I. V.; Kauppinen, E. I.; Tolochko, O. V.; Nasibulin, A. G. *Carbon* **2016,** *100,* 501–507. doi:10.1016/j.carbon.2016.01.035
7. Liu, Y.; Wang, F.; Wang, X.; Wang, X.; Flahaut, E.; Liu, X.; Li, Y.; Wang, X.; Xu, Y.; Shi, Y.; Zhang, R. *Nat. Commun.* **2015,** *6,* 8589. doi:10.1038/ncomms9589
8. Gan, X.; Lv, R.; Bai, J.; Zhang, Z.; Wei, J.; Huang, Z. H.; Zhu, H.; Kang, F.; Terrones, M. *2D Mater.* **2015,** *2,* 034003. doi:10.1088/2053-1583/2/3/034003
9. Eckmann, A.; Felten, A.; Mishchenko, A.; Britnell, L.; Krupke, R.; Novoselov, K. S.; Casiraghi, C. *Nano Lett.* **2012,** *12,* 3925–3930. doi:10.1021/nl300901a
10. Kholmanov, I. N.; Magnuson, C. W.; Piner, R.; Kim, J.-Y.; Aliev, A. E.; Tan, C.; Kim, T. Y.; Zakhidov, A. A.; Sberveglieri, G.; Baughman, R. H.; Ruoff, R. S. *Adv. Mater.* **2015,** *27,* 3053–3059. doi:10.1002/adma.201500785
11. Tristán-López, F.; Morelos-Gómez, A.; Vega-Díaz, S. M.; García-Betancourt, M. L.; Perea-López, N.; Elías, A. L.; Muramatsu, H.; Cruz-Silva, R.; Tsuruoka, S.; Kim, Y. A.; Hayahsi, T.; Kaneko, K.; Endo, M.; Terrones, M. *ACS Nano* **2013,** *7,* 10788–10798. doi:10.1021/nn404022m
12. Elstner, M.; Porezag, D.; Jungnickel, G.; Elsner, J.; Haugk, M.; Frauenheim, T.; Suhai, S.; Seifert, G. *Phys. Rev. B* **1998,** *58,* 7260. doi:10.1103/PhysRevB.58.7260
13. Elstner, M.; Seifert, G. *Philos. Trans. R. Soc., A* **2014,** *372,* 20120483. doi:10.1098/rsta.2012.0483
14. Mitrofanov, V. V.; Slepchenkov, M. M.; Zhang, G.; Glukhova, O. E. *Carbon* **2017,** *115,* 803–810. doi:10.1016/j.carbon.2017.01.040
15. Landau, L. D.; Lifshitz, E. M.; Pitaevskii, L. P. *Electrodynamics of Continuous Media,* 2nd ed.; Pergamon: Oxford, United Kingdom, 1984.
16. Marder, M. P. *Condensed Matter Physics,* 2nd ed.; Wiley-VCH: Berlin, Germany, 2011.
17. Le, H. A.; Ho, S. T.; Chien, N. D.; Do, V. N. *J. Phys.: Condens. Matter* **2014,** *26,* 405304. doi:10.1088/0953-8984/26/40/405304
18. Pedersen, T. G.; Pedersen, K.; Kriestensen, T. B. *Phys. Rev. B* **2001,** *63,* 201101(R). doi:10.1103/PhysRevB.63.201101

License and Terms

This is an Open Access article under the terms of the Creative Commons Attribution License (http://creativecommons.org/licenses/by/4.0), which permits unrestricted use, distribution, and reproduction in any medium, provided the original work is properly cited.

The license is subject to the *Beilstein Journal of Nanotechnology* terms and conditions: (https://www.beilstein-journals.org/bjnano)

The definitive version of this article is the electronic one which can be found at: doi:10.3762/bjnano.9.125

BEILSTEIN JOURNAL OF NANOTECHNOLOGY

Tailoring polarization and magnetization of absorbing terahertz metamaterials using a cut-wire sandwich structure

Hadi Teguh Yudistira[1,2], Shuo Liu[3], Tie Jun Cui[3] and Han Zhang[*1]

Full Research Paper

Open Access

Address:
[1]SZU-NUS Collaborative Innovation Centre for Optoelectronic Science & Technology and Key Laboratory of Optoelectronic Devices and Systems of Ministry of Education and Guangdong Province, College of Optoelectronic Engineering, Shenzhen University (SZU), Shenzhen 518060, China, [2]Mechanical Engineering Program, Institut Teknologi Sumatera (ITERA), Lampung 35365, Indonesia, and [3]State Key Laboratory of Milimeter Waves, Southeast University, Nanjing 210096, China

Email:
Han Zhang[*] - hzhang@szu.edu.cn

* Corresponding author

Keywords:
absorber; cut-wire; metamaterial; terahertz

Beilstein J. Nanotechnol. **2018,** *9,* 1437–1447.
doi:10.3762/bjnano.9.136

Received: 10 November 2017
Accepted: 18 April 2018
Published: 16 May 2018

This article is part of the Thematic Series "Light–Matter interactions on the nanoscale".

Guest Editor: M. Rahmani

© 2018 Yudistira et al.; licensee Beilstein-Institut.
License and terms: see end of document.

Abstract

The permittivity and permeability of a cut-wire sandwich structure can be controlled by laterally shifting the upper and lower layers. The use of this process for designing specific application-oriented devices may lack clear-cut guidelines because the lateral misalignment will significantly change the permittivity and permeability simultaneously. Therefore, in this work, we designed, fabricated and characterized a cut-wire sandwich device capable of tailoring the polarization and magnetization separately, thereby providing a promising recipe for achieving specific application objectives, such as a high-performance absorber. Accumulated charges effectively provided the polarization at the edge of cut-wires, and the surface current density on the cut-wires at top and bottom layers effectively generated the magnetization. By controlling and optimizing the geometrical configurations of the entire sandwich device (without lateral misalignment), the impedance could be matched to that of free space while generating a large imaginary part in the refractive index. This work characterizes the absorption performance of such sandwich structures in the terahertz regime. This mechanism could be further extended to other metamaterial devices in the terahertz and other frequency ranges because polarization and magnetization can now be selectively controlled in a straightforward manner.

Introduction

The terahertz spectrum is located between the infrared and microwave spectrum. This part of the spectrum has unique properties, such as being non-ionizing and subject to considerably less Rayleigh scattering than the visible or infrared spectrum [1]. The terahertz spectrum has been widely used in research fields such as medical imaging [1-3] and security applications [4].

Optical [5-7] and microwave metamaterials [8-10] have been intensively investigated in the past decades. Although detecting

the terahertz wavelengths is somewhat difficult, through the development of terahertz detection technology, the study of terahertz metamaterials has been reported as early as 2004 [11], which is earlier than the study of optical metamaterials.

The materials consist of multiple tiny metallic structures fabricated on dielectric substrates for metamaterial applications. The length of the tiny metallic structures of terahertz metamaterials is usually approximately hundreds of micrometers [12-14], which is much smaller than the wavelength of the terahertz electromagnetic (EM) wave. Thus, such structures can be considered a homogeneous medium from the perspective of the EM wave. The existence of multiple metallic structures in a device may affect the EM properties, such as permittivity and permeability.

Several works on metamaterial absorbers have been presented such as split-ring resonators [15], electric-field-coupled (ELC) resonators [16], lossy cut-wire bars [17], and donut-type resonators [18]. Most previous works on the perfect absorber have been explained by interference theory [19-23], for example that presented by Chen [19] who described a perfect metamaterial absorber based on the interference theory. He demonstrated numerical simulations and analytical calculations of the metamaterial absorber. The design of the metamaterial absorber comprised two parts: a metallic plane, which serves as the background, and the metamaterial structure. The two parts are separated by a dielectric spacer. Another necessary condition found was that absorbers can be achieved by increasing the imaginary part of the refractive index and matching the impedance of the metamaterial with air impedance [24,25].

Cut-wire and split-ring structures are often used as electric resonators that can control the permittivity of a metamaterial [26-28]. By using a cut-wire sandwich structure, the permeability can be controlled due to the existence of a looping surface current between the cut-wire structures. The cut-wire structure is sensitive to polarization. Symmetric geometries are required to produce a metamaterial with arbitrary polarization. The cross-shaped structure is one example of a symmetric geometry that is based on the cut-wire structure and has been used to design terahertz absorbers [29]. The star-shaped structure is another structure with a symmetric geometry that is based on the cut-wire structure. One of the unique features of the star-shaped structure is its capability to exhibit more than one resonance peak [30].

Presently, the permittivity and permeability of the cut-wire sandwich structure can be adjusted by laterally shifting the upper and lower layers of the cut-wire structure [27,31,32]. The symmetric breaking in cut-wire sandwich structures can simultaneously generate negative values for permittivity and permeability [27,32], thereby making a perfect lens [33]. The cut-wire sandwich structure can be organized to achieve another specific application objective, that is, a high-performance absorber. By controlling and optimizing the geometrical configurations of the entire sandwich device without lateral misalignment, the impedance can be matched to that of free space while generating a large imaginary part in the refractive index.

In this work, we theoretically and experimentally studied the absorbance of a thin terahertz metamaterial that was based on the cut-wire sandwich structure, which was demonstrated to generate polarization and magnetization simultaneously. By using cut-wire sandwich structures, we could control the permittivity and permeability of the metamaterial to match its impedance to that of free space and realize a high imaginary refractive index value. Simple cut-wire, cross-shaped and star-shaped sandwich structures, composed of one, two, and four metallic cut-wire bars, respectively, are presented in this paper. By arranging the cut-wire structure on a unit cell, we could obtain a metamaterial absorber with a specific polarization response (arbitrary response or sensitive response) and a specific resonance feature.

Experimental

Figure 1a illustrates the geometry of the cut-wire sandwich structure. The width of the gold metallic bar (W), the length of gold metallic bar (L), the gap size between two unit cells (g), the thickness of the gold metallic bar (Z_g), the thickness of the dielectric (polyimide (PI)) (Z_d), and the lattice constant ($D = L + g$) are 20 μm, 100 μm, 5 μm, 100 nm, 5 μm and 105 μm, respectively. Gold was selected for the metallic bars to ensure good conductivity and avoid oxidation in air. We fabricated three samples: cut-wire (Figure 1b), cross-shaped (Figure 1c) and star-shaped sandwich structures (Figure 1d). ϕ is the angle that described the EM polarization direction. The cross-shaped sandwich structure was composed of two cut-wires that were arranged perpendicular to each other. The star-shaped sandwich structure was composed of four cut-wires that were arranged every 45° of ϕ.

The impedance (z) and refractive index (n) are the two main parameters that describe the EM properties of a material and can be defined as $z = \sqrt{\mu_r/\varepsilon_r}$ and $n = \sqrt{\mu_r\varepsilon_r}$, respectively, where ε_r and μ_r are the relative permittivity, and relative permeability, respectively. The relative permittivity of the material can be defined as $\varepsilon_r = 1 + (P / \varepsilon_r E)$, and the relative permeability can be defined as $\mu_r = 1 + M / H$, where E, H, P, and M are the electric field, magnetic field, polarization, and magnetization [12], respectively. Magnetization and polarization are two factors that can be used to tailor the relative permeability and relative

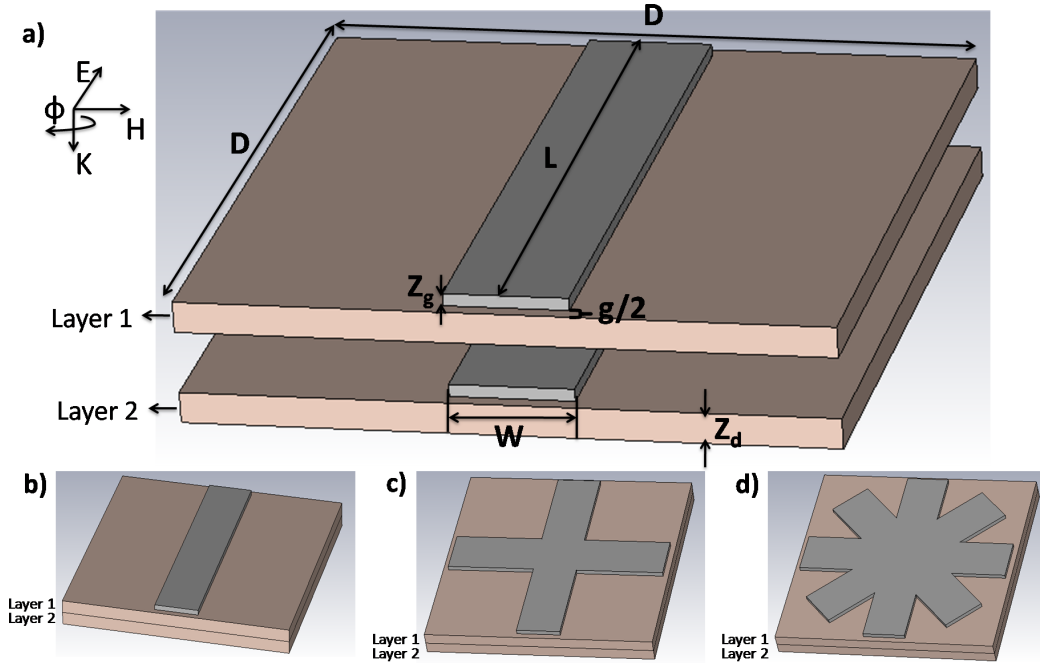


Figure 1: a) Illustration of cut-wire sandwich structure. *W*, *L*, *g*, Z_d and Z_g are width of cut wire (20 μm), length of cut wire (100 μm), the gap size of cut wire with its neighbor (5 μm), polyimide substrate thickness (5 μm), and tge cut-wire structure thickness (100 nm), respectively. *D* is the lattice constant (*D* = *L* + *g*). b) Sample 1: cut-wire sandwich structure, c) Sample 2: cross-shaped sandwich structure, d) Sample 3: star-shaped sandwich structure.

permittivity, respectively. The important parameters of a cut-wire sandwich structure are the gap size between two unit cells and the thickness of the dielectric spacer. Accumulation charge is located at the edge of the arm and generates a very large electric dipole moment, which then leads to a large effective permittivity. The effective permittivity increases with a decrease in gap width [12]. The anti-parallel surface current density on the gold electrode line at layer 1 and 2 effectively generate magnetization, which results in a large effective permeability. Both cut-wire structures were separated by a thin polyimide (PI) layer. To match the impedance of the metamaterial to that of free space, the effective permittivity should be equal to the effective permeability at the desired frequencies.

Samples with area of 10 × 10 mm were fabricated. First, a PI layer (Yi Dun New Materials, Suzhou Co., Ltd.) was spin-coated on a silicon wafer and then baked on a hot plate at 80 °C, 120 °C, 180 °C and 250 °C for 5, 5, 5 and 20 min, respectively. Then, standard photolithography was performed [34,35], and another Ti/Au layer (30/100 nm) was deposited onto the PI substrate by electron beam evaporation. A standard lift-off process was employed to enable the formation of the final metallic pattern. The second layer was fabricated by repeating the above processes. The final process involved peeling off the cured PI layer from the silicon wafer. Figure 2 exhibits microscopy images of the fabricated samples.

Results and Discussion

The absorbance ($A(\omega)$) of the material was calculated from the reflectance ($R(\omega)$) and transmittance ($T(\omega)$) by using the following equation: $A(\omega) = 1 - R(\omega) - T(\omega)$. Smith et al. [36] defined transmittance and reflectance as

$$T(\omega) = |t(\omega)|^2 = \left| \frac{1}{\cos(nk_0 d) - \frac{\mathrm{i}}{2}\left(z + \frac{1}{z}\right)\sin(nk_0 d)} \right|^2 \quad (1)$$

and

$$R(\omega) = |r(\omega)|^2 = \left| \frac{\mathrm{i}}{2}\left(\frac{1}{z} - z\right)\sin(nk_0 d) \right|^2, \quad (2)$$

Where $t(\omega)$, $r(\omega)$, n, k_0, d and z are the transmissivity, reflectivity, refractive index, wave number in free space, substrate thickness and impedance, respectively. In the matching air impedance condition (i.e., $z = 1 + \mathrm{i}0$), the reflectance would be zero and Equation 1 is expressed as

$$T(\omega) = \left| \frac{1}{\cos(nk_0 d) - \mathrm{i}\sin(nk_0 d)} \right|^2 = \left| \frac{1}{\exp\left(-\mathrm{i}\left(n_\mathrm{r} + \mathrm{i}n_\mathrm{i}\right)k_0 d\right)} \right|^2 \quad (3)$$

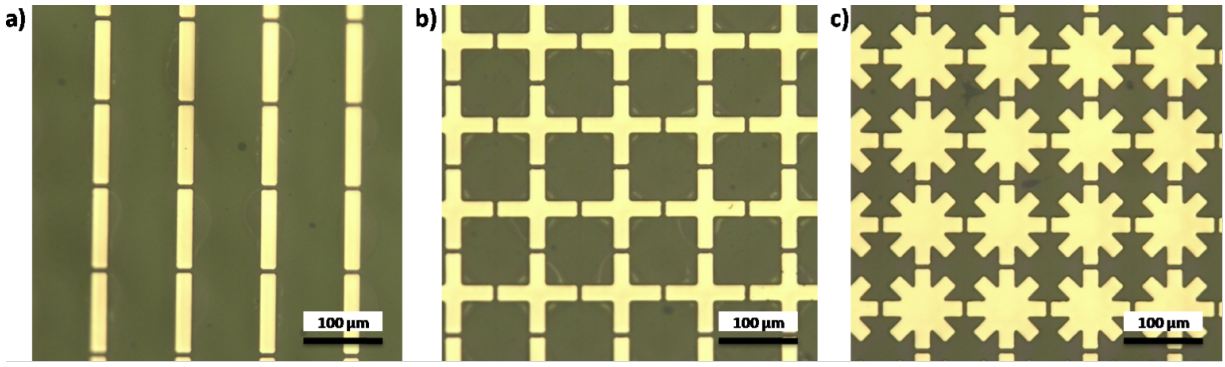


Figure 2: Microscopy images of the fabrication samples: a) Cut-wire sandwich structure, b) cross-shaped sandwich structure, and c) star-shaped sandwich structure.

where n_r and n_i are the real and imaginary parts of the refractive index, respectively. Equation 3 can be simplified as

$$T(\omega)=\left|\frac{1}{\exp(n_i k_0 d)\exp(-in_r k_0 d)}\right|^2=\frac{1}{\exp(2n_i k_0 d)}. \quad (4)$$

Equation 4 shows that a high imaginary refractive index is required to achieve zero transmittance. To achieve high absorbance, the impedance of the metamaterial should match the air impedance and the imaginary part of the refractive index value should be high.

The electrical properties of the thin metallic bar deposited on the substrate strongly deviated from that of the bulk metallic [37]. The Drude model [38] was used for calculating the permittivity of thin gold metallic bars in the software CST microwave studio [39], where

$$\varepsilon_{Au}(\omega)=1-\frac{\omega_{p,Au}}{\omega^2+i\omega\Gamma_{Au}},$$

with $\omega_{p,Au} = 1.38 \times 10^{16}$ rad/s and $\Gamma_{Au} = 0.11 \times 10^{15}$ s^{-1}. ω, $\omega_{p,Au}$ and Γ_{Au} are the angular frequency, angular plasma frequency of gold, and damping constant of gold, respectively. Figure 3 presents the reflectance–transmittance–absorbance (RTA) simulation result of cut-wire (Figure 3a), cross-shaped (Figure 3b) and star-shaped sandwich structures (Figure 3c). The simulation results of the cut-wire sandwich structure exhibited a narrow absorbance of 63% at 0.78 THz. The absorbance of the cross-shaped sandwich structure reached 78% at 0.82 THz. The full width at half maximum absorbance of the cut-wire sandwich structure and that of the cross-shaped sandwich structure are 0.05 and 0.06 THz, respectively. The narrow absorbance of these structures may due to the conductivity of the thin metallic bar. The frequency peak of the absorbance of the cut-wire sandwich structure differed from that of the cross-shaped sandwich structure, and this discrepancy could be explained as follows. The existence of the cut-wire width of the cross-shaped sandwich structure at $\phi = 90°$ reduced the metallic bar length parallel to the external electric field by a few micrometers, thereby, increasing the resonance frequency. Figure 4 shows the simulation result of the absorbance difference as the cut-wire width (w1) of the cross-shaped sandwich structure at $\phi = 90°$ was varied from 5 µm to 20 µm. The frequency peak of the absorbance of the cross-shaped sandwich structure decreased to near that of the cut-wire sandwich structure when the cut-wire width of the cross-shaped sandwich structure at $\phi = 90°$ was decreased. This change in cut-wire width of the cross-shaped sandwich structure at $\phi = 90°$ resulted in an alteration of the polarization and magnetization on the unit cell and thus altered the absorbance magnitude and location of the frequency peak. The surface current flowed only on the cut wire that was parallel to the external electric field. Meanwhile, no surface current flowed along on the cut wire at $\phi = 90°$ on the cross-shaped sandwich structure. Consequently, polarization and magnetization were generated only on the cut wire that was parallel to the external electric field. The star-shaped sandwich structure had three absorbance peaks: 78% at 0.81 THz, 43% at 1.31 THz and 45% at 1.5 THz. The full width at half maximum absorbance of the star-shaped sandwich structure at 0.81 THz was 0.06 THz, which is close to that of the cut-wire sandwich structure. The direction of the surface current flow was parallel to the external electric field at 0.81 THz on the star-shaped sandwich structure, and this pattern was similar to that of the cross-shaped structure. At 1.31 THz, the surface current flow was along the cut wire not only at $\phi = 0°$, but also at $\phi = 45°$. Magnetization was generated on the cut wire at $\phi = 45°$ at 1.33 THz because an anti-parallel surface current existed on both cut-wires at $\phi = 45°$. The surface current flow direction at 1.5 THz was opposite to that at 1.31 THz.

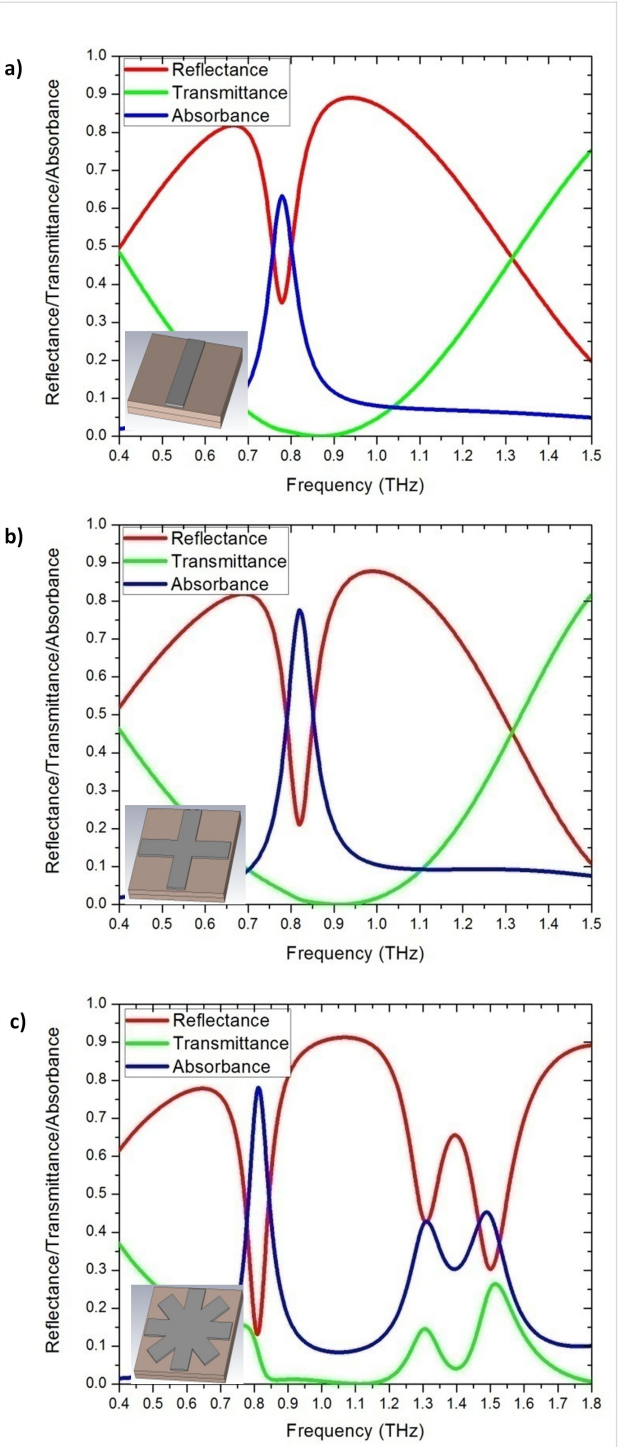


Figure 3: Reflectance–transmittance–absorbance (RTA) simulation results: a) Cut-wire sandwich structure, b) cross-shaped sandwich structure, and c) star-shaped sandwich structure.

The scattering parameters (S-parameters) were used to extract the EM properties of the proposed absorber [36,40]. The refractive index and impedance were obtained using Equation 5 and Equation 6 [40] as

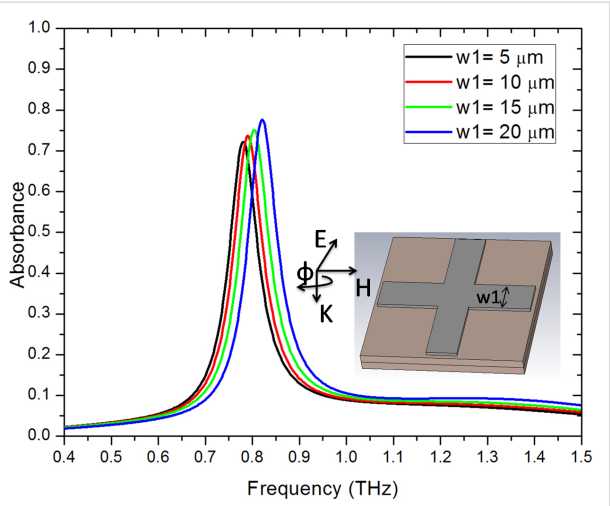


Figure 4: The simulation result of the absorbance difference for the cut-wire width of the cross-shaped sandwich structure at ϕ = 90° with w1 varying from 5 μm to 20 μm.

$$z = \pm\sqrt{\frac{(1+S_{11})^2 - S_{21}^2}{(1-S_{11})^2 - S_{21}^2}} \tag{5}$$

$$\exp(ink_0 d) = X \pm i\sqrt{1-X^2}, \tag{6}$$

where $X = (1 / 2S_{21}^2)(1 - S_{11}^2 + S_{21}^2)$. The metamaterial was considered a passive medium; hence, the sign in Equation 5 and Equation 6 was determined according to $z_r \geq 0$ and $n_i \geq 0$, where z_r is the real part of the impedance. The refractive index and impedance are related to permittivity and permeability by the relations $\varepsilon = n / z$ and $\mu = nz$ [36,40]. Figure 5a–c presents the EM properties of the cut-wire, cross-shaped and star-shaped sandwich structures, respectively. The narrow band absorbance was obtained by matching the impedance of the absorber with the impedance of air, thus realizing a high imaginary part of the refractive index at absorption frequencies. To achieve an impedance that was close to that of air, the permeability (μ) value should approach the permittivity (ε) value. The black and red curves in Figure 5 represent the real and imaginary values, respectively. Figure 5a shows that the μ (real), ε (real), μ (imaginary) and ε (imaginary) parts of the cut-wire sandwich structure at 0.78 THz were −38.62, 12.4, 33.13 and 6.88, respectively. The Z value of the cut-wire sandwich structure at 0.78 THz was 1.08 + i1.55, which was close to the impedance of air, i.e., 1 + i0. The refractive index (n) of the cut-wire sandwich structure at 0.78 THz was 2.71 + i26.72. The imaginary part of the refractive index of the cut-wire sandwich structure was high and could thus yield low transmittance. The Z-value of cross-shaped structure at 0.82 THz and the star-shaped sandwich structure at 0.81 THz were 1.48 + i1.15 and 1.18 + i0.75, respectively,

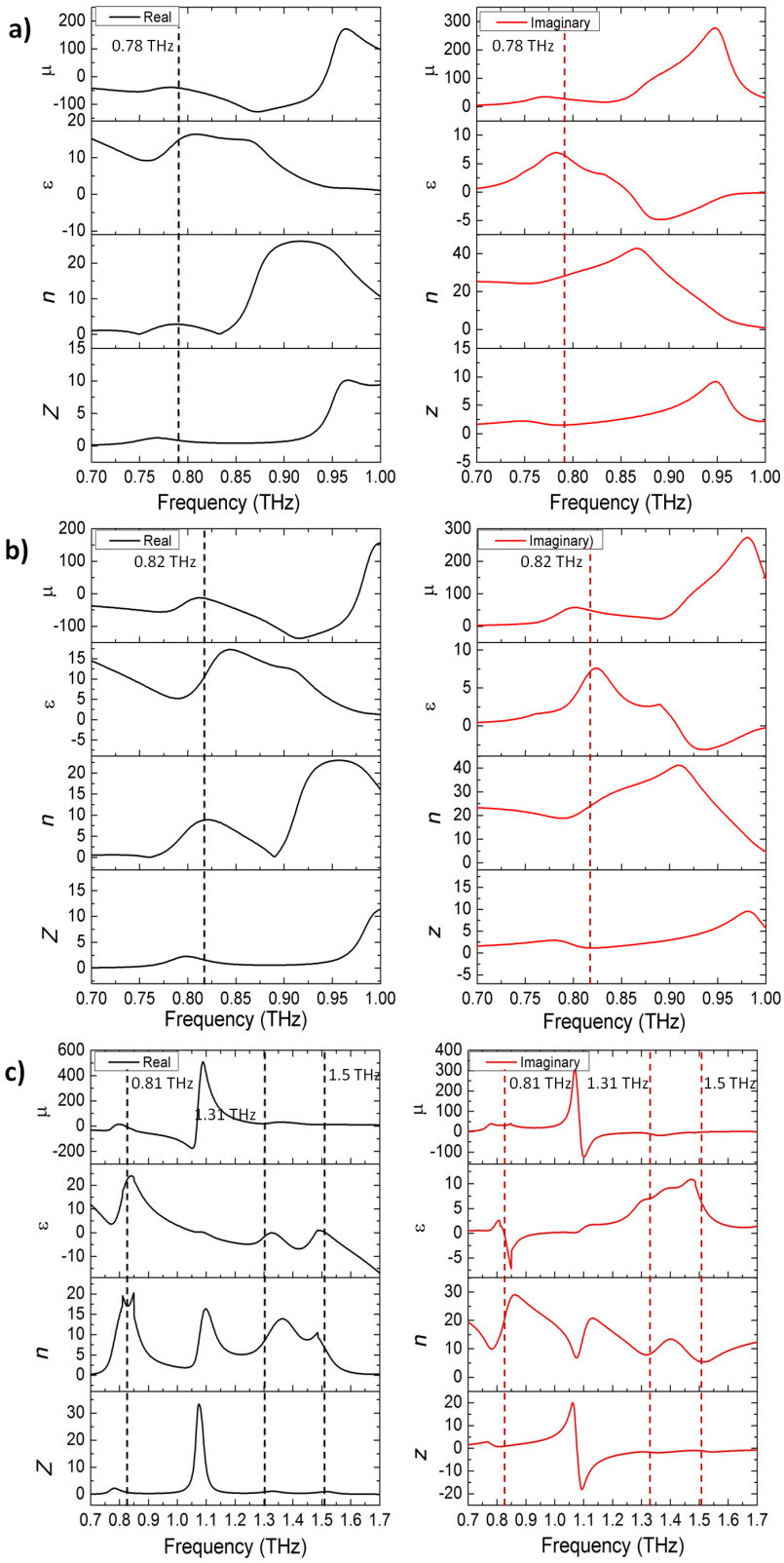


Figure 5: Permeability (μ), permittivity (ε), refractive index (*n*), and impedance (*Z*) properties of: a) Cut-wire sandwich structure, b) cross-shaped sandwich structure, and c) star-shaped sandwich structure. The black and red curves represent the real and imaginary part of each value, respectively.

which were also near the air impedance value and thus could yield a low reflectance. The absolute *Z*-values of the cut-wire sandwich structure at 0.78 THz, the cross-shaped sandwich structure at 0.82 THz and the star-shaped sandwich structure at 0.81 THz were 1.89, 1.87 and 1.4, respectively. The absolute *Z*-values of the star-shaped sandwich structure were the closest to the absolute air impedance value of 1, and thus yielded the lowest reflectance of all samples. The reflectance of the cut-wire sandwich structure at 0.78 THz was slightly higher than that of the cross-shaped sandwich structure at 0.82 THz because the absolute *Z*-value of the cross-shaped structure was closer to the absolute air impedance value as compared to that of the cut-wire sandwich structure. The *n*-values of the cross-shaped structure at 0.82 THz and the star-shaped sandwich structures at 0.81 THz were 8.94 + i24.79 and 19.59 + i14.96, respectively. The imaginary part of the refractive index of the star-shaped sandwich structure at 0.81 THz is lower than that of the cut-wire sandwich structure at 0.78 THz and the cross-shaped sandwich structure at 0.82 THz. The transmittance of the star-shaped sandwich structure at 0.81 THz could not reach zero due to the small value of the imaginary part of the refractive index. The *Z*-values of the star-shaped sandwich structure at 1.31 THz and 1.5 THz were 1.01 − i1.51 and 0.87 − i0.98, respectively. These values were close to the impedance of air, and therefore, were able to achieve a low reflectance. The imaginary parts of the refractive index of the star-shaped sandwich structure at 1.31 THz and 1.5 THz are 7.99 and 5.64, respectively. These figures were much lower than the imaginary part of refractive index of the star-shaped sandwich structure at 0.82 THz. Therefore, the transmittance of the star-shaped sandwich structure at 1.31 THz and 1.5 THz was higher than that of the star-shaped sandwich structure at 0.82 THz.

Figure 6a–c presents the peak magnitude of the electric and magnetic fields of the cut-wire, cross-shaped and star-shaped sandwich structures, respectively. The frequencies of the peak values of the electric and magnetic fields were similar to those of the absorbance peaks. This condition indicated the existence of a high absorption when the high electric field and magnetic field are stored on the metamaterial structure. The electric and magnetic field distributions are presented in the inset of Figure 6. The electric field distribution showed that the maximum value of the electric field was at the gap between two unit cells. The magnetic field distribution showed that the maximum value of the magnetic field was between layers 1 and 2. The anti-parallel surface in the gold metallic bars on layers 1 and 2 generated magnetization. The maximum value of the electric and magnetic fields was found here, while the *Z*-values of the samples were close to the impedance of air and the imaginary value of the refractive index was high at a similar frequency (Figure 5). Figure 7a–c presents the simulation results of absorbance with different polarization directions for the cut-wire, cross-shaped and star-shaped sandwich structures, respectively. The cut-wire sandwich structure was demonstrated to be a metamaterial with sensitive polarization. Figure 7a shows that

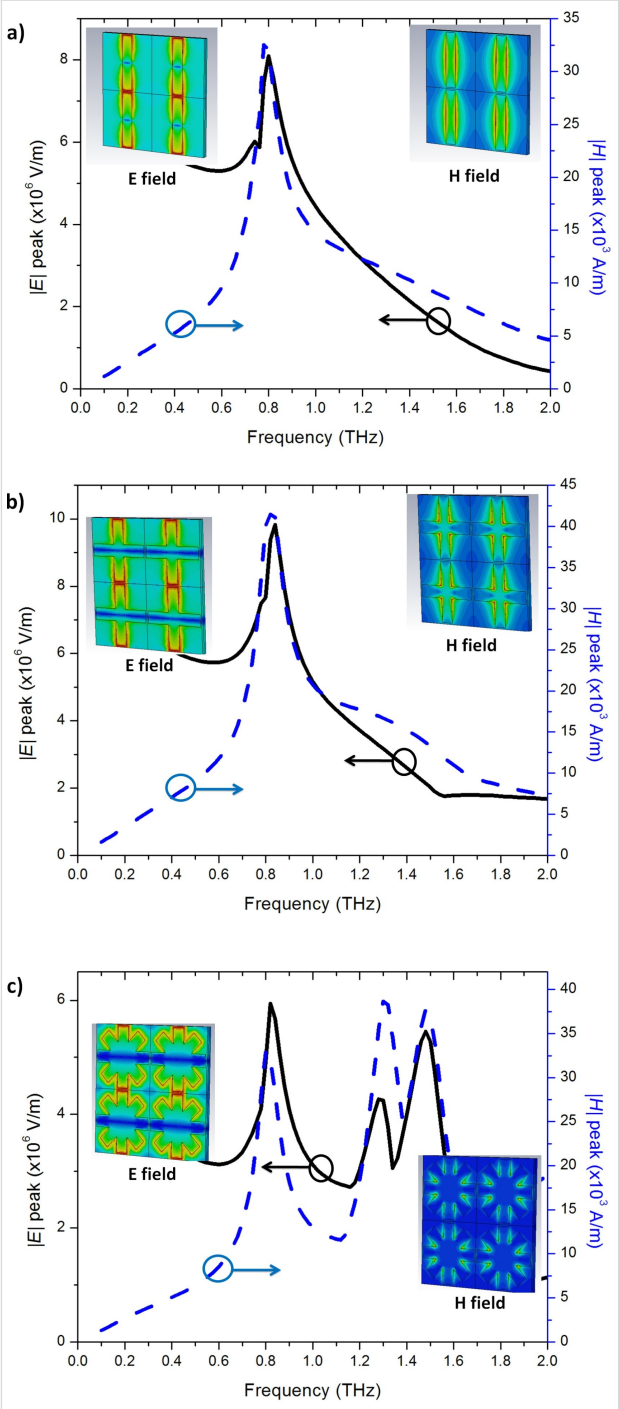


Figure 6: The peak value of electric field and magnetic field of: a) Cut-wire sandwich structure, b) cross-shaped sandwich structure, and c) star-shaped sandwich structure. The insets of (a–c) in each panel show electric and magnetic field distributions of the cut-wire sandwich structure at 0.78 THz, cross-shaped sandwich structure at 0.82 THz, and star-shaped sandwich structure at 0.81 THz, respectively.

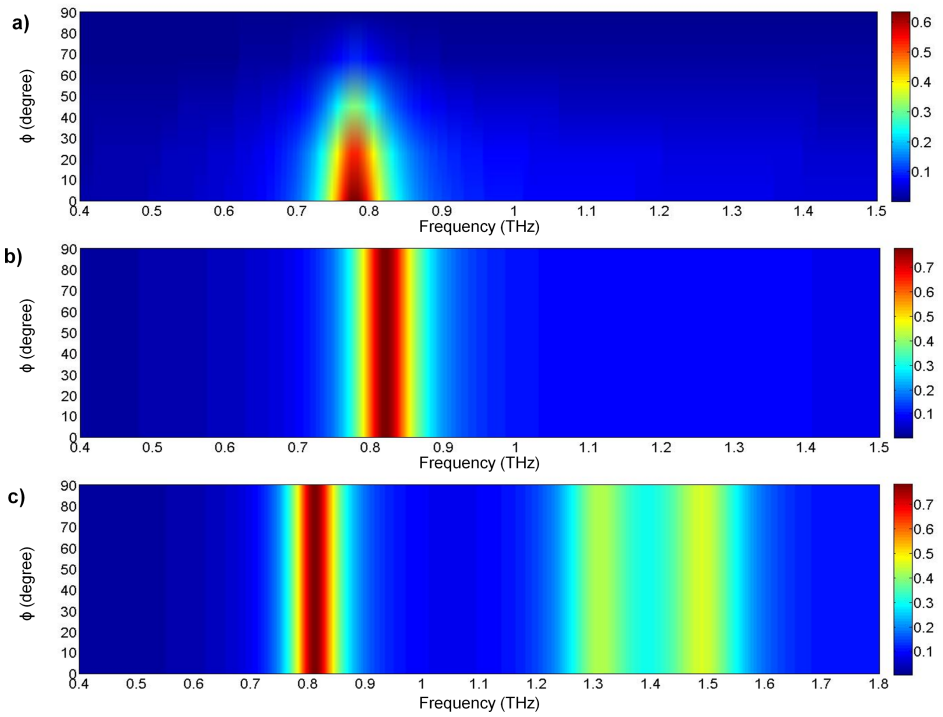


Figure 7: The simulation result of the absorbance difference for polarization angles from 0° to 90° of: a) Cut-wire sandwich structure, b) cross-shaped sandwich structure, and c) star-shaped sandwich structure.

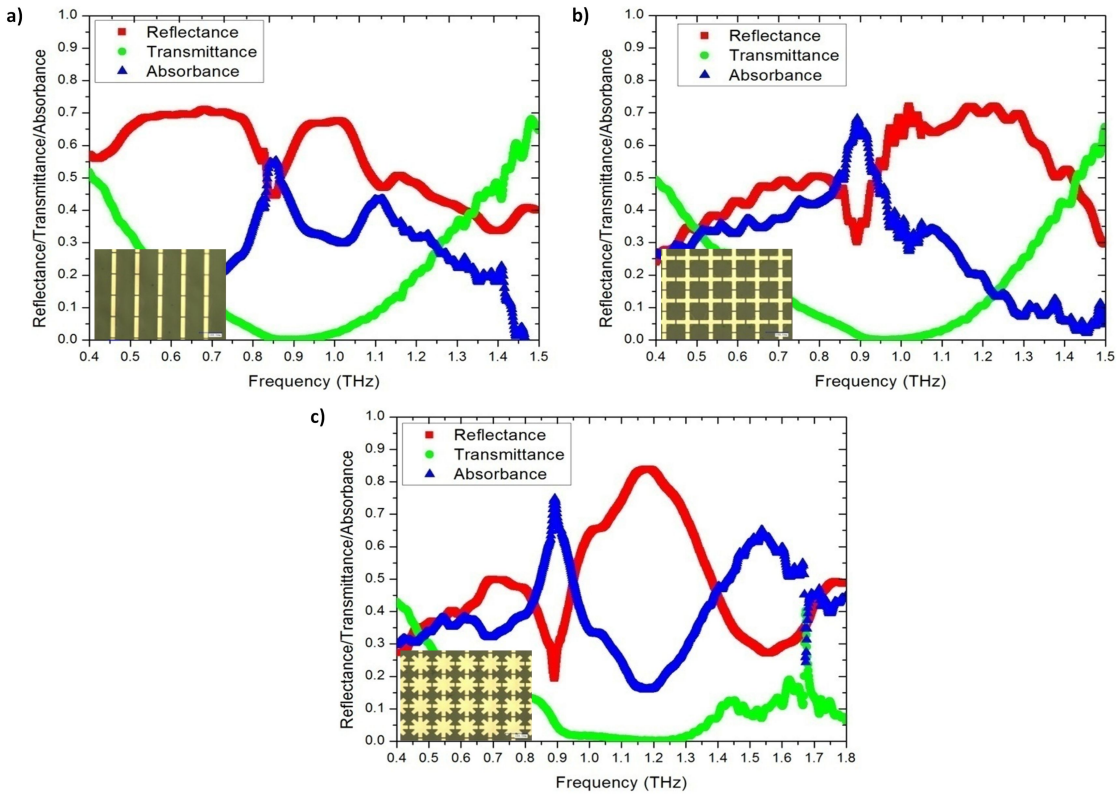


Figure 8: The measured results of reflectance, transmittance and absorbance under normal incidence: a) Cut-wire sandwich structure, b) cross-shaped sandwich structure, and c) star-shaped sandwich structure.

the absorbance of the cut-wire sandwich structure was zero when the external electric field was rotated by $\phi = 90°$. The EM wave was fully transmitted through the cut-wire sandwich structure when the external electric field is rotated by $\phi = 90°$ because polarization and magnetization were not generated. Meanwhile, the cross-shaped and star-shaped sandwich structures presented metamaterials with arbitrary polarization. The absorbance of these structures presented an identical performance when the external electric field was arbitrarily polarized.

A commercial terahertz time domain spectrometer (Zomega-Z3), whose available spectrum range was from 0.3 THz to 3.0 THz, was applied to characterize the transmission and reflection of the designed absorber. All measurements were conducted in a nitrogen environment (humidity less than 1%) at 25 °C. We first recorded the waveform reflected from an opaque gold film as reference for the reflection. For the transmission reference, we recorded the waveform transmitted without any sample. Figure 8a–c presents the measured RTA results of the cut-wire, cross-shaped and star-shaped sandwich structures, respectively. The measured absorbance reached the peak value of 55% at 0.85 THz for the cut-wire sandwich structure, 68% at 0.89 THz for the cross-shaped sandwich structure, and 75% at 0.89 THz for the star-shaped sandwich structure. The reduction of the measured resonance frequencies and the slightly reduced absorbance measurement results in all of the samples were due to fabrication inaccuracies. The corner of the metallic bar structure was slightly rounded (Figure 2) and the PI thickness were slightly different than anticipated. The EM properties of the samples were also altered due to inaccuracies in the fabrication process. Landy et al. reported similar phenomena [25]. The authors fabricated an absorber composed of a two-layer metamaterial. A cross-shaped structure and an electrically coupled ring resonator (ERR) were separated by a layer of benzocyclobutane (BCB) as a dielectric substrate. The sample was fabricated on a high-resistivity thick silicon substrate with

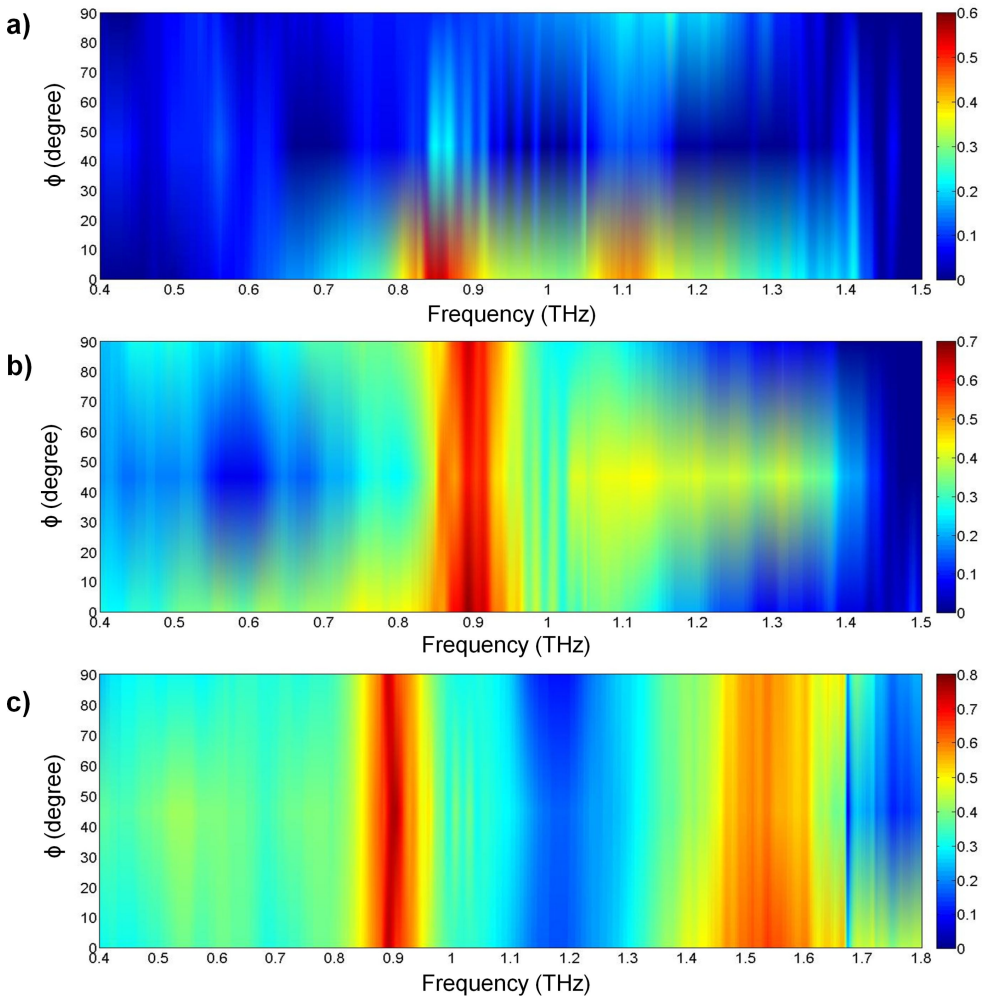


Figure 9: Measured absorbance results for polarization angles from 0° to 90° for: a) Cut-wire sandwich structure, b) cross-shaped sandwich structure, and c) star-shaped sandwich structure.

1 mm thickness. Their simulation results showed that a peak absorptivity of 95% at 1.13 THz was reached and the fabricated structure reached a measured absorptivity of 65% at 1.145 THz. Moreover, the authors found that the metallic bar in the fabrication structure was slightly rounded and the thickness of the BCB layer deviated from that predicted. Figure 9a–c presents the measured absorbance with different polarization directions for the cut-wire, cross-shaped and star-shaped sandwich structures, respectively. Figure 9 shows good agreement with the simulation results shown in Figure 7.

Conclusion

We theoretically and experimentally presented a thin terahertz metamaterial absorber that is based on the cut-wire sandwich structure. The gap between two unit cells and the anti-parallel surface current on the metallic bars yielded polarization and magnetization, respectively. The cut-wire sandwich structure was shown to be a metamaterial with sensitive polarization, whereas the cross-shaped and star-shaped sandwich structures were found to be metamaterials with arbitrary polarization. The star-shaped sandwich structure generated triple-peak absorbance in the simulation. However, the measured results showed a dual-peak absorbance spectrum. A high absorbance performance was obtained in the simulation. The slightly reduced measurement results were mainly due to inaccuracies in the fabrication process. Overall, the trend of the measured absorbance agreed well with the trend of the simulated absorbance.

Acknowledgements

This work was partially supported by the National Science Fund of China (Grant No. 61222505, 61435010) and we thank Dr. Xiaojian Fu for discussions about the terahertz TDS system.

ORCID® iDs

Hadi Teguh Yudistira - https://orcid.org/0000-0001-5189-4698

References

1. Fitzgerald, A. J.; Berry, E.; Zinovev, N. N.; Walker, G. C.; Smith, M. A.; Chamberlain, J. M. *Phys. Med. Biol.* **2002,** *47,* R67. doi:10.1088/0031-9155/47/7/201
2. Pickwell, E.; Wallace, V. P. *J. Phys. D: Appl. Phys.* **2006,** *39,* R301. doi:10.1088/0022-3727/39/17/R01
3. Taylor, Z. D.; Singh, R. S.; Bennett, D. B.; Tewari, P.; Kealey, C. P.; Bajwa, N.; Culjat, M. O.; Stojadinovic, A.; Lee, H.; Hubschman, J.-P.; Brown, E. R.; Grundfest, W. S. *IEEE Trans. Terahertz Sci. Technol.* **2011,** *1,* 201–219. doi:10.1109/TTHZ.2011.2159551
4. Federici, J. F.; Schulkin, B.; Huang, F.; Gary, D.; Barat, R.; Oliveira, F.; Zimdars, D. *Semicond. Sci. Technol.* **2005,** *20,* S266. doi:10.1088/0268-1242/20/7/018
5. Valentine, J.; Zhang, S.; Zentgraf, T.; Ulin-Avila, E.; Genov, D. A.; Bartal, G.; Zhang, X. *Nature* **2008,** *455,* 376–379. doi:10.1038/nature07247
6. Vignolini, S.; Yufa, N. A.; Cunha, P. S.; Guldin, S.; Rushkin, I.; Stefik, M.; Hur, K.; Wiesner, U.; Baumberg, J. J.; Steiner, U. *Adv. Mater.* **2012,** *24,* OP23–OP27. doi:10.1002/adma.201103610
7. Alù, A.; Engheta, N. *Phys. Rev. Lett.* **2009,** *103,* 143902. doi:10.1103/PhysRevLett.103.143902
8. Wang, K.; Zhao, J.; Cheng, Q.; Dong, D. S.; Cui, T. J. *Sci. Rep.* **2014,** *4,* 5935. doi:10.1038/srep05935
9. Cui, T. J.; Qi, M. Q.; Wan, X.; Zhao, J.; Cheng, Q. *Light: Sci. Appl.* **2014,** *3,* e218. doi:10.1038/lsa.2014.99
10. Jiang, W. X.; Qiu, C.-W.; Han, T.; Zhang, S.; Cui, T. J. *Adv. Funct. Mater.* **2013,** *23,* 4028–4034. doi:10.1002/adfm.201203806
11. Yen, T. J.; Padilla, W. J.; Fang, N.; Vier, D. C.; Smith, D. R.; Pendry, J. B.; Basov, D. N.; Zhang, X. *Science* **2004,** *303,* 1494–1496. doi:10.1126/science.1094025
12. Yudistira, H. T.; Tenggara, A. P.; Nguyen, V. D.; Kim, T. T.; Prasetyo, F. D.; Choi, C.-g.; Choi, M.; Byun, D. *Appl. Phys. Lett.* **2013,** *103,* 211106. doi:10.1063/1.4832197
13. Yudistira, H. T.; Tenggara, A. P.; Oh, S. S.; Nguyen, V.; Choi, M.; Choi, C.-g.; Byun, D. *J. Micromech. Microeng.* **2015,** *25,* 045006. doi:10.1088/0960-1317/25/4/045006
14. Iwaszczuk, K.; Strikwerda, A. C.; Fan, K.; Zhang, X.; Averitt, R. D.; Jepsen, P. U. *Opt. Express* **2012,** *20,* 635–643. doi:10.1364/OE.20.000635
15. Tao, H.; Kadlec, E. A.; Strikwerda, A. C.; Fan, K.; Padilla, W. J.; Averitt, R. D.; Shaner, E. A.; Zhang, X. *Opt. Express* **2011,** *19,* 21620–21626. doi:10.1364/OE.19.021620
16. Li, H.; Yuan, L. H.; Zhou, B.; Shen, X. P.; Cheng, Q.; Cui, T. J. *J. Appl. Phys.* **2011,** *110,* 014909. doi:10.1063/1.3608246
17. Wakatsuchi, H.; Greedy, S.; Christopoulos, C.; Paul, J. *Opt. Express* **2010,** *18,* 22187–22198. doi:10.1364/OE.18.022187
18. Park, J. W.; Van Tuong, P.; Rhee, J. Y.; Kim, K. W.; Jang, W. H.; Choi, E. H.; Chen, L. Y.; Lee, Y. *Opt. Express* **2013,** *21,* 9691–9702. doi:10.1364/OE.21.009691
19. Chen, H.-T. *Opt. Express* **2012,** *20,* 7165–7172. doi:10.1364/OE.20.007165
20. Shen, X.; Yang, Y.; Zang, Y.; Gu, J.; Han, J.; Zhang, W.; Cui, T. J. *Appl. Phys. Lett.* **2012,** *101,* 154102. doi:10.1063/1.4757879
21. Shi, C.; Zang, X.; Wang, Y.; Chen, L.; Cai, B.; Zhu, Y. *Appl. Phys. Lett.* **2014,** *105,* 031104. doi:10.1063/1.4890617
22. Peng, Y.; Zang, X.; Zhu, Y.; Shi, C.; Chen, L.; Cai, B.; Zhuang, S. *Opt. Express* **2015,** *23,* 2032–2039. doi:10.1364/OE.23.002032
23. Liu, S.; Chen, H.; Cui, T. J. *Appl. Phys. Lett.* **2015,** *106,* 151601. doi:10.1063/1.4918289
24. Landy, N. I.; Sajuyigbe, S.; Mock, J. J.; Smith, D. R.; Padilla, W. J. *Phys. Rev. Lett.* **2008,** *100,* 207402. doi:10.1103/PhysRevLett.100.207402
25. Landy, N. I.; Bingham, C. M.; Tyler, T.; Jokerst, N.; Smith, D. R.; Padilla, W. J. *Phys. Rev. B* **2009,** *79,* 125104. doi:10.1103/PhysRevB.79.125104
26. Powell, D. A.; Lapine, M.; Gorkunov, M. V.; Shadrivov, I. V.; Kivshar, Y. S. *Phys. Rev. B* **2010,** *82,* 155128. doi:10.1103/PhysRevB.82.155128
27. Burokur, S. N.; Sellier, A.; Kanté, B.; de Lustrac, A. *Appl. Phys. Lett.* **2009,** *94,* 201111. doi:10.1063/1.3141729
28. Liu, L.; Chen, W.-c.; Powell, D. A.; Padilla, W. J.; Karouta, F.; Hattori, H. T.; Neshev, D. N.; Shadrivov, I. V. *Appl. Phys. Lett.* **2014,** *105,* 151102. doi:10.1063/1.4897949
29. Liu, X.; Starr, T.; Starr, A. F.; Padilla, W. J. *Phys. Rev. Lett.* **2010,** *104,* 207403. doi:10.1103/PhysRevLett.104.207403

30. Dincer, F.; Karaaslan, M.; Unal, E.; Sabah, C. *Prog. Electromagn. Res.* **2013,** *141,* 219–231. doi:10.2528/PIER13061105
31. Lam, V. D.; Kim, J. B.; Tung, N. T.; Lee, S. J.; Lee, Y. P.; Rhee, J. Y. *Opt. Express* **2008,** *16,* 5934–5941. doi:10.1364/OE.16.005934
32. Sellier, A.; Burokur, S. N.; Kanté, B.; de Lustrac, A. *Opt. Express* **2009,** *17,* 6301–6310. doi:10.1364/OE.17.006301
33. Pendry, J. B. *Phys. Rev. Lett.* **2000,** *85,* 3966–3969. doi:10.1103/PhysRevLett.85.3966
34. Chen, Z. C.; Hong, M. H.; Dong, H.; Gong, Y. D.; Lim, C. S.; Shi, L. P.; Chong, T. C. *Appl. Phys. A* **2010,** *101,* 33–36. doi:10.1007/s00339-010-5755-4
35. Chen, Z. C.; Hong, M. H.; Lim, C. S.; Han, N. R.; Shi, L. P.; Chong, T. C. *Appl. Phys. Lett.* **2010,** *96,* 181101. doi:10.1063/1.3424793
36. Smith, D. R.; Vier, D. C.; Koschny, T.; Soukoulis, C. M. *Phys. Rev. E* **2005,** *71,* 036617. doi:10.1103/PhysRevE.71.036617
37. Walther, M.; Cooke, D. G.; Sherstan, C.; Hajar, M.; Freeman, M. R.; Hegmann, F. A. *Phys. Rev. B* **2007,** *76,* 125408. doi:10.1103/PhysRevB.76.125408
38. Cai, W.; Shalaev, V. Optical Properties of Metal-Dielectric Composites. *Optical Metamaterials;* Springer: New York, NY, U.S.A., 2009. doi:10.1007/978-1-4419-1151-3_2
39. Wu, B.-I.; Wang, W.; Pacheco, J.; Chen, X.; Grzegorczyk, T. M.; Kong, J. A. *Prog. Electromagn. Res.* **2005,** *51,* 295–328. doi:10.2528/PIER04070701
40. Chen, X.; Grzegorczyk, T. M.; Wu, B.-I.; Pacheco, J., Jr.; Kong, J. A. *Phys. Rev. E* **2004,** *70,* 016608. doi:10.1103/PhysRevE.70.016608

License and Terms

This is an Open Access article under the terms of the Creative Commons Attribution License (http://creativecommons.org/licenses/by/4.0), which permits unrestricted use, distribution, and reproduction in any medium, provided the original work is properly cited.

The license is subject to the *Beilstein Journal of Nanotechnology* terms and conditions: (https://www.beilstein-journals.org/bjnano)

The definitive version of this article is the electronic one which can be found at: doi:10.3762/bjnano.9.136

BEILSTEIN JOURNAL OF NANOTECHNOLOGY

Excitation of nonradiating magnetic anapole states with azimuthally polarized vector beams

Aristeidis G. Lamprianidis*[1,2] and Andrey E. Miroshnichenko[3]

Full Research Paper

Open Access

Address:
[1]Nonlinear Physics Centre, The Australian National University, Canberra, ACT 2601, Australia, [2]Department of Mathematics and Applied Mathematics, University of Crete, 70013 Heraklion, Crete, Greece and [3]School of Engineering and Information Technology, University of New South Wales, Canberra, ACT 2600, Australia

Email:
Aristeidis G. Lamprianidis* - aris.lamprianidis@anu.edu.au

* Corresponding author

Keywords:
anapole excitation; dielectric nano-optics; multipolar expansion; T-matrix method; vector beams

Beilstein J. Nanotechnol. **2018,** *9,* 1478–1490.
doi:10.3762/bjnano.9.139

Received: 15 November 2017
Accepted: 13 April 2018
Published: 17 May 2018

This article is part of the Thematic Series "Light–Matter interactions on the nanoscale".

Guest Editor: M. Rahmani

© 2018 Lamprianidis and Miroshnichenko; licensee Beilstein-Institut.
License and terms: see end of document.

Abstract

Nonradiating current configurations have been drawing the attention of the physics community for many years. It has been demonstrated recently that dielectric nanoparticles provide a unique platform to host such nonradiating modes, called “anapoles”. Here we study theoretically the excitation of such exotic anapole modes in silicon nanoparticles using structured light. Alternative illumination configurations, properly designed, are able to unlock hidden behavior of scatterers. Particularly, azimuthally polarized focused beams enable us to excite ideal anapole modes of magnetic type in dielectric nanoparticles. Firstly, we perform the decomposition of this type of excitation into its multipolar content and then we employ the T-matrix method to calculate the far-field scattering properties of nanoparticles illuminated by such beams. We propose several configuration schemes where magnetic anapole modes of simple or hybrid nature can be detected in silicon nanospheres, nanodisks and nanopillars.

Introduction

The triumph of Maxwell’s equations is associated with the unification of electric and magnetic phenomena on the same footing, which has led to the prediction of existence of an electromagnetic radiation, which can carry energy and momentum. As it is explained in all classical textbooks [1], any accelerated motion of a charged particle should result in the excitation of electromagnetic waves propagating away from the source, leading to radiative decay. Despite the success at the macroscopic scale, it fails when one tries to apply it at the microscopic level and attempts to explain the stability of an atom, where the electrons are confined and in constant motion, so they are inevitably accelerated. In quantum mechanics it was postulated that electrons live at certain orbits, which do not radiate. And this postulate was taken for granted, since it does not contradict any experimental observation at the microscale. But still, there were numerous attempts to find confined classical trajectories of charged particles that do not produce far-field radiation, and many interesting examples are known by now

[2-6]. The key ingredient in their explanation is destructive interference in the far-field.

Despite the purely fundamental aspect of them, nonradiating sources have attracted a great deal of attention in various nanoscale structures. Recently, it was suggested that silicon nanodisks can support a nonradiating excitation known as anapole [7], literary meaning "without poles", in which the electric dipole radiation vanishes completely. It was demonstrated that such states can be explained by the co-existence of electric and toroidal dipole moments, simultaneously excited inside dielectric nanoparticles. Despite their different near-field configurations both dipole moments emit with the same radiation pattern allowing for the complete destructive interference in the far-field. Toroidal dipole moments became extremely popular in the metamaterial community [8,9], which focused on designing optimal structures for their strong excitation. It turns out that the superposition of comparable toroidal and electric dipoles might result in nonradiating anapole excitation [10-14]. It has a number of interesting features and can be used to design near-field laser [15], to obtain high-efficiency harmonic generation [16], to achieve pure magnetic dipole scattering without admixture of other components under plane-wave illumination [17] as well as for a variety of other promising applications [18,19].

One may wonder now: Can nanostructures be a platform of hosting such nonradiating current configurations? The answer is yes. Actually, particular designs have been proposed and fabricated that experimentally verified the excitation of anapole states either in microwaves [20,21] or at optical frequencies [7,22]. One convenient way of approach is to analyze the scattered field into a superposition of vector spherical harmonics (VSHs). Due to their completeness and orthogonality any radiation profile can be uniquely decomposed in a series of such partial waves. It turns out, that high-index dielectric particles can exhibit infinite number of conditions where the scattering contribution of any such partial wave vanishes. As was mentioned above, the first zero of the electric dipole scattering, for example, can be explained in terms of destructive interference of Cartesian electric and toroidal dipoles. But for higher-order zeros additional terms are required and currently there is an effort to identify them all [23]. As highlighted in [24], according to the reciprocity theorem, a nonradiating anapole current configuration implies a poloidal current distribution that is orthogonal, in an integral manner, to the incident E-field distribution inside the volume of the particle. Moreover, it has also been proved that a nonradiating current configuration will bear no spatial frequencies that are able to be coupled with free space radiation [25]. In that sense, a multipolar anapole condition corresponds to a current configuration that has a spatial frequency spectrum on the spherical cell of radius k_0, that is orthogonal to the far field radiation of that particular multipolar partial wave. Recently, the excitation of anapole states in pure dielectric nanoparticles was studied under the prism of a Weierstrass-type product expansion in terms of the resonant-state frequencies that correspond to zeros of the elements of the S-matrix of the particle in the complex frequency plane [26]. Moreover, excitation of anapole states has also been examined under a projection scheme on Fano–Feshbach resonances [27]. For our purposes, we associate any zeros of the partial scattered power of spherical harmonics with the potential of nonradiating anapole excitation.

Importantly, high-index dielectric nanoparticles, in addition to multipolar modes of electric type, also support magnetic ones. In analogy with anapole excitations of electric type, one might also expect the existence of magnetic anapoles, associated with the vanishing scattering contribution of the magnetic dipole term. It now raises the question of how such conditions can be experimentally observed. The problem is that under plane-wave illumination such vanishing partial wave scattering will usually be overshadowed by stronger contributions of other modes. The answer to this question was recently suggested by a number of groups and incorporates the use of so-called structured-light excitations. Lately, vector beams generally attracted lots of scientific attention since they can have various interesting applications [28-31]. With such illumination schemes we are able to shape the multipolar content of the incident field. For example, by using a radially polarized focused beam, only spherical harmonics of electric type will be present at the focal point of the beam, without any magnetic. It was suggested that such a type of illumination offers an ideal condition for the electric anapole excitation, which can be tested experimentally [24,32]. It turns out, that if we change the polarization from radial to azimuthal, then, only magnetic harmonics will be present. Thus, using such an illumination scheme will be ideal to test the possibility of the magnetic anapole excitation. An excited magnetic anapole is expected to have useful applications in biosensing, i.e., in the detection of molecules that interact strongly once exposed to magnetic field hotspots, which nanoparticles in a magnetic anapole state can offer in their near field. Moreover, the signal-to-noise ratio of an MRI machine, that is defined as the ratio of the local magnetic to electric field intensity, could be significantly improved by employing these nano-optical properties that a magnetic anapole can offer.

In this paper we discuss in detail the possibility of magnetic anapole excitation under various configurations and suggest how they can be tested experimentally. We begin with a general multipolar analysis in vector spherical harmonics of arbitrary focused beams. We generalize the results of [33,34] for arbi-

trary focused beams under 2π- or 4π-illumination schemes and for arbitrarily translated frames of reference compared to the coordinate system of the beam. Next, we describe the T-matrix method that we use to treat the scattering process of nanoparticles under arbitrary illumination schemes and we highlight important properties of the T-matrix under several symmetry conditions. We also discuss the implications that an anapole excitation condition would have on the coupling of the external field with the natural modes of the nanoparticle under the prism of the singular value decomposition of its T-matrix. Last, we present our results on the excitation of magnetic anapole states under various illumination schemes and various geometries of hosting nanoparticles.

Multipolar Decomposition of Focused Beams

Physicists have been lately concerned with the multipolar decomposition of various types of structured light, in order to study its interaction with particles [33-37]. Here, we consider a focused beam propagating along $+\hat{z}$, with xOy being its focal plane. An arbitrary paraxial beam, with sufficiently large waist in order to neglect its longitudial z-component, can be considered as a superposition of one radially ($\hat{\rho}$) and one azimuthally ($\hat{\phi}$) polarized beam with different complex transverse profiles for each one of this parts. According to [38], such a beam, after being focused by a lens, has an electric field intensity that is given near its focal point, with respect to the O($\mathbf{r}$) coordinate system, by the following formula:

$$\mathbf{E}_{\text{inc}}(\mathbf{r}) = \mathrm{A}_0 \sum_{\mathrm{p}=(\hat{\rho},\hat{\phi})} \int_0^{2\pi}\int_0^{\delta_0} \sqrt{\cos\delta}\, \mathrm{I}_{\mathrm{p}}(\gamma,\delta)\hat{\mathrm{e}}_{\mathrm{p}}(\gamma,\delta) e^{\mathrm{j}k_0\hat{\mathrm{i}}(\gamma,\delta)\cdot\mathbf{r}} \sin\delta\,\mathrm{d}\delta\,\mathrm{d}\gamma, \quad (1)$$

where $\mathrm{A}_0 = -\mathrm{j}\mathcal{F}/\lambda_0$ is a constant, with $\mathcal{F}$ being the focal length of the objective and λ_0 the free-space wavelength. k_0 is the correspondent wavevector. δ_0 is the angle of the marginal ray that passes through the entrance pupil of the objective, which has a numerical aperture of NA. So, $\delta_0 = \sin^{-1}(\mathrm{NA})$. The term $\sqrt{\cos\delta}$ derives from the conservation of the energy flux of each ray that is refracted through the Gaussian reference sphere of the objective. The indicator p stands either for the radial ($\hat{\rho}$) or the azimuthal ($\hat{\phi}$) part of the input beam. The field at the focal plane of the objective is a kind of 2D inverse Fourier transform of the input to the lens field. So, in that sense, it is expressed as a superposition of plane waves propagating in angles γ,δ, with γ being the azimuthal and δ the polar angle of the direction of the propagation vector of each plane wave. Each pixel of the input to the objective field with cylindrical coordinates $(\rho_0,\phi_0,-\mathcal{F})$ gives birth to a plane wave that propagates along the direction

$$\hat{\mathrm{i}}(\gamma,\delta) = \hat{\mathrm{i}}\left(\pi+\phi_0, \tan^{-1}\left[\rho_0/\mathcal{F}\right]\right) = \hat{x}\sin\delta\cos\gamma + \hat{y}\sin\delta\sin\gamma + \hat{z}\cos\delta.$$

The radial part of the E-field of such a pixel gives birth to a plane wave in the image space that is polarized along

$$\hat{\mathrm{e}}_{\hat{\rho}}(\gamma,\delta) = \hat{\theta}(\gamma,\delta) = (\hat{x}\cos\gamma + \hat{y}\sin\gamma)\cos\delta - \hat{z}\sin\delta,$$

whereas the azimuthal part of the E-field of such a pixel gives birth to a plane wave polarized along

$$\hat{\mathrm{e}}_{\hat{\phi}}(\gamma,\delta) = \hat{\phi}(\gamma,\delta) = -\hat{x}\sin\gamma + \hat{y}\cos\gamma.$$

$\mathrm{I}_{\hat{\rho}}, \mathrm{I}_{\hat{\phi}}$ are the correspondent complex transverse profiles of the input beam that impinges on the objective.

Next, we decompose the E-field of such a focused beam into an expansion of vector spherical harmonics with respect to a coordinate system $\mathrm{O}_1(\mathbf{r}_1)$, the natural frame of the scatterer, that is translated and parallel to the coordinate system O($\mathbf{r}$) of the focused beam. The position vector of its center O_1, in spherical coordinates, with respect to the coordinate system of the focused beam, is given by the vector $\mathbf{d}(\mathrm{R},\Theta,\Phi) = \mathbf{r} - \mathbf{r}_1$.

$$\mathbf{E}_{\text{inc}}(\mathbf{r}_1) = \sum_{\nu\mu,\alpha} \mathcal{A}_{\alpha,\mu\nu}(\mathbf{d})\mathbf{F}^{(1)}_{\alpha,\mu\nu}(k_0\mathbf{r}_1), \quad (2)$$

where $\mathbf{F}^{(\iota)}_{\alpha,\mu\nu}$ are the VSHs. The indicator α acquires the names M,N for the TE (magnetic) and TM (electric) VSHs respectively, the index ν stands for the angular momentum quantum number, which takes the values 1, 2, … and corresponds to dipoles, quadrupoles, etc. The index μ stands for the azimuthal quantum number, which takes the values −ν, …, −2, −1, 0, 1, 2, …, ν. The exponent (ι) refers to the correspondent Bessel (ι = 1, 2) and Hankel (ι = 3, 4) functions of first and second kind, respectively. For the incident field, being a standing wave, we make use of the Bessel functions. The VSHs are given by the formulas below [39]:

$$\mathbf{F}^{(\iota)}_{\mathrm{M},\mu\nu}(k_0\mathbf{r}) = \mathrm{j}z^{(\iota)}_{\mathrm{M},\nu}(k_0 r)\mathbf{f}_{\mathrm{M},\mu\nu}(\hat{\mathrm{r}}), \quad (3)$$

$$\mathbf{F}^{(\iota)}_{\mathrm{N},\mu\nu}(k_0\mathbf{r}) = \hat{\mathrm{r}}\frac{\nu(\nu+1)}{k_0 r} z^{(\iota)}_{\mathrm{M},\nu}(k_0 r)\gamma_{\mu\nu}P^{\mu}_{\nu}(\cos\theta)e^{\mathrm{j}\mu\phi} + z^{(\iota)}_{\mathrm{N},\nu}(k_0 r)\mathbf{f}_{\mathrm{N},\mu\nu}(\hat{\mathrm{r}}), \quad (4)$$

where

$$\mathbf{f}_{\mathrm{M},\mu\nu}\left(\hat{\mathrm{r}}\right)=\gamma_{\mu\nu}\left[\hat{\theta}\tau_{\mu\nu}^{(1)}\left(\theta\right)+\mathrm{j}\hat{\phi}\tau_{\mu\nu}^{(2)}\left(\theta\right)\right]e^{\mathrm{j}\mu\phi}, \tag{5}$$

$$\mathbf{f}_{\mathrm{N},\mu\nu}\left(\hat{\mathrm{r}}\right)=\gamma_{\mu\nu}\left[\hat{\theta}\tau_{\mu\nu}^{(2)}\left(\theta\right)+\mathrm{j}\hat{\phi}\tau_{\mu\nu}^{(1)}\left(\theta\right)\right]e^{\mathrm{j}\mu\phi}, \tag{6}$$

and $z_{\mathrm{M},\nu}^{(\iota)}(\mathrm{k}_0\mathrm{r})$ is a spherical Bessel ($\iota = 1$) or Hankel ($\iota = 3$) function of the first kind and

$$z_{\mathrm{N},\nu}^{(\iota)}\left(\mathrm{k}_0\mathrm{r}\right)=\frac{1}{\mathrm{k}_0\mathrm{r}}\frac{\mathrm{d}}{\mathrm{d}\left(\mathrm{k}_0\mathrm{r}\right)}\left[\mathrm{k}_0\mathrm{r}\,z_{\mathrm{M},\nu}^{(\iota)}\left(\mathrm{k}_0\mathrm{r}\right)\right]$$

is the corresponding Riccati function. $P_\nu^\mu(\cos\theta)$ is the associated Legendre function of the 1st kind, with

$$\tau_{\mu\nu}^{(1)}\left(\theta\right)=\mu\frac{P_\nu^\mu\left(\cos\theta\right)}{\sin\theta},\ \tau_{\mu\nu}^{(2)}\left(\theta\right)=\frac{\mathrm{d}P_\nu^\mu\left(\cos\theta\right)}{\mathrm{d}\theta}$$

being the generalized Legendre functions.

$$\gamma_{\mu\nu}=\sqrt{\frac{(2\nu+1)(\nu-\mu)!}{4\pi\nu(\nu+1)(\nu+\mu)!}}$$

is a normalization factor for the Legendre functions and plays an important role for the numerical calculation of the elements of the T-matrix that will follow later.

$\mathcal{A}_{\alpha,\mu\nu}(\mathbf{d})$ are the correspondent spherical amplitudes of the multipolar expansion of the incident field with respect to the coordinate system $\mathrm{O}_1(\mathbf{r}_1)$. In order to calculate them we make use of the above plane wave spectrum representation of such an excitation field. In our case they are straightforwardly given by the formula:

$$\begin{aligned}\mathcal{A}_{\alpha,\mu\nu}\left(\mathbf{d}\right)=\mathrm{A}_0\sum_{\mathrm{p}=(\hat{\rho},\hat{\phi})}\int_0^{2\pi}\int_0^{\delta_0}\sqrt{\cos\delta}\,\mathrm{I}_\mathrm{p}\left(\gamma,\delta\right)e^{\mathrm{j}\mathrm{k}_0\hat{\mathrm{i}}(\gamma,\delta)\cdot\mathbf{d}}\\ \times\dot{\mathcal{A}}_{\alpha,\mu\nu}\left(\hat{\mathrm{i}},\hat{\mathrm{e}}_\mathrm{p}\right)\sin\delta\,\mathrm{d}\delta\,\mathrm{d}\gamma,\end{aligned} \tag{7}$$

where we substituted

$$\hat{\mathrm{e}}_\mathrm{p}\left(\gamma,\delta\right)e^{\mathrm{j}\mathrm{k}_\mathrm{o}\hat{\mathrm{i}}(\gamma,\delta)\cdot\mathbf{r}_1}=\sum_{\nu\mu,\alpha}\dot{\mathcal{A}}_{\alpha,\mu\nu}\left(\hat{\mathrm{i}},\hat{\mathrm{e}}_\mathrm{p}\right)\mathbf{F}_{\alpha,\mu\nu}^{(1)}\left(\mathrm{k}_0\mathbf{r}_1\right). \tag{8}$$

It is proven (see Supporting Information File 1) that the spherical amplitudes of the multipolar expansion of each component of the plane wave spectrum of the incident field, denoted as $\dot{\mathcal{A}}_{\alpha,\mu\nu}(\hat{\mathrm{i}},\hat{\mathrm{e}}_\mathrm{p})$, are given by the formula below:

$$\dot{\mathcal{A}}_{\alpha,\mu\nu}\left(\hat{\mathrm{i}},\hat{\mathrm{e}}_\mathrm{p}\right)=4\pi\mathrm{j}^{-\nu+\delta_{\mathrm{p}\hat{\rho}}}\gamma_{-\mu\nu}\tau_{-\mu\nu}^{(2-\Delta)}\left(\pi-\delta\right)e^{-\mathrm{j}\mu\gamma}, \tag{9}$$

where $\Delta=\delta_{\alpha\mathrm{N}}\delta_{\mathrm{p}\hat{\phi}}+\delta_{\alpha\mathrm{M}}\delta_{\mathrm{p}\hat{\rho}}$ and $\delta_{\alpha\beta}$ is the Kronecker delta, which yields 1 for $\alpha=\beta$, or 0 for $\alpha\neq\beta$.

By integrating the flux of the Poynting vector of the incident field over an infinite plane, oriented transverse to the optical axis, we can calculate the total power that such a focused beam carries. It is given by the formula below:

$$\begin{aligned}P_\mathrm{inc}&=\frac{1}{2}\int_{-\infty}^{\infty}\int_{-\infty}^{\infty}\Re\left\{\mathbf{E}_\mathrm{inc}\times\mathbf{H}_\mathrm{inc}^*\right\}_{z=0}\cdot\hat{z}\,\mathrm{d}x\,\mathrm{d}y\\&=\frac{\mathcal{F}^2}{4Z_0}\sum_{\mathrm{p}=(\hat{\rho},\hat{\phi})}\int_0^{2\pi}\int_0^{\delta_0}\left|\mathrm{I}_\mathrm{p}\left(\gamma,\delta\right)\right|^2\sin2\delta\,\mathrm{d}\delta\,\mathrm{d}\gamma,\end{aligned} \tag{10}$$

where Z_0 is the wave impedance of free space.

At this point, we would also like to consider the case of two counterpropagating focused beams that constitute a standing wave excitation. For simplicity, without loss of generality, we consider that both beams are focused by the same optical system. The newly introduced beam travels towards the $-\hat{z}$ direction and is described by the coordinate system $\mathrm{O}'(\mathrm{r}',\theta',\phi')=\mathrm{O}(\mathrm{r},\pi-\theta,-\phi)$. By applying the same rotation transformation to the natural frame of the scatterer and making use of properties of the Legendre functions, we have

$$\mathbf{F}_{\alpha,\mu\nu}^{(1)}\left(\mathrm{k}_0\mathbf{r}_1'\right)=(-1)^\nu\,\mathbf{F}_{\alpha,-\mu\nu}^{(1)}\left(\mathrm{k}_0\mathbf{r}_1\right),$$

where, again, the rotated system attached to the natural frame of the scatterer is denoted with a prime. We end up with the following expression for the spherical amplitudes $\mathcal{A}_{\alpha,\mu\nu}^{(\pm)}$ that correspond to the multipolar decomposition of the superimposed counterpropagating beams around the natural frame of the scatterer $\mathrm{O}_1(\mathbf{r}_1)$:

$$\begin{aligned}\mathcal{A}_{\alpha,\mu\nu}^{(\pm)}\left(\mathbf{d}\right)=\mathrm{A}_0\sum_{\mathrm{p},s}\int_0^{2\pi}\int_0^{\delta_0}\sqrt{\cos\delta}\,\mathrm{I}_\mathrm{p}^{(s)}\left(\gamma,\delta\right)e^{\mathrm{j}\mathrm{k}_0\hat{\mathrm{i}}(\gamma,\delta)\cdot\mathbf{d}^{(s)}}\\ \times\dot{\mathcal{A}}_{\alpha,\mu\nu}^{(s)}\left(\hat{\mathrm{i}},\hat{\mathrm{e}}_\mathrm{p}\right)\sin\delta\,\mathrm{d}\delta\,\mathrm{d}\gamma,\end{aligned} \tag{11}$$

where

$$\dot{\mathcal{A}}^{(s)}_{\alpha,\mu\nu}\left(\hat{\mathrm{i}},\hat{\mathrm{e}}_{\mathrm{p}}\right)=4\pi \mathrm{j}^{-\nu+\delta_{\mathrm{p}\hat{\rho}}}\gamma_{-\mu\nu}\tau^{(2-\Delta)}_{-\mu\nu}(\pi-\delta)\times e^{\mathrm{j}\mu\gamma(-1)^{\delta_{s+}}}(-1)^{(\nu+\mu+\Delta)\delta_{s-}}. \tag{12}$$

The indicator s stands for the propagating direction of the two beams and takes the values + and − for the beam that propagates along the $+\hat{z}$ and $-\hat{z}$ direction, respectively. The complex transverse profile of the first beam with respect to the O(**r**) coordinate system is denoted as

$$\mathrm{I}^{(+)}_{\mathrm{p}}(\gamma,\delta)=\mathrm{I}^{(+)}_{\mathrm{p}}\left(\pi+\phi_0,\tan^{-1}\left[\rho_0/\mathcal{F}\right]\right)$$

and the complex transverse profile of the second beam with respect to the O′(**r**′) coordinate system is denoted as

$$\mathrm{I}^{(-)}_{\mathrm{p}}(\gamma,\delta)=\mathrm{I}^{(-)}_{\mathrm{p}}\left(\pi+\phi'_0,\tan^{-1}\left[\rho'_0/\mathcal{F}\right]\right).$$

Moreover, the spherical coordinates of the position vector with respect to the O(**r**) coordinate system for the two cases are $\mathbf{d}^{(+)}$ = (R, Θ, Φ) and $\mathbf{d}^{(-)}$ = (R, π − Θ, −Φ), respectively.

To access some of the properties of the above multipole expansion of the excitation field, we further simplify the formula by expanding the complex transverse profiles of the beams into Fourier series with respect to the azimuthal angle γ. So, due to its 2π-periodicity, we have: $\mathrm{I}^{(s)}_{\mathrm{p}}(\gamma,\delta)=\sum_m \mathrm{I}^{(s)}_{\mathrm{p},m}(\delta)e^{\mathrm{j}m\gamma}$, which is an expansion into modes with different orbital angular momentum m. Then, we can also perform the integration over the azimuthal angle analytically. This yields the simplified formula of Equation 13 where $J_\nu(x)$ is the cylindrical Bessel function of first kind.

We can observe that in the case of sinΘ = 0, which means that the natural frame of the scatterer is located along the optical axis of the two beams, the argument of the Bessel function becomes zero, and therefore we end up with the condition $\mu = m(-1)^{\delta_{s-}}$. This implies that the orbital angular momentum m of the input beams before their focusing is bequeathed to the azimuthal quantum number of the multipolar expansion of the focused beams with respect to such a reference frame. This would mean, for example, that a focused beam with m = 3 would bear only multipoles of orders higher than ν = 2. It would lack a dipolar and quadrupolar content.

We conclude this section by considering the particular case of rotationally symmetric ($\mathrm{I}^{(s)}_{\mathrm{p},m}$ = 0 for $m \neq 0$) focused beams with the natural frame of the scatterer being along the optical axis (sinΘ = 0). The spherical amplitudes of the field that corresponds to such a case are given by Equation 14.

In Equation 14 we want to place emphasis on the following observations:

(1) The radial part of the beams bears a multipolar content of purely electric type, whereas the azimuthal part bears a multipolar content of purely magnetic type.

(2) Due to the mirror symmetry with respect to the focal plane, if the two counterpropagating beams have the same complex transverse profile, $\mathrm{I}^{(-)}_{\mathrm{p},0}(\delta)=\mathrm{I}^{(+)}_{\mathrm{p},0}(\delta)$, then, for a natural frame of the scatterer placed at their common focal point (R = 0), the excitation field has a multipolar content of purely even order ν. In contrast, if the two counterpropagating beams are out of phase, $\mathrm{I}^{(-)}_{\mathrm{p},0}(\delta)=-\mathrm{I}^{(+)}_{\mathrm{p},0}(\delta)$, then the excitation field has a multipolar content of purely odd order ν, for a natural frame of the scatterer placed at the focal point (R = 0).

$$\mathcal{A}^{(\pm)}_{\alpha,\mu\nu}(\mathbf{d})=8\pi^2 A_0 \mathrm{j}^{-\nu-\mu}e^{-\mathrm{j}\mu\Phi}\gamma_{-\mu\nu}\sum_{\mathrm{p},s}\mathrm{j}^{\delta_{\mathrm{p}\hat{\rho}}}(-1)^{(\nu+\Delta)\delta_{s-}}\times\int_0^{\delta_0}\left[\sum_m \mathrm{j}^m e^{\mathrm{j}m\Phi(-1)^{\delta_{s-}}}J_{m-\mu(-1)^{\delta_{s-}}}\left(\mathrm{k}_0\mathrm{R}\sin\delta\sin\Theta\right)\mathrm{I}^{(s)}_{\mathrm{p},m}(\delta)\right]\times\sqrt{\cos\delta}\,e^{\mathrm{j}\mathrm{k}_0\mathrm{R}\cos\delta\cos\Theta(-1)^{\delta_{s-}}}\tau^{(2-\Delta)}_{-\mu\nu}(\pi-\delta)\sin\delta\,\mathrm{d}\delta, \tag{13}$$

$$\left\{\mathcal{A}^{(\pm)}_{\alpha,\mu\nu}(\mathbf{d})\right\}^{m=0}_{\sin\Theta=0}=-\delta_{\mu 0}8\pi^2 A_0 \mathrm{j}^{\nu}\gamma_{0\nu}\sum_{\mathrm{p},s}\left(\delta_{\alpha\mathrm{N}}\delta_{\mathrm{p}\hat{\rho}}+\delta_{\alpha\mathrm{M}}\delta_{\mathrm{p}\hat{\phi}}\right)\mathrm{j}^{\delta_{\mathrm{p}\hat{\rho}}}(-1)^{\nu\delta_{s-}}\times\int_0^{\delta_0}\mathrm{I}^{(s)}_{\mathrm{p},0}(\delta)\sqrt{\cos\delta}\,e^{\mathrm{j}\mathrm{k}_0\mathrm{R}\cos\delta\cos\Theta(-1)^{\delta_{s-}}}P^1_\nu(\cos\delta)\sin\delta\,\mathrm{d}\delta, \tag{14}$$

To sum up, in this section we began with the plane-wave representation of a focused beam, which is the decomposition of its field into the Cartesian eigenfunctions of the Helmholtz equation of free space. Based on this, we derived formulas for its multipolar decomposition in VSHs, which is the decomposition of its field into the spherical eigenfunctions of the Helmholtz equation of free space. This second expansion, as we will see in the next section, is of crucial importance in studying the far-field scattering properties of particles illuminated by such an excitation field.

T-Matrix Method for Far-Field Scattering Calculations

The T-matrix formulation is a general method of dealing with far-field scattering phenomena. It is based on decomposing both the incident and the scattered field into the basis of the eigenfunctions of the Helmholtz equation of free space. So, both fields can be represented by vectors containing their correspondent expansion amplitudes. Thinking in terms of a multichannel system where the input is the incident field and the output is the scattered field, the scattering process is a linear process that can be described by a square matrix, called the T-matrix, which takes as an input the amplitudes of the incident field and gives as an output the amplitudes of the scattered field. The decomposition of the fields could be performed either on a Cartesian eigenfunction basis, that is in plane waves, or in a spherical eigenfunction basis, that is in VSHs. The plane-wave spectrum is a continuous spectrum that needs to be discretized, whereas the VSHs spectrum is a discrete but infinite spectrum. The great advantage of using VSHs as the basis of those decompositions is that the rows and columns with significant elements of the T-matrix are boiled down to the first fundamental multipolar terms. This means that the infinite T-matrix can be truncated early without loss of accuracy. We end up fully describing the phenomenon of the EM-scattering just by a $N \times N$ matrix, where $N = 2\nu_{max}(\nu_{max} + 2)$, with ν_{max} being the maximum order of the multipolar decomposition of the fields that we will take under consideration. For subwavelength particles, ν_{max} can take values, for example, from 2 or 3 up to 15 or 20. This depends on (1) the size of the particle: small particles can be sufficiently described by just using the very first orders; (2) the geometrical complexity of the particle, that is, to which extent the particle is aspherical; and also (3) the degree of accuracy that we want to achieve. The absolute values of the elements of the T-matrix range from 0 to 1 and usually they decrease while the order of the multipoles they refer to increases. So, practically, the particle can only interact with incoming multipoles of the order of up to ν_{max}. For higher-order multipoles it behaves as if it was transparent and this fact enables us to truncate the matrix.

One other significant feature of the T-matrix is that it is characteristic of the particle in the particular wavelength and it is irrelevant to the incident field. Once computed it can be straightforwardly used for scattering calculations from arbitrary excitation. Hence, one can understand that the T-matrix method plays a key role in capitalizing on the results of the previous section. The spherical amplitudes $\mathcal{A}_{\alpha,\mu\nu}(\mathbf{d})$ of the multipolar decomposition of the excitation field will compose the input vector of the multichannel system with a transfer function given by the T-matrix and the output being the vector of the spherical amplitudes of the multipolar decomposition of the scattered field, which will be denoted as $\mathcal{B}_{\alpha,\mu\nu}(\mathbf{d})$. Shaping the light that is incident to the particle, that is, acting on the input vector of the system, instead of acting upon the inner dynamics of the system, i.e., its transfer function, the geometry of the particle, is an alternative way of designing the output of the system, i.e., the scattering response of the particle. The T-matrix method reveals the inner dynamics of the scattering system. By determining the multipolar content of the field scattered by the particle one has immediate knowledge of its far-field radiation pattern as well. This means that one readily knows its behavior as a nanoantenna. Hence, apart from being useful for analytical purposes, it is also a powerful synthetical tool when it comes to designing the scattering response of a particle. And this is a very special and valuable feature, that other methods of approaching scattering problems rarely offer.

The multipolar expansion of the scattered field with respect to the natural frame of the scatterer is given by:

$$\mathbf{E}_{\text{sca}}\left(\mathbf{r}_1\right) = \sum_{\nu\mu,\alpha} \mathcal{B}_{\alpha,\mu\nu}\left(\mathbf{d}\right)\mathbf{F}^{(3)}_{\alpha,\mu\nu}\left(\mathrm{k}_0\mathbf{r}_1\right), \tag{15}$$

where we make use of the Hankel instead of the Bessel functions for the VSHs since the scattered field is a radiating field. The series of this formula is considered to converge only outside of the circumscription of the particle sphere, and this is known as the Rayleigh hypothesis [40,41]. The spherical amplitudes of the scattered field will be given in the T-matrix formulation by the following expression:

$$\mathcal{B}_{\alpha,\mu\nu} = \sum_{\nu'\mu',\alpha'} \mathbf{T}^{\alpha,\mu\nu}_{\alpha',\mu'\nu'}\mathcal{A}_{\alpha',\mu'\nu'}, \tag{16}$$

or in matrix formulation: $\mathbf{B} = \mathbf{T}\cdot\mathbf{A}$.

Not only the spherical amplitudes of the input vector, but also the elements of the T-matrix, as well as the values of the output vector of the scattered spherical amplitudes, do depend on the choice of the reference frame of the scatterer, i.e., the coordinate system that we will employ for the multipolar decomposi-

tion of the fields. There are analytical formulas to obtain a new version of the T-matrix of a particle that corresponds to a rotated or translated system of coordinates [39,42].

The total power that is scattered by the particle is given by integrating the flux of the Poynting vector of the scattered field over a spherical surface of infinite radius and is given by the formula:

$$\begin{aligned} P_{\text{sca}} &= \frac{1}{2}\iint_{S^{\infty}} \Re\left\{\mathbf{E}_{\text{sca}} \times \mathbf{H}^{*}_{\text{sca}}\right\} \cdot \hat{\mathrm{r}}_1 \mathrm{d}s \\ &= \frac{1}{2Z_0 \mathrm{k}_0^2} \sum_{\nu\mu,\alpha} \left|\mathcal{B}_{\alpha,\mu\nu}\right|^2 . \end{aligned} \tag{17}$$

There are several methods in order to calculate the elements $\mathbf{T}^{\alpha,\mu\nu}_{\alpha',\mu'\nu'}$ of the T-matrix [43-45]. We are going to employ the semi-analytical extended boundary condition method (EBCM) [39,46], also known as null-field method [42], which was originally introduced by Waterman in 1965 [47]. This method best applies for cases of homogeneous, isotropic, star-shaped particles. The elements of the matrix end up being given by Stratton–Chu type integrals, with the Dyadic Green functions being expanded in dyadic products of VSHs, over the surface of the particle that match the boundary conditions of the multipolar field representations inside and outside of the particle. This method is highly efficient for the cases of rotationally symmetric particles, such as cylinders, since the integration over the azimuthal angle can be performed analytically leading to simplified expressions of single integrals over the polar angle (see Supporting Information File 1). One needs to pay special attention on the fact that the EBCM method becomes numerically unstable for particles with extreme aspect ratios, due to numerical calculations with limited digits of precision [48,49]. This is mainly a problem because in these integrals Hankel functions with small arguments are involved, which give outputs that go to infinity and spoil the integration. Limited precision accuracy plagues also the inversion process of a matrix (see Supporting Information File 1) that is usually close to being singular and is needed for the calculation of the T-matrix.

The T-matrix has some important symmetry properties that need to be taken under consideration [39,42]:

(1) A particle that is rotationally symmetric with respect to the z_1-axis of its natural frame has a T-matrix that is diagonal over the index μ, which means that the azimuthal quantum number of the scattered field is inherited by that of the incident field:

$$\left[\mathbf{T}^{\alpha,\mu\nu}_{\alpha',\mu'\nu'}\right]^{rs} = \delta_{\mu\mu'}\mathbf{T}^{\alpha,\mu\nu}_{\alpha',\mu'\nu'}.$$

(2) A particle with N-fold symmetry with respect to the z-axis of the natural frame of the scatterer has the following property:

$$\left[\mathbf{T}^{\alpha,\mu\nu}_{\alpha',\mu'\nu'}\right]^{Nfs} = 0,$$

for $|\mu - \mu'| \neq \kappa N$, with $\kappa = 0, 1, \ldots$ This means that a particle of small size can practically exhibit diagonality over the azimuthal index, which means behave like a rotationally symmetric particle, if it has a N-fold symmetry with N being greater than twice the maximum index $\nu_{\max}$ where we truncate the T-matrix. For example, for a particle small enough, so that it practically interacts only with dipole fields (dipole approximation, $\nu_{\max} = 1$), a three-fold symmetry is enough for it to behave as a rotationally symmetric particle in terms of its far-field scattering [50].

(3) A particle that is rotationally symmetric with respect to the z_1-axis of its natural frame has a T-matrix with also the following property:

$$\left[\mathbf{T}^{\alpha,-\mu\nu}_{\alpha',-\mu\nu'}\right]^{rs} = (-1)^{\alpha+\alpha'}\left[\mathbf{T}^{\alpha,\mu\nu}_{\alpha',\mu\nu'}\right]^{rs},$$

which gives

$$\left[\mathbf{T}^{\alpha,0\nu}_{\alpha',0\nu'}\right]^{rs} = 0,$$

for $\alpha \neq \alpha'$. This means that for a rotationally symmetric excitation, with $\mu' = 0$, the electric multipoles of the incident field give birth only to scattered multipoles of electric type, and the magnetic multipoles give birth only to magnetic multipoles.

(4) A particle with mirror symmetry with respect to the $z_1 = 0$ plane of its natural frame has a T-matrix with the following property:

$$\left[\mathbf{T}^{\alpha,\mu\nu}_{\alpha',\mu'\nu'}\right]^{ms} = \left[1+(-1)^{\alpha+\alpha'+\mu+\mu'+\nu+\nu'}\right]\left[\mathbf{T}^{\alpha,\mu\nu}_{\alpha',\mu'\nu'}\right]^{z_1>0},$$

where with the last notation, integration over only half of the surface of the particle with $z_1 > 0$ is implied. If the particle is rotationally symmetric as well, we have that

$$\left[\mathbf{T}^{\alpha,\mu\nu}_{\alpha',\mu'\nu'}\right]^{ms,rs} = 0,$$

when α = α′ and ν + ν′ is an odd number, or when α ≠ α′ and ν + ν′ is an even number. This means that for a rotationally symmetric excitation (μ′ = 0), the incident multipoles of even order give birth only to scattered multipoles of even order, and, similarly, the incident ones of odd order, only to scattered ones of odd order.

(5) A particle with spherical symmetry has a T-matrix that is diagonal over all its indices α, μ, ν:

$$\left[\mathbf{T}^{\alpha,\mu\nu}_{\alpha',\mu'\nu'}\right]^{ss} = \delta_{\alpha\alpha'}\delta_{\mu\mu'}\delta_{\nu\nu'}\mathrm{b}_{\alpha,\nu},$$

where $\mathrm{b}_{\alpha,\nu}$ are the well-known Mie scattering coefficients, which in the case of homogeneous spheres are given by the formula:

$$\mathrm{b}_{\alpha,\nu} = -\frac{\frac{1}{Z_1}z^{(1)}_{\alpha,\nu}(x_0)z^{(1)}_{\beta,\nu}(x_1) - \frac{1}{Z_0}z^{(1)}_{\beta,\nu}(x_0)z^{(1)}_{\alpha,\nu}(x_1)}{\frac{1}{Z_1}z^{(3)}_{\alpha,\nu}(x_0)z^{(1)}_{\beta,\nu}(x_1) - \frac{1}{Z_0}z^{(3)}_{\beta,\nu}(x_0)z^{(1)}_{\alpha,\nu}(x_1)}. \quad (18)$$

The indices α, β acquire the names M and N with α ≠ β. The abbreviations $x_0 = \mathrm{k}_0\alpha_0$ and $x_1 = n_1\mathrm{k}_0\alpha_0$ are used, with α_0 being the sphere radius and n_1 its refractive index. Z_1 is the wave impedance inside the particle and x_0 is called the size parameter of the sphere.

We will close this section by unveiling the property that the T-matrix of one particle should have in order to be able to host a nonradiating anapole state. For this, we need to perform a singular value decomposition (SVD) of the T-matrix [51]:

$$\mathbf{T} = \mathbf{U}\Sigma\mathbf{V}^{\dagger}, \quad (19)$$

where Σ is a diagonal matrix with real, positive elements σ_i sorted in descending order, **U** and **V** are unitary matrices with columns of the vectors $\mathbf{u}_i$ and $\mathbf{v}_i$, respectively, and both form a different orthonormal basis in *N*-space. Those vectors are called the left- and right-singular vectors of the T-matrix and form pairs of vectors that correspond to the singular values σ_i of the matrix. They have the property $\mathbf{T}\cdot\mathbf{v}_i = \sigma_i\mathbf{u}_i$.

An ideal anapole state, corresponding to zero scattered power, can only be hosted by a particle whose T-matrix has at least one singular value equal to zero. If this condition is satisfied, then the ideal anapole can be excited by illuminating it by a field that has a spherical wave amplitude vector $\mathbf{A}_0$ that can be written as a linear combination of the null-space vectors of the T-matrix, that is as a linear combination of the right-singular vectors that correspond to singular values equal to zero: $\mathbf{A}_0 = \sum_{i:\{\sigma_i=0\}} a_i\mathbf{v}_i$. Then we would have $\mathbf{B} = \mathbf{T}\cdot\mathbf{A}_0 = \sum_{i:\{\sigma_i=0\}} a_i\sigma_i\mathbf{u}_i = 0$. So, this is the ideal condition of the T-matrix that would indicate the ability of the particle to host an ideal non-radiating anapole state. In order to have access to such kind of excitation we need to shape the multipolar content of the illumination field. The result is that the particle is critically coupled with the excitation field inside of which electromagnetic energy is stored without a scattered field needed to fulfill the boundary conditions on its surface. Furthermore, we should also denote that those right-singular vectors of the null-field space should describe nontrivial excitations, that is excitations with significant multipolar content for multipoles of the first order, since, for higher-order multipoles, a nanoparticle is actually behaving as if it was transparent. The incident field in the vicinity of the center of the coordinate system attached to the particle is mainly described by the first few multipolar terms.

However, in practice, when exciting an anapole state, we just aim to minimize, not to eliminate, the norm of the vector **B**. If we define the quality factor of the anapole excitation as $Q = (4P_{\mathrm{inc}}/P_{\mathrm{sca}}) - 1$, then, by expanding the output vector again on the basis of the left-singular vectors, finally we have:

$$\sum_i |a_i\sigma_i|^2 = \frac{8Z_0\mathrm{k}_0^2P_{\mathrm{inc}}}{Q+1}. \quad (20)$$

It becomes obvious now that the ability of a particle to host a nonradiating anapole state with high *Q*, in terms of its T-matrix, means the correspondence of sufficiently small coupling coefficients α_i to the first singular values σ_i, which take the largest values, since they are sorted in descending order. So, in order to achieve a nonradiating state, the key lies in illuminating the particle with a field, the multipolar decomposition of which, will be well described by a linear combination of those right-singular vectors that correspond to small enough singular values. We need to avoid using, for our input, the right-singular basis vectors that are not enough scaled down in magnitude by the T-matrix transformation.

Results and Discussion

We can use the results and conclusions of the previous sections in order to design the scattering response of a nanoparticle at will. We want to achieve a purely magnetic response by the particle, the scattered power of which, will be suppressed for some particular frequency. We will properly design its geometry and, also, its excitation field, in order to achieve the desired scattering response.

In the former sections, we proved that an azimuthally polarized focused beam that is rotationally symmetric, i.e., that has a zero orbital angular momentum: $m = 0$, bears only multipoles of magnetic type for particles that are located over the optical axis. Moreover, it was also proven that if this particle has a rotational symmetry as well, it will only scatter multipoles of magnetic type. So, it will have a purely magnetic response. More specifically, the scattered field would be a superposition of VSHs of type $\mathbf{F}^{(3)}_{\mathrm{M},0\nu}$, with the magnetic dipole, $\mathbf{F}^{(3)}_{\mathrm{M},01}$, corresponding to a dipole moment along the z-axis, $\mathbf{m}_z$, and the magnetic quadrupole, $\mathbf{F}^{(3)}_{\mathrm{M},02}$, corresponding to a Cartesian quadrupole moment $\mathbf{Q}^{\mathrm{m}}_{zz} = -\mathbf{Q}^{\mathrm{m}}_{xx} - \mathbf{Q}^{\mathrm{m}}_{yy}$, and so on. So, for demonstration purposes, we are going to use an azimuthally polarized, rotationally symmetric, focused vector beam with a Bessel–Gauss transverse profile given by

$$\left\{\mathrm{I}^{(s)}_{\mathrm{p,m}}\right\}^{\mathrm{BG}}(\delta) = \delta_{m0}\delta_{\mathrm{p}\hat{\phi}}\, e^{-\beta_0^2\left[\frac{\sin\delta}{\mathrm{NA}}\right]^2} J_1\left(2\beta_0\left[\frac{\sin\delta}{\mathrm{NA}}\right]\right),$$

with a ratio of pupil radius to beam waist $\beta_0 = 1.5$ and a numerical aperture of NA = 0.85. The multipolar decomposition of such an excitation in VSHs is given by Equation 14.

In Figure 1a we plot the normalized total scattered power, (P_{sca}/P_{inc}), at a wavelength of $\lambda_0 = 500$ nm, for golden spheres of various sizes, placed at the focal point of a vector beam like the one described above. As shown there, in such a way, we can even achieve a purely magnetic response by a plasmonic nanoparticle at optical frequencies. Of course, gold has a poor performance in optical frequencies, since it suffers from severe thermal losses, and as a result, the resonances of the particle correspond to Mie scattering coefficients, the amplitudes of which, are usually significantly less than one, and the quality factor of the supported anti-resonances is quite low as well. A plasmonic nanoparticle can only provide us with a very poor (anti-)resonant spectrum to work with.

So, we resort to high-index silicon nanoparticles as a platform to excite a nonradiating anapole state of magnetic type. Silicon nanoparticles suffer negligible losses at infrared light. Due to their high refractive index, they constitute also a good platform to host Mie resonances of magnetic type, since they can confine light and support circulating current loops inside. Now, we replace the golden sphere with a one of silicon and in Figure 1b, we plot the normalized total scattered power ($P_{\mathrm{sca}}/P_{\mathrm{inc}}$) at a wavelength of $\lambda_0 = 1550$ nm, for spheres of various sizes. As we can see, its resonant multipolar content is much richer than the previous case of the plasmonic nanoparticle. We can observe a steep dip of the scattered power for a sphere of size parameter $x_0 = 1.62$, which belongs to a sphere of a radius of

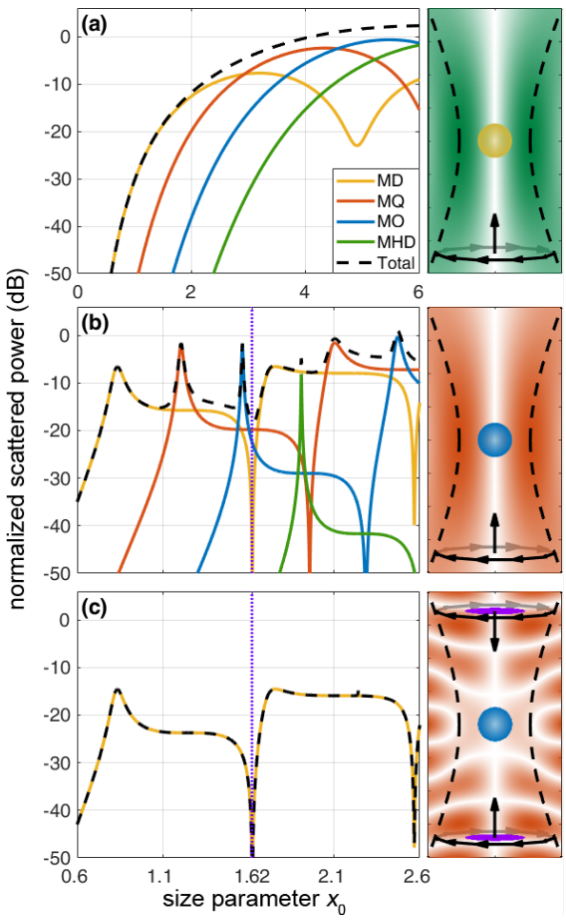


Figure 1: Plots of the normalized scattered power ($P_{\mathrm{sca}}/P_{\mathrm{inc}}$) in dB, decomposed into its multipolar contributions, as a function of the size parameter of the particle, x_0. a) Golden sphere at the focal point of an azimuthally polarized, rotationally symmetric beam at $\lambda_0 = 500$ nm. b) Silicon sphere at the focal point of an azimuthally polarized, rotationally symmetric beam at $\lambda_0 = 1550$ nm. c) Silicon sphere at the focal point of two counterpropagating, out of phase, azimuthally polarized, rotationally symmetric beams, modulated by the proposed phase mask, at $\lambda_0 = 1550$ nm. Purple dotted lines indicate the first anapole condition for a sphere of size $x_0 = 1.62$. On the right-hand side, there are illustrations of the actual E-field intensity of the excitation over a window of 2 × 4 wavelengths at the focal region, on the pOz plane, with a sphere of size $x_0 = 1.62$ placed at the focal point.

$\alpha_0 = 400$ nm. We have already avoided any interference by the electric modes and this sphere could be a promising candidate to host a magnetic anapole state, if it were not, as we can see, for the overlapping magnetic quadrupole and octupole that interfere and spoil the anapole condition of the magnetic dipole.

To overcome this, we take the following two actions: First, we employ a second, similar, counterpropagating beam and illuminate the silicon particle under a standing-wave configuration. As proven in the previous section, if the second counterpropagating beam has the same transverse profile and is out of phase

with the first beam, there would be no excitation of multipoles of even order for a scatterer located at their common focal point. And, since the T-matrix of a spherical particle is diagonal over ν, the scattered multipoles of even order are canceled out. Therefore, there will be no spurious interference by the magnetic quadrupole any more. But we still need to get rid of the octupolar interference. For this, we apply a phase mask to the two beams before their focusing by the objective. The simplest phase mask that we can come up with is introducing a π phase difference inside a circular disk with a radius that corresponds to the angle δ where the cumulative value of the integral of Equation 14 corresponding to the magnetic octupole term takes half of its final value. In our case, this happens for δ = 29.225°. In this way, the octupolar content of the beam is eliminated, finally leading to the excitation of a nearly ideal magnetic anapole state that has a dynamic range of more than three orders of magnitude (Figure 1c). Only spherical particles with perfect dielectric behavior or of perfect conductivity can exhibit truly ideal multipolar dips to zero. We should also note the fact that any silicon nanosphere placed at the focal point of such illumination scheme will exhibit purely magnetic dipole response. However, as one can observe, there is also a price to pay for the phase mask that we introduced: the field intensity at the vicinity of the focal spot drops to less than a third. Nonetheless, one could potentially come up with more efficient ways of shaping the multipolar content of the excitation, i.e., more complex illumination schemes that can also include amplitude modulation or multiple-beam configurations. Alternatively, avoiding the use of such a phase mask, we can observe that one can obtain another anapole corresponding to the magnetic quadrupole of a sphere of size $x_0 = 1.96$. Under illumination of two in phase beams the interfering magnetic dipole and octupole will be diminished, leading to a scattering dip of less than −30 dB between two, hexadecapolar and quadrupolar, resonances. In Supporting Information File 1, one can find a plot with the proposed phase-modulation mask, together with some electric and magnetic field plots that correspond to the illumination of a silicon sphere, with the size of this anapole case, under illumination of both one single and two out of phase beams, with and without the phase mask applied.

Next, we will shift our attention to silicon disks since they represent, in terms of fabrication, experimental verification and applications, more realistic cases. We use the T-matrix theory

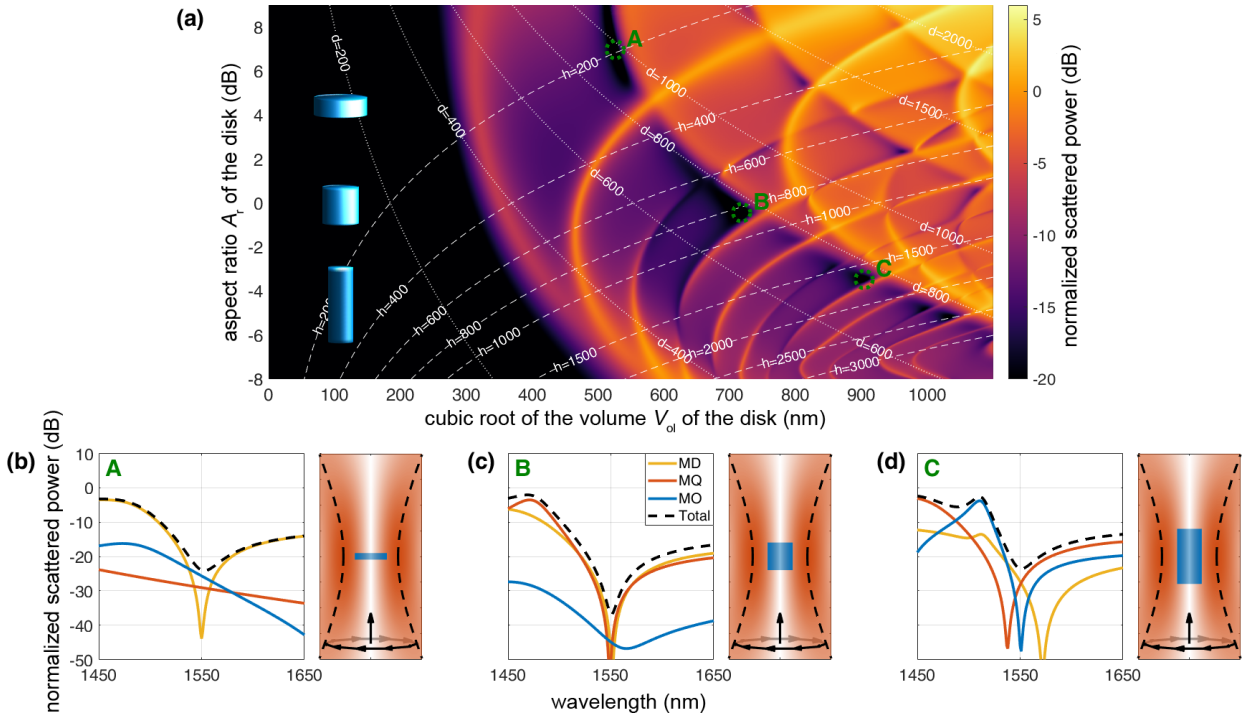


Figure 2: a) 2D plot of the normalized scattered power (P_{sca}/P_{inc}) in dB as a function of the cubic root of the volume V_{ol} of the disks and the aspect ratio A_r of the disks. Isoheight (dashed) and isowidth (dotted) contour lines in terms of the dimensions of the disks (in nm) are plotted as well. The silicon disks are located at the focal point of a rotationally symmetric, azimuthally polarized vector beam at λ_0 = 1550nm. Three cases of excited anapole states are highlighted with A, B and C, the multipolar decomposition of the scattering spectrum of which, is depicted in subfigures b-d respectively. On the right side of them, there are illustrations of the actual E-field intensity of the excitation over a window of 2x4 wavelengths at the focal region, with a disk of the corresponding dimensions placed at the focal point.

described before in order to study numerically the interaction of an azimuthally polarized cylindrical vector beam with the cylinders. As one can see in Figure 2a, we scan the aspect ratio, $A_r = d/h$, and the volume $V_{ol} = (\pi/4)A_r^2h^3$ of various cases disks , with diameter d and height h, located in free space illuminated by a single azimuthally polarized, cylindrically symmetric, focused vector beam at fixed wavelength $\lambda_0 = 1550$ nm, plotting the normalized total scattered power (P_{sca}/P_{inc}) on a logarithmic scale in search of dips that would indicate the presence of some anapole states. The disks are aligned along the optical axis.

The particular design of the excitation is essential in obtaining nonradiating behavior of the cylinders. Again, we want to emphasize that the symmetries of the cylinder are of crucial importance. Such a particle is rotationally symmetric, which means that it will provide the diagonality identity over the index μ, which is zero due to the cylindrical symmetry of the excitation. This will result in the scattered field being of purely magnetic type. In addition, a cylinder exhibits a mirror symmetry with respect to the $z = 0$ plane. This property, as we have shown earlier, will cancel out all scattered multipoles of even order when using the same standing-wave configuration that was employed before for the silicon sphere. This is the case even if the T-matrix of a cylinder disk does not have this diagonality over the index ν that spherical particles have. However, as we can see in Figure 2a, there are several anapole instances already accessible by the single beam illumination scheme. In Figure 2b–d, we focus our attention on three of these cases. The first anapole case is hosted in an oblate disk of small volume, $V_{ol,A}^{(1/3)} = 526$ nm, but with high aspect ratio, $A_{r,A} = 4.98$. It is a magnetic anapole that exhibits a single dip of the magnetic dipole. The two other cases, that appear in larger disks of bigger volumes, $V_{ol,B}^{(1/3)} = 718$ nm and $V_{ol,C}^{(1/3)} = 904$ nm, but with smaller aspect ratios, $A_{r,B} = 0.905$ and $A_{r,C} = 0.45$, respectively, exhibit magnetic anapole states of higher order. There is a hybrid condition where, simultaneously with the magnetic dipole dip, we also have dips of the magnetic quadrupole and of the magnetic octupole. In Supporting Information File 1, there are 2D maps of the multipolar decomposition that corresponds to Figure 2a.

Last, we compare the properties of the T-matrix of the cylinder for which the second anapole case was highlighted previously, with the properties of the T-matrix of a cylinder that has the same aspect ratio, $A_{r,B'} = A_{r,B} = 0.905$, but a larger volume, $V_{ol,B'} = 759$ nm, and yields resonant scattering. We perform a singular value decomposition of the μ = 0 T-submatrices for each of those two cylinders and calculate their singular values σ_i. We also expand the input vector **A**, with the spherical amplitudes of the excitation field, over the basis of the right-singular vectors of each matrix, calculating the coupling coefficients a_i for both of the two cases. We show the corresponding results for multipoles up to the fifth order.

In Figure 3a,b we plot the quantities σ_i^2 and $|a_i|^2/\sum_i|a_i|^2$, as well as their product $|a_i\sigma_i|^2/\sum_i|a_i|^2$ for the two cylinders. As we mentioned above, the sum of the last quantity over the index i is proportional to the total scattered power. Therefore its minimization would lead to an anapole state. We can observe that for the cylinder that hosts an anapole state, there is weak coupling of the excitation field with the right-singular vectors that correspond to the first, largest, singular values of the matrix. The result is suppressed scattering leading to an anapole state. This does not happen in the case of the resonant cylinder. For the anapole case, the strongest part of the scattered power derives from the part of the incident field that corresponds to the sixth right singular vector, and is more than three orders of magnitude weaker than the prevailing scattered power that belongs to the first right singular vector of the T-submatrix of the disk in the resonant case.

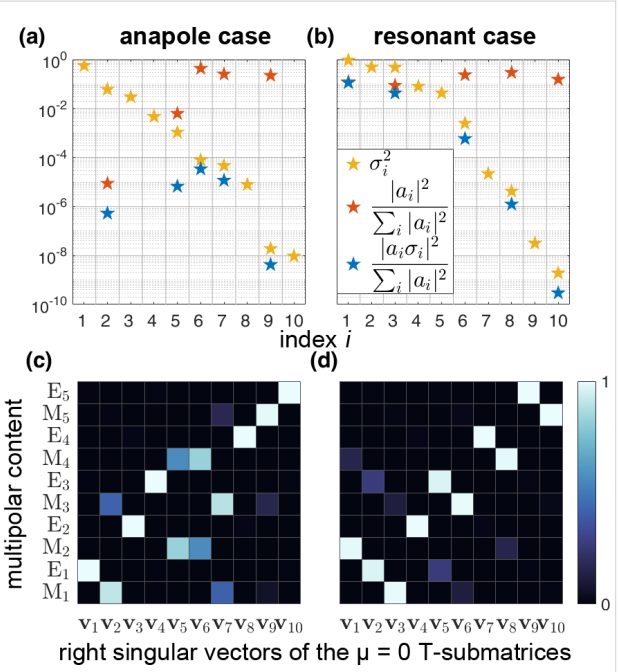


Figure 3: Comparison of the scattering behavior of two disks of the same aspect ratio but of different size under the prism of the singular value decomposition of their μ = 0 T-submatrices. One of them corresponds to an anapole case (a,c) and the other to a resonant case (b,d). In (a,b) we plot the singular values σ_i of the T-submatrices (yellow stars), together with the coupling coefficients a_i of the excitation field with the corresponding right singular vectors (red stars), as well as the final contribution of the correspondent singular mode to the total scattered power (blue stars). In (c,d) the multipolar content of each right singular vector $\mathbf{v}_i$ of the two T-submatrices is plotted. Weak coupling of the external field with the first right singular vectors of the T-submatrix, that correspond to high singular values, leads to the excitation of the anapole state.

Figure 3c,d depicts the multipolar content of the right singular vectors of the T-submatrices that belong to each of those two cylinders. As one can see, there is absolutely no coupling at all with the right singular vectors that have a multipolar content of electric type. In both cases there are no right singular vectors of mixed type multipolar content since for $\mu = 0$ the T-submatrix of a rotationally symmetric particle is diagonal over the indicator α, which represents the type of the multipoles. Furthermore, due to the mirror symmetry of the particles, we can also observe that the right singular vectors are separated into vectors with either purely even or purely odd multipolar content.

Hence, we can claim that the key for the excitation of this particular nonradiating anapole state is connencted to the suppression of the coupling of the external field that we apply, with the first, third and fourth right singular vectors of the T-submatrix of the particle, which have electric multipolar content that is not supported by an azimuthally polarized focused beam. In addition, it is connected with the coincidence of the weak coupling of the excitation with the second right singular vector, which has a multipolar content of magnetic type and corresponds to a significantly large singular value that could potentially spoil the excitation of the anapole state.

Conclusion

In this paper we describe the so-called magnetic anapole modes and discuss various experimental setups of how they can be obtained. Such modes are associated with the complete suppression of magnetic dipole scattering. In order to be able to obtain anapole states experimentally, we employed structured-light excitation of a particular configuration. Usually we use illumination with a plane wave at normal incidence. Such an excitation carries a multipolar content of $\mu = \pm 1$ angular momentum and acts on the correspondent T-submatrices when it comes to scattering by rotationally symmetric particles. By using a rotationally symmetric excitation, instead, we have access to the $\mu = 0$ T-submatrix of these particles, which constitutes a whole new scattering system, a whole new field to work with where new interesting phenomena may wait to be unveiled. It turns out that azimuthally polarized beams contain only spherical harmonics of magnetic type in the focal region. Depending on the size of the particle compared to the incident wavelength it can couple to dipole and/or higher-order harmonics. By using two counter-propagating out of phase beams it is possible to cancel out all harmonics of even order because of symmetry properties. Together with a phase mask applied to the beams, designated to suppress the interfering octupolar content, this provides an ideal condition for the excitation of a magnetic anapole state in a silicon nanosphere. We also discussed realistic setups, based on silicon nanodisks and nanopillars, which can be used for the experimental detection of magnetic anapole states. We also explained, under the T-matrix formalism, the physical mechanism of their excitation in the hosting nanoparticles, by means of a singular value decomposition of their T-matrices.

Supporting Information

Supporting Information features the proof for the multipolar decomposition of an arbitrary plane wave and the formulas with which the elements of the T-matrix are calculated based on the EBCM method. It also includes a plot of the proposed phase mask for Figure 1c, electric and magnetic field plots corresponding to the anapole condition discussed in Figure 1b and Figure 1c, and some extra 2D plots of the multipolar decomposition of the scattered field of cylinders of various geometries illuminated by an azimuthally polarized, rotationally symmetric, focused beam.

Supporting Information File 1

Additional computational data.
[https://www.beilstein-journals.org/bjnano/content/supplementary/2190-4286-9-139-S1.pdf]

Acknowledgements

The authors thank Dr. Lei Xu and Prof. Dragomir Neshev for useful discussions and also acknowledge support from the NANOPHI Erasmus Mundus programme.

ORCID® iDs

Andrey E. Miroshnichenko - https://orcid.org/0000-0001-9607-6621

References

1. Jackson, J. D. *Classical Electrodynamics,* 3rd ed.; Wiley: New York, NY, U.S.A., 1998.
2. Ehrenfest, P. *Phys. Z.* **1910,** *11,* 708.
3. Schott, G. A. *Philos. Mag. (1798-1977)* **1933,** *15,* 752–761. doi:10.1080/14786443309462219
4. Bohm, D.; Weinstein, M. *Phys. Rev.* **1948,** *74,* 1789–1798. doi:10.1103/PhysRev.74.1789
5. Goedecke, G. H. *Phys. Rev.* **1964,** *135,* B281–B288. doi:10.1103/PhysRev.135.B281
6. Gbur, G. Non-radiating sources and the inverse source problem. Ph.D. Thesis, University of Rochester, New York, NY, U.S.A., 2001.
7. Miroshnichenko, A. E.; Evlyukhin, A. B.; Yu, Y. F.; Bakker, R. M.; Chipouline, A.; Kuznetsov, A. I.; Luk'yanchuk, B.; Chichkov, B. N.; Kivshar, Y. S. *Nat. Commun.* **2015,** *6,* 8069. doi:10.1038/ncomms9069
8. Kaelberer, T.; Fedotov, V. A.; Papasimakis, N.; Tsai, D. P.; Zheludev, N. I. *Science* **2010,** *330,* 1510–1512. doi:10.1126/science.1197172
9. Papasimakis, N.; Fedotov, V. A.; Savinov, V.; Raybould, T. A.; Zheludev, N. I. *Nat. Mater.* **2016,** *15,* 263–271. doi:10.1038/nmat4563

10. Fedotov, V. A.; Rogacheva, A. V.; Savinov, V.; Tsai, D. P.; Zheludev, N. I. *Sci. Rep.* **2013,** *3,* 2967. doi:10.1038/srep02967
11. Liu, W.; Shi, J.; Lei, B.; Hu, H.; Miroshnichenko, A. E. *Opt. Express* **2015,** *23,* 24738–24747. doi:10.1364/OE.23.024738
12. Liu, W.; Zhang, J.; Lei, B.; Hu, H.; Miroshnichenko, A. E. *Opt. Lett.* **2015,** *40,* 2293–2296. doi:10.1364/OL.40.002293
13. Liu, W.; Lei, B.; Shi, J.; Hu, H.; Miroshnichenko, A. E. *J. Nanomater.* **2015,** *2015,* 672957. doi:10.1155/2015/672957
14. Nanz, S. *Toroidal Multipole Moments in Classical Electrodynamics;* Springer: Berlin, Germany, 2016.
15. Gongora, J. S. T.; Miroshnichenko, A. E.; Kivshar, Y. S.; Fratalocchi, A. *Nat. Commun.* **2017,** *8,* 15535. doi:10.1038/ncomms15535
16. Shibanuma, T.; Grinblat, G.; Albella, P.; Maier, S. A. *Nano Lett.* **2017,** *17,* 2647–2651. doi:10.1021/acs.nanolett.7b00462
17. Feng, T.; Xu, Y.; Zhang, W.; Miroshnichenko, A. E. *Phys. Rev. Lett.* **2017,** *118,* 173901. doi:10.1103/PhysRevLett.118.173901
18. Luk'yanchuk, B.; Paniagua-Dominguez, R.; Kuznetsov, A. I.; Miroshnichenko, A. E.; Kivshar, Y. S. *Philos. Trans. R. Soc. London, Ser. A* **2017,** *375,* 20160069. doi:10.1098/rsta.2016.0069
19. Mazzone, V.; Totero Gongora, J. S.; Fratalocchi, A. *Appl. Sci.* **2017,** *7,* 542. doi:10.3390/app7060542
20. Basharin, A. A.; Chuguevsky, V.; Volsky, N.; Kafesaki, M.; Economou, E. N. *Phys. Rev. B* **2017,** *95,* 035104. doi:10.1103/PhysRevB.95.035104
21. Nemkov, N. A.; Stenishchev, I. V.; Basharin, A. A. *Sci. Rep.* **2017,** *7,* 1064. doi:10.1038/s41598-017-01127-2
22. Wu, P. C.; Liao, C. Y.; Savinov, V.; Chung, T. L.; Chen, W. T.; Huang, Y.-W.; Wu, P. R.; Chen, Y.-H.; Liu, A.-Q.; Zheludev, N. I.; Tsai, D. P. *ACS Nano* **2018,** *12,* 1920–1927. doi:10.1021/acsnano.7b08828
23. Alaee, R.; Rockstuhl, C.; Fernandez-Corbaton, I. *Opt. Commun.* **2018,** *407,* 17. doi:10.1016/j.optcom.2017.08.064
24. Wei, L.; Xi, Z.; Bhattacharya, N.; Urbach, H. P. *Optica* **2016,** *3,* 799–802. doi:10.1364/OPTICA.3.000799
25. Devaney, A. J.; Wolf, E. *Phys. Rev. D* **1973,** *8,* 1044–1047. doi:10.1103/PhysRevD.8.1044
26. Stout, B.; McPhedran, R. *Europhys. Lett.* **2017,** *119,* 44002. doi:10.1209/0295-5075/119/44002
27. Gongora, J. S. T.; Favraud, G.; Fratalocchi, A. *Nanotechnology* **2017,** *28,* 104001. doi:10.1088/1361-6528/aa593d
28. Zeng, J.; Huang, F.; Guclu, C.; Veysi, M.; Albooyeh, M.; Wickramasinghe, H. K.; Capolino, F. *ACS Photonics* **2018,** *5,* 390–397. doi:10.1021/acsphotonics.7b00816
29. Camacho-Morales, R.; Rahmani, M.; Kruk, S.; Wang, L.; Xu, L.; Smirnova, D. A.; Solntsev, A. S.; Miroshnichenko, A.; Tan, H. H.; Karouta, F.; Naureen, S.; Vora, K.; Carletti, L.; De Angelis, C.; Jagadish, C.; Kivshar, Y. S.; Neshev, D. N. *Nano Lett.* **2016,** *16,* 7191–7197. doi:10.1021/acs.nanolett.6b03525
30. Kozawa, Y.; Sato, S. *Opt. Express* **2010,** *18,* 10828–10833. doi:10.1364/OE.18.010828
31. Nieminen, T. A.; Heckenberg, N. R.; Rubinsztein-Dunlop, H. *Opt. Lett.* **2008,** *33,* 122–124. doi:10.1364/OL.33.000122
32. Das, T.; Schuller, J. A. *Phys. Rev. B* **2017,** *95,* 201111. doi:10.1103/PhysRevB.95.201111
33. Hoang, T. X.; Chen, X.; Sheppard, C. J. R. *J. Opt. Soc. Am. A* **2012,** *29,* 32–43. doi:10.1364/JOSAA.29.000032
34. Orlov, S.; Peschel, U.; Bauer, T.; Banzer, P. *Phys. Rev. A* **2012,** *85,* 063825. doi:10.1103/PhysRevA.85.063825
35. Gouesbet, G.; Gréhan, G. *Generalized Lorenz–Mie Theories;* Springer: Berlin, Germany, 2011.
36. Das, T.; Iyer, P. P.; DeCrescent, R. A.; Schuller, J. A. *Phys. Rev. B* **2015,** *92,* 241110. doi:10.1103/PhysRevB.92.241110
37. Chrissoulidis, D. P.; Richalot, E. *J. Opt. Soc. Am. A* **2017,** *34,* 558–567. doi:10.1364/JOSAA.34.000558
38. Youngworth, K. S.; Brown, T. G. *Opt. Express* **2000,** *7,* 77–87. doi:10.1364/OE.7.000077
39. Mishchenko, M.; D. Travis, L.; Lacis, A. *Scattering, Absorption, and Emission of Light by Small Particles;* Cambridge University Press: Cambridge, United Kingdom, 2002.
40. Auguié, B.; Somerville, W. R. C.; Roache, S.; Le Ru, E. C. *J. Opt. (Bristol, U. K.)* **2016,** *18,* 075007. doi:10.1088/2040-8978/18/7/075007
41. Farafonov, V. G.; Ustimov, V. I. *Opt. Spectrosc.* **2015,** *119,* 1022–1033. doi:10.1134/S0030400X15120103
42. Doicu, A.; Wriedt, T.; Eremin, Y. *Light Scattering by Systems of Particles-Null-Field Method with Discrete Sources-Theory and Programs;* 2006.
43. Fruhnert, M.; Fernandez-Corbaton, I.; Yannopapas, V.; Rockstuhl, C. *Beilstein J. Nanotechnol.* **2017,** *8,* 614–626. doi:10.3762/bjnano.8.66
44. Mackowski, D. W. *J. Opt. Soc. Am. A* **2002,** *19,* 881–893. doi:10.1364/JOSAA.19.000881
45. Demésy, G.; Stout, B.; Auger, J.-C. *arXiv* **2018,** No. 1802.00596.
46. Waterman, P. C. *J. Opt. Soc. Am. A* **2007,** *24,* 2257–2267. doi:10.1364/JOSAA.24.002257
47. Waterman, P. C. *Proc. IEEE* **1965,** *53,* 805–812. doi:10.1109/PROC.1965.4058
48. Somerville, W. R. C.; Auguié, B.; Le Ru, E. C. *J. Quant. Spectrosc. Radiat. Transfer* **2012,** *113,* 524. doi:10.1016/j.jqsrt.2012.01.007
49. Somerville, W. R. C.; Auguié, B.; Le Ru, E. C. *J. Quant. Spectrosc. Radiat. Transfer* **2015,** *160,* 29. doi:10.1016/j.jqsrt.2015.03.020
50. Hopkins, B.; Liu, W.; Miroshnichenko, A. E.; Kivshar, Y. S. *Nanoscale* **2013,** *5,* 6395–6403. doi:10.1039/C3NR01291C
51. Suryadharma, R. N. S.; Fruhnert, M.; Rockstuhl, C.; Fernandez-Corbaton, I. *Phys. Rev. A* **2017,** *95,* 053834. doi:10.1103/PhysRevA.95.053834

License and Terms

This is an Open Access article under the terms of the Creative Commons Attribution License (http://creativecommons.org/licenses/by/4.0), which permits unrestricted use, distribution, and reproduction in any medium, provided the original work is properly cited.

The license is subject to the *Beilstein Journal of Nanotechnology* terms and conditions: (https://www.beilstein-journals.org/bjnano)

The definitive version of this article is the electronic one which can be found at: doi:10.3762/bjnano.9.139

BEILSTEIN JOURNAL OF NANOTECHNOLOGY

Cathodoluminescence as a probe of the optical properties of resonant apertures in a metallic film

Kalpana Singh[*1], Evgeniy Panchenko[1], Babak Nasr[2,3,4], Amelia Liu[5], Lukas Wesemann[1], Timothy J. Davis[*1] and Ann Roberts[*1]

Full Research Paper

Open Access

Address:
[1]School of Physics, University of Melbourne, VIC 3010, Australia, [2]Centre for Neural Engineering, The University of Melbourne, VIC 3010, Australia, [3]Department of Electrical and Electronic Engineering, The University of Melbourne, VIC 3010, Australia, [4]Australian Research Council Centre of Excellence for Integrative Brain Function, The University of Melbourne, VIC 3010, Australia, and [5]Monash Centre for Electron Microscopy and School of Physics and Astronomy, Monash University, Clayton, VIC 3800, Australia

Email:
Kalpana Singh[*] - ksingh1@student.unimelb.edu.au;
Timothy J. Davis[*] - timd@unimelb.edu.au; Ann Roberts[*] - ann.roberts@unimelb.edu.au

* Corresponding author

Keywords:
cathodoluminescence; plasmonics

Beilstein J. Nanotechnol. **2018,** *9,* 1491–1500.
doi:10.3762/bjnano.9.140

Received: 23 November 2017
Accepted: 06 April 2018
Published: 18 May 2018

This article is part of the Thematic Series "Light–Matter interactions on the nanoscale".

Guest Editor: M. Rahmani

© 2018 Singh et al.; licensee Beilstein-Institut.
License and terms: see end of document.

Abstract

Here we present the results of an investigation of resonances of azimuthal trimer arrangements of rectangular slots in a gold film on a glass substrate using cathodoluminescence (CL) as a probe. The variation in the CL signal collected from specific locations on the sample as a function of wavelength and the spatial dependence of emission into different wavelength bands provides considerable insight into the resonant modes, particularly sub-radiant modes, of these apertures. By comparing our experimental results with electromagnetic simulations we are able to identify a Fabry–Pérot mode of these cavities as well as resonances associated with the excitation of surface plasmon polaritons on the air–gold boundary. We obtain evidence for the excitation of dark (also known as sub-radiant) modes of apertures and aperture ensembles.

Introduction

The study of the interaction of electromagnetic waves with apertures in metallic films has been the subject of ongoing research following early investigations motivated by advances in radar and microwave technologies. In 1944 Bethe studied diffraction by small circular apertures in an infinitesimally thin, perfectly conducting film [1]. According to this theory, the transmission through an aperture in the limit where the wavelength (λ) is much smaller than the radius b ($b << \lambda$) varies as $(\lambda/b)^4$. Subsequently, Bouwkamp extended Bethe's result adding further terms in a series expansion [2] and Roberts [3] developed a modal method to accommodate apertures in finite thickness films. A broad range of other apertures have been in-

vestigated including rectangular slots [4,5] and circular apertures [3,6] as well as more complex shapes such as cross-shaped [7-9], and coaxial apertures [10,11]. Interest in sub-wavelength metallic apertures increased significantly after Ebbesen et al. reported optical transmission, enhanced relative to an equivalent hole–area fraction of randomly arranged apertures, through periodic arrangements of holes in a silver film [12]. This enhancement is strongly associated with the ordered arrangement of the apertures. Theoretical and experimental research into isolated rectangular slots [4,5] and coaxial apertures [10,11], however, has shown that these cavities exhibit distinct localized resonances that have a strong dependence on the geometry of the holes including the thickness of the metal film [13]. Other than the excitations discussed above, sharp Fano resonances arising from the interference of two modes [14] have promising applications in sensing, switching and lasing. These resonances have been investigated in various structures such as thin film nanogratings [15], plasmonic oligomers [16], dolmen arrangements of nanorods [17] and ring–disk dimers [18]. Fano resonances have also been observed in nanoholes such as coaxial apertures [19] and dolmen nanocavities [18]. The performance of an array of double split-ring cavities [20] as biosensors using Fano resonances in the terahertz regime has been demonstrated. As is the case with nanoparticles, nanoholes play an important role as basic building blocks in a range of nanophotonic devices, including colour filters [21-24] and compact polarizers [25], exploiting resonant properties of the subwavelength apertures. The high sensitivity of the resonant modes of the apertures to the refractive index of the surrounding media underpins significant potential in realizing highly efficient ultra-compact biological and chemical sensors [26-31], plasmonic electrochemical sensors [32] and as SERS sensors [33]. Furthermore, by varying the geometry of the apertures across a surface, it is possible to introduce specific amplitude and phase profiles to the transmitted optical field [27]. This underpins the development of ultra-compact, planar, alternatives to conventional lenses [34]. Far-field optical investigations of isolated holes are, however, challenging since the throughput and reflectance are low despite the enhanced localized fields. Furthermore, plasmonic cavities exhibit a wide range of modes, many of which are "dark" to normally incident plane waves and challenging to excite using other optical methods. These modes are of intrinsic interest, however, and have also attracted attention due to their relatively high quality factor and long lifetimes that may underpin new optical sensors with a higher sensitivity and figure-of-merit than devices utilising "bright" dipole modes [35] and enhanced coupling to plasmonic cavities by emitters such as quantum dots [36]. One way to enhance the signal-to-noise ratio of transmission measurements is to study the collective optical properties of an array of apertures, choosing the periodicity to minimize both the effects of diffraction and coupling between unit cells [7]. Near field optical microscopy is another method that has been used to probe optical resonances of various nanostructures. Although the technique provides better-than-diffraction-limited resolution, image interpretation is complex due to the interaction between the tip and the sample. Nevertheless, progress has been made into the use of scanning probe methods for analysing modes of optical antennas [37].

Electron microscopy systems can also be used to probe various modes of optical nanostructures. Electrons in motion are accompanied by an electric field that varies in space and time [38], and hence, an electron beam can induce a time-varying polarization in an adjacent material leading to optical excitation. Optical resonances can be probed by studying either the loss in the energy of the electrons (through electron energy loss spectroscopy, EELS) [38,39] or the radiation emitted in the visible part of the electromagnetic spectrum through cathodoluminescence (CL) [38]. The relationship between the information obtained using EELS and CL has been studied theoretically [40]. CL is an established technique which is widely used in various fields to characterize a range of inorganic compounds such as ceramics, minerals and semiconductors [41-43]. CL has also been shown to be an invaluable tool in the investigation of optical modes of nanostructures [44]. These include characterising the plasmonic modes of silver nanoparticles [45] and resonant modes of single GaAs nanowires [46], modes of single and pairs of AlGaAs disks [47], the optical properties of quantum discs of GaN/AlN in GaN nanowires [48] and various modes of gold nanodecahedra [49]. The potential of CL used in transmission to observe various colour centres in nanodiamonds has also been demonstrated [50]. The spectral properties of core–shell CdSe/CdS quantum dots have also been studied using CL in a transmission electron microscope [51]. The same technique has been used to generate single photons and to characterize quantum states and the nature of the emitted beam with subwavelength resolution [52]. Dichroic-sensitive cathodoluminescence imaging has also been used to study the chiral nature of the gold split-ring resonators on a TiO_2 substrate [53]. Most studies have focused on nanoparticles on silicon substrates that can have a significant impact on the optical resonances of plasmonic and other nanophotonic systems. Despite the significant body of work looking at the use of CL in characterising nanoparticles, there has been less attention directed at complementary nanoholes in metallic films. Coenen and Polman [54] investigated the properties of simple circular apertures in a 80 nm thick gold film on a silicon substrate. They showed that there was excitation of a magnetic mode of the aperture when excited near the edge of the aperture. Van de Haar et al. [55] also investigated a metamaterial consisting of a periodic array of metal–insulator–metal coaxial waveguides filled with Si and the

subradiant, whispering gallery modes of circular grooves of various depths milled into a gold film have also been previously studied [56,57]. Symmetric and anti-symmetric modes of nanopore pairs in thin AlN/Au/AlN films [58] have been investigated using CL. Through the use of colloidal lithography, the authors [58] of were able to efficiently investigate a range of hole separations, but were restricted to weakly resonant circular apertures and pairs of holes.

Here we investigate the resonances of small groups of apertures in gold films on a glass substrate. Specifically, we study ensembles of three slot apertures using CL. It is well-known that simple slots in a metal film exhibit resonances, but there is a growing interest in the excitation of apertures complementary to resonant particles. Here we investigate ensembles of three simple slots arranged in the form of a triangle. This structure is complementary to a trimer consisting of three rods with the lowest energy magnetic dipole mode being dark and the next highest energy modes being degenerate orthogonal dipole modes (see Supporting Information File 1). The dominant modes of this structure are a dark mode with radial symmetry where the electric field in each aperture is radially directed from the centroid of the configuration and another, almost degenerate, radiant mode with a net dipole moment (see Supporting Information File 1). In both cases the electric fields in each aperture are similar to the dipole mode of a single slot, but the relative phase between the modes differs between the excitations in each aperture. Insight into our results is obtained through modelling the radiation emitted by a point dipole in close proximity to the air–gold surface using the finite element method.

Experimental

A gold film of nominally 100 nm thickness is deposited using electron beam evaporation (Intvac Nanochrome I) onto a high quality borosilicate glass slide with 5 nm of chromium as an adhesive layer. The rate of deposition of the gold was set to 0.3 Å/s. High quality azimuthal arrangements of three slot apertures with different transverse parameters were milled using a helium ion microscope (Nanofab Orion, Zeiss) operating at an accelerating voltage of 30 kV and a beam current of 0.1 to 100 pA. A Fibics NPVE pattern generator was used to control the milling parameters such as dose, beam step size and dwell time. Test writing was performed on a 100 nm thick Au film on a borosilicate glass substrate. Initial exposures indicated a dose of 15 nC/cm^2 as the optimal initial setting for the ion beam with a 1 µs dwell time and 50% beam overlap. The optimised ion beam current selected for milling was 1.5–2.4 pA, producing the highest quality apertures which typically required approximately 15 minutes of mill time. Slot trimers composed of slots of length L and width W arranged azimuthally in a triangle with a distance from the centre of each slot to the centroid of the configuration of S were fabricated. Scanning electron micrographs of the apertures investigated here are shown in Figure 1 along with a schematic illustrating the relevant parameters.

CL results were obtained using a scanning electron microscope (FEI NOVA Nano SEM 450) fitted with a Delmic SPARC CL system comprising an aluminium parabolic mirror with a moving stage to position the sample at the focus of the mirror [59]. A hole of 600 µm diameter is located in the mirror just above the focal point through which the electron beam passes and is then incident on the sample. A CL signal is emitted as the electron beam of 30 keV interacts with the specimen located at the focal point of the parabolic mirror. The optical CL signal reflected from the parabolic mirror is coupled into a 600 µm core diameter multimode optical fibre via an achromatic mirror. The fibre is connected to a spectrometer (PI Acton SP2300i) for CL spectral analysis. The schematic and details of the experimental CL set up can be found in various papers [60,61]. The background spectrum obtained from an adjacent, unpatterned region of the gold film is subtracted from all data and the result

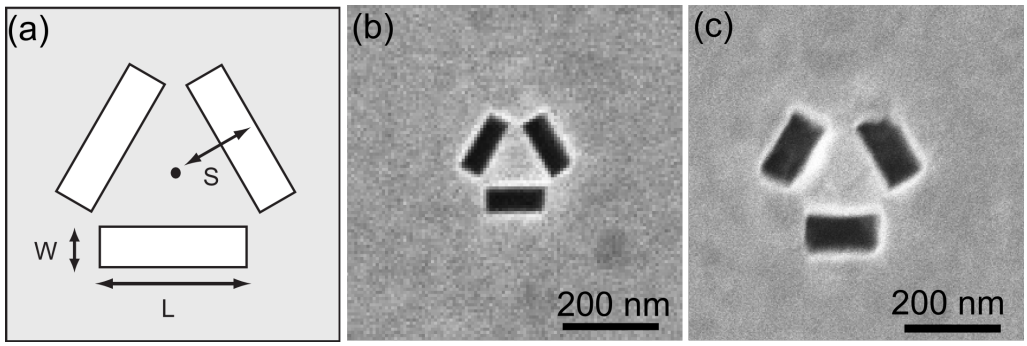


Figure 1: Scanning electron micrographs aperture structures with dimensions defined in (a). Fabricated slot trimer structures with (b) L = 95 nm, W = 34 nm and S = 60 nm, and (c) L = 150 nm, W = 40 and S = 100 nm.

normalized by the system response. The system response function was found by obtaining the spectrum from an unpatterned region of gold film and normalizing this to the theoretical result for gold.

Results

Two different trimeric ensembles of slot apertures shown in Figure 1b and Figure 1c were investigated. In addition to cavity resonances associated with the aperture, this structure may also possess plasmonic resonances in the approximately triangular region between the apertures. We first consider a trimer consisting of slots with nominal length 100 nm, width 40 nm and with a separation of 60 nm as shown in Figure 1b. In the CL spectra shown in Figure 2a, two maxima are apparent when the electron beam is incident inside the region defined by the slots, but only a single, broad peak can be seen when the electron beam is incident just outside one of the slots.

If we examine the spatial maps of the CL emission in the wavelength ranges (Figure 2b) 550–560 nm and (Figure 2c) 595–605 nm, we see that the strongest signal occurs when the beam is incident just outside the edges of the slots, in contrast to the map centred on 615 nm (Figure 2d) where the strongest emission arises when the beam is centrally incident. Asymmetries apparent in Figure 2 arise from defects introduced during the fabrication process and there is discontinuity in the data resulting from a glitch in the electron beam scan that can be discerned in the concurrent SEM image.

The results from another structure with a length of 150 nm, width 65 nm and separation 100 nm with SEM shown in Figure 1c is shown in Figure 3 with spectra shown in Figure 3a along with spatial maps of emission in bands from 550–560 nm (Figure 3b), 575–585 nm (Figure 3c) and 665–675 nm (Figure 3d). Again, it is apparent that the CL spectrum obtained

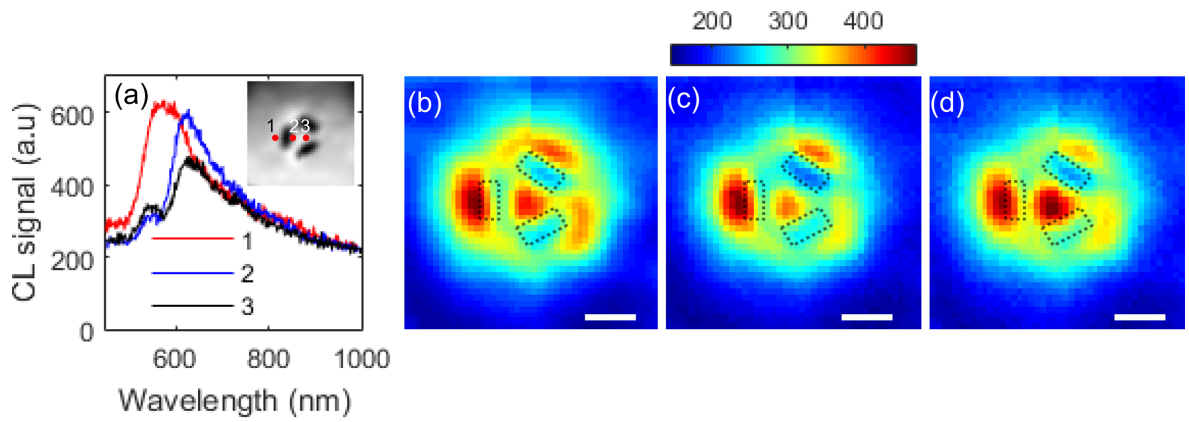


Figure 2: (a) CL spectra obtained from trimer slot structures with L = 95 nm, W = 40 nm and S = 60 nm obtained at different positions shown in the inset. The spatial dependence of CL emission in spectral bands (b) 550–560 nm, (c) 595–605 nm and (d) 610–620 nm are also shown. The scale bar in (b–d) is 100 nm.

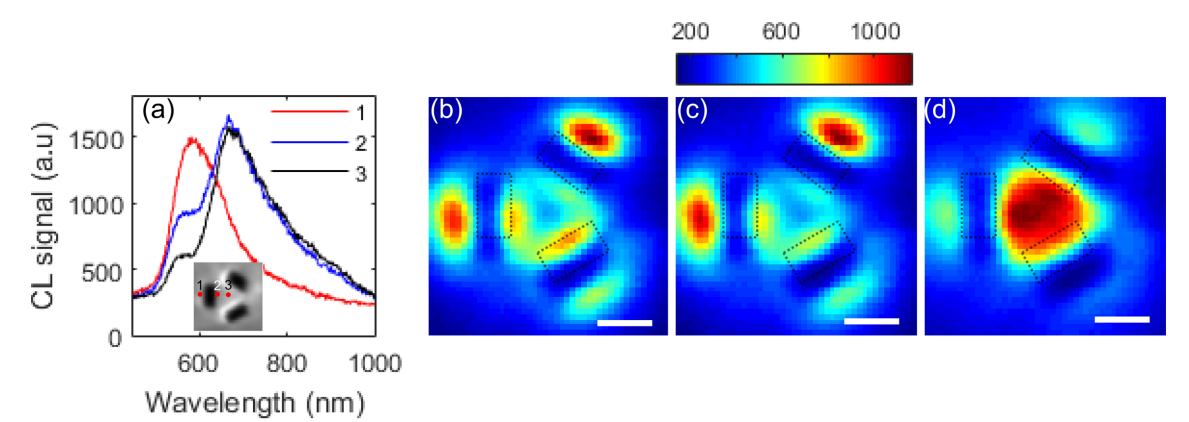


Figure 3: (a) CL spectrum from trimer slot structures with slot length 150 nm, width 65 nm and separation 100 nm obtained at different positions shown in the inset. Spatial variation of CL emission at wavelength bands (b) 550–560 nm, (c) 575–585 nm and (d) 665–675 nm. The scale bar in (b–d) is 100 nm.

depends on the excitation point and that the emission into different wavelength bands depends on the spatial location. At shorter wavelengths, we see that excitation just outside the slots produces the strongest CL emission, but when electrons are incident in the central region, the peak in emission is red-shifted.

There are clear similarities between the CL responses from the two structures. Both appear to have two peaks in the CL spectrum when the electrons are incident on the centre of the ensemble. In both cases, the shorter wavelength resonance is located around 550 nm and appears to dominate when electrons are incident on position (1), that is, on the outer edge of one of the slots. The longer wavelength peak, however, is more strongly dependent on the geometry and is red-shifted for the larger structure.

Simulations

The finite element method implemented in COMSOL Multiphysics (v 5.3) was used to gain insight into the experimentally obtained CL results shown in Figure 2 and Figure 3. In the model, a vertically oriented electric dipole placed at a height of 30 nm above the surface of the film [62] excites different resonances of the structure, leading to spectral variations in the back-emitted radiation and transmission through the apertures that depend on the transverse location of the dipole. A second order scattering boundary condition is used and no backscattering from the boundary into the modelled region was apparent. The far-field spectrum (which excludes evanescent contributions) radiated into a range of angles corresponding to a numerical aperture of 0.95 above the surface of the film is calculated by integrating $|E|^2$ over the surface of the sphere subtended by this range of angles. Similarly, the far-field transmission through the apertures into a NA 0.95 cone is also calculated.

Results for trimers with slots of length 100 nm and width 40 nm arranged with a separation of 60 nm are shown in Figure 4 corresponding approximately to the structure of Figure 1b with CL results shown in Figure 2. We plot both the back-emitted radiation toward the side of the gold film on which the dipole is located as well as the power transmitted through the aperture. Two distinct peaks in the back-emission spectra can be discerned as is the case with Figure 2a. For a centrally located dipole, the transmission through the aperture has a distinct maximum centred on 690 nm. As the dipole is moved to the outer edge of the ensemble, the transmission through the structure decreases and a broad peak, possibly associated with two resonances, located near 580 nm can be seen. This is consistent with the shorter wavelength maximum seen in the experimentally obtained CL spectrum of Figure 2a. This suggests that the longer wavelength feature in the back-emission is associated with strong coupling to the aperture. Looking at the spatial dependence of the backward emission at wavelengths of 580 nm (Figure 4b), 690 nm (Figure 4c) and 710 nm (Figure 4d), we can see that at the shorter wavelength, the backward emission at 580 nm is strongest when the dipole is centrally located, whereas at 690 nm (corresponding to the peak in the transmission spectrum if Figure 4a), we see strongest backward emission when the dipole is located over the outside edges of the slots. At slightly longer wavelengths (Figure 4d), however, we see a decrease in transmission and the sensitivity of the upward radiated power to position confined to the central region defined by the slots.

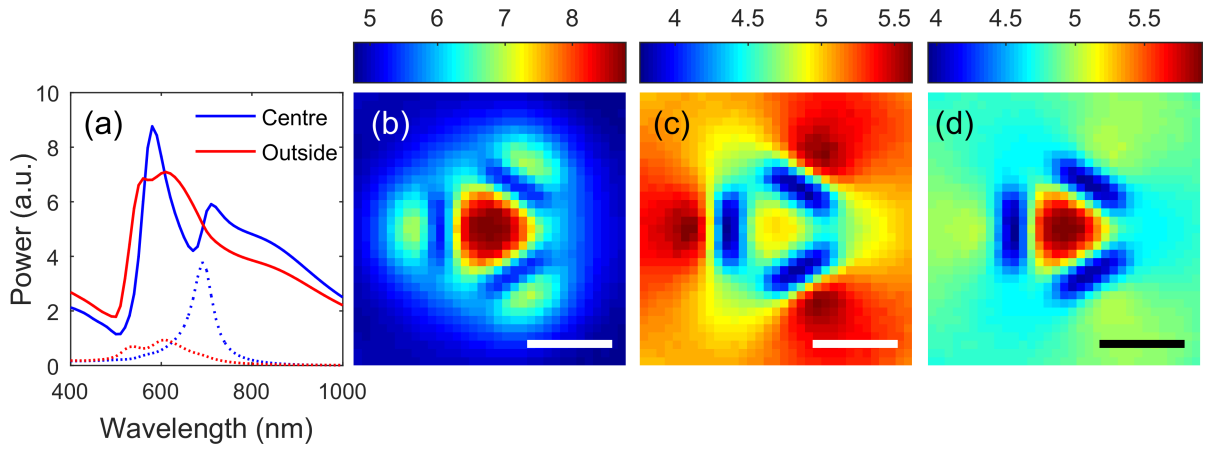


Figure 4: Simulated power radiated by a vertically oriented point dipole located 30 nm above a 100 nm thick gold film with three slots arranged in a triangular arrangement with length 100 nm and width 40 nm and separation of 60 nm. The spectra reflected from (solid curves) and transmitted through (dashed curves) the surface for dipoles located above the centre of the configuration and 5 nm outside the outer edge of one of the slots. The reflected power as a function of transverse dipole position is shown at wavelengths of (b) 580 nm, (c) 690 nm and (d) 710 nm. Scale bar is 100 nm.

We can gain further insight by examining the electric field produced inside the cavities on resonance when excited by a centred dipole and the accompanying surface charge on the dielectric–metal or air–dielectric boundary (Figure 5). The white regions observable in the surface charge distributions correspond to the air-filled holes. Figure 5a shows the magnitude of the electric field with the arrows showing the direction of the electric field at a wavelength of 690 nm in a plane just above the lower surface of the gold film.

The dominant lowest order modes of this cavity ensemble consist of nearly degenerate "radial" and "dipole" modes. The dark radial mode has the electric field in each cavity directed radially from the centroid of the ensemble and has zero net dipole moment. The degenerate dipole modes, on the other hand, have orthogonally directed net dipole moments, but, as is the case with the radial mode, the electric field in each slot is directed normal to the long axis of slots, but each slot is not equally excited. An examination of the dispersion relations of a waveguide consisting of these three slots (see Supporting Information File 1) indicates that these radial and dipole modes have an effective "cut-off" at around 600 nm and a zeroth order Fabry–Pérot would be expected at a slightly longer wavelength in an aperture in a metal film with the same geometry. It is apparent from Figure 5a that the mode excited with a centred dipole has radial symmetry. Figure 5b shows that at 690 nm, where there is a maximum in transmission, the electric field penetrates the cavity. This is accompanied by a substantial induced surface charge on the interior walls of the cavity (Figure 5d) and the relative uniformity of the field and surface charge within the cavity as a function of depth (Figure 5b) suggests that this is a zeroth order Fabry–Pérot resonance of a cavity mode. The electric field (not shown) and induced surface charge at a wavelength of 580 nm (Figure 5c) corresponding to the shorter wavelength maximum in the back-emission spectrum are consistent with only weak penetration into the cavity and the resonance being associated with a resonance of surface plasmon polaritons (SPPs) of the approximately triangular region on the surface of the film defined by the apertures. Although a mode with radially symmetry is apparent, it was difficult to identify the dipole mode, even with off centre excitation.

Comparing the results of these simulations with the CL measurements of Figure 2 suggests that the longer wavelength resonance is associated with coupling into the cavity, which is consistent with the observation that the spectral location is dependent on geometry. The shorter wavelength resonance, on the other hand, is only weakly dependent on the aperture geometry and is likely to be more strongly related to the surface geometry defined by the inner edges of the apertures.

The results of simulations of the structure with larger slots (length 150 nm, width 65 nm and separation 100 nm) corresponding approximately to the structure discussed in Figure 1c and the data of Figure 3 are shown in Figure 6. If we look at the emission spectrum (Figure 6a) obtained when the dipole is centrally located above the centre of the ensemble, we again see two distinct peaks in the back-radiated spectrum. Furthermore, two distinct, but close, resonances appear in the transmission spectrum. Moving the dipole to a location sitting above a point close to the inner edge of one of the slots produces both stronger back-radiation and transmission through the apertures. Comparing the spectra to those of the ensemble investigated in Figure 4, we see that the shorter wavelength resonance remains at approximately 600 nm, but the longer wavelength back-emission maximum has red-shifted to around 860 nm. Furthermore, the increased separation of the slots is accompanied by clear evidence for the excitation of a higher order SPP resonance on the gold–air boundary in the region between the slots (Figure 6b) at 600 m with a characteristic modal sensitivity to dipole position. At 790 nm (Figure 6c), corresponding to the longer wavelength maximum in the transmission spectra, we see a spatial dependence of emission with strong enhancement near the edges of the apertures consistent with the excitation of cavity modes. At a wavelength of 860 nm (Figure 6d) we see strong emission

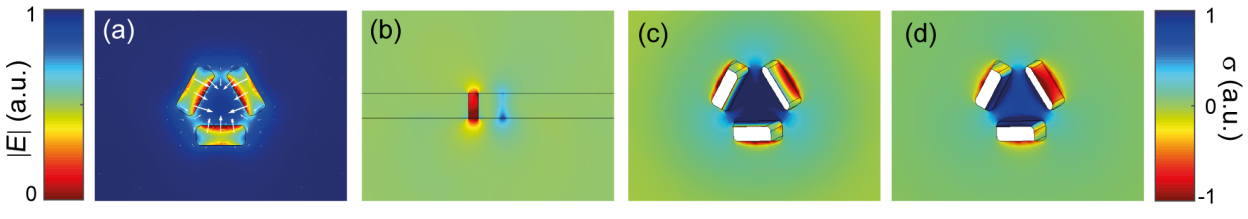


Figure 5: Electric field inside a trimer of rectangular slots of length 100 nm and width 40 nm in a gold film of thickness 100 nm at a wavelength of 690 nm excited by an electric dipole located 30 nm above the upper surface of the film and centred above the structure. The magnitude of the electric field (arrows showing direction) a distance of 5 nm above the lower surface of the gold film is shown in (a), while (b) shows the vertical component of the electric field in a vertical plane with reference to the geometry shown in (a). The (instantaneous) surface charge density on the metal boundary at a wavelength of (c) 580 nm and (d) 690 nm is also shown.

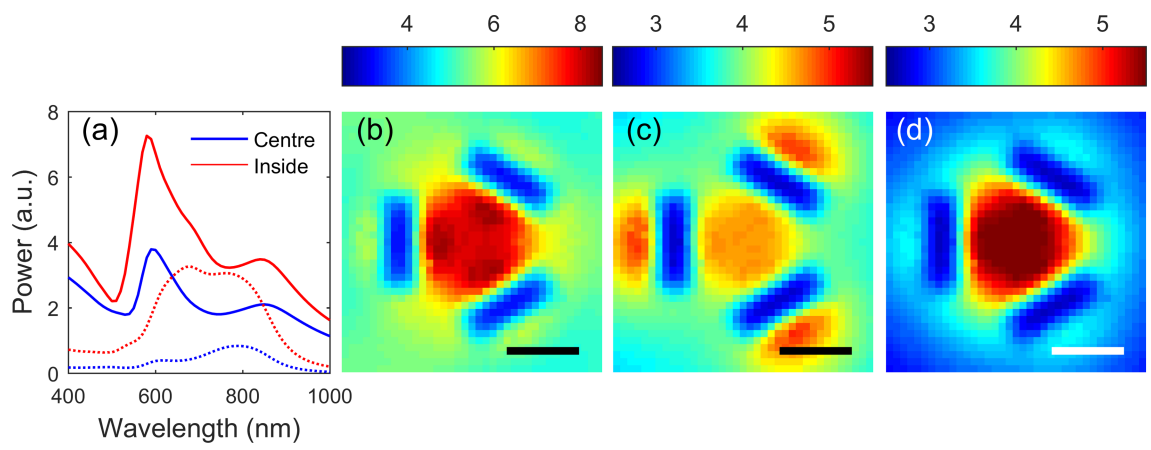


Figure 6: Simulated power radiated by a vertically oriented point dipole located 30 nm above a 100 nm thick gold film with three slots arranged in a triangular arrangement with length 150 nm and width 65 nm and separation of 100 nm. The spectra reflected from (solid curves) and transmitted through (dashed curves) the surface for dipoles located above the centre of the configuration and 5 nm outside the inner edge of one of the slots. The reflected power as a function of transverse dipole position is shown at wavelengths of (b) 600 nm, (c) 790 nm and (d) 860 nm. Scale bar is 100 nm.

over the central region suggesting that the excitation of SPPs dominates the emission process.

Examples of the electric field in the vicinity of the trimer when excited with an electric dipole sitting close to the inner edge of one of the slots are shown in Figure 7. The choice of dipole location was informed by the strong transmission through the structure for a dipole at this location as shown in Figure 6a and the fields are plotted at wavelengths of 680 nm and 800 nm, corresponding to peaks in the transmission (rather than the back-emission) spectrum. If we look at the electric field in a plane 5 nm above the bottom surface of the gold film at 680 nm (Figure 7a) and the surface charge (Figure 7c), we see that there is a net electric dipole moment associated with this mode. On the other hand, the electric field in the same plane at 800 nm (Figure 7b) has a radial symmetry indicating that this is the dark radial mode. This suggests that the degeneracy of the dipole and radial modes of the slot structure have been broken due to coupling between the apertures. This is consistent with the dispersion relation for the corresponding waveguide modes (see Supporting Information File 1) indicating a zeroth order Fabry–Pérot resonance for the radial mode at a longer wavelength than for the dipole mode. This effect is, however, too subtle to be seen in the CL measurements.

Discussion

It is apparent that irradiation with an electron beam excites several resonances of these slot aperture structures. Although quantitative agreement between the CL results and simulations looking at radiation by a point electric dipole is weak, it appears that there are two distinct, but potentially coupled, processes occurring. Firstly, the electrons can excite SPPs on the gold–air interface and the regions defined by the boundaries of the apertures will support various resonances that depend on the geometry of that region. Secondly, modes of the cavities can be excited that transport energy through the aperture. The latter depend strongly on the geometry of the aperture configuration. The FEM simulations suggest that both these types of reso-

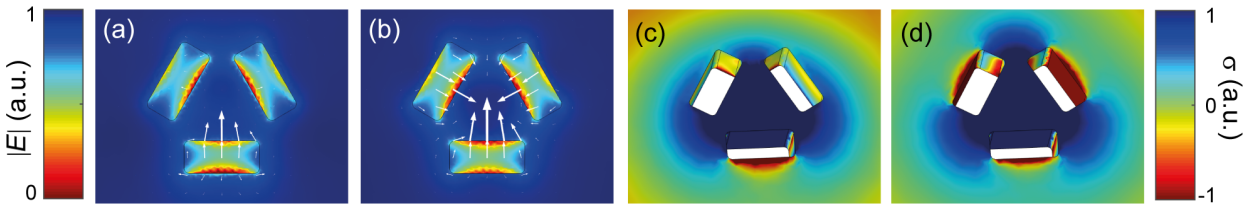


Figure 7: Electric field inside a trimer of rectangular slots of length 150 nm and width 65 nm separated by a distance of 100 nm in a gold film of thickness 100 nm excited by an electric dipole located 30 nm above a point on the film 5 nm inside the inner edge of the lower slot. The magnitude of the electric field (direction shown with arrows) in a plane a distance of 5 nm above the lower surface of the gold film at wavelengths of (a) 680 nm and (b) 800 nm. The (instantaneous) surface charge densities on the metal–dielectric boundary at wavelengths of (c) 600 nm and (d) 800 nm are also shown.

nances are being excited in our experiments and producing measurable CL emission.

In the case of the rectangular aperture trimers investigated here, the cavities are only weakly coupled, but some evidence can be seen in the excitation of both the dipole and radial modes in the simulations. Angle-resolved CL measurements could be used to obtain further information to assist in the identification of different modes since the far-field radiation patterns are quite different for radial and dipolar modes. Ongoing work is aimed at exploring different geometries in gold films of varying thickness. This will provide an opportunity to elucidate the role played by the thickness of the film, if significant, in various resonances. Although challenging, studying the optical transmission through these apertures may similarly yield interesting results.

Conclusion

We have investigated ensembles of rectangular slots in a gold film on a glass substrate and using CL we have shown that various modes of the system can be excited. Modelling results show that these resonances may be accompanied by transmission through the aperture, suggesting that cavity resonances of the apertures are being excited. There are however, spectral features that are not accompanied by any significant transmission through the aperture, suggesting that these are more closely associated with resonances arising from the surface structure on the air–metal boundary and have more in common with previous studies on metallic nanoantennas. The existence of these two different modes within this structure raises the prospect of designing aperture structures where the transverse geometry could be tailored to facilitate coupling between cavity and plasmonic resonances. This could underpin novel approaches to controlling the emission of molecules and quantum dots for applications ranging from sensing through to new types of displays.

Supporting Information

Supporting Information File 1

Additional figures.
Background material relating to the modes of rod and aperture ensembles.
[https://www.beilstein-journals.org/bjnano/content/supplementary/2190-4286-9-140-S1.pdf]

Acknowledgements

This work was performed in part at the Melbourne Centre for Nanofabrication (MCN) in the Victorian Node of the Australian National Fabrication Facility (ANFF). The authors acknowledge the financial support of the Australian Research Council Discovery Projects scheme (DP160100983).

ORCID® iDs

Kalpana Singh - https://orcid.org/0000-0002-8247-3789
Lukas Wesemann - https://orcid.org/0000-0001-9142-1342
Timothy J. Davis - https://orcid.org/0000-0002-7299-4900
Ann Roberts - https://orcid.org/0000-0003-4295-9730

References

1. Bethe, H. A. *Phys. Rev.* **1944,** *66,* 163. doi:10.1103/PhysRev.66.163
2. Bouwkamp, C. J. *Rep. Prog. Phys.* **1954,** *17,* 35. doi:10.1088/0034-4885/17/1/302
3. Roberts, A. *J. Opt. Soc. Am. A* **1987,** *4,* 1970–1983. doi:10.1364/JOSAA.4.001970
4. Lee, D.; Kim, D.-S. *Sci. Rep.* **2016,** *6,* 18935. doi:10.1038/srep18935
5. Xie, Y.; Zakharian, A. R.; Moloney, J. V.; Mansuripur, M. *Opt. Express* **2004,** *12,* 6106–6121. doi:10.1364/OPEX.12.006106
6. Chen, C.-C. *IEEE Trans. Microwave Theory Tech.* **1971,** *19,* 475–481. doi:10.1109/TMTT.1971.1127548
7. Lin, L.; Roberts, A. *Opt. Express* **2011,** *19,* 2626–2633. doi:10.1364/OE.19.002626
8. Lin, L.; Hande, L. B.; Roberts, A. *Appl. Phys. Lett.* **2009,** *95,* 201116. doi:10.1063/1.3267080
9. Compton, R. C.; McPhedran, R. C.; Derrick, G. H.; Botten, L. C. *Infrared Phys.* **1983,** *23,* 239–245. doi:10.1016/0020-0891(83)90071-4
10. Roberts, A.; McPhedran, R. C. *IEEE Trans. Antennas Propag.* **1988,** *36,* 607–611. doi:10.1109/8.192136
11. Roberts, A.; Compton, R. C. *Int. J. Infrared Millimeter Waves* **1990,** *11,* 165–174. doi:10.1007/BF01010513
12. Ebbesen, T. W.; Lezec, H. J.; Ghaemi, H. F.; Thio, T.; Wolff, P. *Nature* **1998,** *391,* 667. doi:10.1038/35570
13. Roberts, A.; Goh, X. M. Resonant Nanomteric Apertures in Metallic films. In *Nanoplasmonics: Advanced Device Applications;* Chon, J. W. M.; Iniewski, K., Eds.; Taylor and Francis: Boca Raton, FL, U.S.A., 2013; pp 159–182.
14. Rahmani, M.; Luk'yanchuk, B.; Hong, M. *Laser Photonics Rev.* **2013,** *7,* 329–349. doi:10.1002/lpor.201200021
15. Xiao, B.; Pradhan, S. K.; Santiago, K. C.; Rutherford, G. N.; Pradhan, A. K. *Sci. Rep.* **2015,** *5,* 10393. doi:10.1038/srep10393
16. Yang, J.; Rahmani, M.; Teng, J. H.; Hong, M. H. *Opt. Mater. Express* **2012,** *2,* 1407–1415. doi:10.1364/OME.2.001407
17. Zhang, S.; Genov, D. A.; Wang, Y.; Liu, M.; Zhang, X. *Phys. Rev. Lett.* **2008,** *101,* 047401. doi:10.1103/PhysRevLett.101.047401
18. Verellen, N.; Sonnefraud, Y.; Sobhani, H.; Hao, F.; Moshchalkov, V. V.; Dorpe, P. V.; Nordlander, P.; Maier, S. A. *Nano Lett.* **2009,** *9,* 1663–1667. doi:10.1021/nl9001876
19. Shu, J.; Gao, W.; Xu, Q. *Opt. Express* **2013,** *21,* 11101–11106. doi:10.1364/OE.21.011101
20. Debus, C.; Bolívar, P. H. Terahertz biosensors based on double split ring arrays. In *Proceedings of the Interntional Society for OPtics and Photonics 6987,* Strasbourg, France, May 6, 2008; 69870U. doi:10.1117/12.786069
21. Yokogawa, S.; Burgos, S. P.; Atwater, H. A. *Nano Lett.* **2012,** *12,* 4349–4354. doi:10.1021/nl302110z
22. Rajasekharan Unnithan, R.; Sun, M.; He, X.; Balaur, E.; Minovich, A.; Neshev, D. N.; Skafidas, E.; Roberts, A. *Materials* **2017,** *10,* 383. doi:10.3390/ma10040383

23. Chen, Q.; Cumming, D. R. S. *Opt. Express* **2010,** *18,* 14056–14062. doi:10.1364/OE.18.014056
24. Chen, Q.; Chitnis, D.; Walls, K.; Drysdale, T. D.; Collins, S.; Cumming, D. R. S. *IEEE Photonics Technol. Lett.* **2012,** *24,* 197–199. doi:10.1109/LPT.2011.2176333
25. Kurosawa, H.; Choi, B.; Sugimoto, Y.; Iwanaga, M. *Opt. Express* **2017,** *25,* 4446–4455. doi:10.1364/OE.25.004446
26. Jakšić, Z. Optical Metatmaterials as the Platform for a Novel Generation of Ultrasensitive Chemical or Biological Sensors. In *Metamaterials: Classes, Properties and Applications;* Tremblay, E. J., Ed.; Nova Science Publishers: Hauppauge, NY, U.S.A., 2010; pp 1–42.
27. Yu, N.; Capasso, F. *Nat. Mater.* **2014,** *13,* 139–150. doi:10.1038/nmat3839
28. Ahmadian, D.; Ghobadi, C.; Nourinia, J. *Opt. Quantum Electron.* **2014,** *46,* 1097–1106. doi:10.1007/s11082-013-9832-8
29. Mazzotta, F.; Johnson, T. W.; Dahlin, A. B.; Shaver, J.; Oh, S.-H.; Hook, F. *ACS Photonics* **2015,** *2,* 256–262. doi:10.1021/ph500360d
30. Jonsson, M. P.; Dahlin, A. B.; Feuz, L.; Petronis, S.; Höök, F. *Anal. Chem.* **2010,** *82,* 2087–2094. doi:10.1021/ac902925e
31. Larsson, E. M.; Alegret, J.; Käll, M.; Sutherland, D. S. *Nano Lett.* **2007,** *7,* 1256–1263. doi:10.1021/nl0701612
32. Dahlin, A. B.; Dielacher, B.; Rajendran, P.; Sugihara, K.; Sannomiya, T.; Zenobi-Wong, M.; Vörös, J. *Anal. Bioanal. Chem.* **2012,** *402,* 1773–1784. doi:10.1007/s00216-011-5404-6
33. Xu, K.; Wang, Z.; Tan, C. F.; Kang, N.; Chen, L.; Ren, L.; Thian, E. S.; Ho, G. W.; Ji, R.; Hong, M. *ACS Appl. Mater. Interfaces* **2017,** *9,* 26341–26349. doi:10.1021/acsami.7b06669
34. Verslegers, L.; Catrysse, P. B.; Yu, Z.; White, J. S.; Barnard, E. S.; Brongersma, M. L.; Fan, S. *Nano Lett.* **2008,** *9,* 235–238. doi:10.1021/nl802830y
35. Gallinet, B.; Martin, O. J. F. *ACS Nano* **2013,** *7,* 6978–6987. doi:10.1021/nn4021967
36. Gómez, D. E.; Teo, Z. Q.; Altissimo, M.; Davis, T. J.; Earl, S.; Roberts, A. *Nano Lett.* **2013,** *13,* 3722–3728. doi:10.1021/nl401656e
37. Olmon, R. L.; Krenz, P. M.; Jones, A. C.; Boreman, G. D.; Raschke, M. B. *Opt. Express* **2008,** *16,* 20295–20305. doi:10.1364/OE.16.020295
38. García de Abajo, F. J. *Rev. Mod. Phys.* **2010,** *82,* 209. doi:10.1103/RevModPhys.82.209
39. García de Abajo, F. J.; Kociak, M. *New J. Phys.* **2008,** *10,* 073035. doi:10.1088/1367-2630/10/7/073035
40. Losquin, A.; Kociak, M. *ACS Photonics* **2015,** *2,* 1619–1627. doi:10.1021/acsphotonics.5b00416
41. Boggs, S.; Krinsley, D. *Application of cathodoluminescence imaging to the study of sedimentary rocks;* Cambridge University Press: Cambridge, United Kingdom, 2006. doi:10.1017/CBO9780511535475
42. Brillson, L. J.; Ruane, W. T.; Gao, H.; Zhang, Y.; Luo, J.; von Wenckstern, H.; Grundmann, M. *Mater. Sci. Semicond. Process.* **2017,** *57,* 197–209. doi:10.1016/j.mssp.2016.10.032
43. Nichols, G. *Eur. J. Pharm. Sci.* **2012,** *45,* 19–42. doi:10.1016/j.ejps.2011.10.017
44. Coenen, T.; Haegel, N. M. *Appl. Phys. Rev.* **2017,** *4,* 031103. doi:10.1063/1.4985767
45. Gómez-Medina, R.; Yamamoto, N.; Nakano, M.; García de Abajo, F. J. *New J. Phys.* **2008,** *10,* 105009. doi:10.1088/1367-2630/10/10/105009
46. Heiss, M.; Fontana, Y.; Gustafsson, A.; Wüst, G.; Magen, C.; O'Regan, D. D.; Luo, J. W.; Ketterer, B.; Conesa-Boj, S.; Kuhlmann, A. V.; Houel, J.; Russo-Averchi, E.; Morante, J. R.; Cantoni, M.; Marzari, N.; Arbiol, J.; Zunger, A.; Warburton, R. J.; Fontcuberta i Morral, A. *Nat. Mater.* **2013,** *12,* 439. doi:10.1038/nmat3557
47. Marino, G.; McPollin, C.; Gili, V.; Carletti, L.; De Angelis, C.; Leo, G.; Zayats, A. V. Cathodoluminescence imgaing spectroscopy of single and dimer AlGaAs nano-disks. In *Conference n Lasers and Electro-Optics Europe & European Quantum Electronics Conference (CLEO/Europe-EQEC, 2017),* Munich, Germany; 2017; pp 25–29.
48. Zagonel, L. F.; Rigutti, L.; Tchernycheva, M.; Jacopin, G.; Songmuang, R.; Kociak, M. *Nanotechnology* **2012,** *23,* 455205. doi:10.1088/0957-4484/23/45/455205
49. Myroshnychenko, V.; Nelayah, J.; Adamo, G.; Geuquet, N.; Rodríguez-Fernández, J.; Pastoriza-Santos, I.; MacDonald, K. F.; Henrard, L.; Liz-Marzán, L. M.; Zheludev, N. I.; Kociak, M.; García de Abajo, F. J. *Nano Lett.* **2012,** *12,* 4172–4180. doi:10.1021/nl301742h
50. Tizei, L. H. G.; Kociak, M. *Nanotechnology* **2012,** *23,* 175702. doi:10.1088/0957-4484/23/17/175702
51. Mahfoud, Z.; Dijksman, A. T.; Javaux, C.; Bassoul, P.; Baudrion, A.-L.; Plain, J.; Dubertret, B.; Kociak, M. *J. Phys. Chem. Lett.* **2013,** *4,* 4090–4094. doi:10.1021/jz402233x
52. Tizei, L. H. G.; Kociak, M. *Phys. Rev. Lett.* **2013,** *110,* 153604. doi:10.1103/PhysRevLett.110.153604
53. Fang, Y.; Verre, R.; Shao, L.; Nordlander, P.; Käll, M. *Nano Lett.* **2016,** *16,* 5183–5190. doi:10.1021/acs.nanolett.6b02154
54. Coenen, T.; Polman, A. *ACS Nano* **2014,** *8,* 7350–7358. doi:10.1021/nn502469r
55. van de Haar, M. A.; Maas, R.; Brenny, B.; Polman, A. *New J. Phys.* **2016,** *18,* 043016. doi:10.1088/1367-2630/18/4/043016
56. Vesseur, E. J. R.; García De Abajo, F. J.; Polman, A. *Nano Lett.* **2009,** *9,* 3147–3150. doi:10.1021/nl9012826
57. Vesseur, E. J. R.; Polman, A. *Nano Lett.* **2011,** *11,* 5524–5530. doi:10.1021/nl203418c
58. Sannomiya, T.; Saito, H.; Junesch, J.; Yamamoto, N. *Light: Sci. Appl.* **2016,** *5,* 16146. doi:10.1038/lsa.2016.146
59. Coenen, T. Angle-resolved cathodoluminescence nanoscopy. Ph.D. Thesis, Universiteit van Amsterdam, Amsterdam, Netherlands, 2014.
60. Coenen, T.; Brenny, B. J. M.; Vesseur, E. J.; Polman, A. *MRS Bull.* **2015,** *40,* 359–365. doi:10.1557/mrs.2015.64
61. Coenen, T.; Vesseur, E. J. R.; Polman, A.; Koenderink, A. F. *Nano Lett.* **2011,** *11,* 3779–3784. doi:10.1021/nl201839g
62. Li, G.; Clarke, B. P.; So, J.-K.; MacDonald, K. F.; Zheludev, N. I. *Nat. Commun.* **2016,** *7,* 13705. doi:10.1038/ncomms13705

License and Terms

This is an Open Access article under the terms of the Creative Commons Attribution License (http://creativecommons.org/licenses/by/4.0), which permits unrestricted use, distribution, and reproduction in any medium, provided the original work is properly cited.

The license is subject to the *Beilstein Journal of Nanotechnology* terms and conditions: (https://www.beilstein-journals.org/bjnano)

The definitive version of this article is the electronic one which can be found at: doi:10.3762/bjnano.9.140